

Global climate impacts from changes in Antarctic Intermediate Water

A thesis submitted to the School of Environmental Sciences of the
University of East Anglia in partial fulfilment of the requirements for the
degree of Doctor of Philosophy

By Jennifer A Graham

November 2011

© This copy of the thesis has been supplied on condition that anyone who consults it is understood to recognise that its copyright rests with the author and that no quotation from the thesis, nor any information derived therefrom, may be published without the author's prior, written consent.

© Copyright 2011

by

Jennifer A Graham

Abstract

Observations suggest that properties of Antarctic Intermediate Water (AAIW) are changing. An understanding of how changes in the ocean may interact with the atmosphere is crucial for understanding how Earth's climate will evolve in the future. The impact of variations in AAIW is explored using a series of idealised perturbation experiments in a coupled climate model, HadCM3. Two sets of ensembles have been used. The first varied initial atmospheric states; the second varied initial states in the ocean and atmosphere. The ensemble simulations were integrated over 120 and 100 years, respectively, altering AAIW from 10-20°S in the Atlantic, Pacific and Indian oceans separately. Potential temperature was changed by $\pm 1^\circ\text{C}$, along with corresponding changes in salinity, maintaining constant potential density.

There is a surface response to changes in AAIW in each of the three major ocean basins. When the water mass surfaces in the equatorial regions, there is no significant change in sea surface temperature (SST). However, there is a SST response for each experiment when the anomalies surface at higher latitudes ($> 30^\circ$). The spatial pattern of SST anomalies in the North Pacific resembles the Pacific Decadal Oscillation. Heat and salt distribution in the Indian Ocean is influenced by the Indonesian Through-Flow (ITF), with long-term trends in transport caused by bottom pressure anomalies in the Pacific.

Anomalous sea-to-air heat fluxes leave density anomalies in the ocean, resulting in non-linear responses to opposite perturbations. In the Southern Ocean, these affect the meridional density gradient, leading to changes in Antarctic Circumpolar Current transport. The North Atlantic is particularly sensitive to cool, fresh perturbations, with density anomalies causing a reduction in the meridional overturning circulation of up to 1 Sv. Resultant changes in meridional ocean heat transport, along with surfacing anomalies, cause basin-wide changes in the surface ocean and overlying atmosphere on multi-decadal timescales. Cooling in the North Atlantic Current may be self-sustaining as it leads to high pressure anomalies in the overlying atmosphere, and increased wind stress over the sub-polar gyre. All these experiments indicate that the response to cooler, fresher AAIW would be both greater and more significant than that for warmer, saltier AAIW.

Acknowledgements

There are a number of people who have provided me with support through the course of this project. Firstly, I will thank those involved in the technical side of things. A huge amount of thanks must go to my supervisors - Karen Heywood, David Stevens and Zhaomin Wang. Without them, I would not be here today. They have kept me on track throughout my PhD, providing guidance on both the science and organisation of the project. It has been a pleasure working with them for the past 3+ years. I would also like to thank everyone in the wider Met & Oceans group at UEA. Although not directly involved in the project, they have provide a fantastic environment to study for the past few years, and have enabled me to build my knowledge through seminars, meetings and lectures in the department. Thanks has to go to Ian Stevens, who assisted with the initial set up of HadCM3 experiments. I would also like to thank the HPC support staff (Chris and Julie). They kept Cluster1 up and running, and were always available to answer my emails, whenever problems arose. Thank you to you all.

Secondly, to all my family who have supported me in my life in general during my PhD. I would like to thank my parents, who since my first year, have provided gentle encouragement to finish as soon as possible. After weekly questioning on how the thesis is going, I can now tell you that it has finally been handed in, and I look forward to giving you the final bound copy. I should also thank you for putting a roof over my head for the final year of my studies. It is a lovely house, thank you. To my younger brother, Robert, who has been living with me in Lound Rd after following me to Norwich, thank you for cooking dinner for me on the odd occasion when I may have been writing later into the evening.

Thirdly, to my many friends both at UEA and elsewhere, who have provided me with enjoyment and breaks away from my studies. I won't name you all (for fear of offending those I miss!), but will summarise a few key groups. To those away from UEA, I apologise for being distracted by my work, and not seeing you as much as I would have liked over the past few years. Thank you for putting up with me. As for those in Norwich, I have to thank James Clark, who founded the ENV Happy Hour, and all the other Happy Hour regulars, both past and present. I have enjoyed our weekly gatherings. To everyone who

took part in our Grad Bar quiz nights. We won it once! To particular friends in the years above (who will remain nameless), the examples that you set have provided me with much motivation to finish before you, and not to make the same mistakes! To Lee Gumm, who organised the ENV bike rides, which encouraged me to take up a healthy hobby. In my final year, to all involved in UEA Triathlon, who provided me with a further source of healthy procrastination. Final thanks has to go to my office mates, formerly in the Beach, and now in Monkey Island. You provided a very enjoyable working environment, with plenty of banter (occasionally science related). In all seriousness, my time as a PhD student would not have been nearly as much fun without you all. Thank you.

Contents

Abstract	v
Acknowledgements	vii
1 Introduction	1
1.1 Oceans in the climate system	1
1.2 Antarctic Intermediate Water	5
1.2.1 Formation of AAIW	5
1.2.2 AAIW Circulation	11
1.2.3 Changes in AAIW	13
1.2.4 This thesis	17
2 HadCM3 and methodology	19
2.1 Introduction	19
2.2 Model description	21
2.2.1 Ocean-atmosphere coupling	21
2.2.2 Ocean component	22
2.2.3 Atmospheric component	26
2.3 Model Evaluation	26
2.3.1 Ocean	26
2.3.2 Atmosphere	29
2.3.3 AAIW in HadCM3	30
2.4 Model perturbation experiments	36
2.4.1 Idealised perturbations using HadCM3	37
2.4.2 Past experiments with AAIW	38

2.5	Conclusion	41
3	Climate response to changes in Antarctic Intermediate Water in the Atlantic	43
3.1	Introduction	43
3.2	Method	44
3.3	EXP1 Results	48
3.3.1	Where does the anomalous water go?	48
3.3.2	Changes seen at the sea surface and in the MOC	55
3.3.3	Atmospheric responses to the anomaly	63
3.4	EXP2 Results	70
3.4.1	Where does the anomalous water go?	70
3.4.2	Changes seen at the sea surface	74
3.4.3	Atmospheric responses to SST	77
3.5	Discussion	81
3.6	Summary	83
4	Sensitivity to Initial Ocean Conditions	87
4.1	Introduction	87
4.2	Method	87
4.3	Results	88
4.3.1	Warmer, saltier AAIW	88
4.3.2	Cooler, fresher AAIW	98
4.4	Discussion	109
4.5	Summary	111
5	Response to perturbing AAIW in the Pacific	113
5.1	Introduction and Methods	113
5.2	Response to warmer, saltier AAIW	115
5.2.1	Response to surfacing in the equatorial Pacific?	115
5.2.2	Response when varying initial ocean states	122
5.3	Response to cooler, fresher AAIW	133
5.3.1	Where does the anomalous water go?	133
5.3.2	Anomalies at the ocean surface	136

5.3.3	Atmospheric response	144
5.4	Discussion	145
6	Response to perturbing AAIW in the Indian Ocean	149
6.1	Introduction and Methods	149
6.2	Results	151
6.2.1	Warmer, saltier AAIW	151
6.2.2	Cooler, fresher AAIW	161
6.3	Discussion	170
7	Discussion	173
7.1	Does perturbing AAIW affect climate?	173
7.2	Non-linear responses	174
7.3	Atmospheric responses	177
7.4	What response can we expect in reality?	179
7.5	Possibilities for future work?	180
7.6	Summary	182
A	List of Experiments	185
	References	195
	List of Acronyms	196

List of tables

A.1	List of perturbation experiments carried out.	186
-----	---	-----

List of figures

1.1	Meridional salinity section through the Atlantic, showing locations of key water masses.	3
1.2	Glacial transect of $\delta^{13}\text{C}$ for the western Atlantic.	4
1.3	Schematic of major ocean currents in the southern hemisphere.	6
1.4	Regions used for the analysis of Subantarctic Mode Water types.	8
1.5	Potential temperature–salinity distributions in northern Drake Passage. . .	10
1.6	Observed trends in AAIW core properties, from 1970s to 2009.	15
1.7	Projected change in temperature and salinity in the Southern Hemisphere ocean (21 st C – 20 th C.)	16
2.1	SST errors in HadCM3 and HadCM2 (with and without flux adjustments).	20
2.2	SST and SAT over western Europe in HadCM3, showing grid spacing.	21
2.3	Zonal-mean temperature in the Atlantic for a 500-year control simulation in HadCM3, showing grid spacing.	22
2.4	Bathymetry used in HadCM3	23
2.5	Mean monthly seasonal cycle of sea ice area in the Northern and Southern Hemispheres of HadCM3.	28
2.6	Zonal-mean salinity in the Atlantic, Pacific and Indian oceans in HadCM3	30
2.7	Tracer concentration at intermediate depths after year 1.	31
2.8	Tracer concentration at intermediate depths after year 5.	32
2.9	Mean total and eddy vertical velocities, over top 240 m.	33
2.10	Mean zonal velocity in Drake Passage.	34
2.11	Mean maximum mixed layer depth and annual ocean-atmosphere heat flux.	35
2.12	Zonal mean ocean temperature anomalies resulting from a surface freshwater perturbation around Antarctica.	39

2.13	Water mass formation regions, and region used for salinity perturbations, in an intermediate complexity model.	40
3.1	θ -S plots of control conditions in the Atlantic basin for ~ 0 – 40° S.	44
3.2	θ -S plot for perturbation and control start dumps used in EXP1 and EXP2.	45
3.3	Zonally averaged initial temperature and salinity perturbations in the Atlantic.	46
3.4	Timeseries of temperature and salinity in the core of Atlantic AAIW.	47
3.5	Zonally averaged temperature, salinity and potential density anomalies in the Atlantic for years 41-50 of EXP1.	49
3.6	Decadal salt content anomalies within columns for EXP1.	50
3.7	Schematic to show the perturbed region of the Atlantic, 10 – 20° S, and the mean locations of the strongest currents at ~ 500 m	52
3.8	Zonal average decadal salinity anomalies in the Atlantic for EXP1.	53
3.9	Total salt content anomalies in the Atlantic, for shallow, intermediate and deep depth levels in EXP1.	54
3.10	Decadal average sea surface temperature anomalies for EXP1.	56
3.11	Decadal average heat flux and surface air temperature anomalies for years 21-30 of EXP1.	57
3.12	Mean meridional streamfunction in the Atlantic.	58
3.13	Decadal average meridional overturning circulation strength anomalies within the Atlantic for EXP1.	59
3.14	Timeseries of response in six climate indices for EXP1.	60
3.15	Decadal average MOC strength anomalies and steric height difference anomalies within the Atlantic for EXP1.	61
3.16	Hovmöller plots of heat content anomalies and zonal mean steric height anomalies in the Atlantic for EXP1.	62
3.17	Timeseries of sea surface temperature and meridional ocean heat flux anomalies in the North Atlantic Current for EXP1.	64
3.18	Significant mean barotropic streamfunction anomalies in the subpolar gyre and Greenland, Iceland and Norwegian Seas, for years 51-100 of EXP1.	65
3.19	Mean anomalies of four atmospheric variables for years 51-100 of EXP1.	66

3.20	North Atlantic Oscillation indices for first 20 years of the control ensemble, calculated from annual and winter data.	67
3.21	Decadal salt content anomalies within columns for EXP2.	69
3.22	Salt content anomalies along the western boundary of the North Atlantic basin for EXP2.	70
3.23	Zonal average decadal salinity anomalies in the Atlantic for EXP2.	72
3.24	Total salt content anomalies in the Atlantic, for shallow, intermediate and deep depth levels in EXP2.	73
3.25	50-year-average anomalies of sea surface temperature and ocean-atmosphere heat flux in EXP2.	74
3.26	Decadal average meridional overturning circulation strength anomalies, and steric height difference anomalies, in the Atlantic for EXP2.	75
3.27	Hovmöller plots of heat content anomalies and zonal mean steric height anomalies in the Atlantic for EXP2	76
3.28	Timeseries of sea surface temperature and meridional ocean heat flux anomalies in the North Atlantic Current for EXP2	78
3.29	Timeseries of response in six climate indices for EXP2.	79
3.30	Mean anomalies of four atmospheric variables for years 51-100 of EXP2.	80
3.31	Zonally averaged density anomalies in the tropical Atlantic, for years 1-10 of EXP1 and EXP2.	83
3.32	Schematic to demonstrate the non-linear response to initially density-compensating perturbations (EXP1 and EXP2).	84
4.1	Timeseries of decadal-mean Atlantic meridional overturning streamfunction index, for 500 years of the control run.	88
4.2	Decadal salt content anomalies in columns for EXP1b.	89
4.3	Zonally averaged decadal salinity anomalies in the Atlantic for EXP1b.	91
4.4	Decadal sea surface salinity anomalies for the first 40 years of EXP1b and EXP2b.	92
4.5	Decadal sea surface temperature anomalies for the first 40 years of EXP1b and EXP2b.	93

4.6	Decadal ocean-atmosphere heat flux anomalies for the first 40 years of EXP1b and EXP2b.	94
4.7	Decadal anomalies for three Atlantic meridional overturning circulation indices for EXP1b.	96
4.8	Hovmöller plots of heat content anomalies and zonal mean steric height anomalies in the Atlantic for EXP1b.	97
4.9	Timeseries of response in six climate indices for EXP1b.	98
4.10	Surface air temperature and mean sea level pressure anomalies for years 31-40 of EXP1b.	99
4.11	Sea surface temperature anomalies for years 41-60 of EXP1b.	99
4.12	Decadal salt content anomalies in columns for EXP2b.	100
4.13	Zonally averaged decadal salinity anomalies in the Atlantic for EXP2b.	102
4.14	Anomalies of sea surface temperature and ocean-atmosphere heat flux, for years 51-100 of EXP2b.	104
4.15	Decadal anomalies for three Atlantic meridional overturning circulation indices for EXP2b.	105
4.16	Decadal Atlantic meridional overturning strength at 45°N, for each en- semble member of EXP2b.	106
4.17	Hovmöller plots of heat content anomalies and zonal mean steric height anomalies in the Atlantic for EXP2b.	106
4.18	Timeseries of response in six climate indices for EXP2b.	107
4.19	Mean anomalies of four atmospheric variable for years 51-100 of EXP2b.	108
4.20	Schematic to illustrate possible predisposed responses to varying initial conditions.	111
5.1	θ -S diagram for control conditions between 10 and 20°S in the Atlantic, Pacific and Indian oceans	114
5.2	θ -S plot for perturbation and control start dumps used in EXP3 and EXP4	114
5.3	Decadal sea surface temperature anomalies for the first 40 years of EXP3 and EXP3b.	116
5.4	Decadal sea surface salinity anomalies for the first 40 years of EXP3 and EXP3b.	117

5.5	Timeseries of response in six ocean climate indices for EXP3.	118
5.6	Schematic to show the perturbed region of the Pacific, 10–20°S, and the mean locations of the strongest currents at ~ 500 m.	119
5.7	Decadal salt content anomalies within columns for the first 40 years of EXP3 and EXP3b.	120
5.8	Timeseries of response in four atmospheric climate indices for EXP3. . .	121
5.9	Schematic to show the coupled ocean-atmosphere response to a positive phase of the Southern Annular Mode.	122
5.10	Decadal salt content anomalies within columns for years 41-50, 51-60, 71-80 and 91-100 of EXP3b.	123
5.11	Total salt content anomalies in the Pacific, for shallow, intermediate and deep levels in EXP3b.	125
5.12	Decadal anomalies of sea surface salinity and temperature for years 41- 50, 51-60, 81-90 and 91-100 of EXP3b.	126
5.13	Timeseries of response in six ocean climate indices for EXP3b.	127
5.14	Timeseries of response in ocean-atmosphere heat flux for Niño 3.4 region in EXP3b.	129
5.15	Timeseries of response in four atmospheric climate indices for EXP3b. . .	131
5.16	Decadal salt content anomalies within columns for the first 40 years of EXP4 and EXP4b.	134
5.17	Decadal salt content anomalies within columns for years 41-50, 51-60, 71-80 and 91-100 of EXP4b.	135
5.18	Total salt content anomalies in the Pacific, for shallow, intermediate and deep levels in EXP4b.	137
5.19	Decadal sea surface salinity anomalies for the first 40 years of EXP4 and EXP4b.	138
5.20	Timeseries of response in six ocean climate indices for EXP4b.	139
5.21	Decadal sea surface temperature anomalies for the first 40 years of EXP4 and EXP4b.	140
5.22	Ocean-atmosphere heat flux and surface air temperature anomalies for years 41-50 of EXP4b.	141

5.23	Decadal sea surface salinity anomalies for years 41-50, 51-60, 81-90 and 91-100 of EXP4b.	142
5.24	Timeseries of response in four atmospheric climate indices for EXP4b. . .	143
5.25	Timeseries of response in Southern Annular Mode and Southern Oscillation Index for EXP4.	144
5.26	Mean overturning streamfunction anomaly in the top 1000 m of the Indo-Pacific for 100 years of EXP3b.	147
5.27	Schematic to demonstrate the response to a cold, fresh perturbation (e.g. EXP4b) as it shoals towards the south (EXP4b).	148
6.1	θ -S plot for perturbation and control start dumps used in EXP5 and EXP6.	150
6.2	Schematic of the perturbed region of the Indian Ocean, 10–20°S, and the mean locations of the strongest currents at ~ 500 m.	150
6.3	Decadal salt content anomalies within columns for EXP5b.	152
6.4	Zonally averaged decadal salinity anomalies for years 91-100 of EXP5b, in the Indian, Atlantic and Pacific oceans.	153
6.5	Decadal anomalies of sea surface salinity and temperature for years 1-11, 21-30, 41-50, 81-90 and 91-100 of EXP5b.	155
6.6	Timeseries of response in eight ocean climate indices for EXP5b.	157
6.7	Timeseries of response in six atmospheric climate indices for EXP5b. . .	159
6.8	Decadal salt content anomalies within columns for EXP6b.	162
6.9	Zonally averaged decadal salinity anomalies for years 91-100 of EXP6b, in the Indian, Atlantic and Pacific oceans.	163
6.10	Decadal anomalies of sea surface salinity and temperature for years 1-11, 21-30, 41-50, 81-90 and 91-100 of EXP6b.	165
6.11	Timeseries of response in eight ocean climate indices for EXP6b.	166
6.12	Timeseries of response in six atmospheric climate indices for EXP6b. . .	168
6.13	Timeseries of response in Drake Passage transport for EXP5b and EXP6b.	171
7.1	Key regions where AAIW reaches the surface layers.	174
7.2	Percentage salt perturbation left at upper, intermediate and deep levels after 100 years in each basin.	175

7.3	Percentage salt perturbation left in each basin for each experiment after 100 years.	176
7.4	Schematic to illustrate global atmospheric responses to perturbations. . .	177
7.5	Schematic to illustrate temperature and salinity changes on isopycnals in a warming ocean.	180

Chapter 1

Introduction

1.1 Oceans in the climate system

The Earth's climate system is fuelled by the energy it receives from solar radiation. The curvature of the Earth and its surrounding atmosphere leads to an uneven distribution of heat arriving at the surface. This, along with the varying surface albedo, leads to a net gain of heat at the tropics, and a net loss of heat towards the poles. This distribution ultimately leads to circulation cells in both the atmosphere and ocean. Large-scale circulation cells, along with smaller scale eddies (deviations from the mean flow), act to carry heat away from the equator. Overall, atmospheric transport is known to dominate, with peak transports of 5 PW (1 PW = 10^{15} W) occurring at mid-latitudes (Trenberth and Caron, 2001). However, the ocean makes a significant contribution, dominating the total heat transport between 0-17°N, and having a peak total zonal transport of 2 PW (e.g. Trenberth and Caron, 2001; Ganachaud and Wunsch, 2003; Talley, 2003). The greatest meridional ocean heat transport occurs in the North Atlantic, where there is a heat flux of 1.3 PW at 24°N (Ganachaud and Wunsch, 2003). This heat transport is directly related to the strength of the meridional overturning circulation (MOC) in the Atlantic.

Oceans cover over 70% of the Earth's surface, and have a heat capacity approximately 1000 times that of the atmosphere. This large heat capacity allows the ocean to act as a large source or sink of heat in the climate system, and enables it to affect climate on long (decadal to centennial) timescales. One of the best known features of ocean circulation, particularly for those living in the UK and Western Europe, is the Gulf Stream. This current carries warm, salty water northwards along the coast of the USA. After it leaves

the coast, it is carried towards Europe in the North Atlantic Current (NAC). The warm water then allows the UK to enjoy an average temperature which is comparatively high for its latitude. East Anglia lies at $\sim 52^\circ\text{N}$, with a mean daily maximum temperature of 13.8°C for 1971-2000 (UK Met Office). However, on the opposite side of the Atlantic, at the same latitude, Labrador and Newfoundland have significantly lower temperatures. The capital of this Canadian province is St John's, which lies further south, at $\sim 47^\circ\text{N}$, yet had a mean daily maximum temperature of just 8.7°C for 1971-2000 (Environment Canada).

The Gulf Stream and NAC form part of the global MOC, which is driven by temperature and salinity variations in the ocean, and surface wind stress. Interaction between the ocean and atmosphere is crucial for determining temperature and salinity variability, and hence the global thermohaline circulation (THC). As warm, saline water is carried polewards, its heat is released to the overlying atmosphere. As it cools, water becomes denser, allowing it to sink to greater depths in the ocean. In polar regions, ocean-ice interactions can also affect salinity, through either the addition of melt-water or the subtraction of fresh water as it freezes (brine rejection).

In particular regions, prolonged exposure of the ocean to specific meteorological conditions can lead to the formation of water masses. The term water mass is used to describe a body of water which can be identified throughout the oceans by characteristic values of conservative properties, such as potential temperature, salinity and potential vorticity. These conservative properties can only change whilst the water is in contact with the atmosphere. Once the water sinks into the interior ocean, these properties will remain constant, only changing through mixing with adjacent masses. This allows water masses to be traced within the ocean to their origins at the surface. In order for a water mass to form, the water must remain in the surface mixed layer for long periods of time. As the water sinks below this layer, it will become isolated.

The location of some key water masses at depth in the Atlantic is shown in Figure 1.1. Intermediate water masses tend to be known for their salinity extremes. For example, the Mediterranean Intermediate Water (MIW) has a characteristic salinity maximum (along with warm temperatures) due to the high evaporation rates in the semi-enclosed Mediterranean Sea (Figure 1.1). This water mass spreads throughout the North Atlantic from the

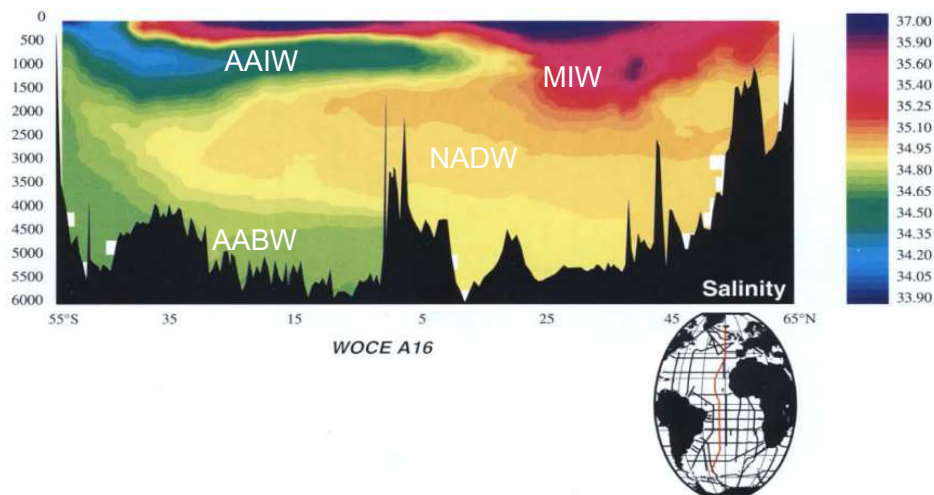


Figure 1.1: Salinity versus depth (m) for meridional WOCE section (A16) through the Atlantic Ocean. Location of the transit is shown in red on the map inset. Location of four key water masses with characteristic salinity properties are shown: Antarctic Intermediate Water (AAIW); Antarctic Bottom Water (AABW); Mediterranean Intermediate Water (MIW); North Atlantic Deep Water (NADW). Figure adapted from Plate 1.2.4, Clarke et al. (2001).

Strait of Gibraltar, beneath the less saline surface waters. In contrast, Antarctic Intermediate Water (AAIW) forms in the Southern Ocean and has a signature salinity minimum, accompanied by lower temperatures. The fresh tongue can be seen extending northwards in Figure 1.1. The northward flow of AAIW and overlying mode and thermocline waters, along with the southward flow of North Atlantic Deep Water (NADW), forms the Atlantic MOC. Antarctic Bottom Water (AABW) also moves northwards through the Atlantic. This water mass acquires its high density through a combination of cooling and brine rejection in the Antarctic shelf seas. As this cold water mass moves northwards, it contributes a southward heat flux.

As climate conditions change in water mass formation regions, this can feed into the properties of water masses at depth, potentially altering circulation patterns. Paleoclimate studies can use proxies to reconstruct the state of the ocean during past climates. For example, carbon isotope ratios can be used as tracers in the ocean, as they are determined by the productivity and air-sea exchanges in the water mass formation regions. Water masses from the Southern Ocean are characterised by low $\delta^{13}\text{C}$, whereas water masses sinking in the North Atlantic have higher $\delta^{13}\text{C}$ ratios. By analysing the $\delta^{13}\text{C}$ content in core samples from various depths on the ocean floor (for example on continental shelves and slopes, or mid-ocean ridges), this can give an indication of what depth the various water masses could be found in the ocean in the past. Figure 1.2 shows the $\delta^{13}\text{C}$ content for a section of

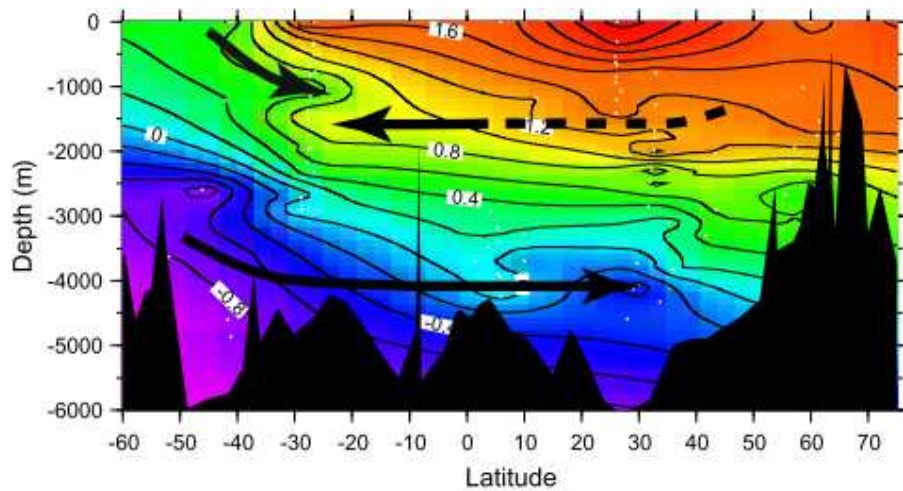


Figure 1.2: Glacial transect of $\delta^{13}C$ of ΣCO_2 for the western Atlantic Ocean basin. From Curry and Oppo (2005).

the western Atlantic ocean during the last glacial maximum (LGM). This figure indicates that during this time, the water mass from the northern Atlantic can be found at 1500 m, and be detected as far as 30°S. The deep water from the Southern Ocean can be found as far as 60°N. However, the shallower water mass from the Southern Ocean is not seen to reach the Northern Hemisphere. Comparing this with the water mass distribution of the present day (Figure 1.1), the water mass from the North Atlantic moves southwards at a shallower, intermediate depth during the LGM, and the intermediate water from the Southern Ocean does not reach as far north. However, there is a lack of proxy data at intermediate water depths between 25°S and 25°N in the western Atlantic, therefore the true extent of the glacial water masses in this region is uncertain. Although the structure of the circulation appears quite different, it is believed that the total volume transport in the glacial Atlantic may have been similar to the present day, due to an increased northward transport of deep waters (Curry and Oppo, 2005). Using a coupled climate model, Hewitt *et al.* (2001) show that the ocean heat transport in the Atlantic may have actually increased for several centuries during the LGM, reducing the cooling in parts of the North Atlantic.

Presently, the Earth's climate is warming as a result of increased volumes of greenhouse gases being released to the atmosphere (IPCC, 2007). The Fourth Assessment Report of the Intergovernmental Panel on Climate Change (IPCC AR4) stated that "key oceanic water masses are changing" (Bindoff *et al.*, 2007). Globally, the upper oceans (0-700 m) warmed by 0.17°C over years 1969-2008 (Levitus *et al.*, 2009). Changes in

precipitation and ice extent can also lead to salinity changes within the ocean. In general, there has been a freshening at high latitudes, and increased salinification at low latitudes, due to an increased hydrological cycle (Wong *et al.*, 2001; Curry *et al.*, 2003). Research is now being carried out by a number of groups to monitor how these changes in the Earth's climate system may affect the Atlantic MOC (e.g. RAPID-WATCH, THOR). However, it is still unclear how long it will take to detect any trends outside the range of internal variability (Baehr *et al.*, 2008).

1.2 Antarctic Intermediate Water

1.2.1 Formation of AAIW

For this thesis, we are primarily concerned with Antarctic Intermediate Water (AAIW), and the role that it plays in the climate system. This water mass is formed north of the Subantarctic Front (SAF, shown in Figure 1.3), before spreading northwards at intermediate depths ($\sim 1000\text{m}$) in each of the three major ocean basins. It is the most widespread of intermediate water masses, and plays an important role as part of the northward component of the MOC.

AAIW was first discovered by George Wüst during the Meteor expedition (1925-1927), when he noted the salinity minimum that was seen progressing northwards through the Atlantic (Wüst, 1935). The cold, fresh nature of this water mass initially led Deacon (1937) to suggest circumpolar formation due to the sinking of Antarctic Surface Water (AASW) beneath the SAF. Sverdrup (1940) also proposed a theory, suggesting sinking through wind-driven convergence. This was later replaced by the idea of renewal of AAIW in specific regions of the Southern Ocean, namely the southeast Pacific and southwest Atlantic (e.g. McCartney, 1977; Piola and Gordon, 1989). McCartney (1977) proposed this theory after discovering the Subantarctic Mode Water (SAMW) layer, noting that the densest form of this water mass shared the same characteristics as AAIW. From this, he concluded that it was this densest SAMW that in fact formed the source of AAIW.

SAMW is found to the north of the SAF, which is the northernmost front within the Antarctic Circumpolar Current (ACC). This front moves progressively southwards, from

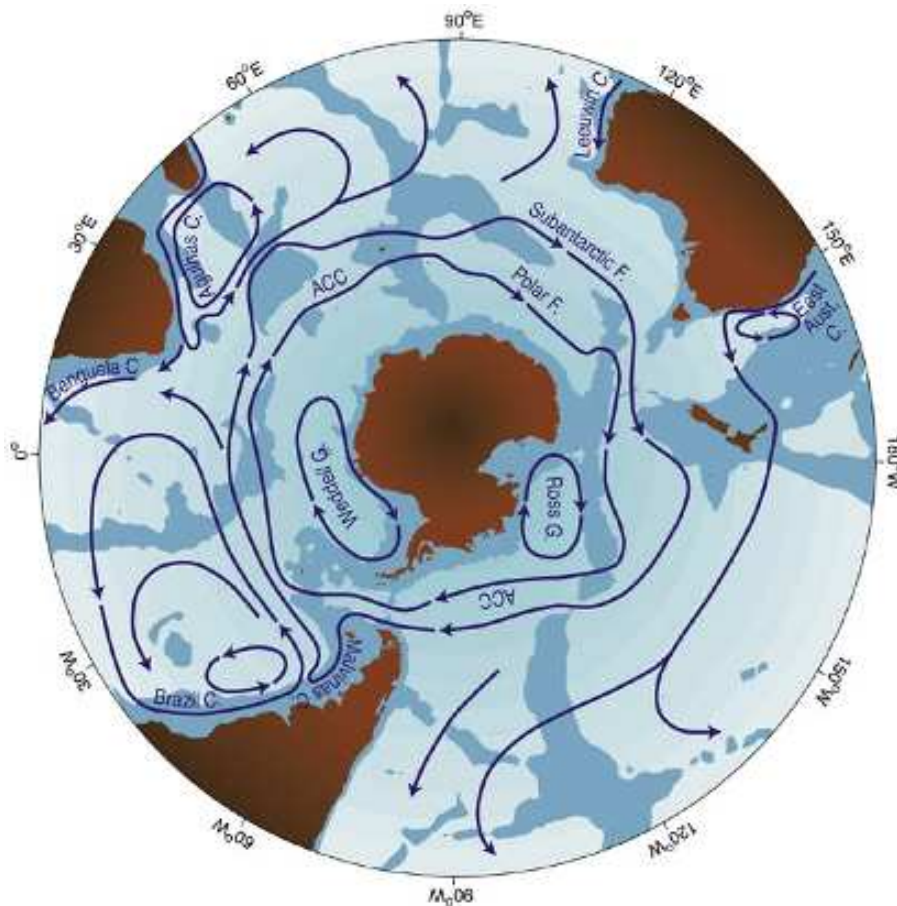


Figure 1.3: Schematic showing major currents in the southern hemisphere oceans south of 20S. Depths shallower than 3500 m are shaded. The Subantarctic Front and Polar Front form the two major cores of the Antarctic Circumpolar Current (ACC). Abbreviations used are F for front, C for current and G for gyre. From Rintoul et al. (2001).

its most northern point in the southwest Atlantic to its most southern point in the southeast Pacific, before making an abrupt turn to the north after Drake Passage (Figure 1.3). There is no single characteristic that can be used to indicate the presence of the front; rather it is seen as a deep thermal front, with steep thermoclines. In contrast, the SAMW is seen as a layer of water with a low temperature gradient, known as a thermostad, which is formed through late winter convective mixing. During autumn and winter months, cooling at the surface removes the seasonal thermocline and decreases the surface buoyancy. This drives deep convection in late winter which is seen to reach depths of more than 700 m (Rintoul *et al.*, 2001). Potential vorticity is a conservative property in the ocean, and is defined as the total vorticity (sum of planetary and relative vorticity) divided by the depth of the water column. Deep mixed layers give SAMW a characteristic potential vorticity minimum (McCartney, 1982). During the spring and summer, surface heating then leads

to the return of the seasonal thermocline, isolating the mode water beneath the surface.

Although SAMW is a circumpolar water mass, its properties vary. The warmest waters are found at the most northern point in the southwest Atlantic. As the water is advected by the SAF, it becomes progressively cooler and fresher due to the deep winter mixing, with the lower salinity resulting from the high precipitation-to-evaporation ratio in the subantarctic region. By the time it reaches the most southern point in the southeast Pacific, the freshest, coldest, and densest form of SAMW can be found. At the end of winter, the mixed layers found here have salinities and temperatures falling in the range of AAIW types seen within the subtropical gyres (McCartney, 1977). It is believed that this densest SAMW is subducted as Pacific AAIW, which then spreads northwards in the ocean.

As well as spreading north through the Pacific, a portion of SAMW is also left to travel eastwards with the ACC, through Drake Passage and then northwards past the Falkland Islands. McCartney (1977) suggested that this SAMW - colder than 4.5°C - would go on to form Atlantic AAIW and then Indian AAIW. He proposed that the denser SAMW entering the Atlantic would sink below the warmer SAMW formed in this region. The main location where this could be seen was noted as the confluence region of the Brazil and Falkland (Malvinas) currents.

Georgi (1979) later showed that the southwest Atlantic AAIW had significantly different properties to that found in the southeast Pacific. Four regions were chosen in which to determine the temperature, salinity and dissolved oxygen concentration, three of which are shown in Figure 1.4. Region 1 was chosen to lie in the southeast Pacific, where McCartney (1977) proposed that the coldest SAMW would form. Region 2 was chosen to be sufficiently far north of the Polar Frontal Zone, that no SAMW formation or AAIW renewal would occur. Region 3 then lies at the same latitude in the southwest Atlantic and was chosen to represent the 'newest' form of AAIW within this ocean. A fourth region, not shown in Figure 1.4, was chosen for comparison at the same latitude on the eastern side of the Atlantic. Observations from these four regions showed that AAIW in the Atlantic was typically colder and denser than that in the Pacific (Georgi, 1979). In regions 1 and 2, there were salinity ranges of 34.10-34.34 and 34.10-34.36, and potential temperature ranges of 3.4 - 6.0°C and 3.4 - 7.0°C , respectively. This corresponds to typical

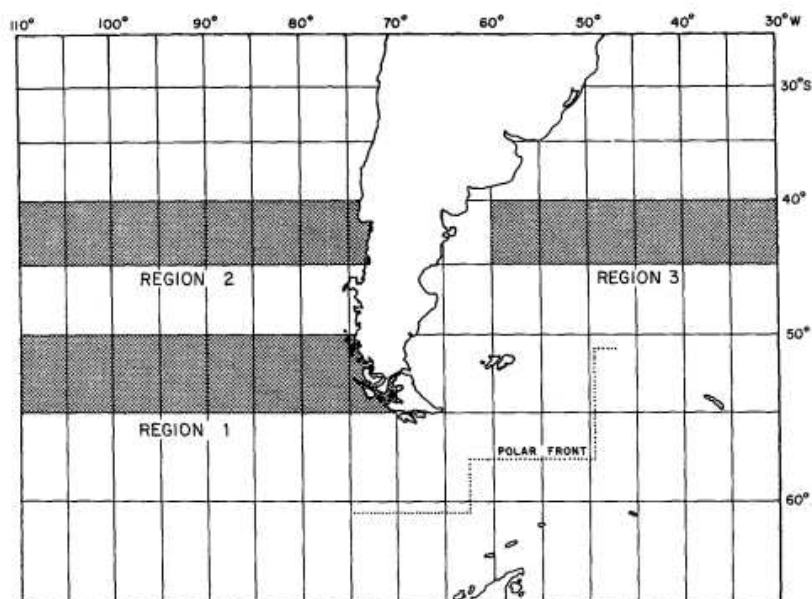


Figure 1.4: Regions used for the analysis of Subantarctic Mode Water types (Georgi, 1979). Region 1 is the proposed site of AAIW by McCartney (1977).

potential densities of 27.16 and 27.15¹. However, for region 3, there is a typical density of 27.27 due to a cooler temperature range of 2.2-6.0°C. The water in region 3 is also slightly fresher, with a range of 34.10-34.32. Georgi (1979) proposes that the difference in temperature between region 3 and the coldest AAIW in region 1 must be accounted for by heat loss processes in Drake Passage and the western Scotia Sea. However, the heat losses to the atmosphere within a 4 month transit, which were the main basis of the McCartney (1977) theory, are shown to contribute less than half of the required value. It is suggested that the additional heat loss required may be accounted for by a combination of ocean-atmosphere and cross-frontal heat fluxes (Georgi, 1979).

Oxygen concentrations can also be used to give an indication of water mass ages. After water leaves the surface, biological activity uses up the dissolved oxygen. Region 3 has similar oxygen concentrations to that of region 2, however oxygen is more soluble in lower temperatures. Therefore, the lower temperature AAIW in the southwest Atlantic has oxygen saturation values of just 82-89%, compared with values of over 90% in the southeast Pacific (Georgi, 1979). This indicates that there must be either some form of oxygen utilisation occurring during the transit, or else there is a large volume of low oxygen AAIW present. The water seen at region 4 is both saltier and oxygen poorer than

¹Potential density (σ) has units of kg m^{-3} , which are typically omitted. Values here are quoted as $\sigma - 1000 \text{ kg m}^{-3}$.

that in region 3, which suggests that circulation within the basin may introduce this saltier, lower oxygen water to the southwest Atlantic at a density of 27.32. Georgi (1979) then proposes that the water seen in region 3 was a mixture of two different sources. Southeast Pacific SAMW would be cooled further as it passed through Drake Passage and account for the salinity minimum of the Atlantic AAIW. However, the main bulk of the water is both saltier and oxygen poorer. This could be either an older, recirculated form of AAIW, or may originate from some other source.

An alternative method of formation was introduced by Molinelli (1981), proposing the theory of isopycnal exchange of AASW across the Polar Front, with significant inputs near Kerguelen Island (80°E), and again in the southeast Pacific. This differed from Wüst's original model of AASW origin, as Molinelli suggests that the surface waters are altered during the formation process, before flowing northwards as AAIW. Molinelli (1981) shows that isopycnal exchange across the Polar Front occurs at densities greater than that of SAMW, leading to the formation of isohaline thermoclines in the southeast Pacific. It is proposed that this accounts for the source of AAIW in this region, with densities of 27.2-27.3. Other sources were also noted in the Indian Ocean, near Kerguelen and near New Zealand.

Further support for McCartney's method of winter convection came from Piola and Georgi (1982). They also showed further evidence for the difference in properties between the ocean basins. Large changes in temperature and density are shown to occur in Drake Passage, south of South Africa, and south of New Zealand. In these transition regions, intense finestructure occurs, due to the presence of two different water masses. Piola and Georgi (1982) infer that as neither air-sea heat losses or cross-frontal exchange can account for the colder water in the southwest Atlantic, little AAIW from the Pacific must contribute to the Atlantic water mass. A further source must come from near the Polar Front, as proposed by Molinelli (1981).

Piola and Gordon (1989) effectively combined the two theories, proposing that the AAIW source from the southeast Pacific undergoes further deep winter mixing as well as exchange of AASW across the Polar Front, producing colder, fresher AAIW by the time it reaches the southwest Atlantic. Within northern Drake Passage, they identify two particular water masses, shown in Figure 1.5. Water mass A is the densest form of SAMW

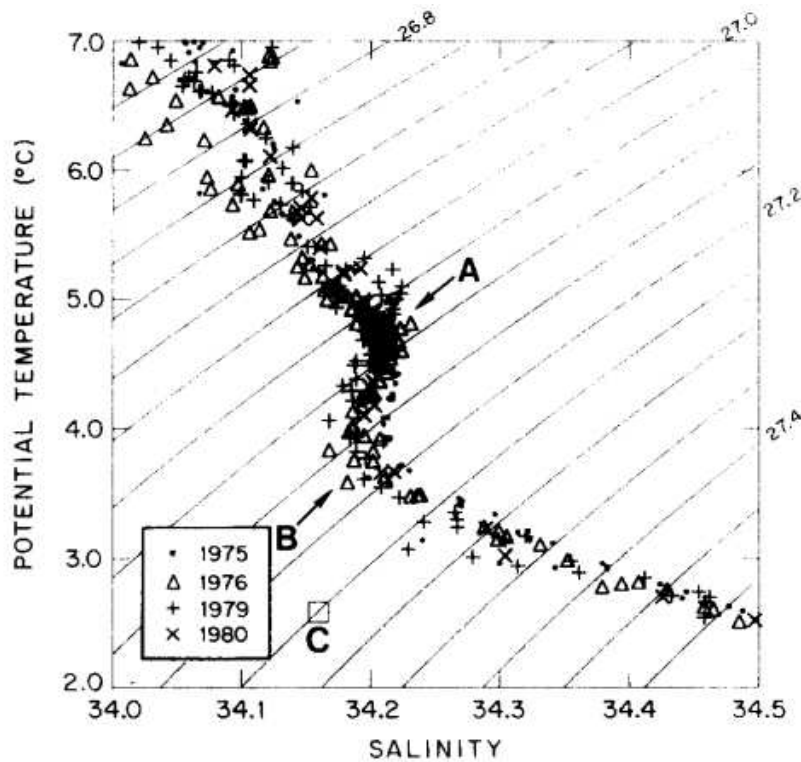


Figure 1.5: Potential temperature–salinity distributions in northern Drake Passage. Water types A and B indicate end members of AAIW. Water type C corresponds to the base of the isohaline thermocline of the southeast Pacific. From Piola and Gordon (1989).

from the southeast Pacific, whereas water mass B contains colder, fresher AASW. Water mass C occurs as the coldest end-member of an isohaline thermocline (Molinelli, 1981), and is found further south in Drake Passage. Water mass B can be considered to be composed of equal parts of masses A and C, showing that cross-frontal mixing must occur further upstream of this location (Piola and Gordon, 1989).

Downstream of Drake Passage, the intermediate water masses are advected northwards with the Malvinas current. Water mass A has its thermohaline characteristics modified by winter sea-air interaction near Burdwood Bank and mixing with the surrounding waters further north. The denser water mass (B) follows a different path, during which it is influenced primarily by isopycnal processes. Further addition of low salinity water from the Polar Front contributes to the formation of a denser water mass, from the cyclonic circulation feature described by the Malvinas Current and its return to the south (Piola and Gordon, 1989).

More recently, Talley (1996) has also cited mixing between the Brazil and Malvinas currents as a cause for the increased density in the Atlantic. This formation of Atlantic

AAIW is analogous to that of the North Pacific Intermediate Water (NPIW), where the Kuroshio and Oyashio waters meet. The contrast between the two current waters can lead to cabbeling, whereby waters of differing salinity and temperature mix to form a higher density water mass. The salinity and temperature will mix proportionally, however the non-linearity of the equation of state means that the new values will correspond to a net contraction of the water and hence a denser product (McDougall, 1987; Talley and Yun, 2001). The minimum potential vorticity, which arises from deep convection, is preserved through subduction and found throughout the Pacific AAIW. However, this feature is less persistent in the Atlantic, providing evidence for the strong role of mixing (Talley, 1996). The role of eddies in the mixing process has also been strongly recognised in a number of further studies (e.g. Marshall, 1997; Sørensen *et al.*, 2001; Sloyan *et al.*, 2010).

The key mechanisms for AAIW production can be summarised as:

- Deep winter convection north of the SAF, with the coldest, freshest water found in the southeast Pacific.
- Cross-frontal exchange of AASW.
- Mixing with surrounding water masses accounts for different AAIW properties in the southwest Atlantic.

The relative importance of the various mechanisms in determining the formation and variability of AAIW properties is still uncertain. Santoso and England (2004) also suggested that melt-water rates around the Antarctic continent were important in a circumpolar formation process, along with surface heat and freshwater fluxes. Other studies have shown that wind forcing, leading to cross-frontal Ekman transport, plays a key role (Rintoul and England, 2002; Oke and England, 2004). However, it is believed that on longer (decadal) timescales, the role of surface fluxes is likely to be more important (Downes *et al.*, 2011).

1.2.2 AAIW Circulation

Antarctic Intermediate Water is injected into the subtropical gyres in the southeast Pacific and southwest Atlantic (Talley, 1996). In the southeast Pacific, the water mass enters the gyre through a process of gradual subduction (Talley, 1996). Iudicone *et al.* (2007) propose that this process may be controlled by basin-scale meridional pressure gradients.

However, eddy transport in the Brazil/Malvinas confluence is believed to be responsible for injection in the southwest Atlantic (Talley, 1996; Tanaka and Hasumi, 2008). AAIW then travels around the subtropical gyres, spreading northwards in each of the three major ocean basins. Rather than spreading in a purely diffusive manner, Tomczak (2007) observes that the salinity field at intermediate depths in the Pacific also shows signs of eddies and fronts.

The path of AAIW can be determined by measuring a combination of its conservative properties, along with the measurement of chemical tracers within the water mass. Chemical tracers can be used to track the path of water masses throughout the oceans as they are absorbed by the water at the surface and then, like the conservative physical properties, remain constant within the ocean interior. As AAIW is renewed on decadal timescales (Sen Gupta and England, 2007b), chlorofluorocarbons (CFCs) have proved a particularly useful tracer due to the accurate atmospheric content known for the past century. The concentration of CFCs within AAIW can allow dates to be determined for when the water was last at the surface and hence allow assessment of the renewal rates and rates of flow. The use of artificial tracers in climate models has also helped to test the validation of model simulations, as well as further our understanding of these water masses (England and Maier-Reimer, 2001).

Sen Gupta and England (2007b) carried out a series of model tracer experiments, showing that the age of AAIW found in the subtropical gyres ranges from 50-150 years. It is found that AAIW in the Pacific is almost completely sourced in the same basin. AAIW that forms in the Atlantic is carried further east, south of South Africa, where it forms the source for the Indian Ocean. Previous studies suggest that although there is interaction between Indian and Atlantic water masses, there is no net transfer between the basins (Piola and Georgi, 1982; Rintoul, 1991; Suga and Talley, 1995). However, Sen Gupta and England (2007b) propose that the majority of AAIW in the Atlantic arrives from the Indian Ocean. Observations have shown that properties of intermediate waters in the South Atlantic may be influenced by variations in the Agulhas leakage (McCarthy *et al.*, 2011).

In the Atlantic, the flow of AAIW is of particular importance as it contributes to the northward component of the MOC, along with AABW. As it spreads into the North

Atlantic it forms a major warm source of the NADW, which then acts as the southward component of the MOC. This overturning cell then leads to a net equatorward transport of heat (Suga and Talley, 1995). Wüst (1935) initially proposed that AAIW would be carried northwards, across the equator, in a continuous western boundary current. It is now known that the majority of the flow lies within the subtropical gyres, however a western boundary flow does still exist beneath the southward flowing Brazil Current. Flow along the coast of Brazil carries the water mass across the Equator, after which it can enter the western boundary current in the North Atlantic (Oudot *et al.*, 1999). As the water mass spreads northwards, mixing with the surrounding water dilutes the core AAIW properties. In the northern hemisphere, the AAIW's salinity minimum becomes hard to detect around 20°N. However, traces of the water mass (from its silica minima) may still be found up to 60°N, consistent with the path of the North Atlantic Current (Tsuchiya, 1989).

As well as travelling northwards within the basins, a portion of AAIW continues to travel around Antarctica in the ACC. Rintoul (1991) showed that a surplus amount of AAIW was carried into the South Atlantic through Drake Passage, which is then compensated by a surplus of deep and bottom water leaving south of Africa. This process of deep water leaving the Atlantic to be replaced by intermediate water through Drake Passage closes the global thermohaline cell.

1.2.3 Changes in AAIW

Observations have shown that the properties of the ocean are changing along with our changing climate. A freshening trend has been observed in both the Pacific and Indian Ocean intermediate waters (Wong *et al.*, 1999; Bindoff and McDougall, 2000; Aoki *et al.*, 2005). Wong *et al.* (1999) showed that there had been a cooling and freshening of the salinity minimum in the South Pacific, with a mean freshening of 0.02 in the AAIW layer. They also noticed a freshening trend in the North Pacific Intermediate Water (NPIW), providing evidence for increased precipitation at high latitudes. In the Indian Ocean, Bindoff and McDougall (2000) showed that there had been a cooling and freshening of AAIW between the 1960s and 1987, along a section at 32°S. This was attributed to warming of surface waters and an increased hydrological cycle, both signatures of anthropogenic climate change (Banks and Bindoff, 2003). However, Bryden *et al.* (2003) showed that

between 1987 and 2002, the upper thermocline mode waters along this same section had become saltier, reversing the previous trend. This demonstrates that more frequent observations are needed to determine whether changes observed on such sections lie within the range of internal variability, or are part of a long-term trend.

In the Atlantic Ocean, observations have not shown a consistent trend. The Intergovernmental Panel on Climate Change (IPCC) Fourth Assessment Report (of the IPCC) (AR4) pointed towards a general freshening trend, with Curry *et al.* (2003) providing the evidence for the Atlantic Ocean. Their results, from a transect between 50°S to 60°N, show a freshening of 0.02 in AAIW towards the southern end of the section between the late 1950s and 1990s. However, Arbic and Owens (2001) have shown an increased salinification, along with a general warming of $0.5^{\circ}\text{C century}^{-1}$, in Atlantic intermediate waters (1000 - 2000 db). The results shown by Arbic and Owens (2001) cover a wider range of longitudes in the Atlantic than those of Curry *et al.* (2003), but only extend between 32°S and 48°N. Therefore, they may not capture more recent changes in AAIW and its surface formation regions, which would be seen further south. The freshening observed by Curry *et al.* (2003) occurs south of 15°S, with more saline intermediate waters further north. It should also be noted that the salinity trends shown by Arbic and Owens (2001) are acknowledged to be less significant than their temperature results, and Curry *et al.* (2003) do not present any significant temperature trends for AAIW.

More recently, Naveira Garabato *et al.* (2009) show that there has been a freshening of AAIW in Drake Passage, by ~ 0.05 , between 1970s and the early 21st century. They explain that this freshening is due to climate change in the region west of the Antarctic Peninsula, with an increased precipitation and decrease in winter sea ice extent. Despite the freshening of water entering the Atlantic from the Pacific, McCarthy *et al.* (2011) observed an increased salinity in AAIW along 24°S in the Atlantic. A warming trend was also found in the South Atlantic intermediate waters, along with an increased Apparent Oxygen Utilisation (AOU, difference between saturation and observed oxygen content). McCarthy *et al.* (2011) show that this increased AOU is due to the influence of Indian Ocean water, and increased Agulhas Leakage. As a greater portion of AAIW in the Atlantic arrives from the Indian Ocean, this is also shown to account for the increased salinity in the basin.

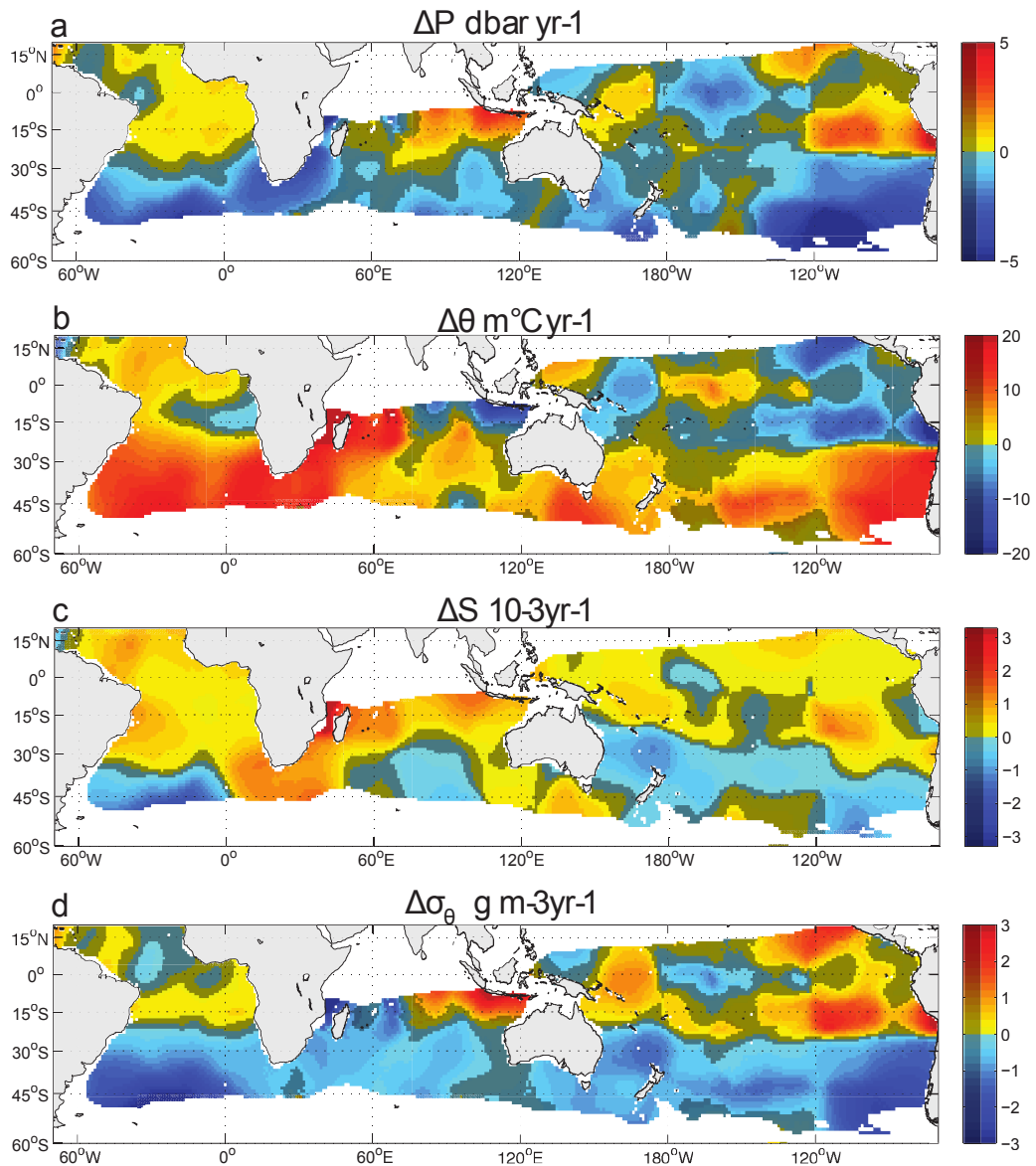


Figure 1.6: Maps of linear trends in AAIW core properties, from 1970s to 2009, for (a) pressure, (b) potential temperature, (c) salinity, and (d) potential density. Trends have been calculated from Argo and ship-based CTD data. Shaded regions indicate trends that are not significantly different from zero at the 95% confidence level. From Schmidtko and Johnson (2011).

Schmidtko and Johnson (2011) use a combination of recent Argo float observations, ship-based conductivity, temperature, depth (CTD) measurements, and bottle data, to analyse trends in AAIW core properties since the 1920s. Maps of trends observed since the 1970s are shown in Figure 1.6. The salinity minimum is found to have warmed and shoaled, with a decreased density (Figures 1.6a,b, and d). Salinity trends are found to be small, with signs varying regionally (Figure 1.6c), and contribute relatively little to the density trends. The rate of warming has increased since the 1970s, with zonal-mean increases of $0.14^{\circ}\text{C decade}^{-1}$, $0.08^{\circ}\text{C decade}^{-1}$ and $0.06^{\circ}\text{C decade}^{-1}$ between 50°S

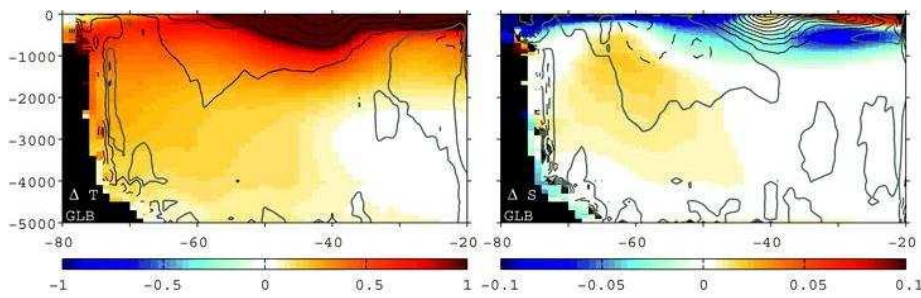


Figure 1.7: Projected change in the global zonal average potential temperature ($[\text{°C}]$, left) and salinity (right) ($21^{\text{st}} \text{ C} - 20^{\text{th}} \text{ C}$, colour contours). Superimposed contours indicate the changes that would result from a southward shift of the 20^{th} century temperature distribution by 1° latitude, with zero contour in grey and positive (negative) values shown by black solid (dashed) lines. Left: contour interval is 0.2°C . Right: contour interval is 0.01 . Values shown are averaged from a multimodel ensemble of IPCC AR4 model projections. From Sen Gupta *et al.* (2009).

in the Atlantic, Pacific and Indian oceans, respectively. Although the sea surface temperature (SST) has warmed in AAIW formation regions, the increase is not large enough to account purely for the change in core temperatures. It is suggested that increasing SST, combined with a poleward shift of the Southern Hemisphere westerlies since the mid-1970s, may result in the observed increasing trend (Schmidtko and Johnson, 2011).

Although some of the observational evidence may appear to be conflicting, IPCC AR4 climate models have shown that this water mass is likely to change by the end of the century as we see changes in the atmospheric properties in the surface formation regions (Sen Gupta *et al.*, 2009; Downes *et al.*, 2011). Sen Gupta *et al.* (2009) show a projected warming throughout intermediate depths in the Southern Hemisphere, of up to 1°C , over the next century (Figure 1.7, left). The projections of salinity changes are less consistent between basins, but suggest a decreased salinity in the upper 1000 m, and increased salinity at greater depth, within $60\text{--}40^{\circ}\text{S}$ (Figure 1.7, right). Downes *et al.* (2011) show that heat and freshwater fluxes in the formation regions lead to a warming and freshening of both SAMW and AAIW. The rate of subduction also decreases due to increased buoyancy and decreased mixed layer depths in these regions. As the water masses move to lighter densities, this accounts for the cooling and freshening observed on isopycnals lighter than 27.4 (Downes *et al.*, 2011). Downes *et al.* (2011) and Schmidtko and Johnson (2011) both mention the potential impacts of AAIW changes in relation to carbon uptake in the Southern Ocean and ventilation of the tropical thermocline. However, none of these previous studies have focused on how changes in AAIW temperature and salinity may feed back within the climate system.

1.2.4 This thesis

An understanding of what impact changes in the oceans may have on the atmosphere is crucial to our understanding of how the climate will change in the future. Given the fact that AAIW is renewed on timescales of less than 100 years, and plays a key role in global circulation, this water mass could be of particular importance within climate projections. For example, if warmer or cooler AAIW upwells in the tropics (or further north) as it progresses northwards in the ocean, then this may alter the surface temperature of the ocean in this region, and hence lead to an atmospheric response over the ocean and surrounding continents. This thesis aims to investigate the potential climate response to changes in AAIW temperature and salinity. A series of experiments are presented, investigating the impact of changing properties in each of the three major ocean basins - Atlantic, Pacific and Indian (Chapters 3-6). Through these, we will look to see where the altered AAIW influences the surface waters, and if it comes to the surface, whether there is an atmospheric response. The experiments are carried out with the use of a coupled climate model, HadCM3, a description of which is provided in Chapter 2, along with an introduction to the methods that will be used. Final conclusions and discussions will be presented in Chapter 7.

Chapter 2

HadCM3 and methodology

2.1 Introduction

HadCM3 is a coupled ocean-atmosphere general circulation model (OAGCM), produced by the Hadley Centre at the UK Met Office (Gordon *et al.*, 2000). OAGCMs play an important role in our attempts to understand and predict climate change. Although HadCM3 is not one of the most recent of these, it is still recognised as one of the leading models, and was used in both the Third and Fourth Assessment Reports (TAR and AR4) of the Intergovernmental Panel on Climate Change (IPCC) (McAvaney *et al.*, 2001; Randall *et al.*, 2007). This model evolved from a previous version of the Hadley Centre model, HadCM2 (Johns *et al.*, 1997).

The improvements made allow HadCM3 to run without the need for flux adjustments. In order to maintain a stable climate, the interactions between the ocean and atmosphere must conserve energy transports. If the transport of heat across the boundary is not balanced by transport in or out of the ocean cell, then the climate will begin to drift. One major problem with HadCM2, as well as other early OAGCMs, is that large drifts would tend to occur when simulating the current climate. Figure 2.1c shows that the drift in HadCM2 leads to a decrease in SST across most of the world's oceans. Flux adjustments could be used to correct this drift, adding to the surface heat, water or momentum fluxes. Figure 2.1b shows the reduced errors in HadCM2 simulations with flux adjustments. However, these flux adjustments have no physical basis and disguise systematic problems in the model, which can be seen in the unflux-adjusted simulations. Figure 2.1a shows the simulation using HadCM3. Although the errors appear higher than that with the flux-adjusted

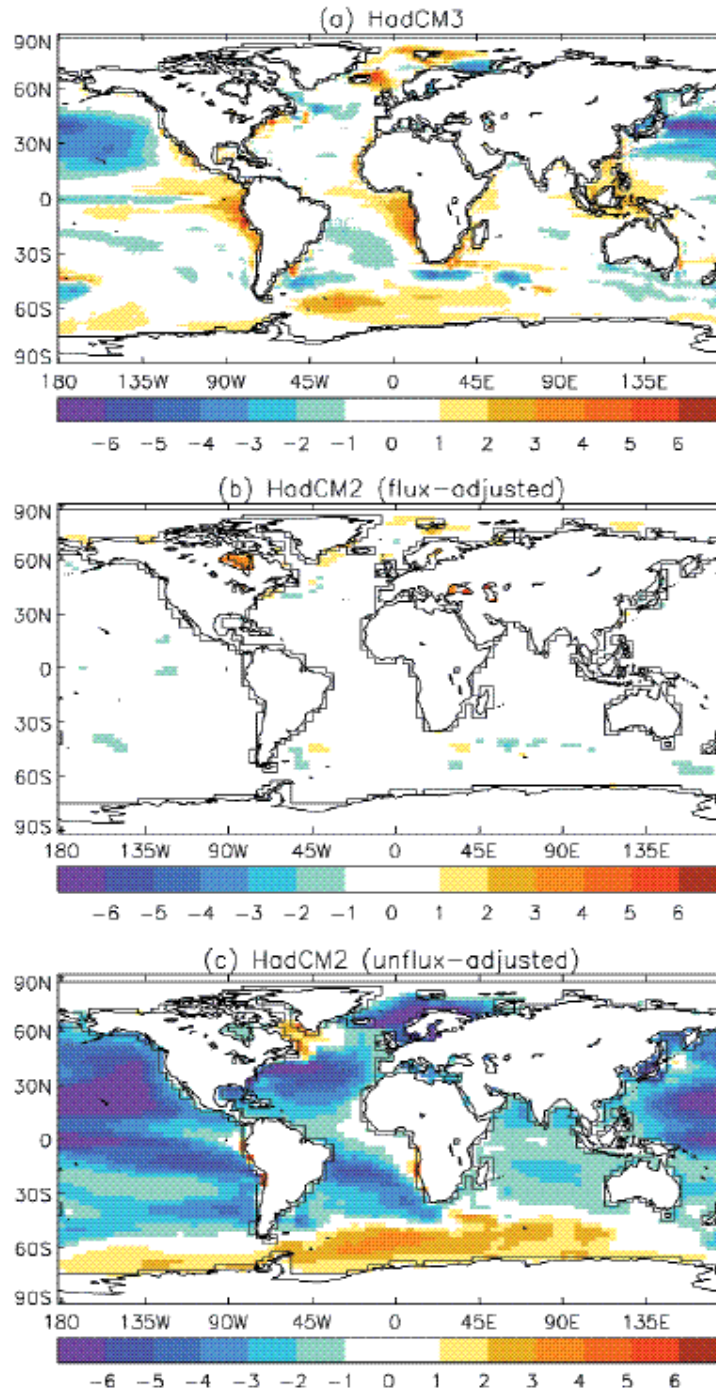


Figure 2.1: Decadal mean SST errors relative to the GISST climatology for (a) the non-flux adjusted model HadCM3 (Gordon et al., 2000), (b) flux adjusted model HadCM2 (Johns et al., 1997), (c) HadCM2 run without flux adjustments. The figures are from representative periods at least 100 years after each control run. From IPCC (2001).

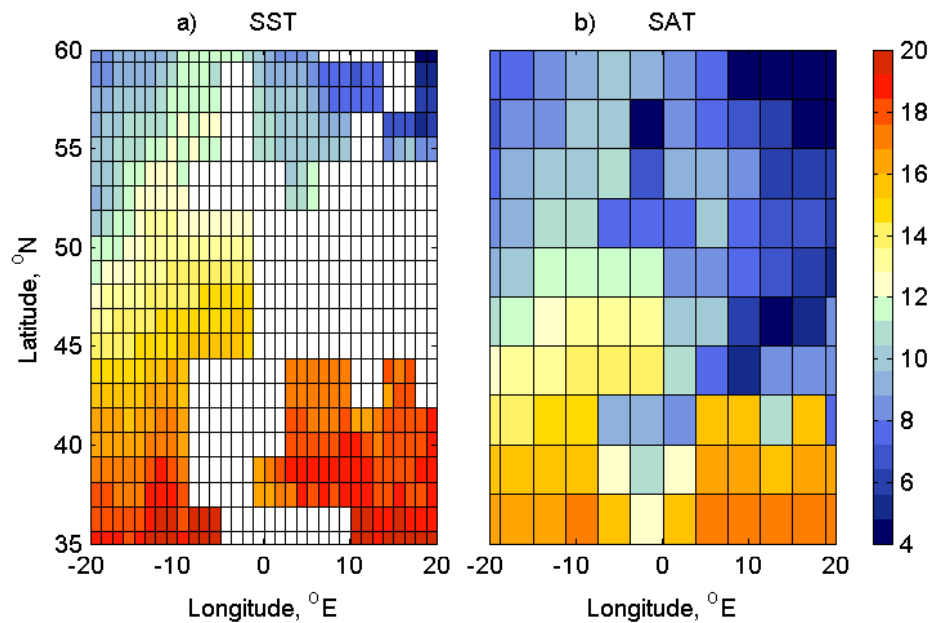


Figure 2.2: Annual mean a) sea surface temperature (SST, [$^{\circ}$ C]); b) surface air temperature (SAT, [$^{\circ}$ C]), over western Europe (20° E – 20° W, 35° – 60° N) from a 500 year control simulation (model years 2789-3289). Grid lines illustrate the different resolution of the ocean and atmosphere components ($1.25^{\circ} \times 1.25^{\circ}$ in HadOM3; $2.5^{\circ} \times 3.75^{\circ}$ in HadAM3).

HadCM2, this model has been run without flux adjustments and is therefore a considerable improvement on the previous model. Without flux adjustments, a major source of error compensation has also been removed. The key changes made between HadCM2 and HadCM3 include the addition of mixing parameterisations, improved mixed layer schemes and higher resolution. Each of these aspects will be discussed in Section 2.2.2.

2.2 Model description

2.2.1 Ocean-atmosphere coupling

The coupled model is split into two main components, each of which can be run separately to study their individual processes. Both the atmosphere (HadAM3) and ocean (HadOM3) are hydrostatic, grid point models, using an Arakawa B grid. Properties such as salinity and temperature are calculated at each grid point, whereas velocities are calculated at the centre of a box formed by four grid points.

The ocean and atmosphere components are coupled once each day. The atmospheric component is integrated first, with constant SSTs and sea ice extents for 24 hours. After

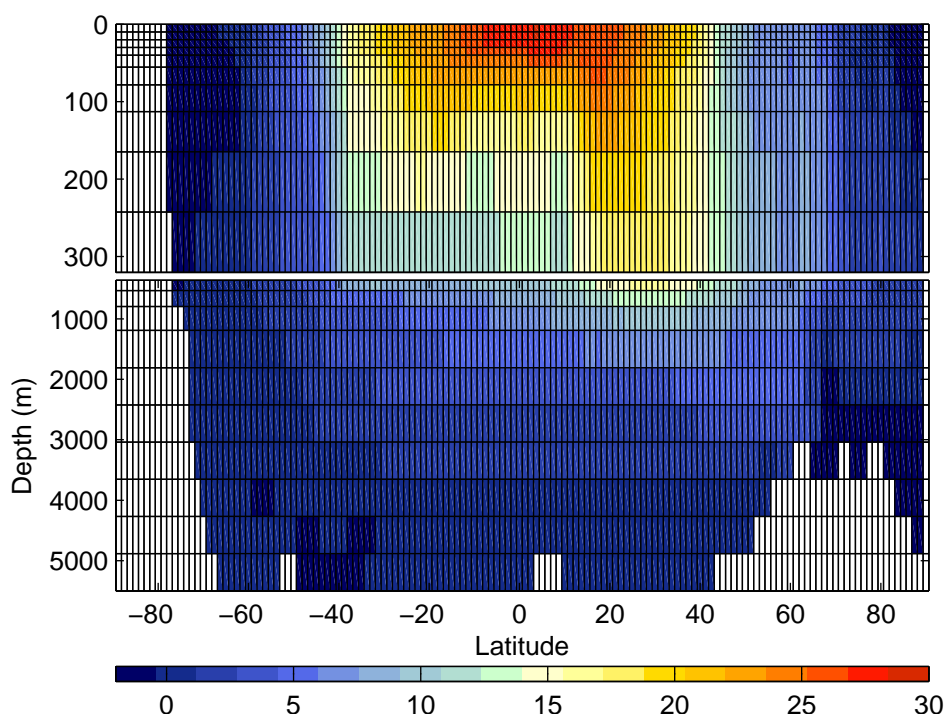


Figure 2.3: Zonal-mean potential temperature [$^{\circ}\text{C}$] in the Atlantic Ocean sector of HadCM3, from a 500-year control simulation (model years 2789-3289). Black grid-lines show the ocean model grid spacing (144×20). The two panels have different vertical axes: top panel shows the upper levels, 1-10; bottom panel shows levels 11-20. White regions indicate model bathymetry.

this, the forcing fluxes from the atmospheric output are used to integrate the ocean forwards by one day. The resulting SSTs and sea ice values can then be passed back to the atmosphere. As there are 6 ocean grid points to each box in the atmosphere (Figure 2.2), a combination of linear interpolation and averaging is used when transferring data between the two grids (Gordon *et al.*, 2000).

2.2.2 Ocean component

The ocean component of HadCM3 is based on a Bryan-Cox primitive equation model (Cox, 1984). The improved horizontal resolution of HadCM3, compared with its predecessor, leads to considerably improved simulations of ocean heat transports. HadCM2 had a resolution of $2.5^{\circ} \times 3.75^{\circ}$ in the ocean (Johns *et al.*, 1997), compared with $1.25^{\circ} \times 1.25^{\circ}$ in HadOM3 (Figure 2.2a). The model has 20 vertical levels, with resolution concentrated near the surface (Figure 2.3). In the upper regions of the ocean, properties can vary more rapidly, both over time and distance. This leads to greater transport rates, requiring greater resolution. The grid thickness therefore increases from an order of 10 m at the surface, to 1 km at the bottom of the ocean.

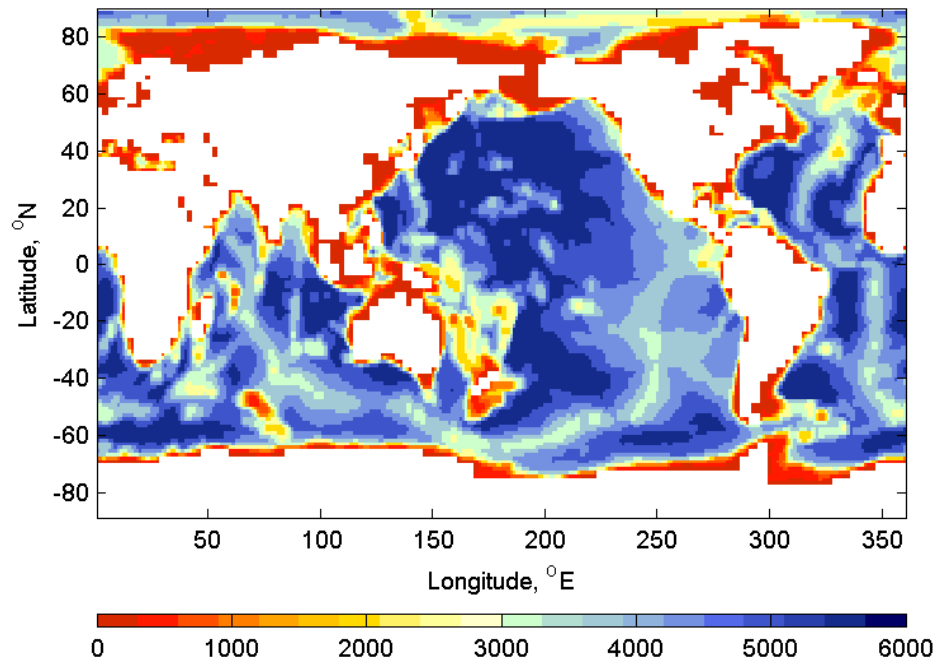


Figure 2.4: Bathymetry used in HadCM3 [m]. Coastline matches the resolution of the atmospheric component ($2.5^\circ \times 3.75^\circ$).

Topography was taken from the ETOPO5 (1998) $1/12^\circ$ resolution dataset and adapted to fit the model grid. A smoother was applied to avoid gridscale noise and the depth of channels within the Greenland-Iceland-Scotland ridge were altered to compensate for their sub-gridscale size. The sensitivity of Bryan-Cox-type ocean models to the depth of the Greenland-Iceland-Scotland ridge is demonstrated by Roberts and Wood (1997). The resulting bathymetry used in HadCM3 is shown in Figure 2.4. An island was placed at the North Pole to avoid a singularity in the spherical coordinate system (Figure 2.3). Near the poles, fields are also fourier-filtered to prevent instabilities due to the Courant-Friedrichs-Lewy (CFL) criteria.

To ease the coupling between ocean and atmosphere, the coastline used is that of HadAM3, with a resolution of $2.5^\circ \times 3.75^\circ$ (Figures 2.2 and 2.4). This means that there are very coarse representations of channels such as the Indonesian Through-Flow (ITF). In the model, this initially led to too much water passing through an unrealistically large gap between Indonesia and Asia. To compensate for this, barotropic flow is now only allowed between Papua New Guinea and Indonesia in the model (Gordon *et al.*, 2000).

Parameterisations are used when grid resolution is not fine enough to represent processes within the model. One key mechanism, which fits into this category, is eddies.

They can act on a number of length- and time-scales, and lead to the dissipation of heat through their eddy viscosity. To represent these sub-gridscale eddies, the model uses the Visbeck *et al.* (1997) version of the Gent and McWilliams (1990) scheme, with a locally determined thickness diffusion coefficient, and the Redi (1982) along isopycnal diffusion scheme. Near surface vertical mixing is represented by a hybrid approach, with a mixed layer sub-model (Kraus and Turner, 1967) and a K-Theory scheme (Pacanowski and Philander, 1981). A parameterisation is also used to simulate the outflow from the Mediterranean, where water is partially mixed across the Strait of Gibraltar.

At high latitudes, each ocean grid box can have partial sea ice cover. Completely unbroken ice is rarely observed, therefore the concentration (0 - 1) is limited to 0.995 in the Arctic and 0.980 in the Antarctic. This parameterisation of concentration is based on that of Hibler (1979). Ice will form when the SST drops below the freezing point of sea water, which is -1.8°C in HadCM3. After formation, ice can then be advected between neighbouring grid boxes. The sea ice model uses a simple thermodynamic scheme (based on the zero-level model of Semtner (1976)) and contains parameterisations of ice drift and leads (Cattle and Crossley, 1995).

Leads are cracks in the ice that form when the ice flows diverge or shear due to wind or currents in the water beneath. As these cracks form, the water is exposed to the cold atmosphere and new ice can then form during the winter, leading to brine rejection and increased salinity. However, in the summer, the open water in leads has a lower albedo than the surrounding ice. This allows the water to absorb more heat and increase the rate of melting. Effects of sea ice melt and formation are accounted for within the model, with a constant salinity of 0.6 assumed for sea ice (Gordon *et al.*, 2000). As well as melt and formation, salinity can also be reduced by snow and rainfall into leads. Sublimation on the ice also increases ocean salinity as the salt is assumed to blow in to the open water.

The albedo of ice is set to vary with temperature. At -10°C and below, the albedo is 0.8, however as temperature increases to 0°C , the albedo falls linearly to 0.5. This value is still significantly larger than that of open water, 0.06. The surface fluxes and temperatures for ice and leads are then calculated separately within the atmospheric component of the model.

The dynamics of sea ice are represented by a simple scheme from Bryan (1969).

Wind stress is applied to the ocean beneath the ice, and ice thickness, concentration and snow depth are then advected using the current within the top ocean layer. Ice rheology is crudely represented by preventing convergence of ice once the depth reaches 4 m, although this depth can be increased by further freezing (Gordon *et al.*, 2000).

The rigid lid in HadCM3 means that any freshwater flux into or out of the ocean does not lead to changes in volume. Instead this flux of water, W , is converted to a flux of salinity, F_s , through $F_s = -WS_o/\rho_o$, where ρ_o is a constant reference density and S_o is a constant salinity of 35. Using this reference salinity, instead of the locally varying values, ensures that there is no drift in the global mean when there is no net water flux. This will lead to exaggerated effects in regions where $S < S_o$, and under-representation of the freshwater flux for those where $S > S_o$, however the impact is generally small.

In HadCM3, the net water flux is not found to be zero (Gordon *et al.*, 2000). A small value of 0.01 mm day^{-1} is applied to allow for internal drainage basins. However, the majority of the imbalance comes from the accumulation of snow on Greenland and Antarctica, equivalent to 7.3 mm year^{-1} . This converts to a salinity drift of 0.1 in 1000 years, and hence a drift in the total salt content of the global ocean. In the real world, the fresh water is returned through the calving of icebergs, which is not represented in the model. Instead, a uniform flux is applied in regions adjacent to ice sheets, where icebergs are known to occur. Although this flux would not be uniform in reality, the state of observations and sensitivity of the model did not justify any more elaborate treatment (Gordon *et al.*, 2000). Over the majority of the ocean these fluxes are less than 1% of the P-E (precipitation - evaporation), however in the area around the coast of Antarctica they can reach over 20%, and are then a significant addition to the model.

The salinity of grid points within the model is limited to lie within the range 0-40, which can lead to problems within the isolated basins, such as the Caspian Sea, and those isolated due to the model's resolution, such as the Baltic (Gordon *et al.*, 2000). When these regions reach the upper limit of salinity, keeping them at this value implies a non-conservation of water equivalent to 0.2 mm year^{-1} averaged over the ocean. The model could therefore be improved by including an exchange across the sub-gridscale straits.

2.2.3 Atmospheric component

The main features of the atmospheric model, HadAM3, are described by Pope *et al.* (2000), along with the improvements over the previous version, HadAM2b. HadAM3 uses a 2.5° latitude by 3.75° longitude grid (Figure 2.2b) and 19 vertical levels on a hybrid coordinate system. This means that the bottom four levels follow the terrain and the top three layers are pure pressure layers, with smooth transitions in between. There is a Eulerian advection scheme with a timestep of 30 minutes.

One of the major differences between HadAM3 and the previous version is the introduction of a new radiation scheme, developed by Edwards and Slingo (1996) and modified by Cusack *et al.* (1998). HadAM2b has four shortwave bands and six longwave bands, and includes the effects of CO_2 , H_2O and O_3 . HadAM3 contains six shortwave bands and eight longwave bands, and includes the effects of CO_2 , H_2O and O_3 , as well as O_2 , N_2O , CH_4 , CFC11 and CFC12, and a parametrisation of background aerosols. The new scheme also treats water droplets differently to ice crystals.

The impact of convection on momentum is included, using a scheme developed by Gregory *et al.* (1997). A new land surface scheme, MOSES (Cox *et al.*, 1999), was also introduced. This can represent the freezing and melting of soil moisture, allowing for a better simulations of surface temperature. It also includes the effects of CO_2 on evaporation.

2.3 Model Evaluation

2.3.1 Ocean

On a global scale, all major features of the SST field are reproduced in the model. This includes the sharp horizontal temperature gradients associated with major ocean currents such as the Kuroshio and the Antarctic Circumpolar Current (ACC). These gradients were not reproduced in previous versions, however the improved resolution of the ocean in HadCM3 makes this possible (Gordon *et al.*, 2000). Throughout most of the ocean, differences between the model SSTs and observations are then kept within 1°C (Figure 2.1a), however when the currents stray from their observed locations, the high temperature gradients can lead to local errors. This effect is seen in the region of the Kuroshio, where the

current separates from the coast too far south. This leads to a region of cooling around the current. The NAC also strays from its observed location, leading to negative temperature anomalies in the North Atlantic. The peak SST errors in the Southern Ocean correspond with the position of the ACC in the model, which could be due to incorrect steering from the topography. However, the errors also peak south of the Cape of Good Hope, which is known to be a region of high eddy activity. Poor resolution could therefore also be a factor here.

As well as these local effects, there are large regions of warming or cooling within the model. The North Pacific is more than 3°C below observed temperatures (Figure 2.1a), due to poor simulation of surface fluxes combined with shallow summer mixed layer depths. Lack of strato-cumulus clouds in the atmospheric component also leads to errors in the central east Pacific, eastern tropical Pacific and Atlantic, and off the Californian coast (Gordon *et al.*, 2000). However, the pattern and magnitude of these errors remains broadly constant within the simulations, therefore should have no significant effect on perturbation experiments.

Improved resolution in the ocean also leads to improvements in the representation of sea ice. Previous versions of the Hadley Centre model, without flux adjustments, showed Arctic sea ice reaching south of Iceland in the winter. Although the ice extent is still greater than that observed (Figure 2.5a), improved simulation of the NAC, advecting warm water northwards, reduces the ice extent in this region. Southern Hemisphere mean ice extents also compare well with the climatology, although Figure 2.5b shows that the winter extents are again too large (Gordon *et al.*, 2000).

As with many coupled models, the strength of the ACC is exaggerated (Russell *et al.*, 2006). Observed values estimate the transport as 135 Sv, however HadCM3 gives a value of 223 Sv. This is believed to be due to the exaggerated salinity gradient across the ACC and the corresponding density gradients, with the model being too salty at high latitudes and too fresh further north (Stark *et al.*, 2005). Pardaens *et al.* (2003) showed that the model's hydrological cycle can be too strong, leading to overly large precipitation and evaporation components, transporting freshwater from low to mid-high latitudes. This stabilises at around 400 years into the control run, with freshwater travelling northwards from the Southern Ocean. Pardaens *et al.* (2003) suggest that these effects could lead to

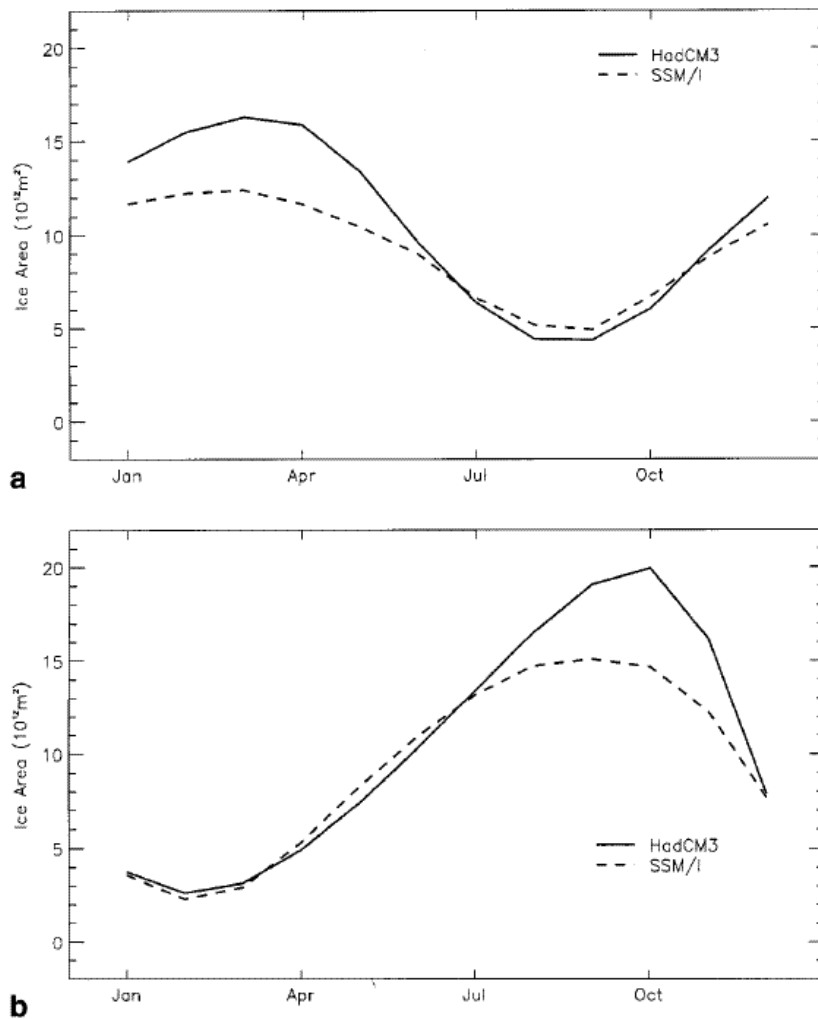


Figure 2.5: The mean monthly seasonal cycle of sea ice area for the model years 361 ± 400 and from SSM/I data for (a) Northern Hemisphere and (b) Southern Hemisphere [10^{12} m^2]. From Gordon *et al.* (2000).

stabilisation of the thermohaline circulation within the model.

Model heat transport within most of the ocean shows reasonable agreement with observational estimates (Gordon *et al.*, 2000), although there are some discrepancies. Banks (2000b) finds that the northward heat flow in the South Atlantic is overestimated. This is due to an underestimate of the northward flux of bottom water. In the Indian Ocean, heat transport matches the observations, moving southwards, although it is larger in magnitude by about 0.3 PW. The main anomaly lies within the South Pacific, where the temperature transport is northwards in the model – the opposite direction to observations. This anomaly is believed to be due to the large transport of the ITF, 24 Sv in the model compared with 12 ± 7 Sv observed (Wijffels *et al.*, 1996), which dominates the transport in

the basin. The large transport in the model ITF is also believed to be responsible for surface heat flux anomalies in the Indian Ocean, when compared with observations (Banks, 2000a). However, combined Indo-Pacific heat transports do show a reasonable agreement with observations (Gordon *et al.*, 2000).

2.3.2 Atmosphere

As with the ocean, most features of the atmosphere are well represented, with a considerable improvement from the previous version (Pope *et al.*, 2000). The pressure at mean sea level is improved in most regions, but one of the main errors is a large high pressure bias over the poles, up to 10 hPa. Simulation of zonal-mean zonal winds has improved through the inclusion of convective momentum transport. The meridional winds have also been improved, but the Hadley and Walker cells are too strong. This has been linked to the increased hydrological cycle in the model by Pardaens *et al.* (2003). Introduction of the new radiation scheme has led to a substantial reduction in temperature bias, however the cold bias at high northern latitudes in the lower tropopause is worse than in the previous versions. Near the surface, global temperatures suffer from a cold bias. HadAM3 also suffers from problems with moisture and cloud cover. At some levels, there is almost no moisture due to the poor resolution and water vapour transport, although a large moist bias can be seen in the winter storm tracks and at high latitudes in the summer (Pope *et al.*, 2000). The lack of strato-cumulus clouds also leads to warm anomalies in SST due to the increased radiation reaching the surface.

Collins *et al.* (2001) looked at the internal variability in the model. In general, the temperature variability agrees well with observations, both temporally and spatially, but the variability over land is exaggerated. In the model, the El Niño Southern Oscillation (ENSO) appears to vary over a 3-4 year period, with an amplitude within the range of observations. However, there appears to be too much ENSO variability in the Western Pacific, where a combination of cooler temperatures and shallow thermoclines means that the ocean is able to respond on shorter timescales than in reality. Interdecadal variability, resembling the observed Pacific Decadal Oscillation (PDO), was also found in the Pacific. However, again there was too much variability in the west. Variability in the Northern Hemisphere winter resembles the North Atlantic Oscillation (NAO), but there

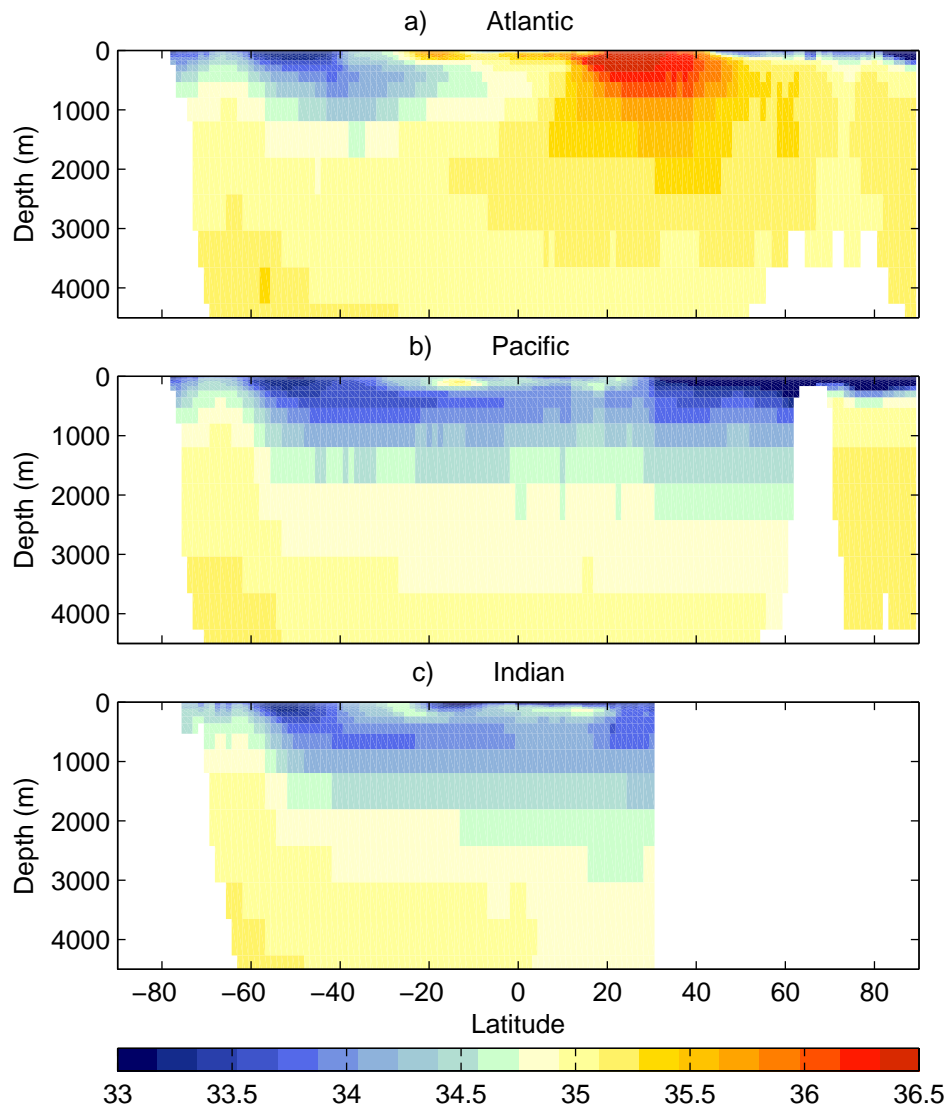


Figure 2.6: Zonal-mean salinity in each of the three major ocean basins in HadCM3, from a 500-year control simulation (model years 2789-3289): a) Atlantic, b) Pacific, c) Indian. White regions indicate model bathymetry.

is an enhanced teleconnection between the North Atlantic and North Pacific, which is not seen in observations.

2.3.3 AAIW in HadCM3

Figure 2.6 shows the progression of a low-salinity tongue, moving northwards from the Polar Frontal Zone, through each of the three major ocean basins. This is the characteristic salinity minimum of AAIW in HadCM3. The depth of this water mass varies between the three basins, but it is usually found between ~ 250 and 1500 m. In general HadCM3 performs well, simulating a salinity minimum at intermediate depths in each of the three

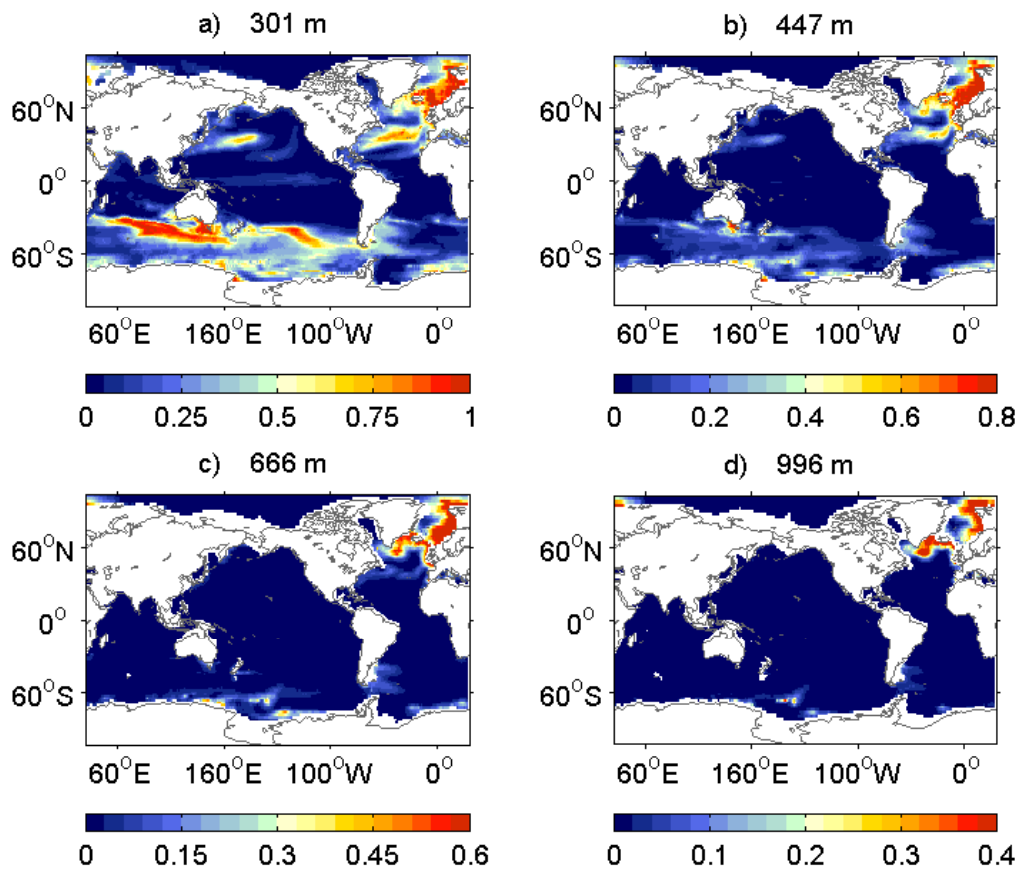


Figure 2.7: Tracer concentration (0–1) at intermediate depths after year 1 at depths of a) 301 m (level 10 in HadCM3); b) 447 m (level 11); c) 666 m (level 12); d) 996 m (level 13).

major ocean basins (Stark *et al.*, 2005). However, the water mass is fresher and lighter than seen in observations (Sloyan and Kamenskovich, 2007).

In order to assess how AAIW forms in HadCM3, data have been analysed from a 5 year tracer experiment (model runs were performed by Glen Richardson; Richardson, 2006). A passive tracer was added to the surface continuously, to maintain a surface value of 1 everywhere, and then allowed to evolve freely within the ocean. Grid points at depth in the ocean can then take any value between 0 and 1 – 1 being completely saturated, and 0 being completely absent. This gives an indication of where water has sunk beneath the surface, with higher concentrations suggesting larger volumes of surface water.

In HadCM3, meridional sections suggest that AAIW moves northwards from $\sim 50^{\circ}\text{S}$ at intermediate depths (Figure 2.6), therefore we must look for regions around this latitude where the tracer can be found extending from the surface to these depths. Significant amounts of tracer are found to reach through depths of 301, to 447 m (levels 10 and 11 in HadCM3), around Drake Passage and the southwest Atlantic, as well as south of Australia

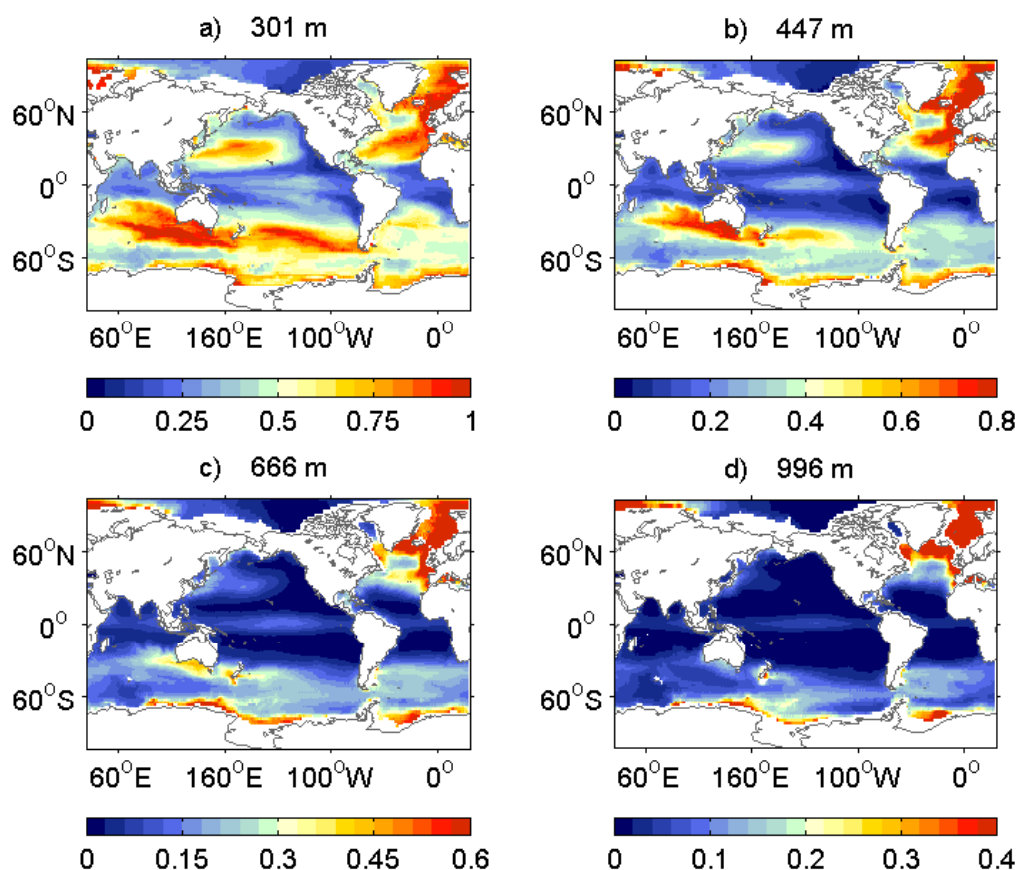


Figure 2.8: Tracer concentration (0–1) at intermediate depths after year 5 at depths of a) 301 m (level 10 in HadCM3); b) 447 m (level 11); c) 666 m (level 12); d) 996 m (level 13).

and east of New Zealand (Figures 2.7a,b). Looking deeper, to 666 m and 996 m (levels 12 and 13), there is a decrease in the amount of tracer found around Australia, however it is still present to the east of Drake Passage (Figures 2.7c,d). This suggests that there is a stronger sinking mechanism in this region, reaching to greater depths within a shorter amount of time. Indeed, Richardson (2006) proposed that Drake Passage was a region where Antarctic Bottom Water may be formed in the model, unrealistically.

After 5 years, large tracer concentrations are found at intermediate depths south of Australia and east of New Zealand (Figures 2.8), suggesting that this could be a key region of AAIW formation in the model. Observations have suggested that this is a site of SAMW formation, due to cross-frontal exchange and deep winter convection (e.g. Molinelli, 1981; Piola and Georgi, 1982; Rintoul *et al.*, 2001; Sen Gupta and England, 2007b). This SAMW can then act as a source for AAIW. Tracer concentrations also have high levels at depth in Drake Passage and the southwest Atlantic, with values $> 20\%$ at depths of 996 m. Tracer concentrations of $> 5\%$ are also found at depths of 3300 m within

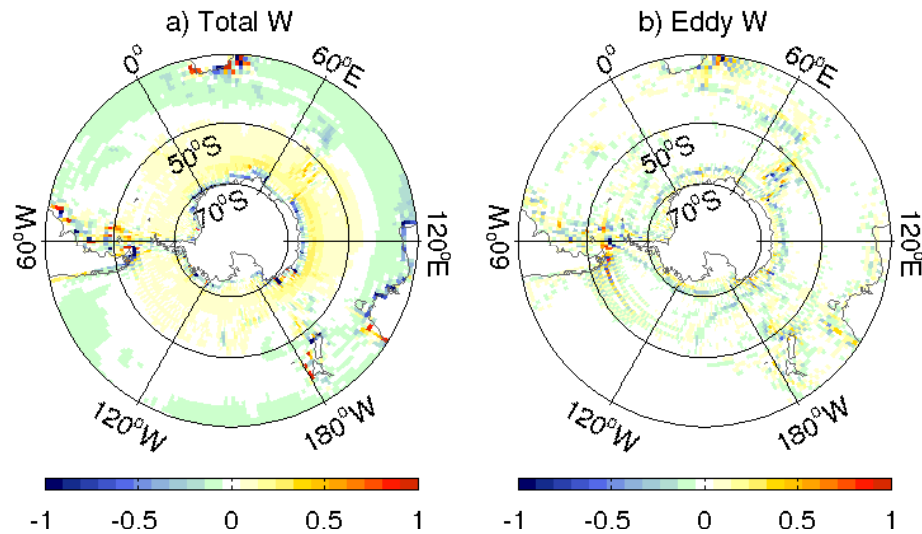


Figure 2.9: Mean vertical velocities (W), over top 240 m (levels 1-9 in HadCM3) from the 5 year tracer simulation [$10^{-3} \text{ cm s}^{-1}$]: a) total W ; b) eddy W (from Gent-McWilliams parameterisation). Negative values indicate downward velocities.

5 years (not shown), supporting the theory that AABW forms in this region. However, it is possible that a contribution to AAIW may take place during the formation process. One interesting point to note is that there is comparatively little tracer found below 300 m in the southeast Pacific. This has been cited as a key region of AAIW production (e.g. McCartney, 1977; Talley, 1996), however the model does not reproduce this (Figure 2.8). Higher concentrations are found along the coast of Chile, so it may be possible that some sinking occurs in this region. The increased strength of the ACC in HadCM3, when compared with observations (Russell *et al.*, 2006), may cause the water mass to be swept through Drake Passage rather than spreading into the Pacific.

From these indications of where water may be leaving the surface in HadCM3, we must now consider what processes may cause this? Firstly, plots of vertical velocity can give an indication of whether the water mass is sinking in these regions, or being advected in from elsewhere. Downward velocities are found to dominate in the region south of Australia, with negative values also found south of New Zealand (Figure 2.9a). Strong downward velocities are also found in Drake Passage and the southwest Atlantic, with typical values of $1 \times 10^{-3} \text{ cm s}^{-1}$, averaged over the top 240 m of the ocean for the 5 year simulation. This corresponds to a distance of 311 m travelled within 1 year. Maximum values found in Drake Passage reach up to $6.5 \times 10^{-3} \text{ cm s}^{-1}$, corresponding to a distance

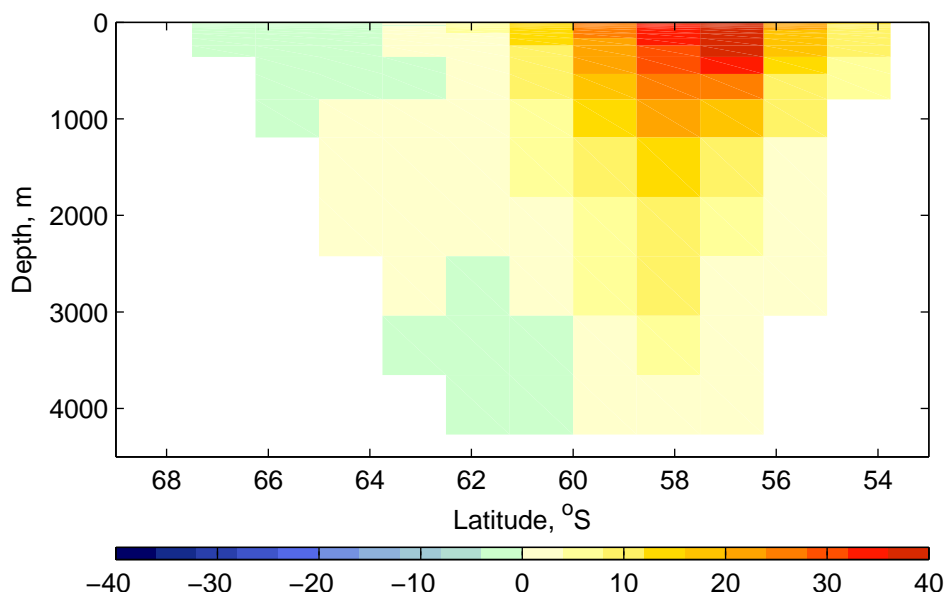


Figure 2.10: Mean zonal velocity [$10^{-3} \text{ cm s}^{-1}$] in Drake Passage ($65\text{--}73^\circ\text{W}$) from a 5 year control simulation in HadCM3. Positive values indicate eastward velocities.

of 2020 m within a year. Although these larger values may only be found for a couple of grid points, they show that by the end of the first year, small tracer concentrations can reach deep levels of the ocean ($> 2000 \text{ m}$). Figure 2.9b shows that the eddy velocities, from the Gent-McWilliams parameterisation scheme, contribute to these downward velocities. This is consistent with the theory that eddy mixing plays a vital role in the formation of AAIW in this region (e.g. Talley, 1996), by allowing cross-frontal transfer of properties. A number of studies have also shown the importance of eddy mixing parameterisations for simulating water mass formation in general circulation models (e.g. England, 1993; Sørensen *et al.*, 2001).

Within Drake Passage, the large zonal velocities must be considered, to check whether the water would have time to sink before being moving further downstream. Figure 2.10 shows that within Drake Passage, mean velocities over a 5 year period can reach $> 40 \text{ cm s}^{-1}$. This corresponds to 1.4 km in an hour; which is one time step in HadCM3. This is much larger than the vertical velocities, and means that water can be advected through the region within a couple of weeks. However, these high velocities are confined to a narrow region. In regions where there are lower horizontal speeds, sinking will be allowed to progress to deeper levels. These strong currents can account for the spread of the tracer to the east of Drake Passage, and also to the east of New Zealand, as the tracer travels with the ACC around the Southern Ocean.

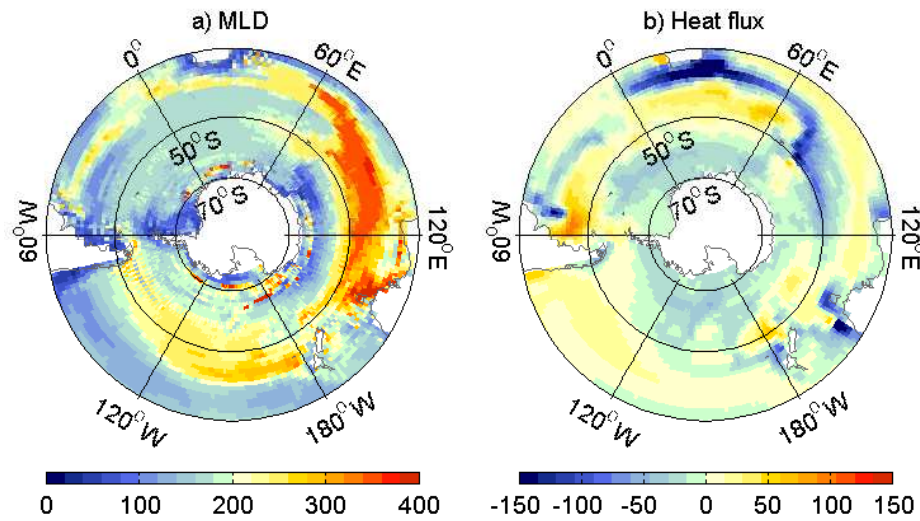


Figure 2.11: a) Maximum mixed layer depth (MLD) [m]; b) Annual mean ocean-atmosphere heat flux [W m^{-2}] (positive heat flux indicates heat transfer in to the ocean). Values are averaged from a 5 year control simulation in HadCM3.

Since AAIW is believed to form partly through deep convective mixing (McCartney, 1977), the maximum mixed layer depth (MLD) can give an indication of where formation may occur. The greatest MLD values can be found north of 50°S , between 60 and 150°E , with values of > 350 m (Figure 2.11a). This can account for the tracer concentrations found at depth in this region (Figures 2.7). Although little tracer was found at depths > 300 m in the southeast Pacific, the MLD in this region is seen to reach at least 250 m beneath the surface. The MLD east of Drake Passage is not as large, supporting the suggestion that eddy mixing may be more important in this region. Surface heat fluxes play an important role in driving convective mixing in the ocean. Figure 2.11b shows that in the region of increased MLD between 60 and 150°E , there is a net loss of heat from the ocean. In general, regions of heat loss appear to coincide with regions of greater MLD (Figure 2.11). As heat is lost from the surface of the ocean, this leads to an increased density of the surface waters, driving deeper convection in the ocean. However, it should be noted that the heat fluxes shown here are annual averages. Therefore, regions which do not show a net loss of heat during the year, may still lose heat during the winter months. Also, MLD can be strongly influenced by wind forcing, however heat loss is likely to play the major role in the Southern Ocean for determining maximum MLD.

2.3.3.1 Discussion

From these results there appear to be two possible sites for AAIW formation in the model. Firstly, to the southwest of Australia and around New Zealand, due to deep convection driven by surface heat loss. The second location is around Drake Passage and the southwest Atlantic, where vertical velocities lead to surface waters sinking to greater depths. Increased eddy velocities and shallower mixed layer depths suggest that eddy mixing may be responsible for production in this region.

Although the southeast Pacific is believed to be a key location for AAIW formation, this does not appear to be the case in the model. Increased tracer concentrations are only found to reach intermediate depths in a narrow region along the coast of Chile. The MLD in the southeast is also shallower than in the southwest of the Pacific basin. Strong currents in the ACC may lead to the tracer being swept through Drake Passage before it can sink to further depths in this region, or spread northwards in to the Pacific. It is likely that AAIW in the Pacific then originates from eastward advection of the source south of Australia and New Zealand.

A likely cause of the shallower MLD in HadCM3 is increased stratification in the Polar Frontal Zone (PFZ). The increased hydrological cycle described by Pardaens *et al.* (2003) leads to fresher surface layers in the extra-tropical oceans. This decreases the density of the surface layers, suppressing deep convection in these regions. Russell *et al.* (2006) and Sloyan and Kamenskovich (2007) show that this freshening in the Southern Ocean leads to an intermediate water mass that is fresher and shallower than seen in both observations and other climate models. However, as described in the following section, Section 2.4, this study involves the use of idealised perturbations with respect to a control experiment. As we are not concerned with initialising or comparing the model with observations, HadCM3 is a useful tool for this study.

2.4 Model perturbation experiments

The aim of this research is to investigate how changes in Antarctic Intermediate Water (AAIW) may lead to changes in climate on a global scale. To do this, idealised perturbation experiments were performed using HadCM3. The principle behind a perturbation

experiment is that only a small component of the model is altered so that the results can be compared with the reference control run, and any effects then attributed to that change. A number of such experiments have been conducted in the past, covering a wide range of perturbations.

In order to better understand anthropogenic climate change, a number of models have been used to study the impacts of increased CO₂ concentrations in the atmosphere. For example, Banks and Bindoff (2003) and Stark *et al.* (2006) have used HadCM3 to investigate whether observed changes of temperature and salinity at intermediate depths in the Indo-Pacific can be attributed to anthropogenic changes in greenhouse gases. Banks and Bindoff (2003) showed that the changes observed could not be reproduced in control conditions. With increased CO₂ concentrations, warming and freshening in the Southern Ocean led to changes in the ocean that were similar to those observed. However, this study involved the use of only one model run, with one set of initial conditions. Stark *et al.* (2006) carried out a series of model runs, additional to the ones used in the previous study, using various initial climate conditions. From this “ensemble” of model runs, it was shown that the changes observed in the Indo-Pacific may be within the range of internal climate variability. This illustrates the importance of ensemble experiments for investigating the climate response to perturbations.

2.4.1 Idealised perturbations using HadCM3

To improve our understanding of large scale ocean circulation, previous studies have used idealised perturbation experiments to test the sensitivity of the Atlantic component of the meridional overturning circulation (MOC) to climate changes. One key process of the MOC is the formation, and sinking, of North Atlantic Deep Water (NADW). In the winter months, cold, saline surface waters may become sufficiently dense to sink, forming this deep water mass. However, a warming climate may lead to a warming and freshening at high latitudes, which has a significant impact on NADW formation, leading to a reduced MOC strength (Gregory *et al.*, 2005). Dong and Sutton (2002b) and Vellinga and Wood (2002) have both used perturbation experiments to investigate the effects of a large freshwater input to the North Atlantic in HadCM3. In the experiment carried out by Dong and Sutton (2002b), a salinity anomaly was introduced to the upper 500 m between

55°N–85°N, 90°W–20°E. Vellinga and Wood (2002) introduced their anomaly over the upper 800 m, between 50°N–90°N, 80°W–20°W. Both anomalies were introduced as a salinity decrease of 2, corresponding to instantaneous freshwater inputs of $3.0 \times 10^{14} \text{ m}^3$ and $6.0 \times 10^{14} \text{ m}^3$ respectively. In order to conserve salt, that which was taken out of the North Atlantic was redistributed globally. Dong and Sutton (2002b) looked at the 10 years immediately following the perturbation, whereas Vellinga and Wood (2002) were concerned with the long term, quasi-equilibrium response over the following century. Although they focused on different aspects of the climate response, both of these experiments led to a collapse of the MOC.

More recently, Richardson *et al.* (2005) used HadCM3 to investigate the effects of salinity perturbations within the Southern Ocean. A freshwater pulse was added around the coast of Antarctica, south of 65°S, by reducing the salinity by 1 within the top 500 m of the ocean (upper 11 levels of HadCM3). The experimental design was comparable to the previous North Atlantic experiments. The location around Antarctica was chosen to investigate the sinking of Antarctic Bottom Water (AABW), which acts as the deep southern limb of the MOC. The effects of this perturbation appeared to be similar to those caused by the previous experiments, with a cooling in the hemisphere where the perturbation was applied, however the effect on the MOC was much smaller. After 10 years, the strength of the AABW overturning cell had decreased by just 5%. This is due to the heat transport in the Southern Hemisphere occurring primarily at mid-depth in the ocean. The initial cooling within the Southern Hemisphere was a result of the cold, fresh surface waters preventing upwelling of the warm deep water. A warm anomaly then grows, and spreads, beneath the surface (Figure 2.12).

2.4.2 Past experiments with AAIW

Until now, no perturbation experiments have been performed with HadCM3 to investigate climate impacts of changes in AAIW. However, experiments have been performed with other models to investigate its impacts on global circulation. Saenko *et al.* (2003) investigated the two modes of the MOC ('on' and 'off'), through the input of freshwater in the regions of AAIW production. They use an intermediate complexity model (Weaver *et al.*, 2001) to apply a freshwater perturbation around the southern tip of South America (Figure

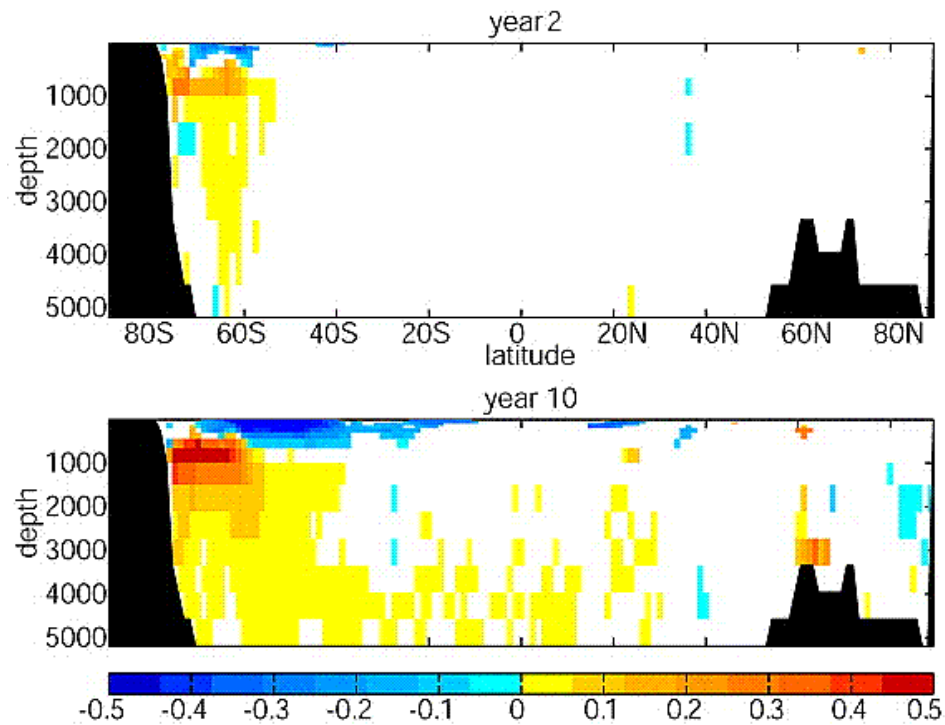


Figure 2.12: Zonal mean ocean temperature [$^{\circ}\text{C}$] anomalies (mean of perturbed ensemble – mean of control ensemble) after years 2 and 10 of a surface freshwater perturbation around Antarctica ($> 65^{\circ}\text{S}$). Only anomalies significant at 95% level are shown. From Richardson et al. (2005).

2.13). This region is north of the ACC and therefore does not have a significant effect on AABW production. The experiment was started in the ‘off’ mode, which has no active NADW formation. The freshwater was then added at a rate that was linearly increasing by $0.2 \text{ Sv} (1000 \text{ yr})^{-1}$. When the system begins to switch to the ‘on’ mode, which has active NADW formation, the rate of freshwater input is then decreased back towards zero and into a negative perturbation, in order to trigger a switch back to the ‘off’ mode. To complete this whole process the model was integrated for more than 11 000 yr.

Saenko *et al.* (2003) found that the transition between the ‘on’ and ‘off’ modes could be described by the relative densities of the AAIW and NADW source regions, ρ_{AAIW} and ρ_{NADW} . In the ‘off’ mode $\rho_{\text{NADW}} < \rho_{\text{AAIW}}$. AAIW is converted into light thermocline water and then recirculated within the upper ocean. As the freshwater input into the AAIW source region increases, ρ_{AAIW} decreases. This leads to a weakening of the AAIW circulation cell, leading to a reduction in the freshwater transport into the North Atlantic. The ρ_{NADW} increases until the two densities become comparable. At this stage there is then a rapid transition from the ‘off’ to the ‘on’ mode ($\rho_{\text{NADW}} > \rho_{\text{AAIW}}$) as the NADW

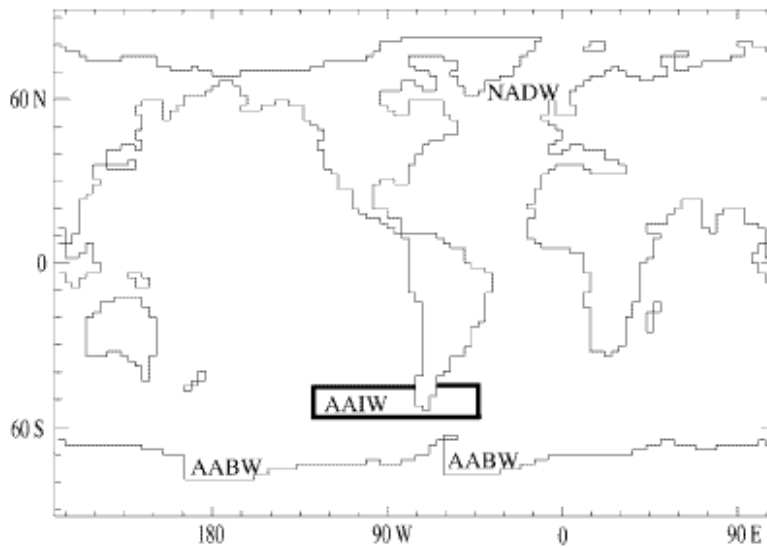


Figure 2.13: Formation areas for NADW, AAIW and AABW within the intermediate complexity coupled model used in Saenko *et al.* (2003). The solid line around AAIW formation region indicates the area where the salinity anomaly was applied.

circulation intensifies and transports more saline subtropical water northwards in a positive feedback scenario. AAIW then feeds the formation of NADW, and the circulation of NADW remains dominant until the negative salinity perturbations once again cause the two densities to become comparable. The switch from the ‘on’ to ‘off’ mode is then triggered, resulting in a collapse in the NADW formation and intensification of the AAIW circulation cell.

Weaver *et al.* (2003) suggest that this process of freshening in the AAIW formation regions may be a cause for the Bolling-Alleröd Warm Interval during the last deglaciation. One prominent feature of the last deglaciation was a large rise in sea-level of ~ 120 m. This event has become known as meltwater pulse 1A (mwp1A), however its location has caused some controversy. Weaver *et al.* (2003) showed that if the source was the Antarctic Ice Sheet, the freshwater could cause changes in density that would lead to an intensification of NADW formation. This could then account for the Warm Interval seen in the Northern Hemisphere.

2.5 Conclusion

For this thesis, perturbation experiments will be carried out using HadCM3, which is available on the high performance computer, Cluster1¹, at UEA. HadCM3 has been shown to give a good representation of global climate, reproducing all major features of both the ocean and atmosphere, without the need for flux adjustments. Whilst the representation of AAIW is fresher and shallower than in observations, our experiments will be using perturbations from a control climate. For this purpose, HadCM3 should perform well, as its climate variability does compare well with observations. It is also relatively fast to run, when compared with models of higher resolution.

Unlike previous perturbations investigating changes in AAIW, the perturbation in this study will not be made in the formation regions. This is partly due to the fact that the model does not form AAIW in the same regions as those observed. Also, the focus of this study is to investigate the response to changes in AAIW properties, not how changes at the surface may feed in to AAIW properties. Therefore, AAIW properties are chosen to be perturbed at depth in the Southern Hemisphere, after the water mass has formed and sunk beneath the surface layers. This allows us to focus on the impact of AAIW as it moves northwards, surfaces and interacts with the atmosphere. The methods used for these perturbations will be discussed in further detail in Chapter 3.

¹Version 4.5 of HadCM3 is available on Cluster1. Cluster1 has been phased out at UEA, with the new EScluster becoming available at the end of 2008, followed by GRACE in 2011. Further details about high performance computing at UEA can be found on the following website: <http://cluster1.uea.ac.uk/eswiki/>.

Chapter 3

Climate response to changes in Antarctic Intermediate Water in the Atlantic

3.1 Introduction

As surface tracer experiments suggest that Antarctic Intermediate Water (AAIW) does not form in the same regions as those observed in HadCM3 (Chapter 2), a perturbation was chosen to be applied at depth in the ocean, far removed from the water mass formation and subduction regions. This perturbation experiment allows us to focus on the impact of AAIW on the surface waters and climate as it moves northwards into the Atlantic Ocean and interacts with the atmosphere.

Previous perturbation experiments have all imposed a change in salinity, which leads to a change in density. It is this change in density that causes changes in ocean circulation patterns. For this experiment, it was decided that the perturbation would enforce a change in temperature, along with a change in salinity, maintaining constant potential density. A constant density should then allow AAIW to progress along its usual paths of circulation. However, the changes in temperature and salinity could have observable impacts on the climate system when they influence the surface waters.

Banks *et al.* (2007) report changes seen in the AAIW within the more recent Hadley Centre model, HadGEM1. As HadGEM1 is adjusted towards equilibrium, the AAIW

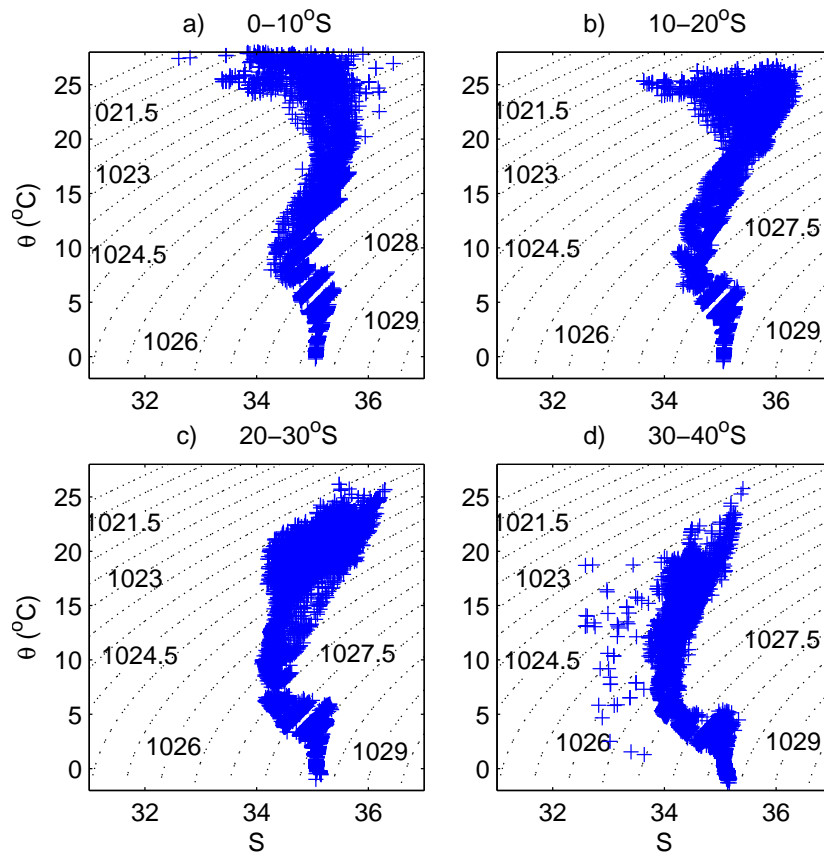


Figure 3.1: Potential temperature - salinity (θ - S) plots of the initial control conditions in the Atlantic basin for, (a) ~ 0 – 10°S , (b) ~ 10 – 20°S , (c) ~ 20 – 30°S , (d) ~ 30 – 40°S . Dotted contours show the corresponding potential density, relative to the surface in HadCM3, with intervals of 0.5.

salinity minimum is eroded as salinity and temperature increase along isopycnals. As the new AAIW outcrops in the North Atlantic it leads to increased SSTs, which then lead to a global adjustment of the radiative balance as well as a thermohaline circulation event. In the first experiment to be conducted in this thesis, temperature of AAIW in the Atlantic will be increased by 1°C , and the salinity increased accordingly. However, this change in temperature will still maintain the characteristic salinity minimum. A second experiment then investigates the impact of a cooler (-1°C), fresher AAIW. This chapter presents the work published in Graham *et al.* (2011).

3.2 Method

For these experiments, the temperature and salinity of AAIW were altered between 10 – 20°S in the Atlantic basin. The characteristic salinity minimum of AAIW can be seen to

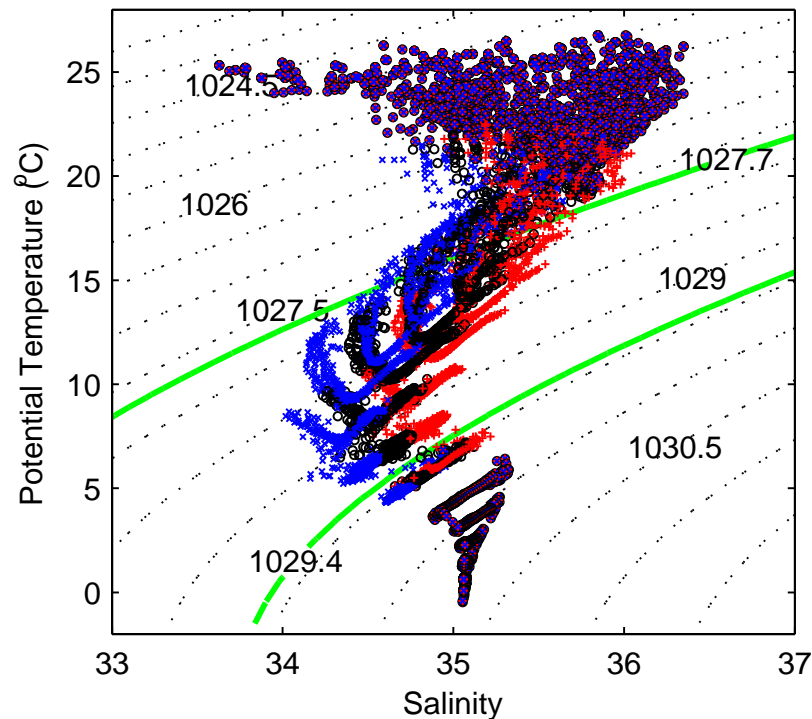


Figure 3.2: θ - S plot for perturbation and control start dumps. Red plusses and blue crosses show the conditions for the $+1^{\circ}\text{C}$ (EXP1) and -1°C (EXP2) perturbations respectively. Black circles show the control conditions. Black dotted contours show the corresponding potential density values calculated relative to a depth of 535 m (level 11 in HadCM3). Green contours show the boundaries of AAIW, 1027.7 and 1029.4.

extend northwards through the Atlantic (Figure 3.1). It does not appear clearly between 20 – 40°S (Figure 3.1c and d) as the surface waters are of a similar salinity. However, by 10 – 20°S (Figure 3.1b), the water mass can be seen clearly beneath the surface thermocline. From analysing the potential temperature-salinity (θ - S) diagrams, the characteristic salinity minimum is found to be centred on level 11 in HadCM3, corresponding to a depth of 447 m. The potential density is then calculated with reference to this depth, using the equation of state from HadCM3. As cold water is more compressible than warm water, referencing to this depth (rather than the surface) gives a more accurate representation of the density range for AAIW. For the chosen perturbation region, the potential density range of Atlantic AAIW was chosen to be 1027.7 – 1029.4 . This encompasses the salinity minimum at depth in the water column (green isopycnals in Figure 3.2).

To run a simulation with HadCM3, start dumps files are used to input all the initial conditions, such as velocity, temperature and salinity. To perform the perturbation, the ocean start dump was rewritten, selecting the grid points with a potential density lying within 1027.7 – 1029.4 . A perturbation of $\pm 1^{\circ}\text{C}$ was applied to all these points within

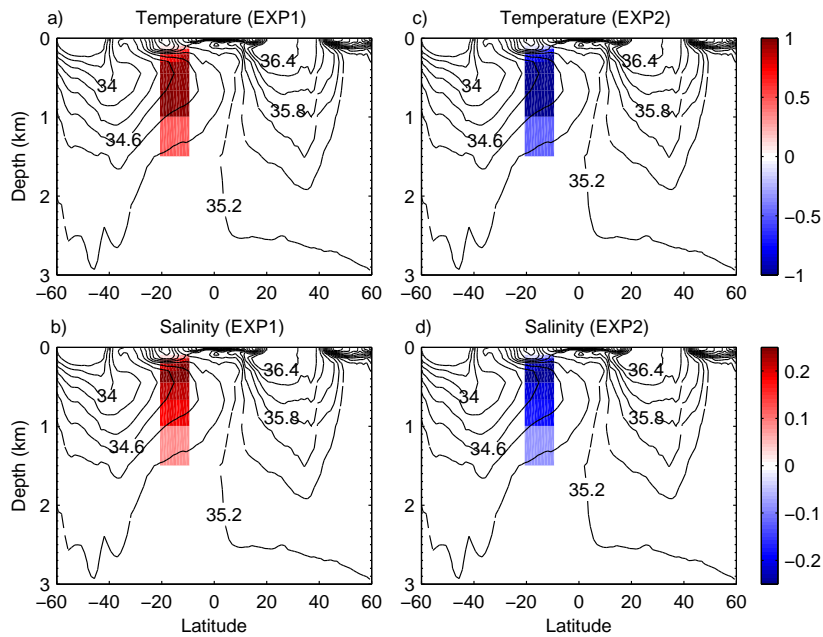


Figure 3.3: Zonally averaged initial conditions for the two perturbation experiments in the Atlantic, all perturbations (anomalies) are calculated as experiment (EXP1 or EXP2)–control: a. Temperature perturbation for EXP1; b. Salinity perturbation for EXP1; c. Temperature perturbation for EXP2; d. Salinity perturbation for EXP2. Contours show the zonally averaged initial salinity in the Atlantic from the control startdump.

10 – 20°S. A density-compensating perturbation was then also applied to the salinity, giving an average change of ± 0.2 in the core of the water mass. The resulting temperature and salinity perturbations for the start dumps are shown in Figure 3.3. New salinity values were chosen using an iterative loop, increasing by steps of 0.005 (close to the measurement accuracy). At each stage the new density was calculated and compared with the original value. The new salinity was then chosen as that with the minimum difference between the new and original densities. The resulting salinity change is substantially larger than the decrease of 0.02 reported by Curry *et al.* (2003). Maintaining a constant density ensures that the dynamics in the model are unaffected (unlike the freshwater perturbations carried out by Saenko *et al.* (2003)). This perturbation then allows AAIW to initially follow its usual paths of circulation (until ocean-atmosphere interactions result in density anomalies due to heat exchanges, or AAIW mixes with surrounding water masses). A perturbation of $\pm 0.5^\circ\text{C}$, along with the corresponding salinity change, was also made in the levels directly above and below the AAIW region, allowing for a smoother transition in the water column.

The resulting θ - S curves for the perturbed region are shown in Figure 3.2, with the

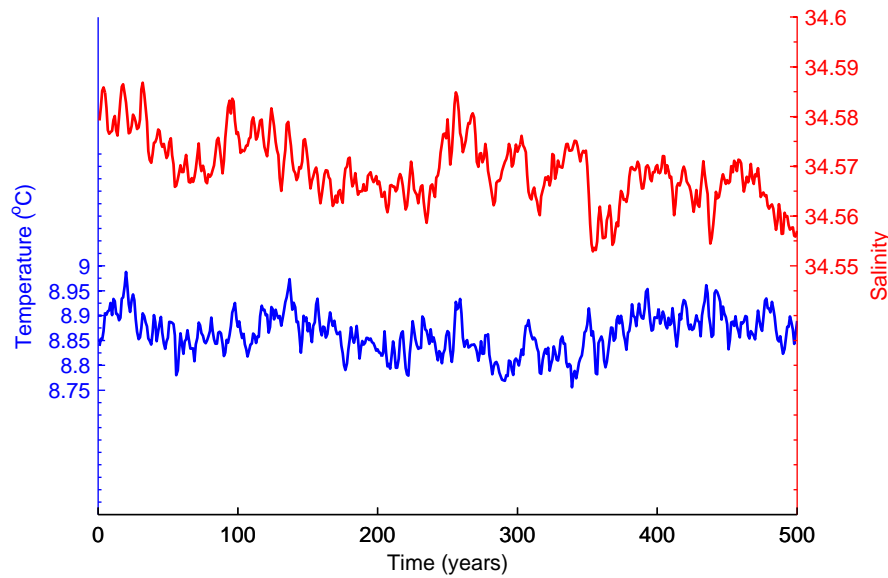


Figure 3.4: Timeseries of mean temperature (blue) and salinity (red) in the core of AAIW in the Atlantic (level 11 in HadCM3), between 10 and 20°S, over a 500 year control run.

perturbed values shown in red (blue) for the +1°C (−1°C) experiment, and the control values shown in black. This shows how points in the chosen potential density range, 1027.7–1029.4, have been shifted along isopycnals, along with the smaller shifts in the levels directly above and below. The resulting density anomalies are negligible, of order $10^{-4} - 10^{-6} \text{ kg m}^{-3}$, with the maximum found to be less than $4 \times 10^{-4} \text{ kg m}^{-3}$. The average temperature and salinity in the core of the water mass between 10 and 20°S in the Atlantic are shown in Figure 3.4, with mean values of 8.86°C and 34.57 over a 500 year control run. The ranges of temperature and salinity during this time are 0.23°C and 0.03, respectively. The imposed changes in temperature and salinity are therefore both much larger than the internal temporal variability in the model. For the warmer, saltier experiment, the total heat added to this region is $2.30 \times 10^{22} \text{ J}$. This change is 16% of the increase reported by Levitus *et al.* (2005) for the top 3000 m of the ocean globally between 1955 and 1998 ($14.2 \pm 2.4 \times 10^{22} \text{ J}$). The total salt input is $1.26 \times 10^{15} \text{ kg}$. Averaged over the whole ocean, this corresponds to a $1.24 \times 10^{-3}\%$ increase, therefore it was not felt that any compensation would be needed. Whilst these are substantial perturbations to the heat and salt content of the water mass, choosing a 1°C change maintains the characteristic salinity minimum of the water mass during the warming perturbation (Figure 3.2). Sen Gupta *et al.* (2009) show that in the Polar Frontal Zone, the IPCC AR4 models project changes of up to +1°C in the upper 1000 m of the ocean by the end of the

21st century. They also show freshening of up to 0.1 in this region of AAIW formation. Although no quantitative analysis is given of changes in AAIW on isopycnals, such as that used by Bindoff and McDougall (2000), this shows that our perturbations may not be far outside the magnitude of projected changes over centennial timescales.

The simulation was integrated for 120 years on the high performance computer, Cluster1, at UEA, with 9 ensemble members for both the perturbed (hereafter referred to as EXP1 and EXP2, for +1°C and -1°C; all experiments are listed in Appendix A) and control simulations. It is essential to have an ensemble of results, so that resulting effects from the experiment can be separated from the range of natural variability in the model. The initial start dumps for the control simulation were taken from a previous control run (model year 2789). Multi-century integration ensures that the module has reached an equilibrium state, and can represent a stable climate system. Ensembles were created using the same ocean initial conditions, but different atmospheric conditions. These were taken from the first 9 consecutive days of the first control run in this experiment. The first ensemble member is then initialised with day one from both the atmosphere and ocean. The second ensemble member is initialised with day one from the ocean, but day two from the atmosphere, and so on. The interaction of these differing atmospheres with the ocean surface provides a spread of internal variability in the ensemble. For both experiments, all initial conditions were identical to those in the control, apart from the relevant perturbation in the ocean start dump. The anomalies shown in the results are calculated as the mean of the control ensemble subtracted from the mean of the EXP1 or EXP2 ensemble, for each given time period.

3.3 EXP1 Results

3.3.1 Where does the anomalous water go?

Heat and salt spread by advection and diffusion at equal rates in the model by definition, along the same paths, maintaining approximately constant density. It is only in the far North Atlantic that stronger anomalies are seen at depth in the density field, as the perturbed water mass has gained heat from the atmosphere, but remains fresh. The temperature, salinity and density anomalies for 41–50 years into the simulation (Figure 3.5)

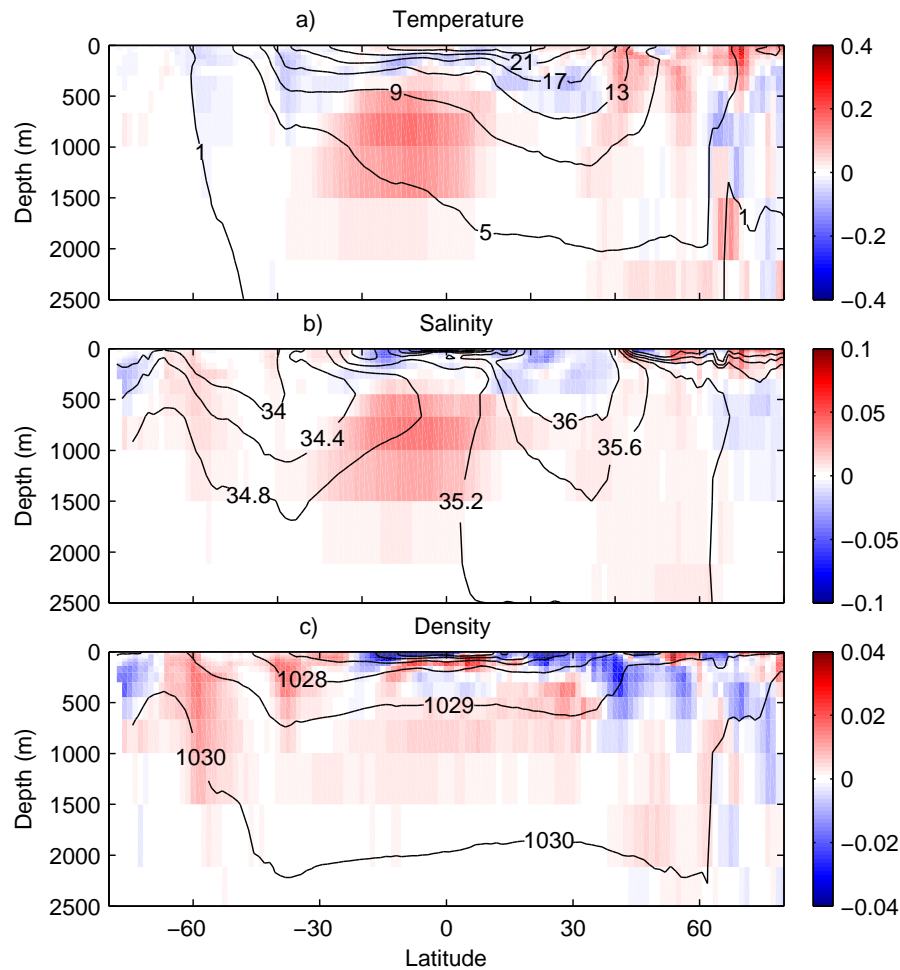


Figure 3.5: Zonal decadal-mean anomalies (*EXP1* – control) in the Atlantic for years 41-50: (a) temperature [$^{\circ}\text{C}$], (b) salinity and (c) potential density calculated relative to a depth of ~ 500 m. Contours show control conditions for years 41-50.

demonstrate that the spread of heat and salt is comparable, resulting in approximately constant density at intermediate depths in the tropical Atlantic (30°S – 30°N). Changes arise when the water mass comes into contact with the atmosphere. Surfacing temperature anomalies can drive an atmospheric response, which can act to reduce the anomaly by increasing atmosphere-to-ocean heat fluxes. However, there is no direct atmospheric response to surface salinity changes, and previous studies suggest that this feedback is weak (Hughes and Weaver, 1996). Therefore, salinity, or salt content, can be used as a tracer for the perturbed water mass.¹

Figure 3.6 shows the column-integrated salt anomalies resulting from the perturbation. Black contours show the regions that are significant at the 95% level. This assessment has

¹Passive tracers can be added in modelling experiments to trace the path of water parcels through the ocean. A tracer was not added in this experiment, and such additions could be a possible avenue for future investigation.

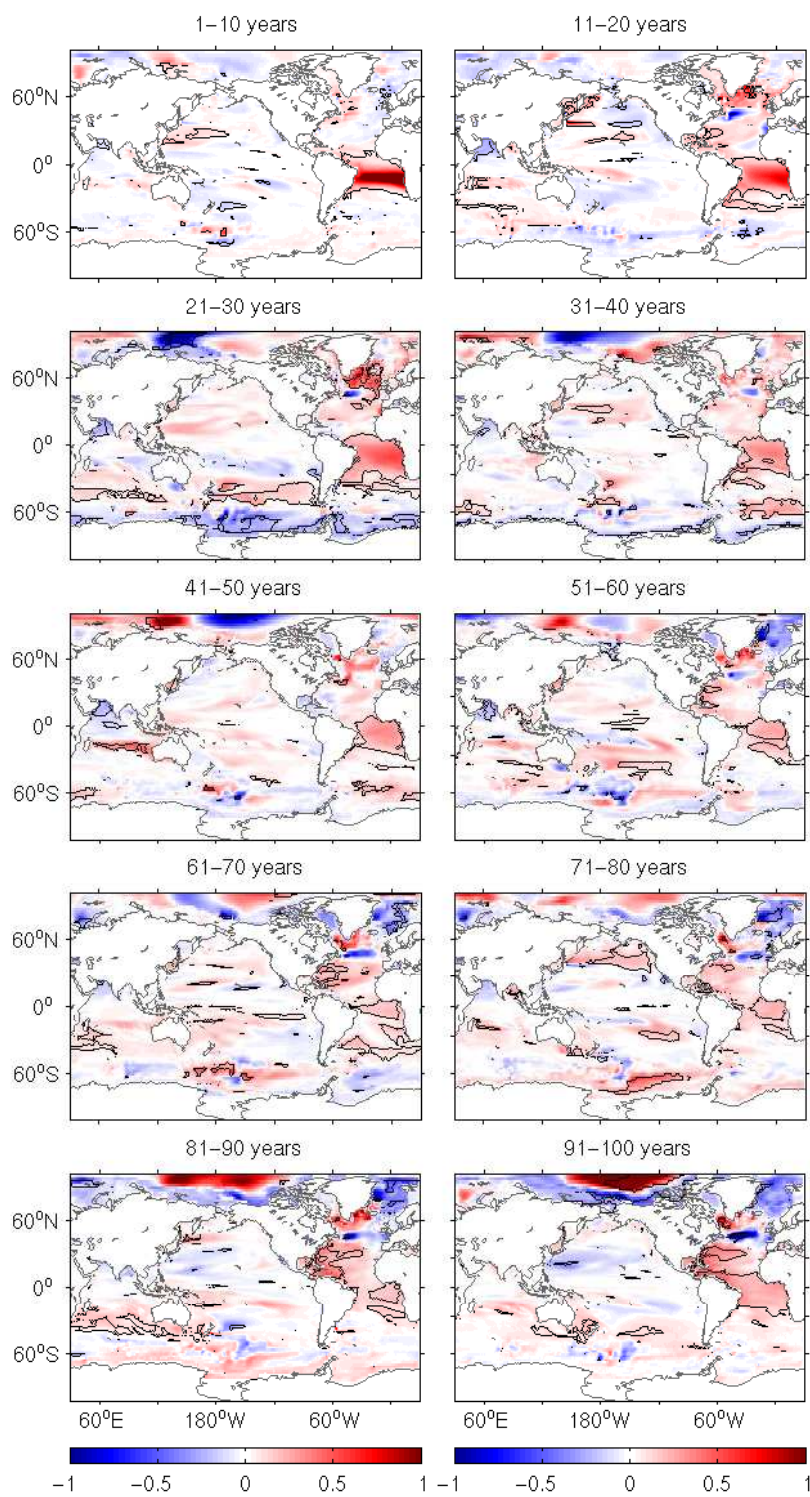


Figure 3.6: Decadal salt content anomalies within columns ($EXP1 - control$) [$\times 10^2 \text{ kg m}^{-2}$]. Black contours show anomalies significant at the 95% confidence level.

been made using a paired t -test calculation. For two samples, X and Y , of size, n , the t value can be found using,

$$t = (\bar{X} - \bar{Y}) \sqrt{\frac{n(n-1)}{\sum_{i=1}^n (\hat{X}_i - \hat{Y}_i)^2}},$$

where

$$\hat{X}_i = (X_i - \bar{X}), \hat{Y}_i = (Y_i - \bar{Y}).$$

The critical values of t for confidence levels can be taken from the appropriate look-up tables (Goulden, 1952), for $n - 1$ degrees of freedom. For example, when assessing the significance of a decadal average anomaly, there is a sample size of 9, from the 9 ensemble members. This then gives a sample size with 8 degrees of freedom. The critical t value for 95% confidence is then 2.31. The larger the value of t , the greater the difference between the two samples, so in this case, the two samples are classed as significantly different if $t > 2.31$. It is important to note that for a 95% confidence level there will still be 5% expected from random fluctuations. Therefore, we must consider the physical processes of how these effects might occur, as well as the statistics, when determining whether results should be considered significant.

The path of the warmer, saltier AAIW can be traced using the increased salt content (Figure 3.6). After 10 years, the saltier water mass is seen to have spread northwards, being carried primarily by the North Brazil Current. From the tropical North Atlantic, the anomaly is carried further northwards with the Gulf Stream. This path of northward transport, along the western boundary, is consistent with both observations and previous modelling studies (e.g., Suga and Talley, 1995; Sen Gupta and England, 2007b; Sijp and England, 2008). The mean locations of these currents, relative to the perturbed region, are illustrated in Figure 3.7. The salt anomalies travel northwards at a speed consistent with advection, reaching the North Atlantic Current (NAC) within the first 10 years due to current speeds $> 6 \text{ cm s}^{-1}$ in the Gulf Stream.² From the NAC, a portion of the water mass travels further north (Figure 3.6). Increased salt content is found in the sub-polar gyre (SPG), around 60°N , by years 11-20 and there is a significant increase in the SPG

²Following the western boundary of the Atlantic basin and into the NAC and SPG, gives a distance of approximately $1.9 \times 10^7 \text{ m}$ to travel from 10°S to 60°N in the Atlantic. For a timescale of 10 years, this requires speeds of 0.06 m s^{-1} .

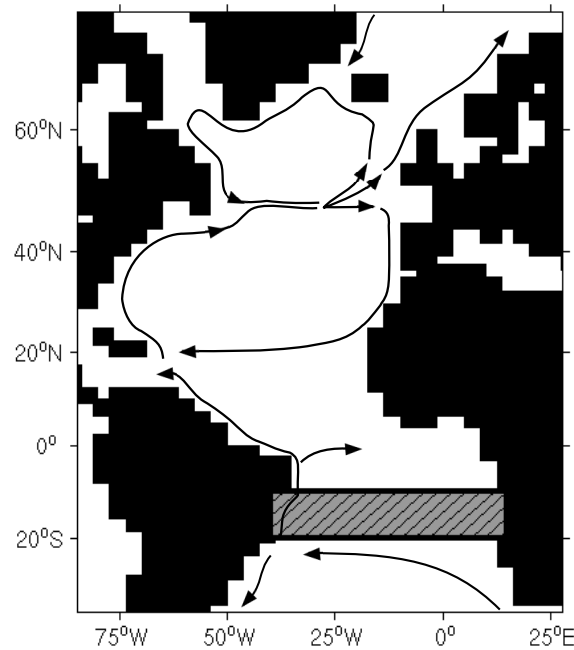


Figure 3.7: Schematic to show the perturbed region of the Atlantic in HadCM3, 10–20°S. Arrows show the mean locations of the strongest currents ($> 1 \text{ cm s}^{-1}$) at $\sim 500 \text{ m}$ (level 11 in HadCM3, the depth of the salinity minimum in the perturbed region). Resolution of the coastline is $2.5^\circ \times 3.75^\circ$, matching the resolution of the atmospheric component.

for years 21-30. The remainder gradually fills the North Atlantic as it recirculates with the subtropical gyre. After 30 years, the majority of the North Atlantic has an increased salt content and significant increases are found in the subtropical gyre after 50 years (Figure 3.6). The region of increased salinity around the tip of Greenland persists for the remainder of the simulation, however, there is no significant increase further north, in the Greenland, Iceland and Norwegian (GIN) Seas. In the later years of the simulation, after 50 years, fresher anomalies are present in the NAC and GIN Seas (Figure 3.6). After 100 years, the majority of the Atlantic remains more saline than the control simulation. It should also be noted that as the perturbed water mass recirculates in the South Atlantic, a significant anomaly remains in the initial perturbation region.

Although it is clear that the perturbation spreads in the horizontal direction, there does not appear to be as much spread in the vertical. Figure 3.8 shows the zonally averaged salinity in the Atlantic. The portion of the anomaly that is initially in the upper layers disperses within the first 10 years as it is advected with currents and enters mixed layers in the upper layers of the ocean. In regions where the chosen AAIW range lies at shallower depths ($< 300 \text{ m}$), particularly in the eastern side of the basin, the surface mixed

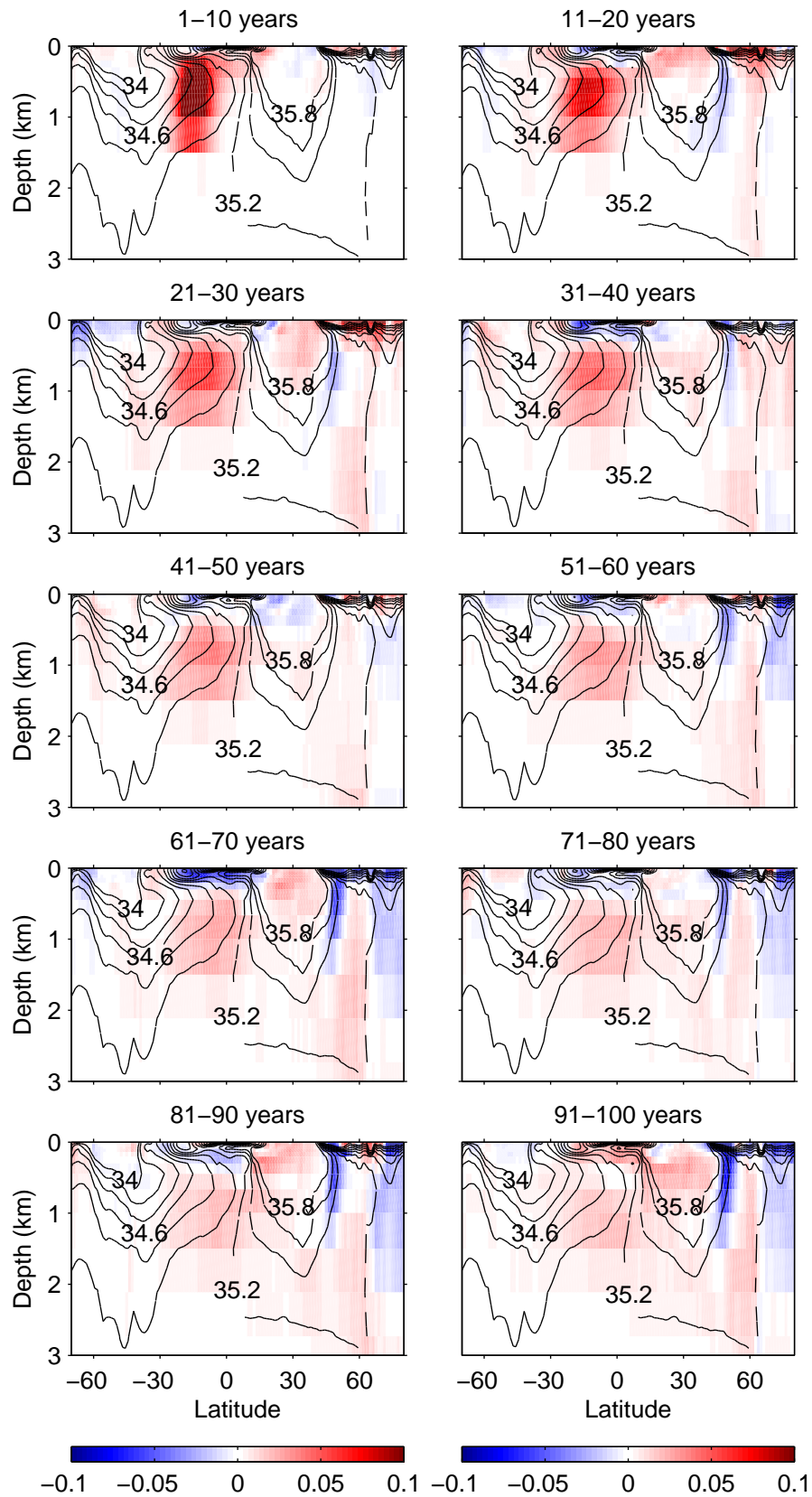


Figure 3.8: Zonal average decadal salinity anomalies (EXPI - control) in the Atlantic for 100 years. Black contours show the mean control salinity for each time period.

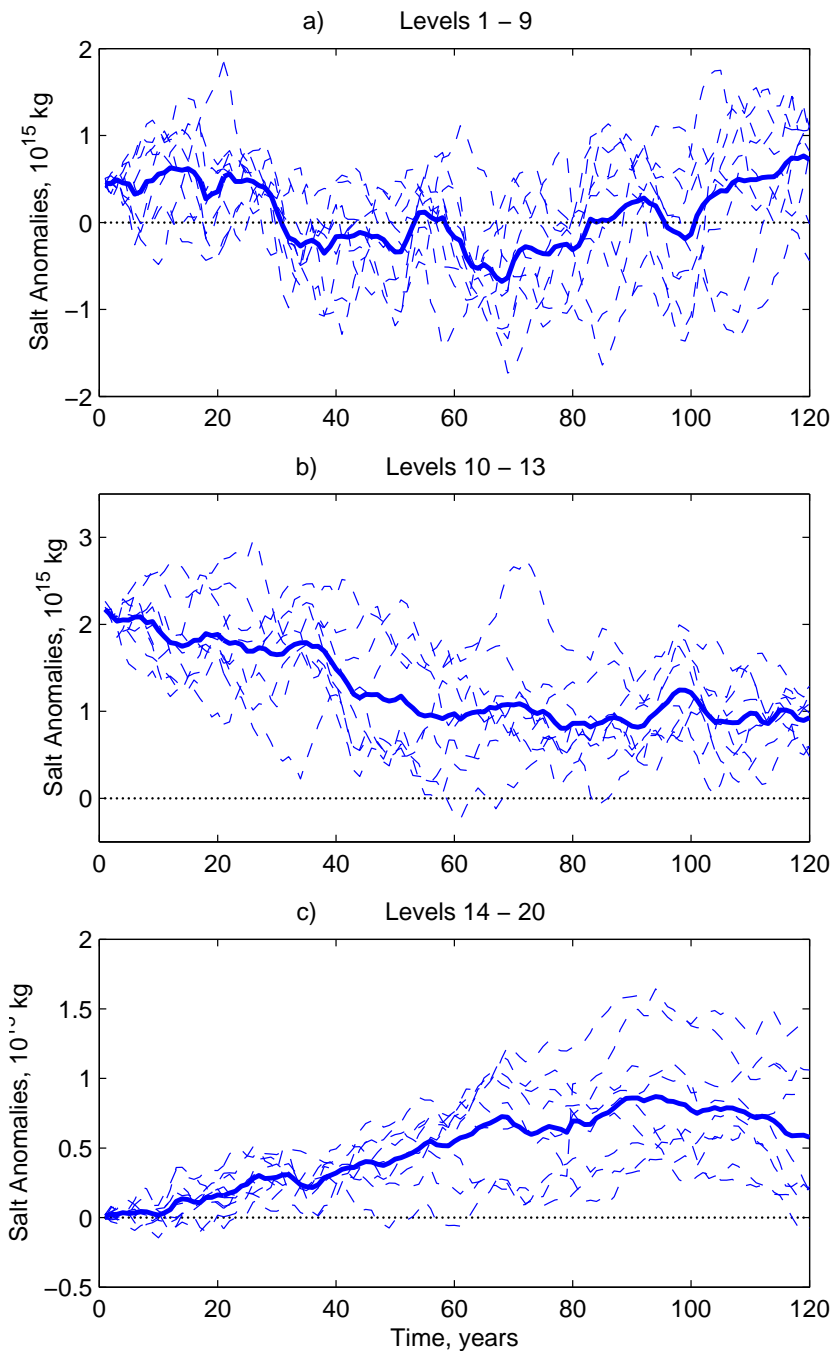


Figure 3.9: Total salt content anomalies in the Atlantic, between 30°S and 70°N , for depth levels a) 1 – 9, $\sim 0 - 300$ m; b) 10 – 13, $\sim 300 - 1500$ m; c) 14 – 20, $\sim > 1500$ m. Solid lines show the ensemble mean anomalies (EXP1 – control); dashed lines show anomalies of individual EXP1 ensemble members minus the mean of the control ensemble.

layer can allow the anomalies to disperse into the upper layers of the ocean. Increased current speeds at shallower depths can then advect the anomalies away from this region and the anomalous heat content can be lost through ocean-atmosphere heat fluxes. The larger portion of the anomaly that lies at intermediate depths (300 – 1500 m), spreads

and remains at these depths (Figure 3.9b). By 11-20 years, a region of increased salinity can be seen around 60°N, corresponding to the increased salt content seen in Figure 3.6. This anomaly is seen at the surface and penetrates to at least 3000 m. Tracer experiments show that in the region around the tip of Greenland, surface waters can sink into the deep levels on very short timescales (< 1 year). Sinking of the anomalous water in this region then leads to an increased salinity of the deep waters in the Atlantic, which can be seen to progress southwards in Figure 3.8 below depths of 1500 m. Figure 3.9 shows that as the salt content increases in the deep waters of the Atlantic, the salt content decreases in the levels above. An increased heat content is also found in the deep layers as the simulation progresses (not shown). As the total salt content is conserved globally, the total salt anomalies in each basin can act as an indicator of how much of the anomalous water mass remains in the region.³ Although some of the perturbed AAIW is lost from the Atlantic itself, or to different depths of the ocean, after 120 years, a heat anomaly of 6.5×10^{21} J and a salt anomaly of 4.6×10^{14} kg remain at intermediate depths in the Atlantic. This corresponds to 27% and 37% of the initial anomalies respectively.

3.3.2 Changes seen at the sea surface and in the MOC

In order for the changes in the ocean to have any influence on the atmosphere, anomalies must enter the surface mixed layer. Although it has been shown that the majority of the changes in heat and salt content remain below the surface layers, effects can be seen at the surface. During years 11-20 there is a significant increase in SST of up to 0.7°C (Figure 3.10). An increase of up to 0.8°C is also seen for years 21-30. The direction of surface heat flux anomalies shows that the changes at the surface are being driven by the ocean rather than the atmosphere, as regions of warmer SST have negative heat flux anomalies, releasing more heat to the atmosphere rather than gaining it (Figure 3.11a). As the perturbed water mass reaches the subpolar gyre, south of Greenland, deeper mixed layer depths (> 300 m) in this region allow the warmer waters to reach the surface. As the simulation progresses, this region of significant warming becomes less evident, however regions of increased SST can be found around Greenland during years 51-60, 81-90 and 101-120 (not shown). After 60 years, there is a region of significant cooling in the North

³It is worth remembering that drifts in model salinity (Section 2.2.2) could lead to a greater uncertainty in this method when used over longer timescales.

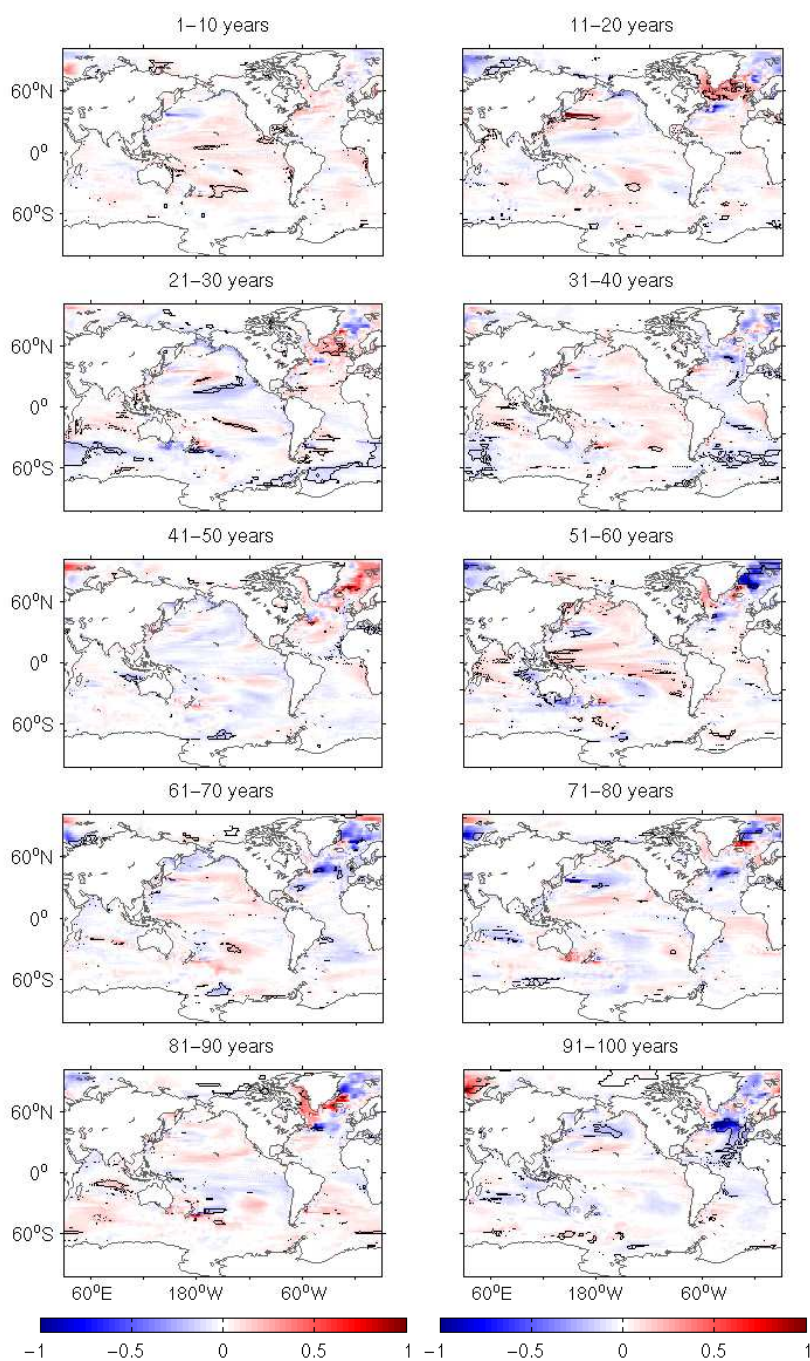


Figure 3.10: Decadal average SST anomalies (EXP1 - control) for 100 years. Contours show anomalies significant at the 95% confidence level.

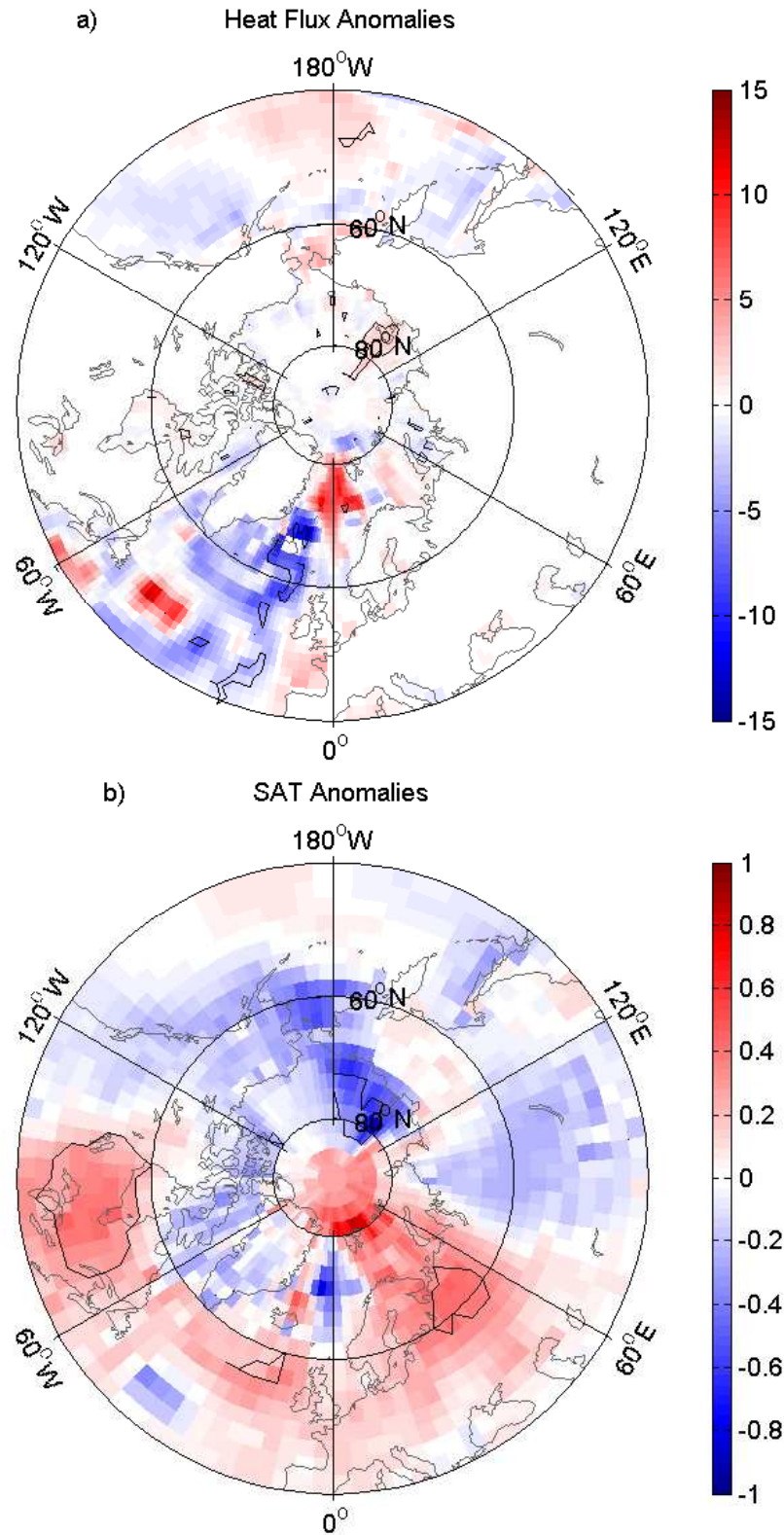


Figure 3.11: Decadal average anomalies for 21-30 years (EXP1 – Control): (a) total heat flux in the atmosphere-ocean direction (positive heat flux anomalies indicating greater flux in the atmosphere-to-ocean direction) [W m^{-2}]; (b) surface air temperature (SAT) [$^{\circ}\text{C}$]. Black contours show anomalies significant at the 95% confidence level.

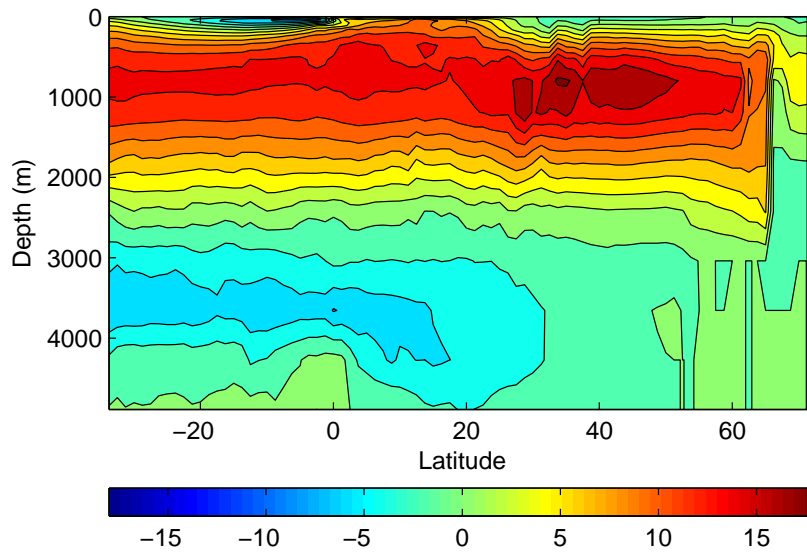


Figure 3.12: Mean meridional streamfunction in the Atlantic for a 100 year mean of the control ensemble. [Sv]

Atlantic Current (NAC). Surface heat flux anomalies show that this cooling is also driven by the ocean rather than the atmosphere. These cooler, fresher waters are advected into the GIN Seas and, for years 91-100, the SST anomalies also show a path of recirculation in the North Atlantic subtropical gyre (Figure 3.10). Throughout the North Atlantic there is a mean reduction in SST for 51-100 years.

Dong and Sutton (2002a) show that changes in ocean heat transport (OHT) are the major cause of SST anomalies in the North Atlantic. In a separate study, they also show that changes in the gyre strength and meridional overturning circulation (MOC) in the Atlantic are the primary cause of OHT anomalies on decadal and multidecadal timescales (Dong and Sutton, 2001). Figure 3.12 shows the mean overturning streamfunction in the Atlantic for 100 years of the control ensemble. Three indices of MOC strength were chosen as the maximum overturning streamfunction at 26.25, 45 and 60°N, the approximate latitudes of the RAPID array (Cunningham *et al.*, 2007), maximum overturning strength and maximum MOC anomalies, respectively. The latitude of maximum overturning for the control ensemble lies further south, at $\sim 35^\circ\text{N}$ (Figure 3.12), however 45°N was chosen as it lies in the region of increased overturning strength (16-18 Sv) and follows the range of indices used in previous studies (Dong and Sutton, 2002b; Vellinga and Wood, 2002). For years 50-100 there is a decrease in the strength of the MOC shown by all three indices (Figure 3.13). Although the decrease is still within the range of the control

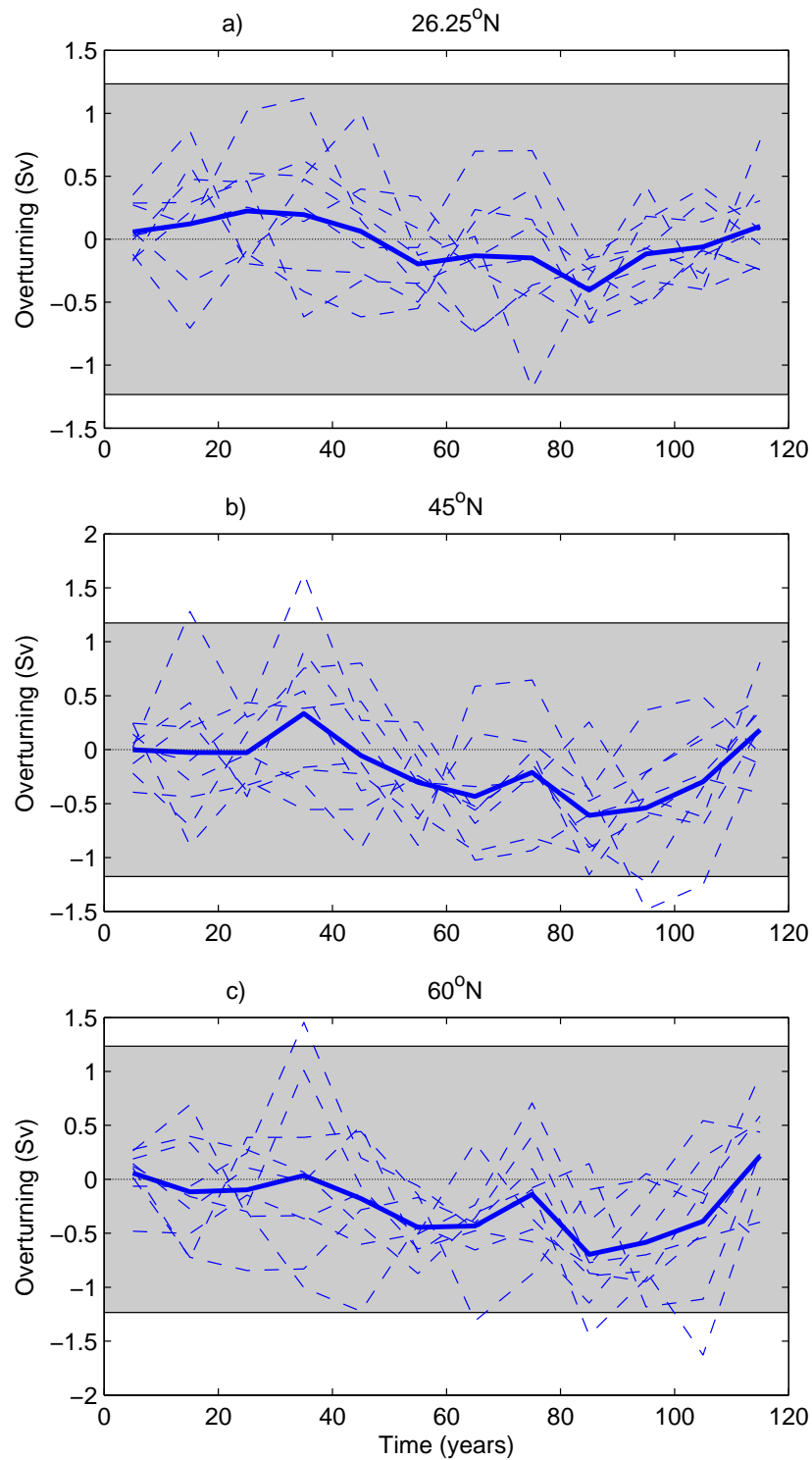


Figure 3.13: Decadal average MOC strength anomalies (*EXP1* – *Control*) within the Atlantic at a. 26.25°N, b. 45°N and c. 60°N. Solid lines indicate the anomaly of ensemble mean values; dashed lines show the anomalies of individual *EXP1* ensemble members minus mean of the control. Shaded region shows the 95% spread of the control ensemble over the 120 year simulation.

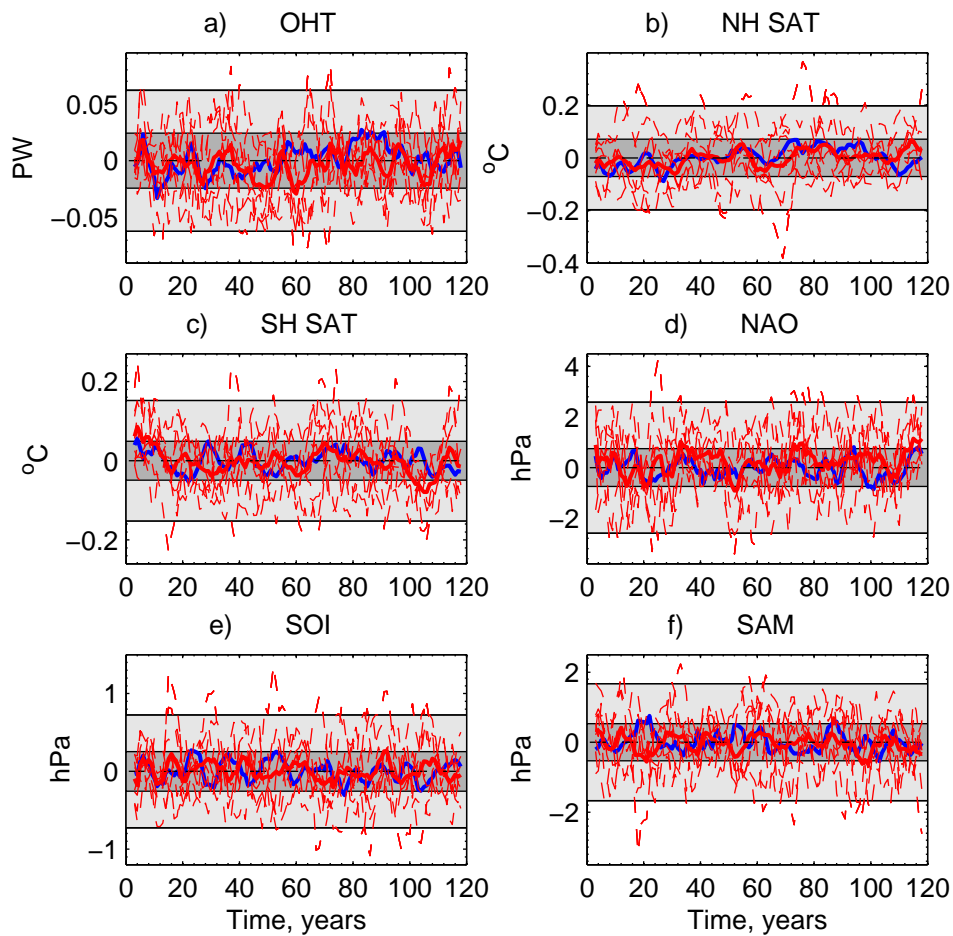


Figure 3.14: Climate indices anomalies for EXP1: (a) Northward ocean heat transport (OHT) at 26°N in the Atlantic; (b) mean Northern Hemisphere (NH) surface air temperature (SAT) (c) mean Southern Hemisphere (SH) SAT; (d) North Atlantic Oscillation (NAO) index : annual MSLP difference from Gibraltar-Iceland; (e) Southern Oscillation Index (SOI) : annual MSLP difference from Tahiti-Darwin; (f) Southern Annular Mode (SAM) : annual MSLP difference between 40 and 65°S . Light (dark) shaded area shows the 2σ (95%) spread of the control ensemble (mean) around the 120 year mean. Dashed (solid) red lines show the ensemble (mean) anomalies for EXP1 (EXP1 – time-mean of control). Blue line shows the mean of the control ensemble around the 120 year mean. Data are smoothed using a 5 year running mean. Dashed black line indicates the reference time-mean value for the control ensemble over the 120 year simulation (at zero).

ensemble, t -test analysis shows that it is statistically significant at the 95% confidence level for all three indices during years 81-90. The maximum decrease occurs during these years, with reductions of 0.4, 0.6 and 0.7 Sv for 26.25 , 45 and 60°N . For 60°N this is a 4.6% reduction in the overturning strength. The decreased MOC strength throughout the North Atlantic can account for the mean reduction in the northward OHT (Figure 3.14), and hence reduced SST (Figure 3.10). After 100 years the MOC begins to recover, and by the end of the simulation positive anomalies are present at each of the three latitudes, with a mean maximum overturning strength of 18.0 Sv at 45°N for EXP1, compared with

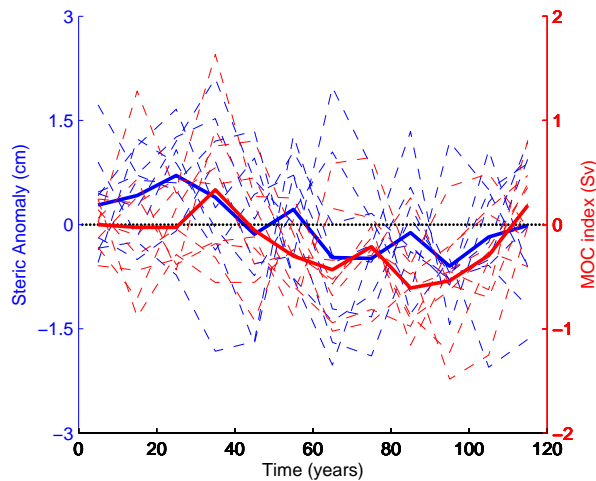


Figure 3.15: Decadal average MOC strength anomalies at 45°N (red) and steric height difference anomalies, 30°S-60°N within the Atlantic (blue). Solid lines indicate the anomaly of ensemble mean values (EXP1 – Control); dashed lines show the anomalies of individual EXP1 ensemble members minus mean of the control.

17.8 Sv for the control ensemble.

Thorpe *et al.* (2001) show that on decadal timescales the strength of the Atlantic MOC in HadCM3 is correlated with the steric height gradient in the Atlantic, between 30°S-60°N. The steric height is given by

$$- \int_H^0 \frac{\delta\rho}{\rho_0} dz,$$

where ρ_0 is a constant reference potential density and $\delta\rho$ is the density anomaly (EXP1–Control). Following Thorpe *et al.* (2001), we take H to be 3000 m, equivalent to level 16 in the model. Positive anomalies indicate a greater steric height difference between 30°S and 60°N in the perturbation experiment, and vice versa. The timeseries of these anomalies has a positive correlation of 0.64 with the MOC strength anomalies at 45°N (Figure 3.15). This relationship is driven primarily by the steric height at 60°N, as there is relatively little change in density in the South Atlantic. This is illustrated in Figure 3.16b, which shows the zonally averaged steric height anomalies between 35°S and 80°N in the Atlantic and further north into the Labrador and GIN seas. Positive anomalies in the steric height indicate a decrease in density in the water column. At 60°N there is an overall increase in steric height and decrease in density after 50 years, compared with the control ensemble. Although there is also an increased steric height in the South Atlantic, this is smaller than that in the north. The control climate has a negative steric height

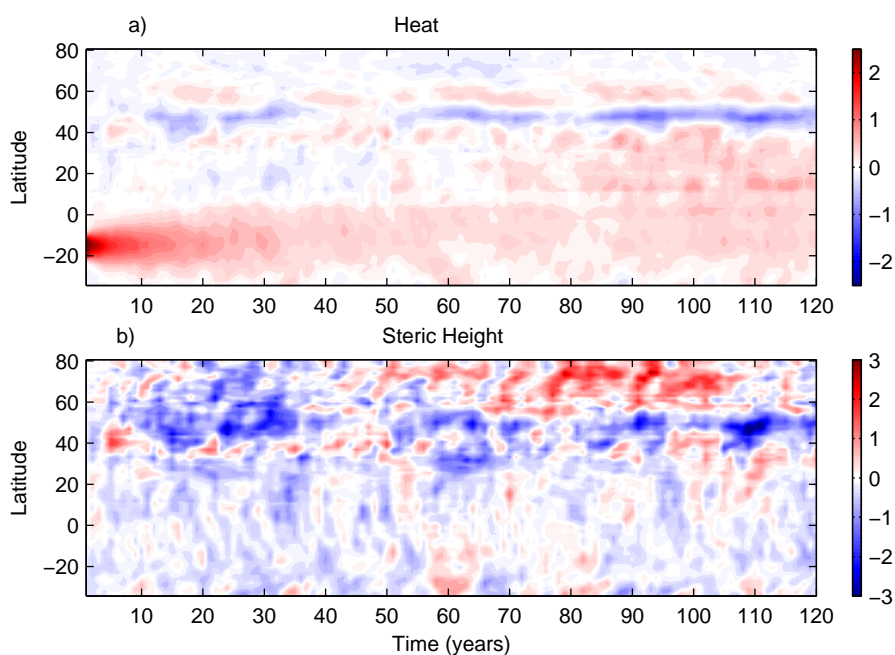


Figure 3.16: Hovmöller plots of (a) heat content anomalies ($EXPI - Control$), within 0-3000 m [10^{21} J]; (b) zonal mean steric height anomalies ($EXPI - Control$) [cm], in the Atlantic basin.

gradient. Therefore, the resulting difference ($30^{\circ}S - 60^{\circ}N$) is reduced during the course of this experiment, compared with the control ensemble.

The reduction in overturning strength is therefore driven by decreasing density at $60^{\circ}N$. Such a change could be caused by either a warming or freshening at this latitude. Figure 3.16a shows the total zonal heat content anomalies in the Atlantic. Increased heat content is found around $60^{\circ}N$ after 10 years, corresponding with the increased salt content and SST anomalies around the tip of Greenland for years 11-20 (Figures 3.6 and 3.10). These warm, heat content anomalies persist at this latitude for the remainder of the simulation, and increase as more of the warmer water mass spreads northwards through the Atlantic. The maximum anomalies at $60^{\circ}N$ occur between years 80-100, when a maximum decrease was also observed in the MOC strength. After 40 years, the warm anomalies lead to decreased density through the water column and hence the increase in steric height. A southward progression of positive heat anomalies can also be seen from year 40 onwards, corresponding to the warm anomalies sinking and then travelling southward in the deep waters (Figures 3.8 and 3.9).

The timescale for the anomalies to propagate northwards, and lead to significant changes at $60^{\circ}N$, is consistent with those seen in previous experiments. For example, Sen Gupta and England (2007) performed tracer release experiments in AAIW formation

regions using a $1/4^\circ$ resolution model. Tracer released at the surface in the southeast Indian Ocean was found to reach 1% concentration at 60°N in the Atlantic within 60 years on $\sigma_0 > 27.0$, ~ 40 years after reaching our perturbation region. At shallower depths ($\sigma_0 = 26.8$), the tracer reaches 45°N within 25 years. They also show that the ventilation timescale for AAIW in the Atlantic ranges from 50–150 years, consistent with observations (Holzer *et al.*, 2010).

3.3.2.1 Anomalies in the NAC

The cool, fresh anomaly in the NAC region extends to a depth of 1500 m (Figure 3.8). This, along with the sign of the surface heat fluxes in the region (Figure 3.11), indicates that anomalous water may be surfacing in this region. Further analysis of this anomaly shows that there is a divergence of meridional ocean heat fluxes from this region (bounded by 45°N and 53°N), with increased heat transport leaving to the north, as well as a reduction of heat arriving from the south (Figure 3.17). Between 45°N and 53°N , the subtropical gyre (STG) and subpolar gyre (SPG) meet in the Atlantic (Figure 3.7). From the south, the reduction in the MOC strength can account for the reduced heat transport. To the northern side of the region, the increased heat transport may be accounted for by an increased volume of cool water moving southward from $> 53^\circ\text{N}$. Hátún *et al.* (2005) show that during periods of increased SPG transport, water from this gyre constitutes a larger proportion of that in the NAC, compared with water from the subtropical gyre. During this simulation, there is an increased transport in the SPG (Figure 3.18), although it is worth noting that there is no change in the southern limit of the gyre. The increased gyre transport seen in this experiment may then lead to increased transport of cool, fresh water southward from the Labrador Sea. The strongest surface cooling is found for years 91–100. This follows the decade of the strongest MOC anomalies, and during this time there is a significant increase in the SPG transport (Figure 3.18). The atmospheric response to this persistent anomaly is discussed in further detail in the following section (Section 3.3.3).

3.3.3 Atmospheric responses to the anomaly

The majority of the surface air temperature (SAT) anomalies match those seen in the SST field, with the warmer (colder) surface ocean releasing (absorbing) more heat to (from)

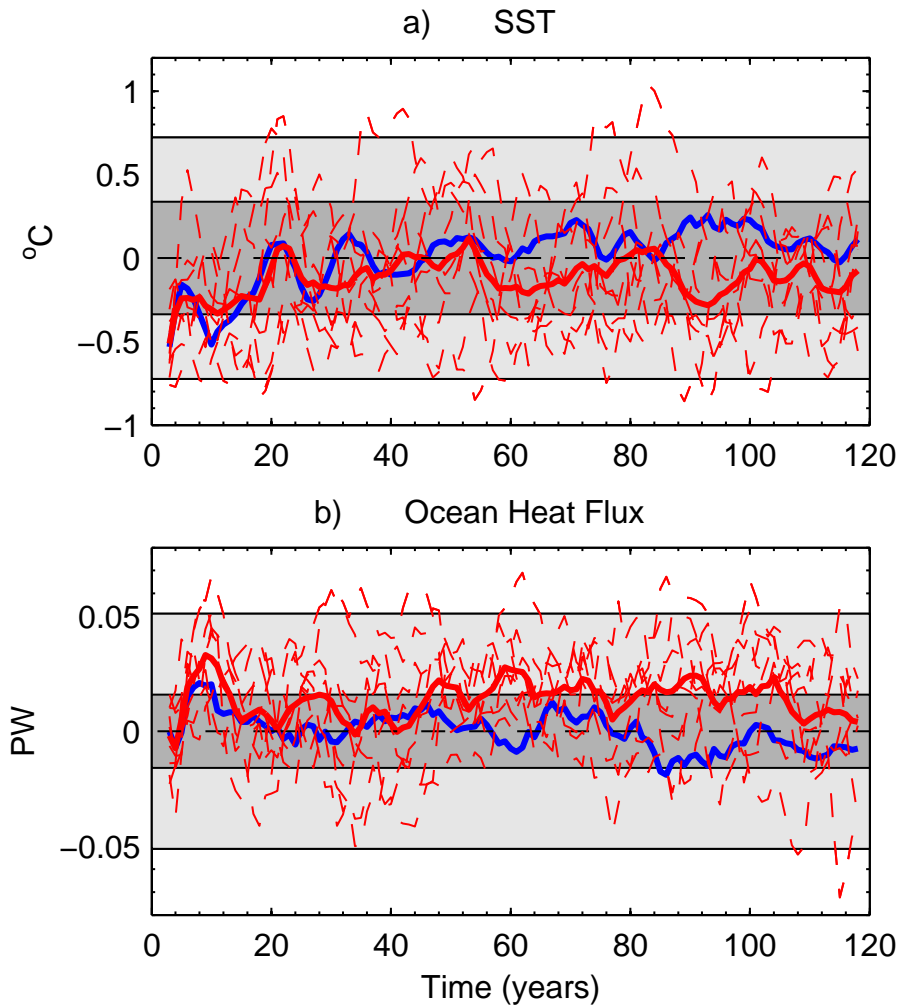


Figure 3.17: Heat anomalies in the region of the North Atlantic Current: (a) average SST anomaly between 45 and 53°N in the Atlantic; (b) meridional ocean heat flux anomaly ($53^{\circ}\text{N} - 45^{\circ}\text{N}$). Light (dark) shaded area shows the 2σ (95%) spread of the control ensemble (mean) around the 120 year mean. Dashed (solid) red lines show the ensemble (mean) anomalies for EXP1 (EXP1 – time-mean of control). Blue line shows the mean of the control ensemble around the 120 year mean. Data are smoothed using a 5 year running mean. Dashed black line indicates the reference time-mean value for the control ensemble over the 120 year simulation (at zero).

the atmosphere. Figure 3.11 shows that the warmer atmosphere over the North Atlantic, for years 21-30, is driven by the anomalous heat flux from the warmer surface ocean. For this decade there is also an increased SAT over Europe and North America. The mean SAT over the Northern Hemisphere (NH) increases during this decade (Figure 3.14b), however this increase is not significant. As the simulation progresses, the cooler waters through the North Atlantic and GIN Seas lead to reductions in SAT for years 51-100, which are significant over the NAC and GIN Seas (Figure 3.19). There are also regions of significant cooling over North America and the Middle East. Figure 3.14b shows that there is a mean decrease in the NH SAT for years 50-100, when compared with the control

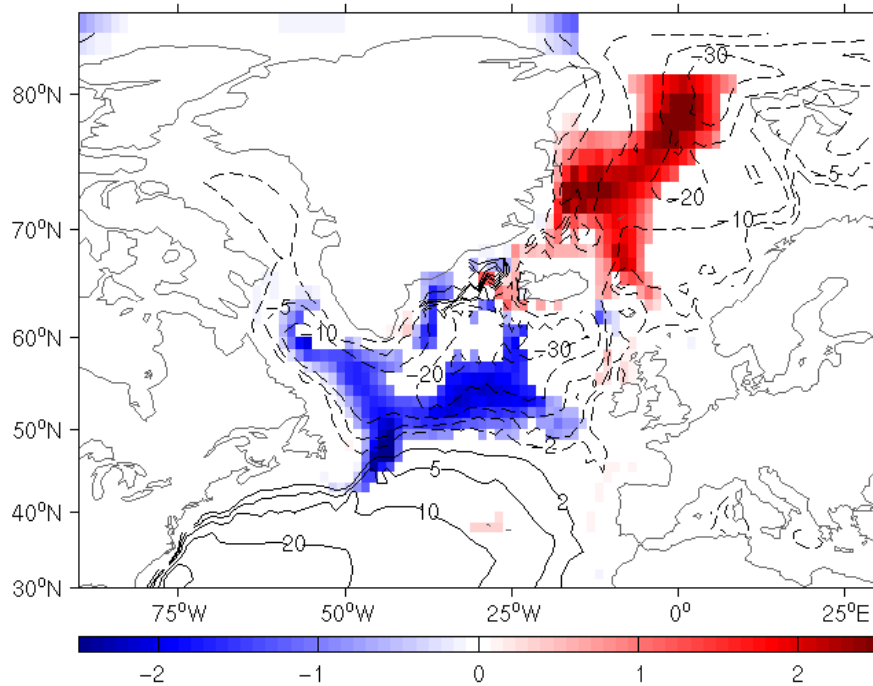


Figure 3.18: Mean barotropic streamfunction anomaly ($EXP1 - Control$) for years 51-100. Only anomalies significant at the 95% confidence level are shown. Contours show the 100 year mean values for the control ensemble, with solid (dashed) contours indicating positive (negative) values [Sv].

ensemble, corresponding with the decreased OHT. However, there is no significant trend in either Northern Hemisphere (NH) or Southern Hemisphere (SH) SAT (Figure 3.14b,c).

Previous studies of the atmospheric response to the basin-wide shifts in Atlantic SST, known as the Atlantic Multidecadal Oscillation (Delworth and Mann, 2000), have shown responses in the rainfall patterns across the southern US and Sahel region of Africa (Sutton and Hodson, 2005). The average precipitation for years 51-100 (Figure 3.19b) shows that there is little significance in the precipitation changes. However, there is a small region of significant decrease (up to 2.4 cm year^{-1}) over northwest Africa and southwest Europe. This response is likely a result of the warm surface anomalies found around Iceland and in the Labrador sea (Figure 3.10). The precipitation and mean sea level pressure (MSLP) responses to North Atlantic SST described by Sutton and Hodson (2005) show that the effects over Europe and Africa are due to the cooling in the subtropical Atlantic ($> 30^\circ N$). The warming around $60^\circ N$ may then account for the smaller atmospheric anomalies in these regions.

The response over the USA is also weaker than that usually associated with the AMO (Sutton and Hodson, 2005), with only a small region of significance and precipitation

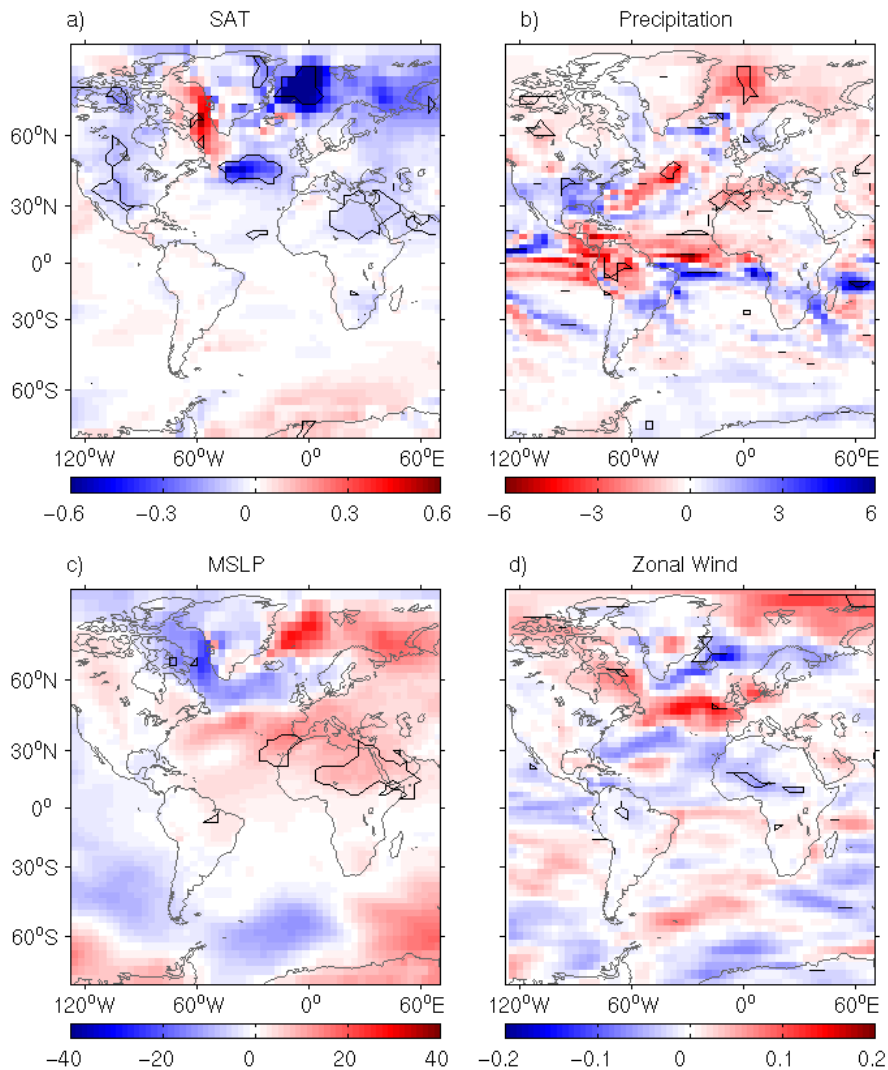


Figure 3.19: Mean atmospheric anomalies for 51-100 years (EXPI – Control): (a) surface air temperature (SAT) [$^{\circ}\text{C}$]; (b) precipitation [cm year^{-1}]; (c) mean sea level pressure (MSLP) [Pa]; (d) zonal wind speed [m s^{-1}]. Black contours show anomalies significant at the 95 % confidence level.

increases of only up to 3.4 cm year^{-1} (Figure 3.19b). This weak response in the precipitation field is associated with a weak MSLP response (Figure 3.19c). Sutton and Hodson (2005) show that the warm phase of the AMO leads to lower pressure over the southern US, and a decrease in rainfall. A cool phase should then lead to the opposite effect. However, although there is a temperature decrease in the North Atlantic for years 51-100, the cooling mostly occurs north of 40°N , in the extratropics. There is also a weak tripole effect with positive anomalies off the east coast of North America (Figure 3.10). As the response over North America is predominantly driven by the SST anomalies in the tropical North Atlantic, $0\text{-}30^{\circ}\text{N}$ (Sutton and Hodson, 2005), this accounts for the weaker

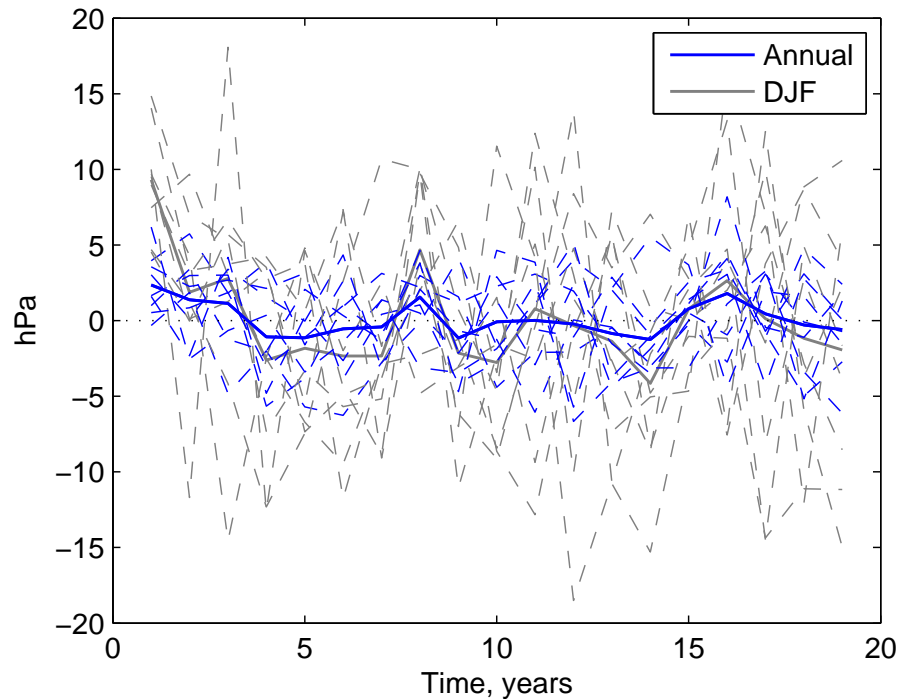


Figure 3.20: NAO indices for first 20 years of the control ensemble: MSLP difference from Gibraltar-Iceland. Blue (gray) lines show the NAO index calculated using annual (winter, Dec-Feb) MSLP. Values shown are relative to the 20 year-mean value (dotted line at zero for reference). Solid lines indicate the ensemble mean values; dashed lines show the individual ensemble members.

atmospheric response seen in these results. The precipitation anomalies seen within the tropics are characteristic of a shift in the Intertropical Convergence Zone (ITCZ), which has been shown to occur with changes in the strength of the MOC (Vellinga and Wu, 2004).

Tripole patterns in the North Atlantic are characteristic of the North Atlantic Oscillation (Deser and Blackmon, 1993; Seager *et al.*, 2000). The NAO index shown in Figure 3.14d is calculated using annual means of MSLP rather than the winter (December-February) values. Winter MSLP values are known to show a stronger signal for the NAO. However, Figure 3.20 shows that whilst there is a stronger signal for the NAO index calculated using the winter MSLP, the same trends are visible when using annual mean data. Therefore, the annual data available here can be used to look for NAO responses in these experiments. Although there is no significant trend, from Figure 3.14d it is possible to see an increased occurrence of positive NAO phases during EXP1. This indicates a greater pressure difference between the Icelandic Low and Azores High, which can also be seen in Figure 3.19c. Such pressure differences can lead to greater wind stress over the North

Atlantic (Figure 3.19d). As mentioned in Section 3.3.2, increased SPG transport may lead to greater volumes of cold SPG water moving southwards, contributing to the divergence of heat transport observed in the NAC (Figure 3.17a). The mean wind stress curl is increased over the SPG for the simulation. The decades which see the strongest increases, for example during years 41-50 (not shown), correspond with increased transport of cold water moving southwards from $> 53^{\circ}\text{N}$ in Figure 3.16a. A feedback mechanism may then contribute to the persistence of the cold anomaly in this region, where the SST anomalies lead to MSLP and wind anomalies that act to increase the transport in the SPG. This in turn increases the proportion of cooler water in the NAC. However, it should be noted that as the MSLP anomalies are not significant, there is not a significant change in the zonal wind strength (Figures 3.19c,d).

The Southern Oscillation Index (SOI) shows the variability in the Pacific, switching between warm, El Niño, and cool, La Niña, phases (Figure 3.14e). These anomalies are within the range of the internal variability and result from the EXP1 and Control ensembles varying out of phase in the Pacific. The Southern Annular Mode (SAM, also known as the Antarctic Oscillation) is the leading mode of variability in the SH (Thompson and Wallace, 2000). The climate index is calculated here as the pressure difference between 40 and 65°S . As with the NAO index, changes in the SAM give indications of the wind strength due to the resulting MSLP patterns, along with many other responses in both the atmosphere and ocean. For this experiment, no significant trend can be seen for the SAM, again with the anomalies shown falling within the range of natural variability in the model (Figure 3.14f). However, a significant anomaly can be seen around year 20, with a shift towards a strong negative phase. Although this change is statistically significant, the large anomaly results primarily from the control ensemble being in a strong positive phase during this period⁴. Therefore, this perturbation appears to have had no real significant effect on the climate in the SH.

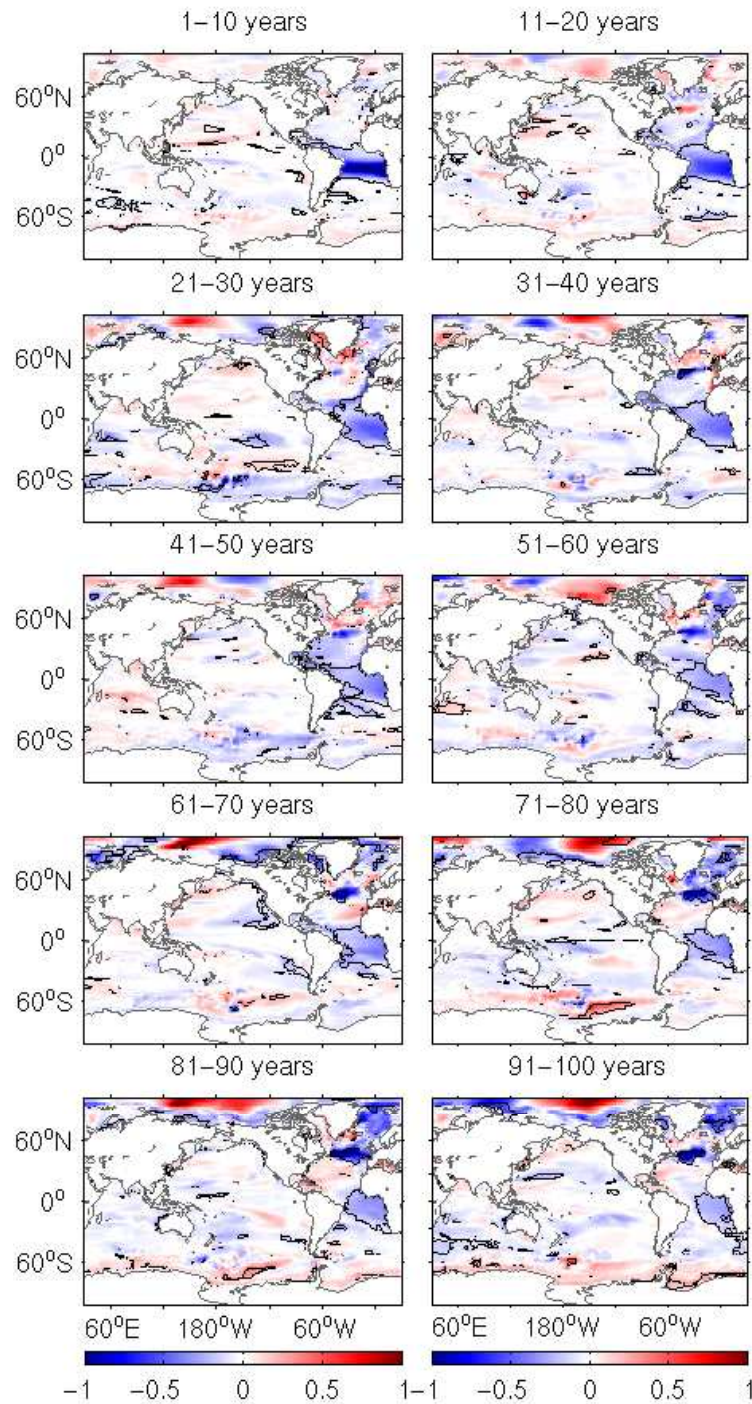


Figure 3.21: Decadal salt content anomalies within columns (EXP2 - control) $[\times 10^2 \text{ kg m}^{-2}]$. Black contours show anomalies significant at the 95% confidence level.

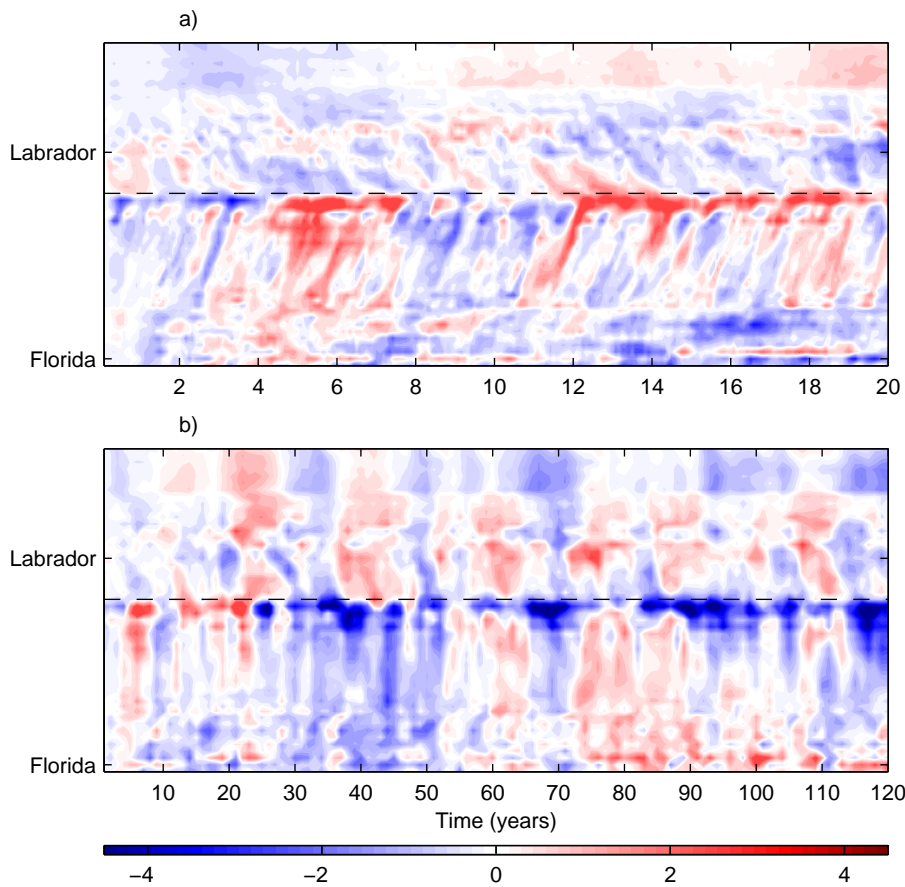


Figure 3.22: Salt content anomalies for a 3 grid-box wide path along the western boundary of the North Atlantic basin, from 28-75°N (EXP2 – control) [10^{12} kg]: (a) monthly anomalies for the first 20 years; (b) annual anomalies for the 120 year simulation. The dashed line lies at 48°N, indicating the partition between the sub-polar and sub-tropical gyres.

3.4 EXP2 Results

3.4.1 Where does the anomalous water go?

The path of the cooler, fresher AAIW can be traced using the reduction in salt content (Figure 3.21). After 10 years, the fresher water mass is seen to have spread northwards, being carried primarily by the North Brazil Current. From the tropical North Atlantic, the anomaly is carried further northwards with the Gulf Stream. Figure 3.22 shows the total salt anomalies along the western boundary of the North Atlantic basin, from Florida to Baffin Bay (28–75°N). The salt anomalies travel northwards at a speed consistent with advection, taking ~ 2 years to reach the NAC due to current speeds $> 6 \text{ cm s}^{-1}$ in the Gulf Stream (Figure 3.22a). From the NAC, a portion is recirculated in the subtropical

⁴The effect of the control ensemble, causing this strong response in the SAM and the Southern Ocean, will be discussed in further detail in relation to the Pacific experiments (Chapter 5).

gyre, and the remainder travels further north (Figure 3.21). Recirculation allows the North Atlantic to gradually fill with the fresher water mass. Significant cool, fresh anomalies are found in the region of the NAC after 30 years. During years 25-50, the anomalies along the western boundary show the northward transport of the fresher water mass (Figure 3.22b) and the majority of the Atlantic basin has a reduced salt content after 50 years (Figure 3.21). However, as the integration progresses, the northward branch of the NAC allows the fresher water to be carried into the SPG and the GIN Seas. Anomalies gradually reduce in the North Atlantic as the cooler, fresher water builds up further northwards. This can be seen in Figure 3.21 for years 71-80 onwards. After 100 years, the majority of the Atlantic remains fresher than the control simulation. A significant volume of fresher water stays in the initial perturbation region as it recirculates in the South Atlantic subtropical gyre.

The zonally averaged salinity in the Atlantic shows that the portion of the anomaly that is initially in the upper layers disperses rapidly as it is advected with currents and enters mixed layers in the upper levels of the ocean (Figure 3.23). However, the portion of the anomaly that lies at intermediate depths (500 - 1500 m), spreads and remains at these depths. After 30 years, a region of freshening can be seen between 40-50°N. This anomaly is seen at the surface and penetrates to at least 2000 m, indicating that cooler, fresher water may be surfacing in this region. At this latitude, in the NAC, the mixed layer depths are > 300 m, allowing the intermediate waters to surface. After 50 years, the majority of the Atlantic is seen to be fresher between depths of 500-2000 m. As the simulation continues, the fresher water builds up north of 60°N (Figure 3.21). After 70 years (Figure 3.23) there is a freshening in this region down to 3000 m (level 16 in HadCM3). This is present throughout the water column as the fresher water sinks during formation of deep waters around the southern tip of Greenland. The impact of this freshening in the north will be discussed in Section 3.4.2. As the fresh anomaly spreads southwards in the deep waters, the mean salt content in the Atlantic decreases in the deep levels (14-20) and increases in the layers above (Figure 3.24). However, by the end of the simulation there is still a clear reduction in salt content at intermediate depths in the Atlantic of 3.5×10^{14} kg, equivalent to 28% of the original perturbation. Along with this, a heat reduction of 4.3×10^{21} J still remains in the intermediate depths between 30°S and 70°N, equivalent to 17% of the initial perturbation.

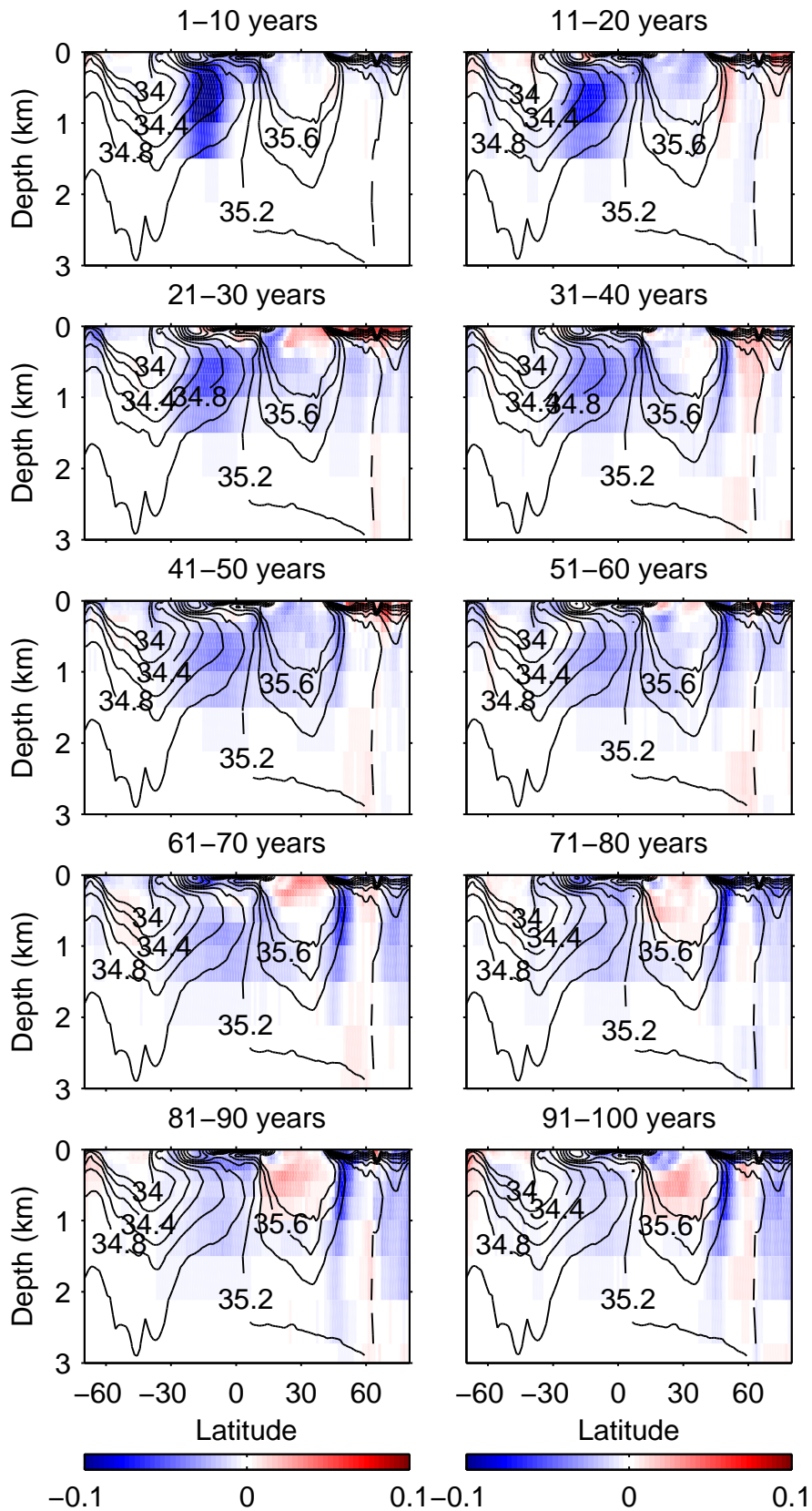


Figure 3.23: Zonally averaged decadal salinity anomalies (*EXP2* – control) in the Atlantic for 100 years.

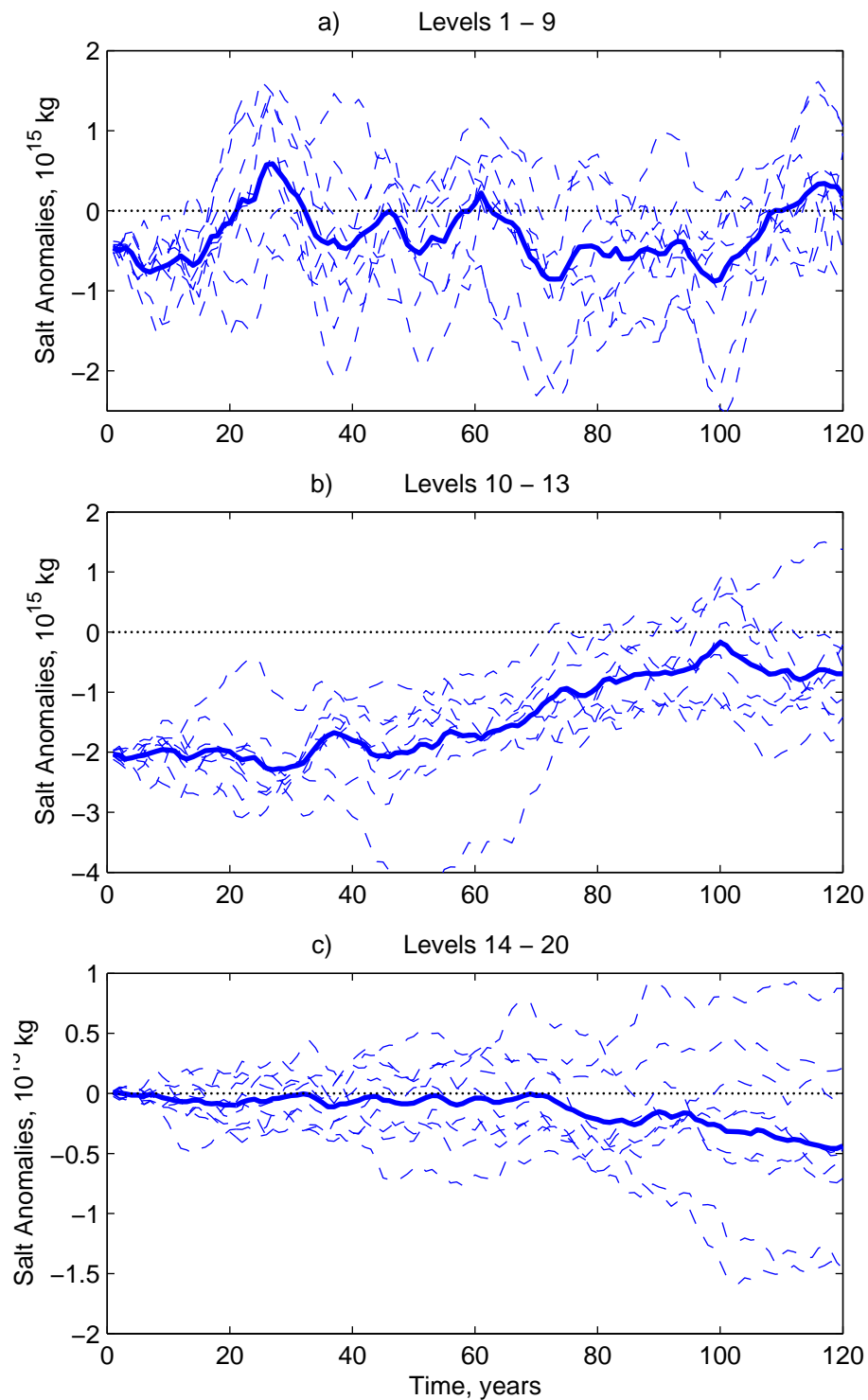


Figure 3.24: Total salt content anomalies in the Atlantic, between 30°S and 70°N , for depth levels (a) 1 - 9, $\sim 0 - 300$ m; (b) 10 - 13, $\sim 300 - 1500$ m; (c) 14 - 20, $\sim > 1500$ m. Solid lines show the ensemble mean anomalies (EXP2 - control); dashed lines show anomalies of individual EXP2 ensemble members minus the mean of the control ensemble.

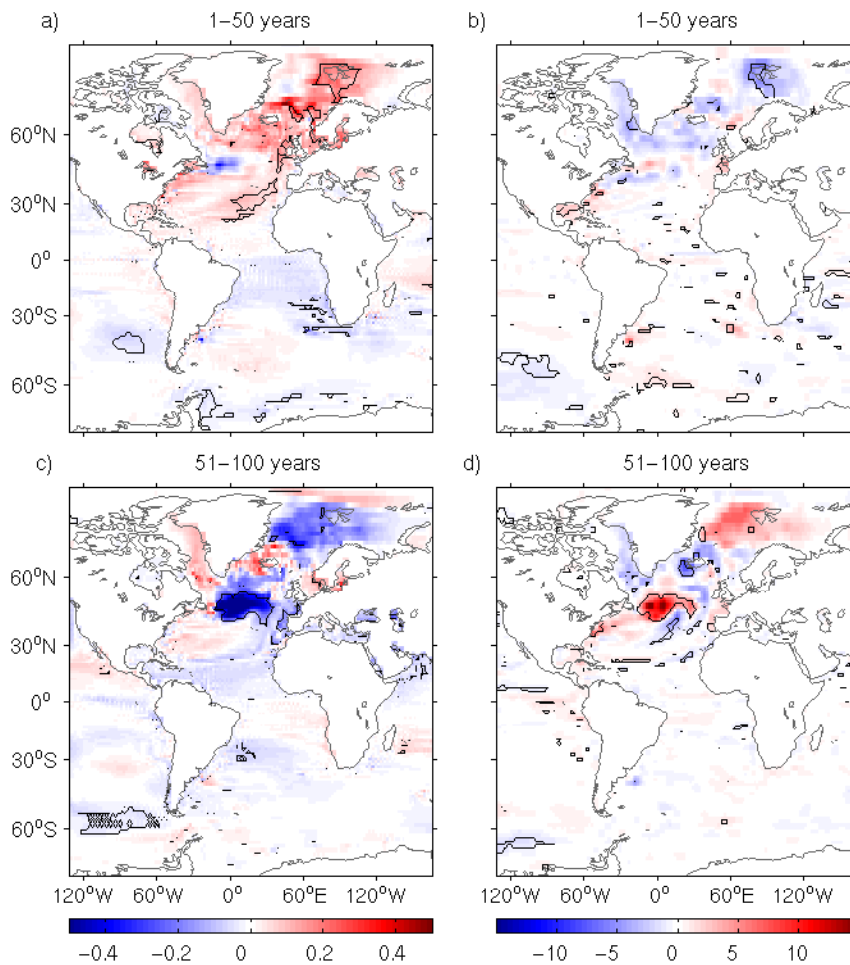


Figure 3.25: 50-year-average anomalies ($EXP2 - control$) for first 100 years of: (a),(c) sea surface temperature (SST) [$^{\circ}C$]; (b),(d) total heat flux in the atmosphere-ocean direction [$W m^{-2}$]. Black contours indicate anomalies significant at the 95 % confidence level.

3.4.2 Changes seen at the sea surface

There is a region of significant cooling in the surface of the North Atlantic during the second half of the simulation (Figure 3.25c). The signs of the heat flux anomalies show that changes at the surface are driven by the ocean rather than the atmosphere, as regions with a cooler SST have positive heat flux anomalies, absorbing more heat from the atmosphere, rather than losing it (Figure 3.25). There is a cooling seen in the NAC region within the first 50 years. The significant anomaly develops after 30 years and grows as the simulation progresses, with a reduction of up to $1^{\circ}C$ in the later decades.

Figure 3.26 shows the timeseries of the MOC indices for the Atlantic (defined in Section 3.3.2). The MOC strength initially shows an increase, followed by a reduction that is significant by years 91-100, corresponding to the decreased SST. The reduction

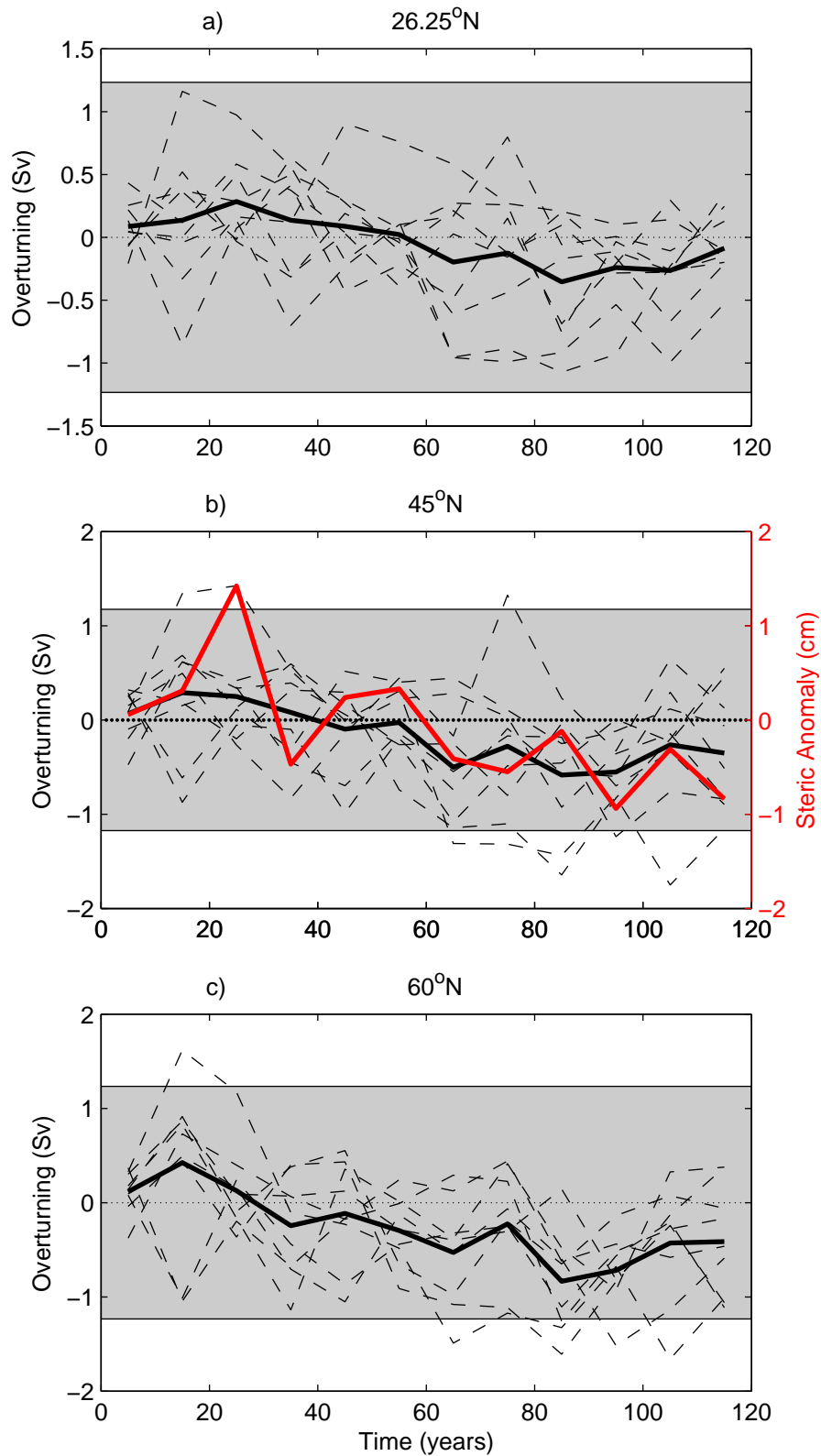


Figure 3.26: Decadal average MOC strength anomalies (black) within the Atlantic at (a) 26.25°N, (b) 45°N and (c) 60°N. Panel (b) also shows the steric height difference anomalies, 30°S–60°N within the Atlantic (red). Solid lines indicate the anomaly of ensemble mean values (EXP2 – Control); dashed lines show the anomalies of individual EXP2 ensemble members minus mean of the control. Shaded region shows the 95% spread of the control ensemble over the 120 year simulation.

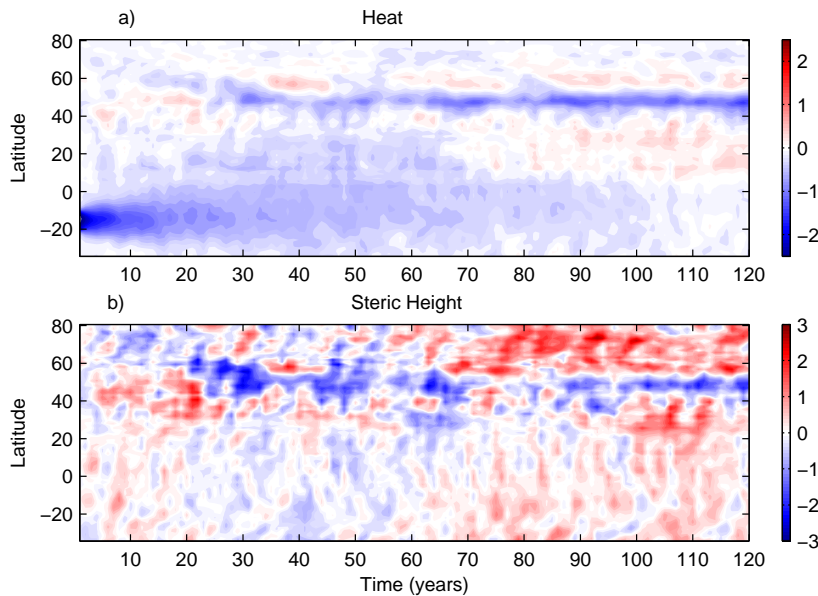


Figure 3.27: Hovmöller plots of (a) heat content anomalies ($EXP2 - Control$), within 0-3000 m [10^{21} J]; (b) zonal mean steric height anomalies ($EXP2 - Control$) [cm].

develops first at $60^{\circ}N$, with the mean index showing negative anomalies at 31-40 years. This decrease then propagates southwards, at $45^{\circ}N$ for 41-50 years, and at $26.25^{\circ}N$ for 61-70 years. The largest anomalies are seen at 81-90 years, with anomalies of -0.8 , -0.6 and -0.4 Sv at 60 , 45 and $26.25^{\circ}N$, respectively. At 45 and $60^{\circ}N$, the reduction for years 91-100 is significant at the 95 % confidence level, and all ensemble members show negative anomalies. After 100 years the MOC strength begins to recover, although by the end of the integration, at 111-120 years, there is still a reduced strength, with a maximum value at $45^{\circ}N$ of 17.4 Sv in the mean of the perturbed runs, compared with 17.8 Sv in the mean of the control simulations.

Steric height anomalies ($30^{\circ}S - 60^{\circ}N$) have a positive correlation with the MOC strength anomalies at $45^{\circ}N$ (Figure 3.26b), driven primarily by density changes at $60^{\circ}N$. Around the tip of Greenland and in the GIN Seas, there is an overall increase in steric height and decrease in density compared with the control ensemble. Although there is also an increased steric height in the South Atlantic, this is smaller than that in the north. Figure 3.27a shows the total zonal heat content anomalies in the Atlantic. The initial cool anomaly advects northwards through the North Atlantic, as described earlier. Within 30 years, the cool anomaly reaches the NAC ($\sim 45^{\circ}N$). It takes a further 30 years before it builds up further north, 60 years into the simulation. As the water moves through the NAC and into the Greenland Sea, it cools the atmosphere above it (Figure 3.25d). This process

of the surface ocean absorbing heat from the atmosphere leaves a warmer, fresher and hence less dense water mass. The effects can be seen in Figure 3.27b, as the decrease in density leads to an increase in steric height around 60°N and further north after 60 years. The strongest reduction in the MOC, at years 81-90, occurs after the arrival of the fresher water moving southward. The timescale for the anomalies to propagate northwards is consistent with those seen in previous experiments with HadCM3. Tracer released at the surface in the tropical North Atlantic took 5 to 6 decades to build to significant concentrations in the GIN Seas, due to the processes of dispersion and recirculation that occur along with the northward advection (Vellinga and Wu, 2004).

The strongest SST anomalies, which develop around the NAC, persist from 30 years through to the end of simulation (Figure 3.28a). This cool, fresh anomaly extends down from the surface to > 2000 m (Figure 3.23). Along with the positive surface heat fluxes in this region (Figures 3.25b,d), this indicates that anomalous water may be surfacing in this region. As with EXP1 (Section 3.3.2.1), this cold anomaly can be attributed to a divergence of heat transport from the region (Figure 3.28). From the south, a combination of cooler AAIW being carried northwards and the reduction in the MOC strength can both account for the reduced heat transport (Figure 3.29a). Increased SPG transport brings cooler, fresher water from the north. The southward transport of anomalous water can be seen in Figures 3.22 and 3.27a, in particular during years 20-30 and 70-80. The link between this southward transport for years 20-30 and the initial increased MOC strength is discussed in Section 3.5. The atmospheric response to this persistent anomaly is presented in Section 3.4.3.

3.4.3 Atmospheric responses to SST

The cooling of the North Atlantic seen in this experiment can have a series of atmospheric responses. The presence of the cooler SSTs leads to a cooling of the overlying atmosphere, and hence we expect to see cooler SATs over the ocean and its surrounding continents. The maximum anomalies in the global surface atmospheric temperature occur for years 65-75, when there is a reduction in both the NH and SH (Figures 3.29b,c). There is a mean global SAT anomaly of -0.07°C at this time. For years 51-100 there is an atmospheric cooling over the areas of cooler SSTs (Figure 3.30a). Anomalies are particularly large

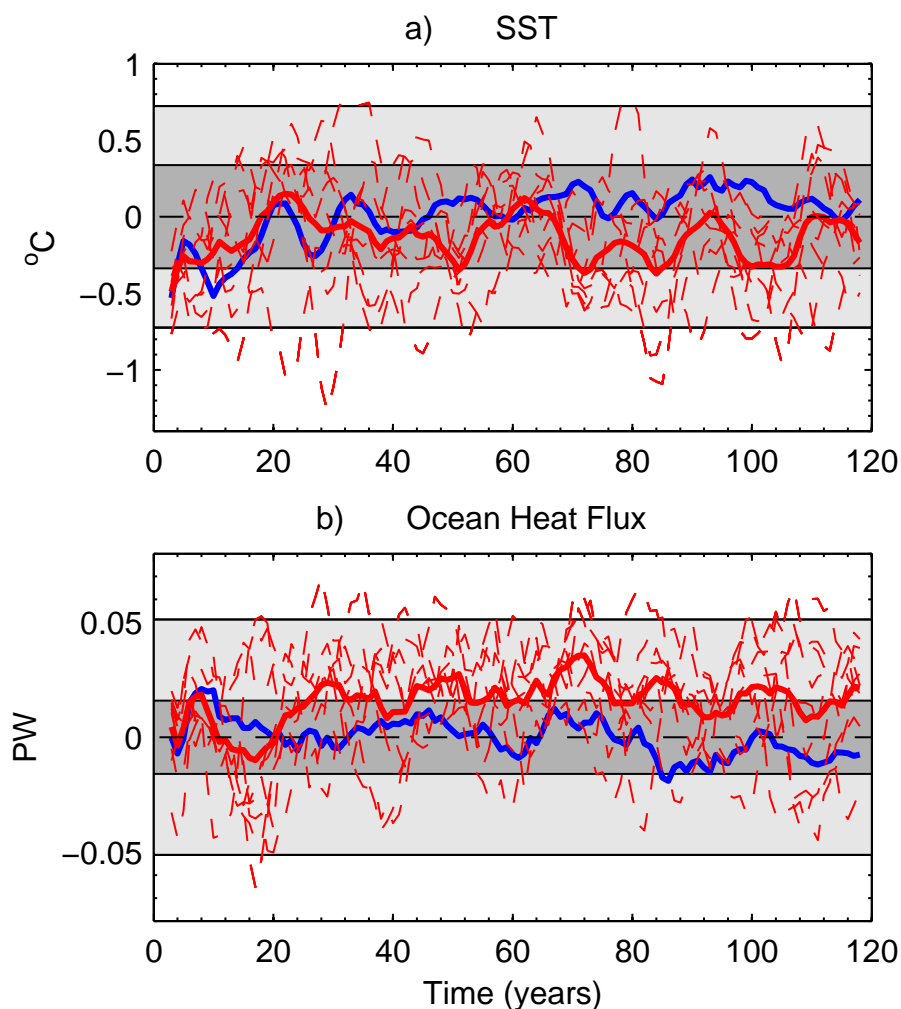


Figure 3.28: Heat anomalies in the region of the North Atlantic Current: (a) average SST anomaly between 45°N and 53°N in the Atlantic; (b) meridional ocean heat flux anomaly ($53^{\circ}\text{N} - 45^{\circ}\text{N}$). Light (dark) shaded area shows the 2σ (95%) spread of the control ensemble (mean) around the 120 year mean. Dashed (solid) red lines show the ensemble (mean) anomalies for EXP2 (EXP2 – time-mean of control). Blue line shows the mean of the control ensemble around the 120 year mean. Data are smoothed using a 5 year running mean. Dashed black line indicates the reference time-mean value for the control ensemble over the 120 year simulation (at zero).

over the GIN Seas, and significant around 45°N in the North Atlantic. As well as leading to a reduction in SAT, the cooler surface waters also have an impact on precipitation and mean sea level pressure (MSLP) (Figures 3.30b,c). Little change is seen over the surrounding continents, although there is a region of significant cooling over the Middle East (Figure 3.30a).

As discussed in Section 3.3.3, basin-wide shifts in SST in the North Atlantic can have climate impacts for the surrounding continents (Sutton and Hodson, 2005; Delworth and Mann, 2000). The average precipitation for years 51-100 (Figure 3.30b) shows that there is little significance in the precipitation changes. However one of the areas that does

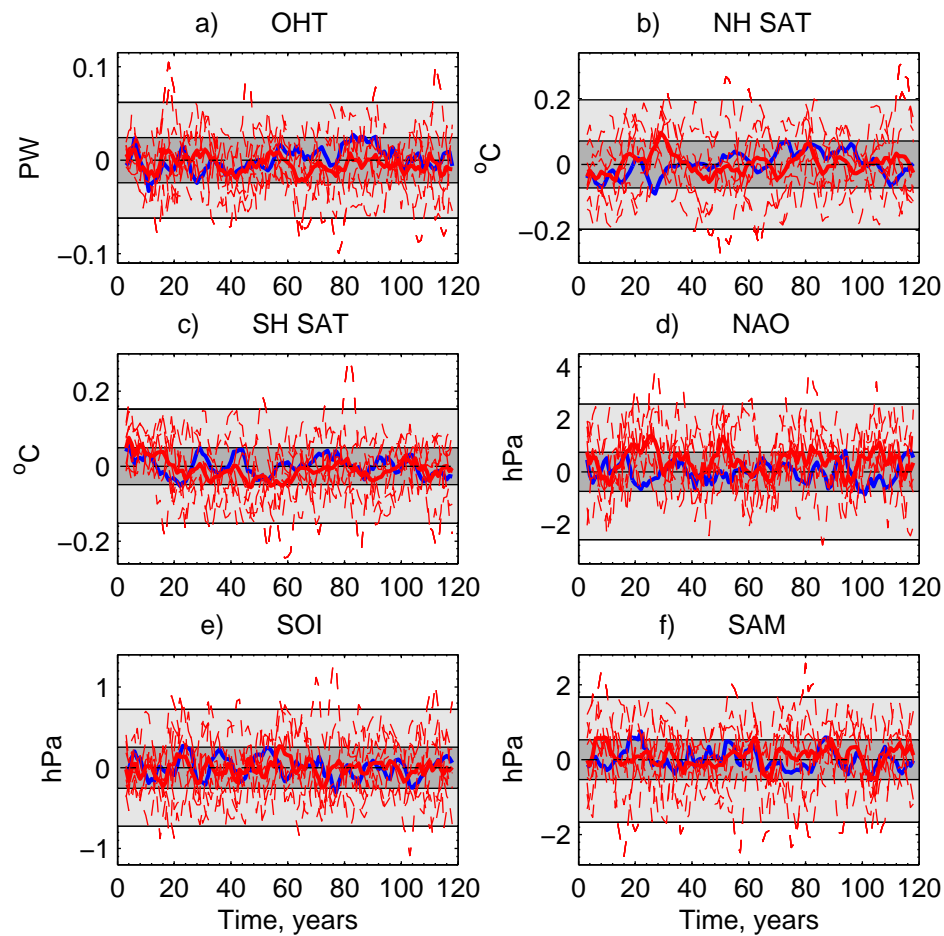


Figure 3.29: Climate indices anomalies for EXP2: (a) Northward ocean heat transport (OHT) at 26°N in the Atlantic; (b) mean Northern Hemisphere (NH) surface air temperature (SAT) (c) mean Southern Hemisphere (SH) SAT; (d) North Atlantic Oscillation (NAO) index : annual MSLP difference from Gibraltar-Iceland; (e) Southern Oscillation Index (SOI) : annual MSLP difference from Tahiti-Darwin; (f) Southern Annular Mode (SAM) : annual MSLP difference between 40 and 65°S . Light (dark) shaded area shows the 2σ (95%) spread of the control ensemble (mean) around the 120 year mean. Dashed (solid) red lines show the ensemble (mean) anomalies for EXP2 (EXP2 – time-mean of control). Blue line shows the mean of the control ensemble around the 120 year mean. Data are smoothed using a 5 year running mean. Dashed black line indicates the reference time-mean value for the control ensemble over the 120 year simulation (at zero).

show a significant decrease is northwest Africa and southwest Europe, where there is a decrease of up to 3.0 cm/year for years 51-100 (5% of the average). Sutton and Hodson (2005) show that the response to the AMO in the Sahel is weaker in the atmospheric component of HadCM3 (HadAM3) than in observations, likely as a result of land surface feedbacks that are not included in the model. The response over this region may then be underestimated in this study.

The response over the USA is weaker than that usually associated with the AMO (Sutton and Hodson, 2005), with no regions of significance and precipitation increases of

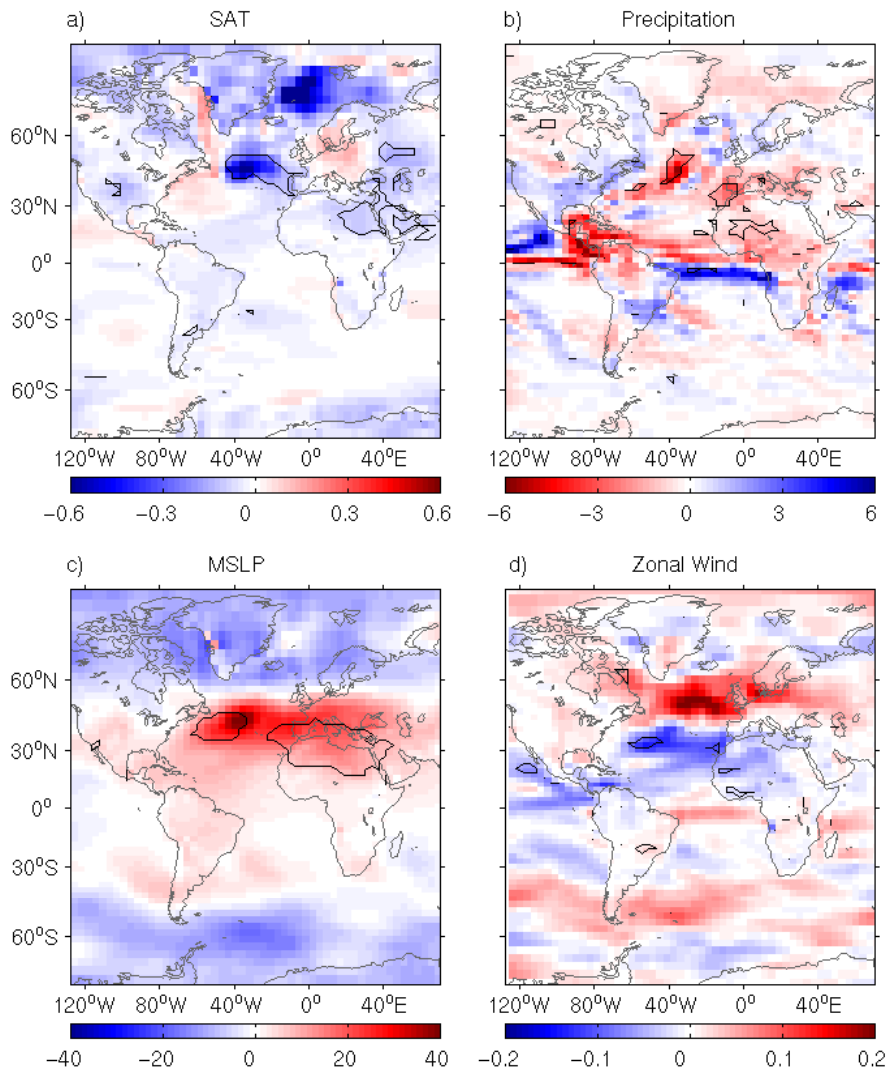


Figure 3.30: Mean atmospheric anomalies for 51-100 years (*EXP2* – Control): (a) surface air temperature (SAT) [$^{\circ}\text{C}$]; (b) precipitation [cm year^{-1}]; (c) mean sea level pressure (MSLP) [Pa]; (d) zonal wind speed [m s^{-1}]. Black contours show anomalies significant at the 95 % confidence level.

only up to 2.4 cm year^{-1} (Figure 3.30b). This weak response in the precipitation field is associated with a weak MSLP response over the USA (Figure 3.30c). Although the majority of the North Atlantic is cooler for years 51-100, the cooling mostly occurs north of 40°N , in the extratropics. There is also a weak tripole effect with positive anomalies off the east coast of North America (Figure 3.25c). As discussed in Section 3.3.3, the response over North America is predominantly driven by the SST anomalies in the tropical North Atlantic, therefore this accounts for the weaker atmospheric response seen in these results. The precipitation anomalies seen within the tropics are again characteristic of a shift in the Intertropical Convergence Zone (ITCZ), which has been shown to occur with

changes in the strength of the MOC (Vellinga and Wu 2004).

The higher MSLP over 15-45°N (Figure 3.30c) is associated with positive phases of the NAO, with stronger westerlies over the North Atlantic storm track (Figure 3.30d). The MSLP and zonal wind anomalies are greater than those for EXP1 (Figures 3.19b-d). This is likely a result of the cooler surface anomalies in the NAC and SPG (Figure 3.25c). As mentioned in Section 3.4.2, anomalous SPG transport may account for the increased volume of cold water moving southwards, contributing to the divergence of heat transport observed in the NAC (Figure 3.28b). Increased wind stress curl is observed over the SPG for years 21-30 and 71-80 (not shown), when increased transport of cold water can be seen moving southwards from $> 53^{\circ}\text{N}$ in Figure 3.27a. The MSLP and zonal wind anomalies may contribute to the persistence of the cool anomaly in the NAC, through the same mechanism described in Section 3.3.3.

3.5 Discussion

With these two experiments (EXP1 and EXP2), we have investigated the response to two opposing perturbations - warming and salting or cooling and freshening. If the climate responded linearly to the perturbations then these experiments should have shown approximately equal but opposite results. However, this is not the case. In EXP1, warmer, saltier water is found in the subpolar gyre and around the tip of Greenland within 20 years (Figure 3.6). This leads to warm SST anomalies, and the anomalous water mass is then seen to sink into the deep waters (Figures 3.10 and 3.9). If the two responses were linear, then we would expect to see cool anomalies around Greenland in the early decades of the simulation for EXP2, with cooler, fresher water then sinking to greater depth. Contrary to this, the first 30 years of EXP2 show a strong warming, followed by a cooling trend in later years as the anomalous water surfaces in the NAC and GIN Seas (Figures 3.25a,c). It is only in the later stages of the simulation, after 70 years, that fresher water is seen to build up in the deep layers of the Atlantic (Figure 3.24).

In the initial stages of the EXP2 simulation, up to year 30, there is an increased SST in the North Atlantic, along with an increased MOC strength. The increased MOC strength and SST appear to be a result of MSLP anomalies over Greenland and the GIN Seas. For years 11-30 there is a reduction in the MSLP in this region compared with the control

ensemble, resulting in an increased wind strength moving southwards over the Labrador Sea. The increased mixed layer depth (MLD) that results from this will lead to increased production of Labrador Sea Water (Cooper and Gordon, 2002), which can be seen as the cooler water moving southwards in Figure 3.27a, from $> 60^{\circ}\text{N}$ to the NAC, during years 10–30. This decreased heat content leads to an increased density and hence a decrease in steric height. The MOC anomalies are not significant for years 21–30, and the mean changes in MSLP lie within the range of internal variability. This suggests that the initial increase in MOC strength may be due to internal variability in the model, rather than a direct result of our perturbation. This is supported by the fact that there is little significance in the heat flux anomalies between the ocean and atmosphere for the first 20 years. Increasing the ensemble size, from 5 to 9 members, showed that the statistical significance of this initial warming decreased, however the cooling and decreased MOC strength in the second half of the simulation remained significant at the 95% level, giving greater confidence in this result.

Both EXP1 and EXP2 show negative temperature anomalies around the NAC. The persistent cold surface anomaly in this region is found to result from a divergence of ocean heat transport between 45 and 53°N . From the south, there is a reduced northward heat transport as the MOC strength decreases. The increased heat transport to the north can be accounted for by the increased transport in the SPG. Increased volumes of cooler water are brought into the region, leading to a higher proportion of SPG water, compared with STG water, in the NAC (Hátún *et al.*, 2005). Higher MSLP over the mid-latitude Atlantic, and corresponding zonal wind anomalies, lead to an increased wind stress curl that acts to strengthen the gyre. As these MSLP anomalies develop over the cool NAC region, this may then lead to the persistence of the SST anomaly through a feedback mechanism. The response is more significant for EXP2, due to the presence of cooler, fresher intermediate water, which is advected northwards and surfaces in this region.

The fact that the two experiments do not show equal and opposite responses is not entirely unexpected. As the perturbed water masses reach the ocean mixed layer and interact with the atmosphere, the loss (gain) of heat in the warming (cooling) experiment will lead to positive (negative) density anomalies. This can be seen in the simulations within the first 10 years (Figure 3.31). These opposing density responses then lead to the

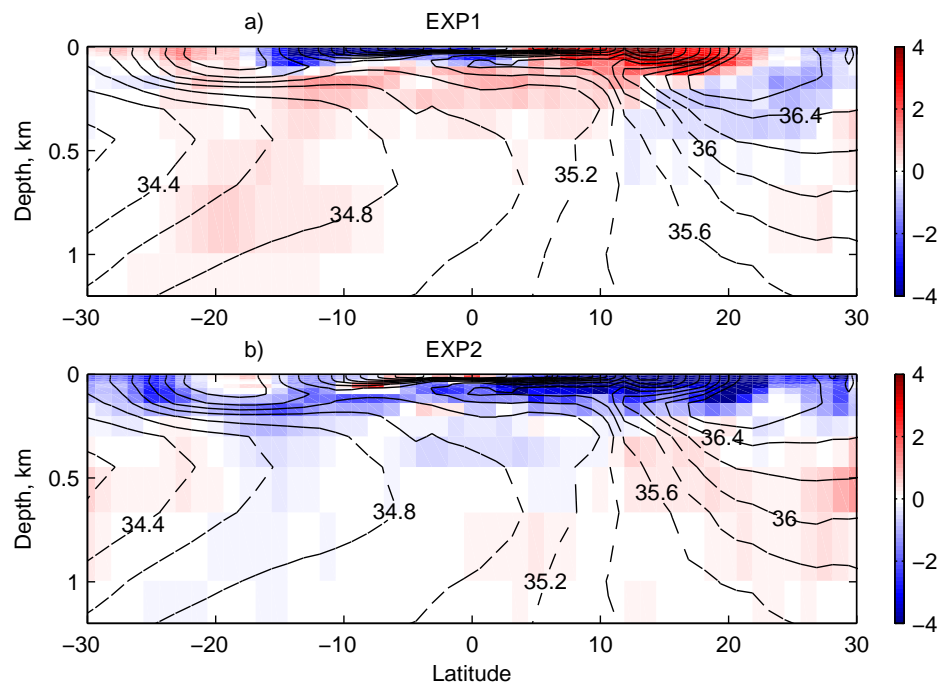


Figure 3.31: Zonally averaged decadal density anomalies ($EXP - control$) in the tropical Atlantic ($30^{\circ}S-30^{\circ}N$), for years 1-10 of a) EXP1; b) EXP2. Black dashed contours show the control salinity values for the same period.

water masses travelling along different paths in the ocean, surfacing in different regions, and spending different lengths of time at the surface. This concept is illustrated by the schematic in Figure 3.32. At the end of the simulations, 28% of the initial salt content anomaly remains at intermediate depths in the Atlantic for EXP2, compared with 37% for EXP1. This supports the suggestion that the perturbations travel along different paths in the ocean, with the warmer, saltier anomaly showing a tendency to remain at greater depth and have less interaction with the atmosphere.

3.6 Summary

This study has investigated the potential climate impacts of changes in AAIW in the Atlantic. AAIW was perturbed between 10 and $20^{\circ}S$, altering the temperature by $\pm 1^{\circ}C$ and making a corresponding change in salinity to maintain a constant density. For these perturbations, the responses can be summarised as:

- Anomalies surface in the NAC, SPG and GIN Seas.

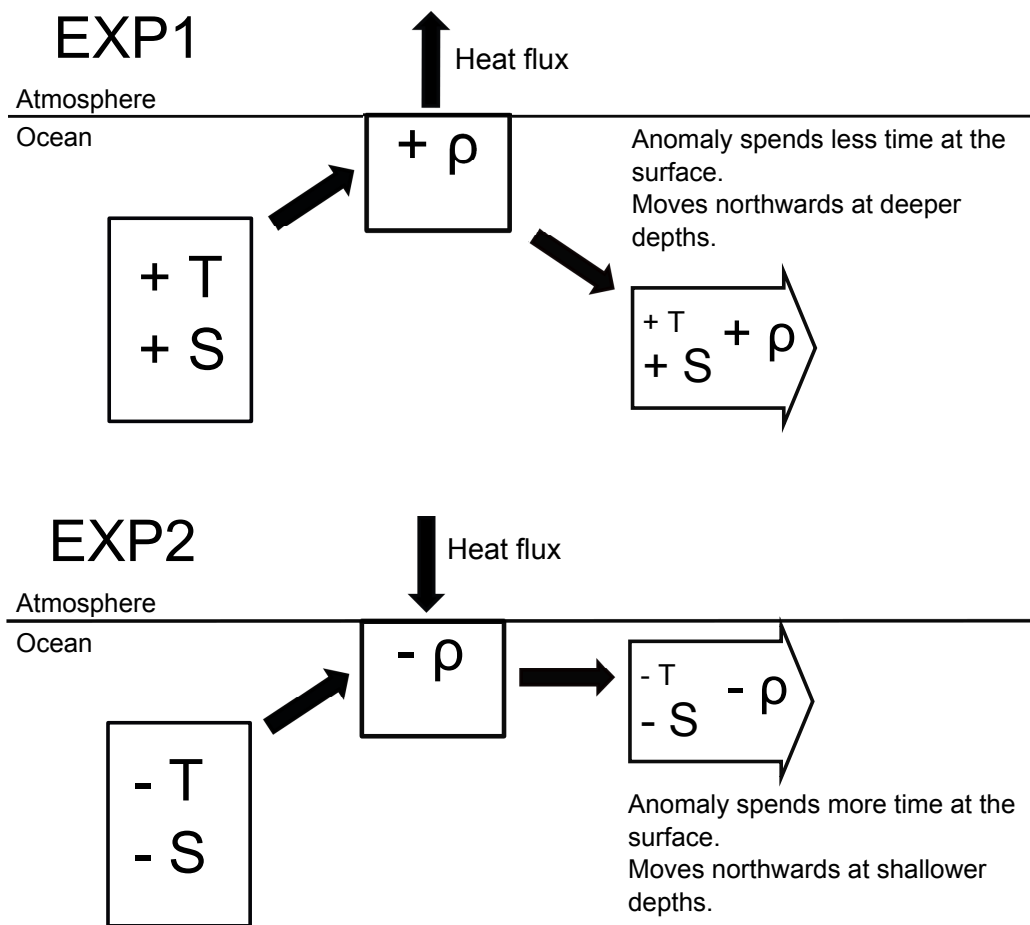


Figure 3.32: Schematic to demonstrate the non-linear response to initially density-compensating perturbations. When the anomalous water mass comes in to contact with the atmosphere, heat fluxes result in opposite density anomalies due to the remaining salinity perturbation. Non-linearity arises as the density anomalies propagate through the ocean at different depths and pathways.

- Anomalous air-sea heat fluxes lead to density anomalies and a non-linear response to perturbations.
- Density anomalies at 60°N are correlated with changes in MOC strength and meridional OHT.
- The combination of reduced MOC strength and surfacing cool anomalies lead to a greater surface response for EXP2 than EXP1.
- Both EXP1 and EXP2 have persistent cooling at the surface in the NAC, due to a divergence in OHT.

For the cooling, freshening experiment the MOC strength in the Atlantic is shown to be positively correlated with the steric height difference between 30°S and 60°N, with the

density variations at 60°N being the key factor. The largest MOC anomalies for EXP2 are found at 60°N for 81-90 years, with a decrease of 0.8 Sv over the decade. A persistent cold surface anomaly is found in the region of the NAC, resulting from a divergence of ocean heat transport between 45 and 53°N . From the south, there is a reduced northward heat transport as the MOC strength decreases and the cooler intermediate water arrives. The increased heat transport to the north can be accounted for by the increased transport in the SPG.

For the warming, salting experiment, the response seen was not equal and opposite to the response in the cooler, fresher experiment, implying that the climate response to these perturbations is non-linear. There is no increase in the SST around the NAC and no significant increase in the MOC. The MOC actually exhibits an average reduction in strength over the course of the simulation, as was seen in EXP2, due to the presence of warmer waters around 60°N . However the trend seen in EXP1 is less persistent, with positive MOC anomalies shown by the end of the simulation. Although there are no positive SST anomalies in the NAC, EXP1 shows significantly increased SST anomalies around the tip of Greenland, suggesting that the warmer, saltier water is surfacing in this region.

For both experiments, the greatest impact on the atmosphere was found over the regions of significant SST anomalies, due to the increased heat flux to or from the ocean. For EXP1, a warming was found over Greenland for years 21-30. Cooling over the North Atlantic and GIN Seas was observed for both experiments due to the decreased MOC strength and reduced SSTs. The results showed greater significance in EXP2 as the surfacing cooler, fresher intermediate water contributed to these anomalies. The cooling through the North Atlantic led to similar atmospheric responses as those shown for a cool phase of the AMO (Sutton and Hodson, 2005).

Chapter 4

Sensitivity to Initial Ocean Conditions

4.1 Introduction

This chapter will address the impact a change of initial ocean conditions could have on the response to a perturbation in the Atlantic Ocean. In Chapter 3, the experiments involved 9 member ensembles, where each ensemble member had identical initial conditions in the ocean but varying initial conditions in the atmosphere, offset by 1 day. Whilst the variation in the atmospheric conditions does impose a variety of responses (evident from the spread in the ensemble results seen for EXP1 and EXP2), it is possible that the initial conditions in the ocean may be predisposed to react in a particularly way. This issue of initial ocean conditions has been addressed by performing a second series of ensemble runs, varying both the initial ocean, as well as the atmosphere, for each ensemble member.

4.2 Method

For these new 9 member ensembles, the start date for each of the ensemble members is separated by 50 years in both the ocean and atmosphere (unlike Chapter 3 where only the atmospheric conditions were separated by 1 day). The first ensemble member is identical to that used for the first experiment, taken from model day 01/12/2789 (dd/mm/yyyy). The varying ocean state for these start dates is illustrated in Figure 4.1. For each member of the control ensemble, the MOC is in a different initial state, and behaves differently

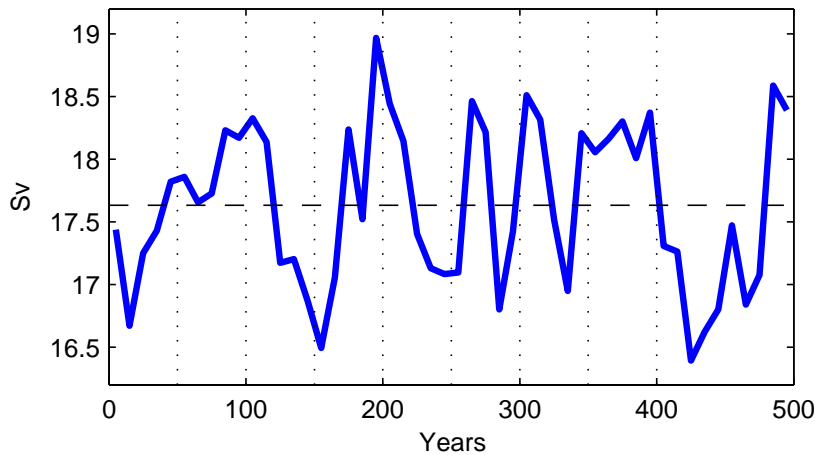


Figure 4.1: Decadal-mean meridional overturning streamfunction index for the Atlantic at 45°N for 500 years of the control run. Dashed black line shows the time-mean for the 500 year control. Dotted lines indicate the start time of the new ensemble members: 50, 100, 150, 200, 250, 300, 350, 400 years, where year 0 refers to model year 2789.

over the following 100 year period. This ensemble experiment can therefore show how the perturbation affects the climate, irrespective of the ocean initial conditions. The same perturbation is made in the Atlantic, between 10 and 20°S , $\pm 1^{\circ}\text{C}$ and compensating changes in salinity, as described in Section 3.2. Simulations are then integrated for 100 years. The two ensemble experiments will be referred to as EXP1b ($+1^{\circ}\text{C}$) and EXP2b (-1°C).

4.3 Results

4.3.1 Warmer, saltier AAIW

As shown in Chapter 3, the path of the perturbed water mass can be traced using the salt content anomalies in the ocean. The warmer, saltier AAIW spreads northwards in the Atlantic, initially with the North Brazil Current (Figure 4.2). The anomalous water mass is then advected northwards with the Gulf Stream and recirculates in the North Atlantic gyre, allowing significantly higher salt contents to be found in the North Atlantic within the first 20 years of the experiment. After leaving the NAC, a portion of the anomalous water recirculates in the STG, and the remainder is carried further north into the SPG and GIN Seas. For years 31-40, the salt content in the SPG and Labrador Sea is higher than that in the control simulation. For years 41-50, the salt content is significantly increased along the Norwegian coast and there is an increased salt content in the GIN Seas (Figure 4.2). As well as spreading northwards in the basin, a portion of the initial perturbation

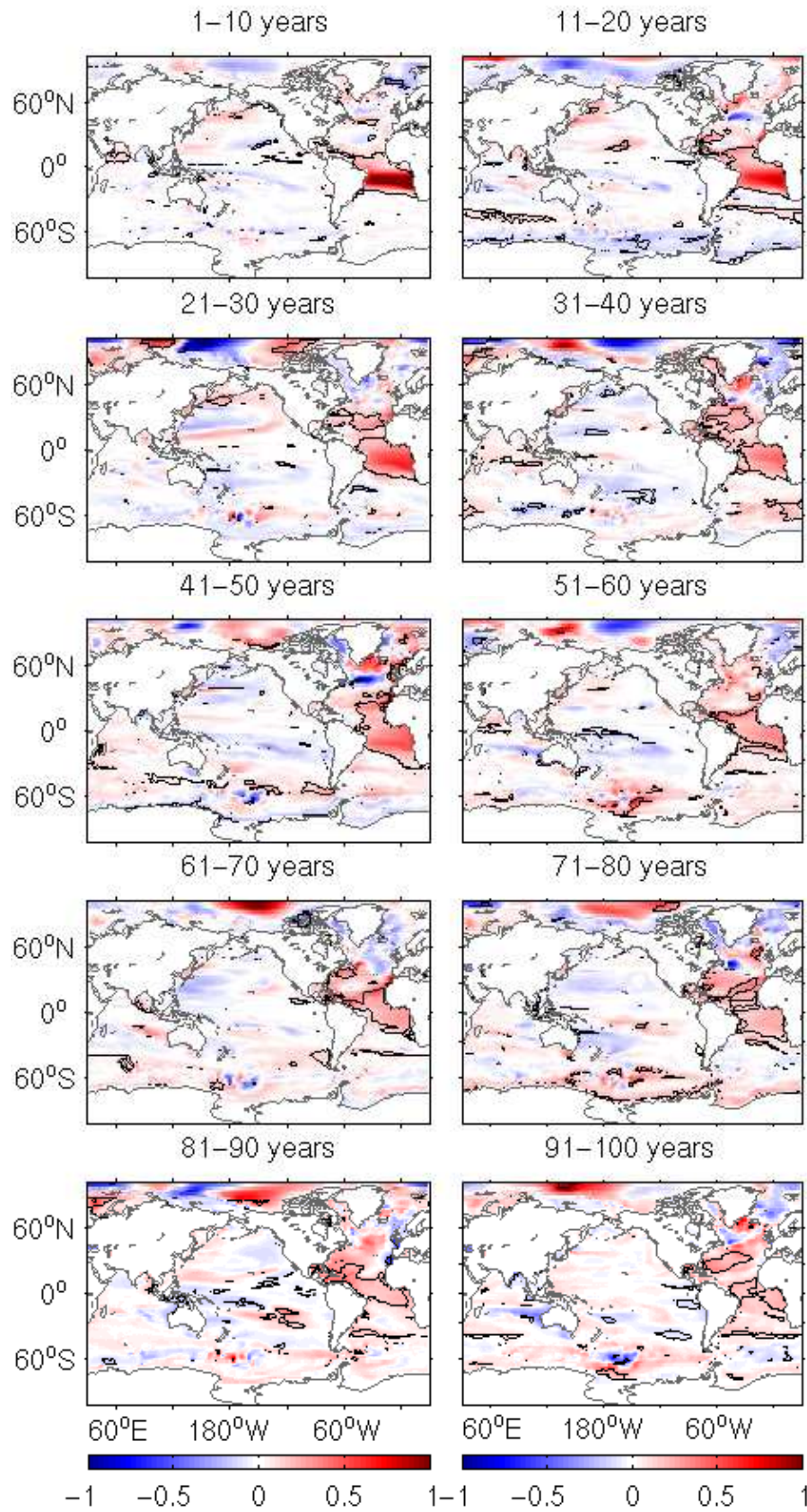


Figure 4.2: Decadal salt content anomalies in columns (EXP1b - control) $[\times 10^2 \text{ kg m}^{-2}]$. Black contours show anomalies significant at the 95% confidence level.

remains in the South Atlantic. At the end of the simulation, the salt content in the South Atlantic is significantly higher than that in the control simulation. Increased salt content is also observed in the Southern Ocean for years 11-20, indicating that a portion of the anomalous AAIW is advected southwards into the path of ACC in the early stages of the experiment. Although some of the anomalous water mass leaves the Atlantic, the majority of the significant anomalies remain in this basin for the duration of the experiment. After 100 years, the total salt content anomaly in the Atlantic basin is 9.1×10^{14} kg, equivalent to 72% of the initial perturbation. The anomaly remaining in the South Atlantic is 3.1×10^{14} kg, compared with 6.0×10^{14} kg in the North Atlantic.

As the perturbed water mass spreads through the Atlantic, a large proportion remains at intermediate depth levels (~ 300 - 1500 m), however increased salinity anomalies do reach the surface (Figure 4.3). For the first 30 years, increased salinity anomalies extend from the surface down to intermediate depths in the tropical Atlantic. This suggests that the anomaly may be surfacing in these regions. Within the first 20 years, increased salinity anomalies are also found further north. For years 11-20, positive anomalies stretch from the surface to depths > 3000 m at $\sim 60^\circ\text{N}$ (Figure 4.3), indicating that anomalies are entering the deep waters in this region. The transport of anomalies to these latitudes on this timescale can be accounted for by the speed of the currents in the Gulf Stream. For years 41-50, positive anomalies are found below the surface at $> 60^\circ\text{N}$, corresponding to the anomalies in salt content shown in Figure 4.2. As the simulation progresses, the majority of the anomalies remain at intermediate depths. For levels 1-10 (< 300 m) in the model, there are few significant salinity anomalies at the end of the simulation, whereas levels 12-14 (~ 500 - 2000 m) show an increased salinity throughout the Atlantic basin (Figure 4.3).

Figure 4.4 shows the sea surface salinity (SSS) anomalies for the first 40 years of the experiment. Significant anomalies can be seen in the tropical North Atlantic, in particular for years 1-20 (Figure 4.4a,c). This corresponds with the anomalies seen in Figure 4.3, supporting the suggestion that anomalous water is surfacing in this region. Equatorial upwelling may bring anomalous water to the surface as AAIW is advected northwards, and enters the equatorial region. However, no significant sea surface temperature anomalies are found in this region (Figure 4.5a,c). Unlike SSS anomalies, SST anomalies can be

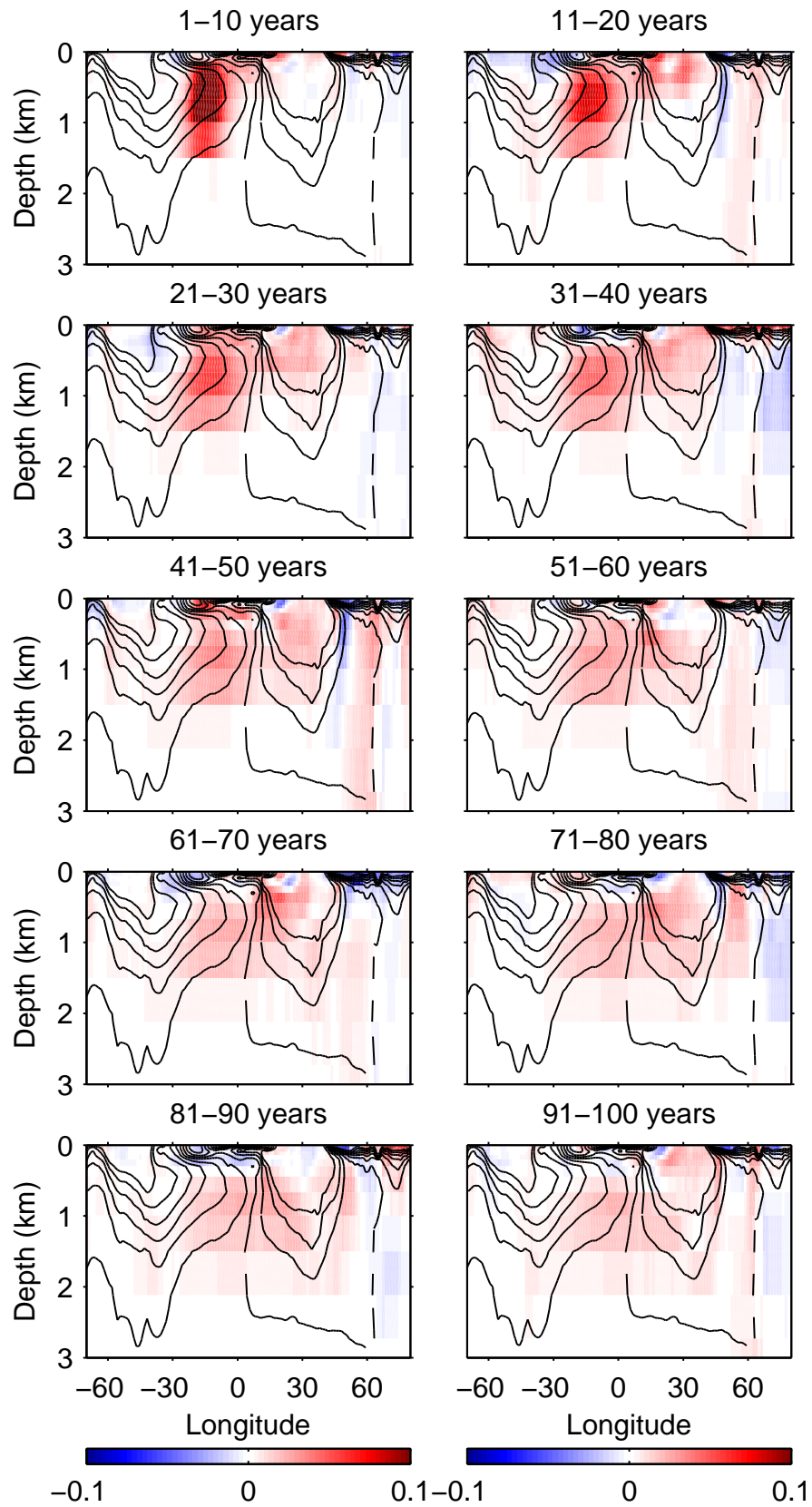


Figure 4.3: Zonally averaged decadal salinity anomalies (*EXP1b* – control) in the Atlantic for 100 years.

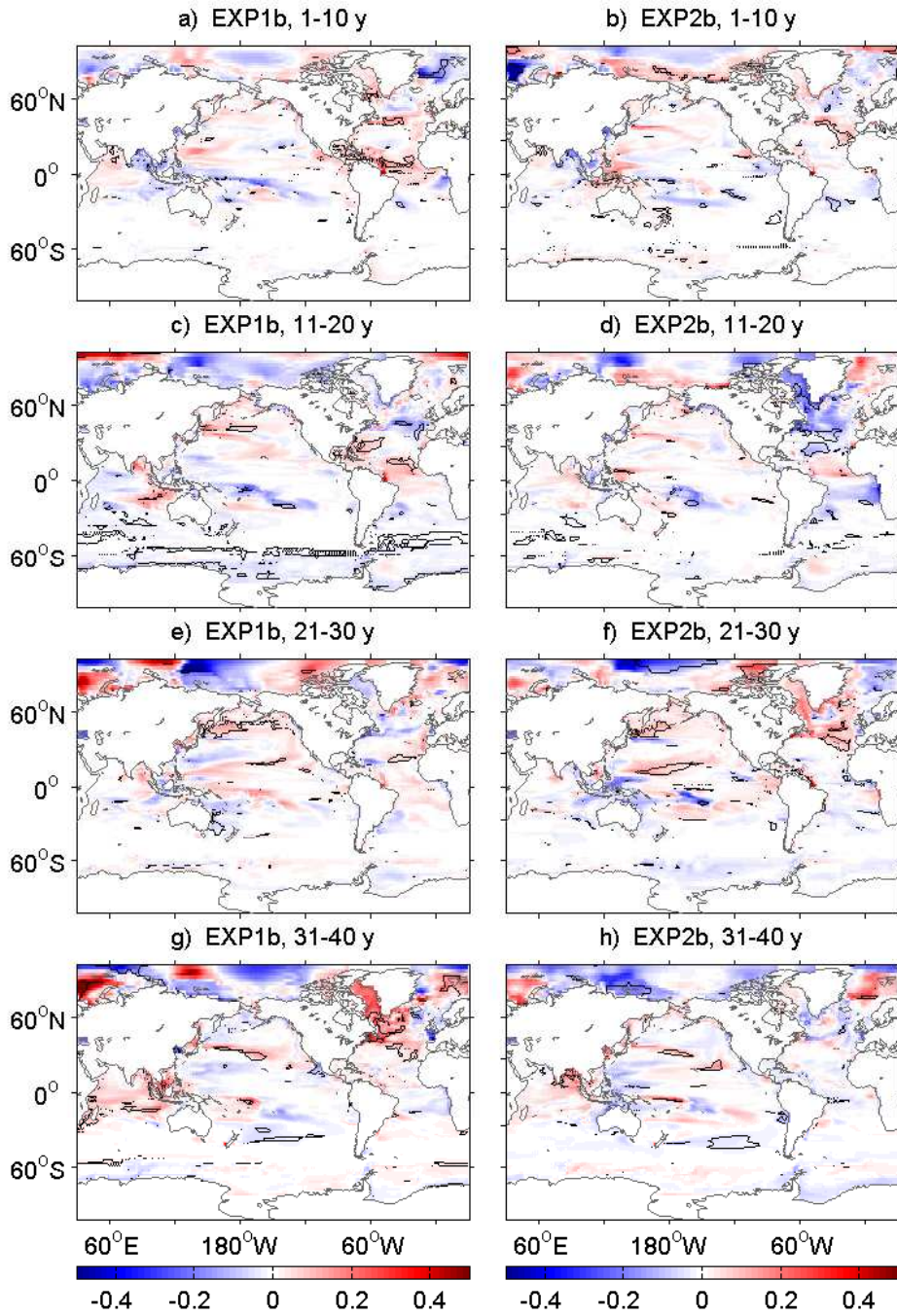


Figure 4.4: Decadal sea surface salinity anomalies ($EXP - control$) for the first 40 years. Figures a, c, e and g show anomalies for EXP1b ($+1^{\circ}C$); b, d, f and h show anomalies for EXP2b ($-1^{\circ}C$). Contours show regions significant at the 95% confidence level.

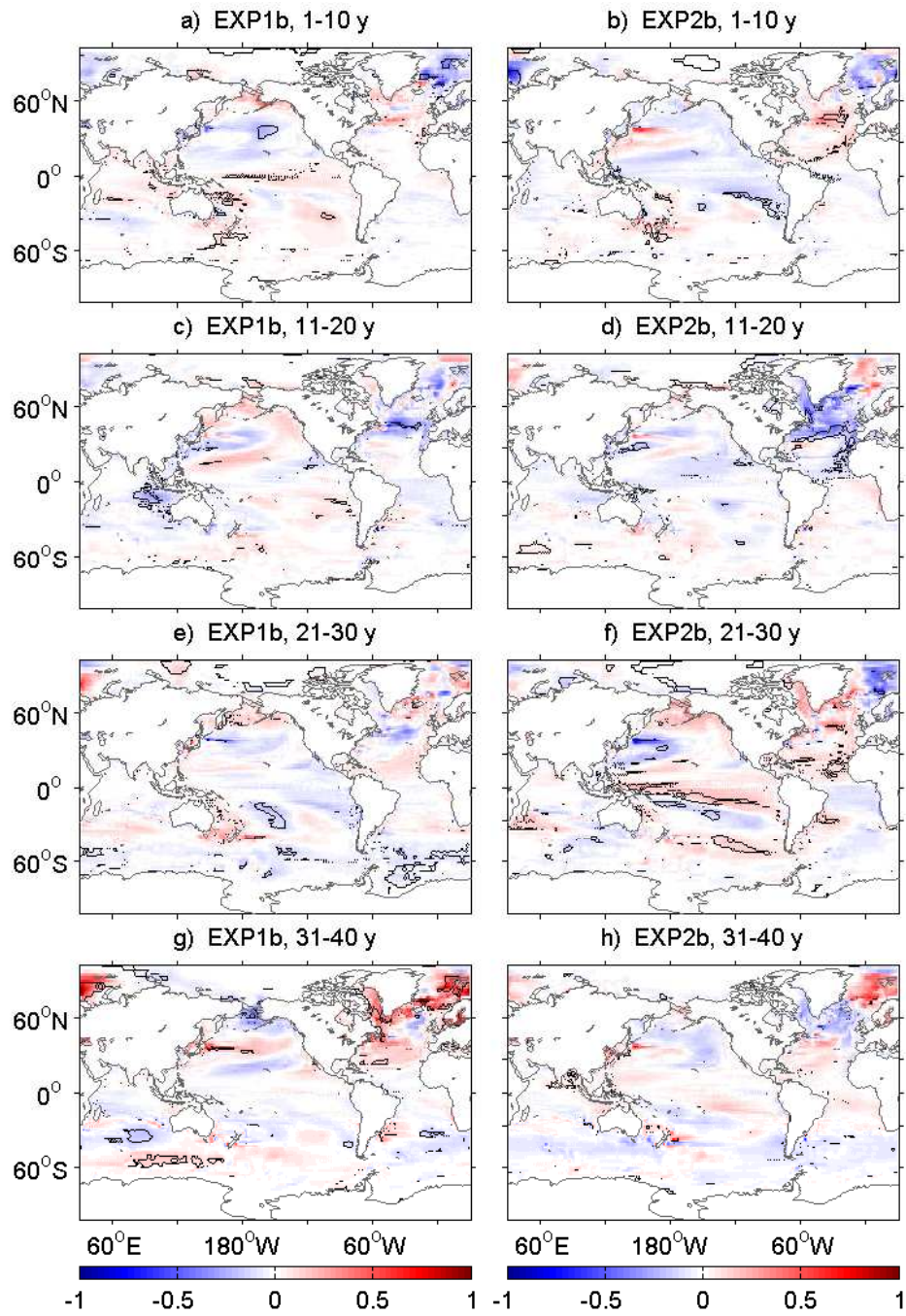


Figure 4.5: Decadal sea surface temperature anomalies (EXP - control) for the first 40 years [$^{\circ}\text{C}$]. Figures a, c, e and g show anomalies for EXP1b (+1 $^{\circ}\text{C}$); b, d, f and h show anomalies for EXP2b (-1 $^{\circ}\text{C}$). Contours show regions significant at the 95% confidence level.

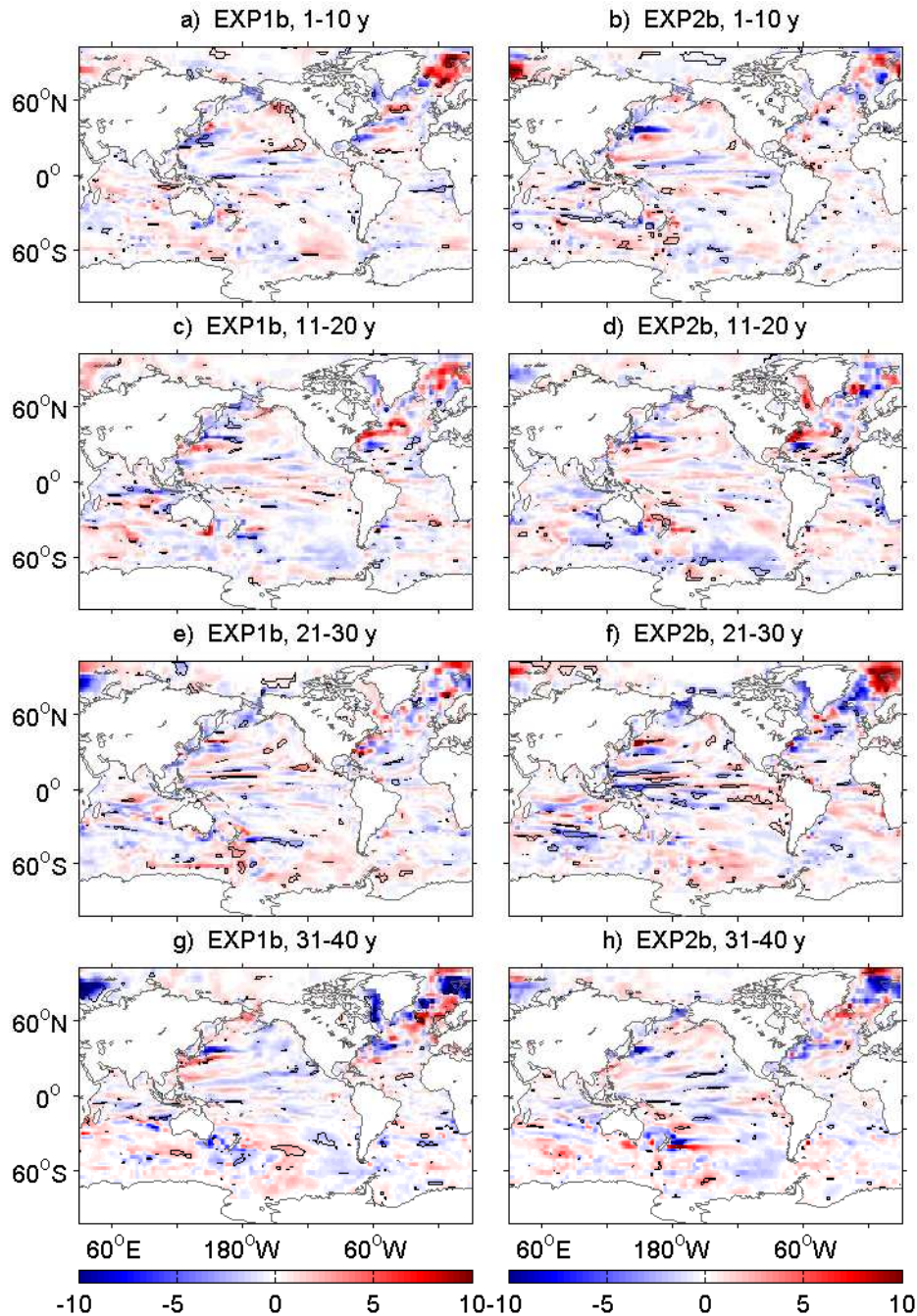


Figure 4.6: Decadal ocean-atmosphere heat flux anomalies ($EXP - control$) for the first 40 years [$W m^{-2}$]. Figures a, c, e and g show anomalies for EXP1b ($+1^{\circ}C$); b, d, f and h show anomalies for EXP2b ($-1^{\circ}C$). Positive anomalies indicate heat flux in the atmosphere-to-ocean direction. Contours show regions significant at the 95% confidence level.

lost through heat fluxes with the atmosphere. For years 1-10, negative heat flux anomalies are found in the tropical South Atlantic, indicating that more heat is being lost from the ocean (Figure 4.6a). Therefore, although a portion of the anomaly may reach the surface here, the anomalous heat content may not be sufficient to result in significant equatorial SST changes. For years 1-10, positive SST anomalies are also seen in the NAC and SPG.

Although not significant, these are in the same location as significant SSS anomalies and therefore may be an indication of anomalies reaching the North Atlantic within the first 10 years. Negative heat flux anomalies also show that these anomalies are not due to heat fluxes from the atmosphere. Currents of $> 6 \text{ cm s}^{-1}$ in the upper layers of the ocean would be sufficient to advect anomalies along the western boundary on this timescale.

For years 31-40, there are regions of significant increases in both SSS and SST in the far North Atlantic, SPG and GIN Seas (Figures 4.4g and 4.5g). These are regions of deep mixed layer depth ($> 300 \text{ m}$), so as the anomalous water mass reaches these locations, this may allow the increased heat and salt content to be brought to the surface. In Section 3.3.2, SST variability in the North Atlantic was shown to be linked to the density variations around 60°N , and resulting changes in the MOC and ocean heat transport (OHT). In this experiment, there is no significant trend in the MOC (Figure 4.7). Figure 4.8 shows the spread of heat content through the Atlantic, and the resulting steric height anomalies. The heat anomalies can be seen spreading northwards through the Atlantic, reaching the NAC region ($\sim 45^\circ\text{N}$) within 20 years. After this point, the majority of the Atlantic basin has an increased heat content up to the end of the simulation (100 years). Portions of the anomaly are found north of the NAC, with increased heat contents being found at 60°N , for example after 10 years and 40 years (Figure 4.8a). These anomalies correspond to the salt content anomalies seen in Figures 4.2 and 4.3. No significant changes are found in the steric height at 60°N , showing that the anomalies that reach this latitude are mostly density compensating. This explains why there is no significant trend in the MOC strength. As there is no significant trend in the MOC and resulting OHT (Figure 4.9a), this rules out changes in the MOC as a cause for the increased SST.

At the end of the simulation, 57% of the initial heat anomaly remains in the Atlantic basin. As this is less than the proportion of salt (72%), it suggests that $\sim 15\%$ of the heat anomaly may have been lost through ocean-atmosphere interaction. The direction of the surface heat fluxes show that the SST anomalies in the North Atlantic for years 31-40 are a result of ocean rather than atmospheric forcing. For the remainder of the experiment, little trend is seen in the surface temperature of the ocean, therefore little trend in the atmospheric response (Figure 4.9). For years 31-40, there is an increased SAT over the North Atlantic (Figure 4.10a). The direction of the ocean-atmosphere heat flux shows

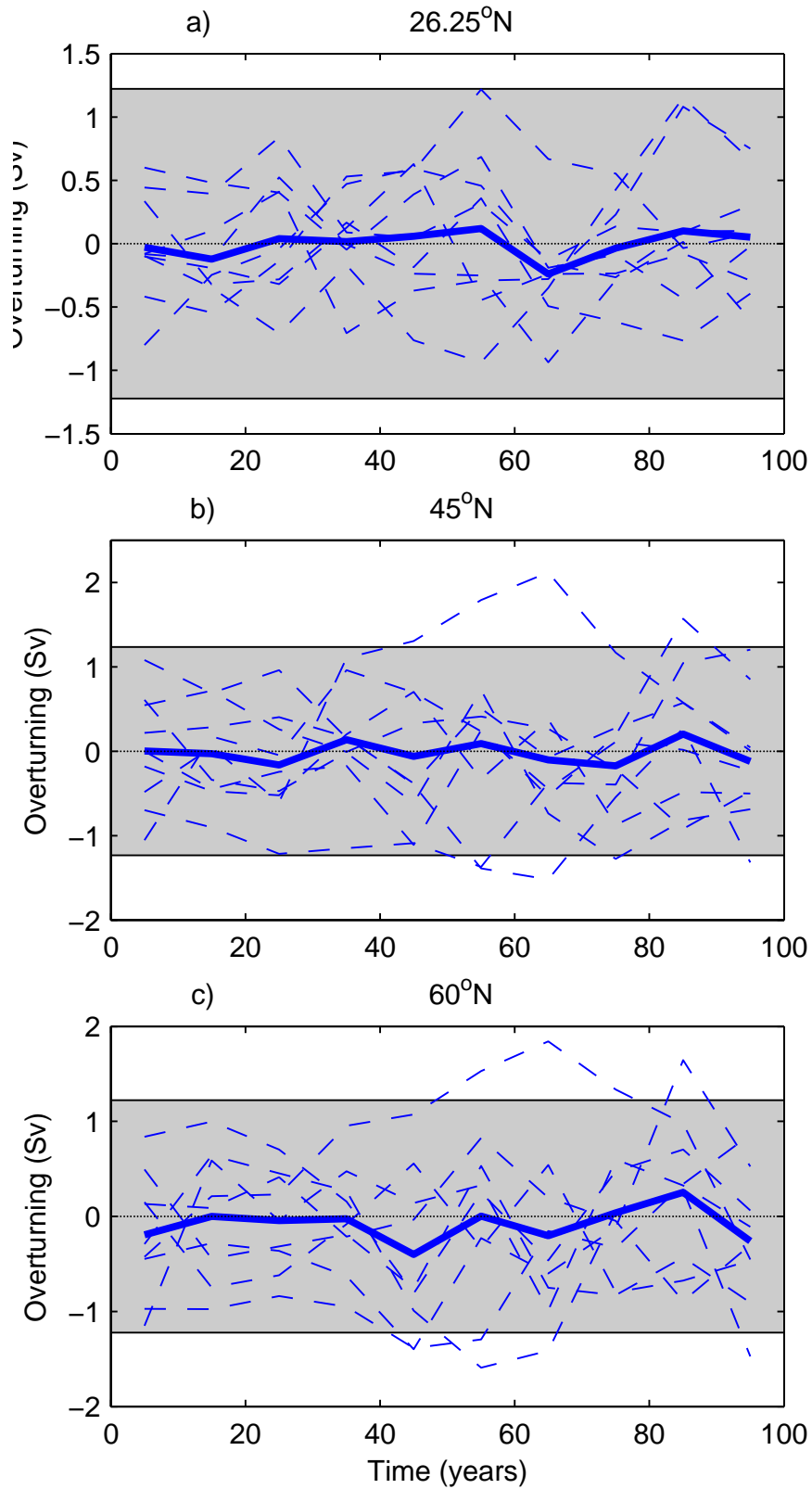


Figure 4.7: Decadal anomalies for three meridional overturning streamfunction indices (EXP1b–control) at: a. 26.5°N; b. 45°N; c. 60°N. Solid lines indicate the anomaly of ensemble mean values (EXP1b – Control); dashed lines show the anomalies of individual EXP1b ensemble members minus mean of the control. Shaded region shows the 95% spread of the control ensemble over the 100 year simulation.

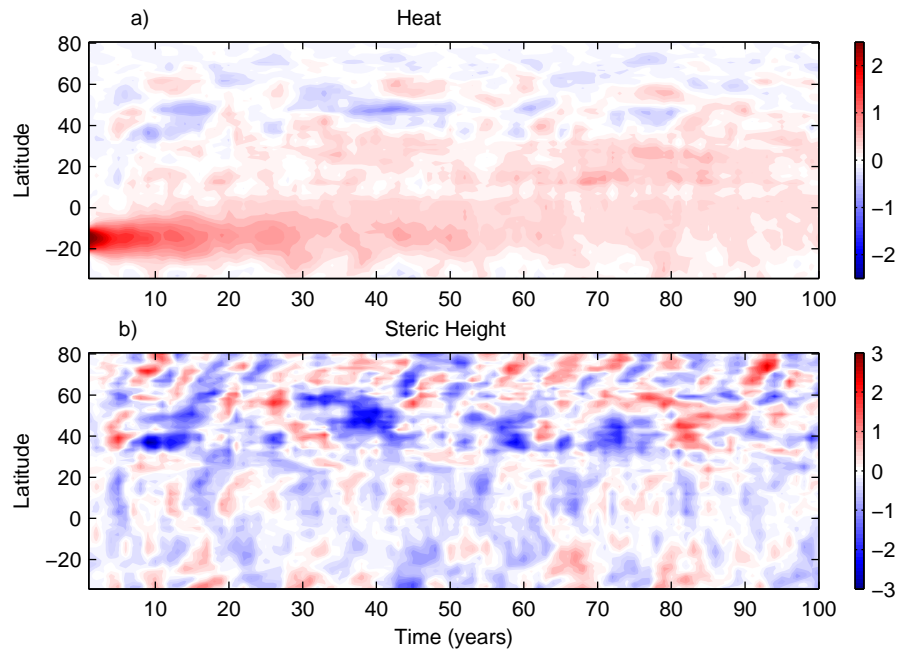


Figure 4.8: Hovmöller plots of a. total heat content anomalies (*EXP1b* – Control), within 0-3000 m [10^{21} J]; b. zonal mean steric height anomalies (*EXP1b* – Control) [cm].

that this increased temperature is predominantly due to the increased heat being released from the ocean (Figure 4.6g). Around 30 years, there is also an increase in the NAO index (Figure 4.9d). Reduced MSLP is found over the increased SST in the SPG and GIN Seas (Figures 4.10b and 4.5g), strengthening the Icelandic Low. This surface pressure response to SST anomalies is consistent with previous theoretical studies and perturbation experiments (Kushnir *et al.*, 2002). For years 40-60, there is a reduction in SAT over both the Northern and Southern Hemispheres (Figures 4.9b,c). The anomalies during this time are most likely to be driven by atmospheric variability, with positive anomalies in the SOI and SAM (Figures 4.9e,f). Although the decadal-mean sea level pressure anomalies show few patterns of significance for this time period, the SST anomalies for 41-50 years show a pattern consistent with a negative phase of the Pacific Decadal Oscillation (Mantua *et al.*, 1997) and for years 51-60 there are negative SST anomalies in the equatorial Pacific (Figure 4.11). For years 41-50 there is also a cooling in the Southern Ocean and South Atlantic SST, which corresponds to the reduced SH SAT. Changes in the Atlantic SST have been shown to be linked with phases of the El Niño Southern Oscillation (Enfield and Mayer, 1997). The cooling in the South Atlantic may then be linked with the negative SOI anomalies seen during this decade. It is worth noting that although there are significant anomalies in the atmosphere, the decreases in SAT and SAM indices for

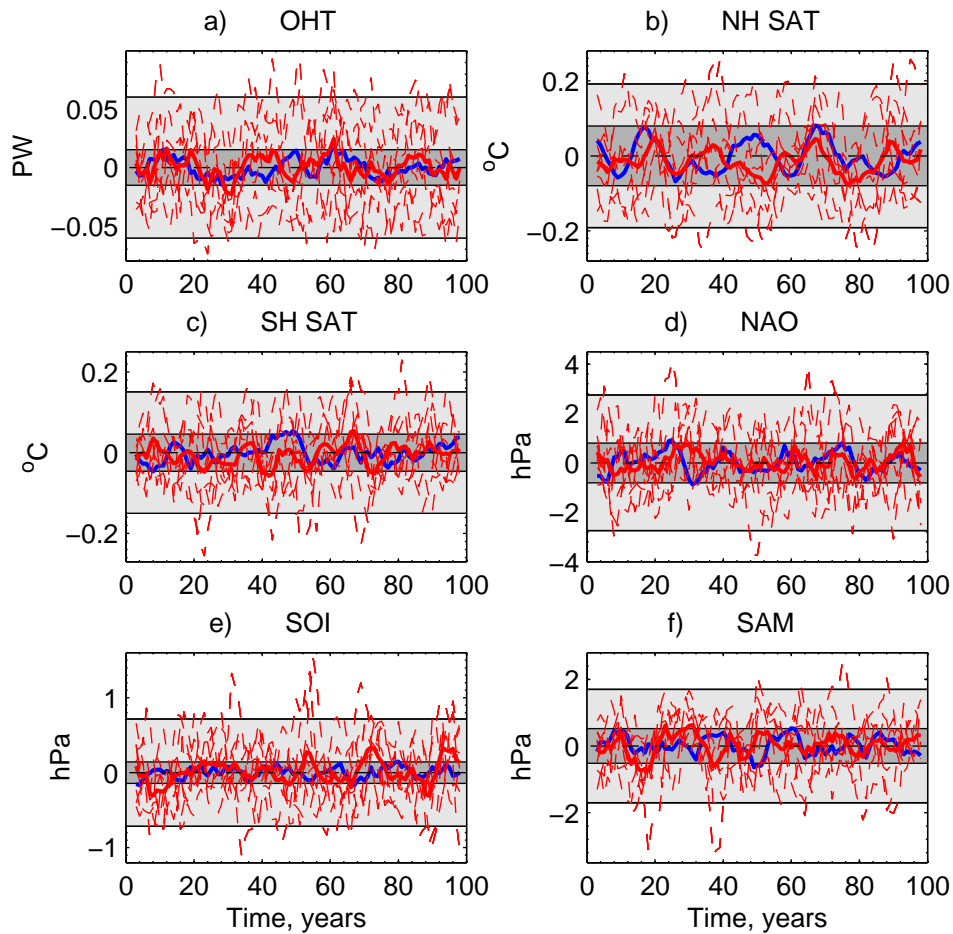


Figure 4.9: Absolute values of climate indices for EXP1b: a) Northward ocean heat transport (OHT) at 26°N in the Atlantic; b) mean Northern Hemisphere (NH) surface air temperature (SAT) c) mean Southern Hemisphere (SH) SAT; d) North Atlantic Oscillation (NAO) index : annual MSLP difference from Gibraltar-Iceland; e) Southern Oscillation Index (SOI) : annual MSLP difference from Tahiti-Darwin; f) Southern Annular Mode (SAM) : annual MSLP difference between 40 and 65°S . Light (dark) shaded area shows the 2σ (95%) spread of the control ensemble (mean) around the 100 year mean. Dashed (solid) red lines show the ensemble (mean) anomalies for EXP1b (EXP1b – time-mean of control). Blue line shows the mean of the control ensemble around the 100 year mean. Data are smoothed using a 5 year running mean. Dashed black line indicates the reference time-mean value for the control ensemble over the 100 year simulation (at zero).

EXP1b are comparable with the increases seen in the control ensemble during the same time period.

4.3.2 Cooler, fresher AAIW

The cooler, fresher AAIW takes a similar path through the ocean, spreading northwards initially as it is advected in the western boundary current (Figure 4.12). During the first 10 years, a progression of anomalously fresh water is seen along the north coast of Brazil, extending from the initial perturbation region. Although there are only small regions

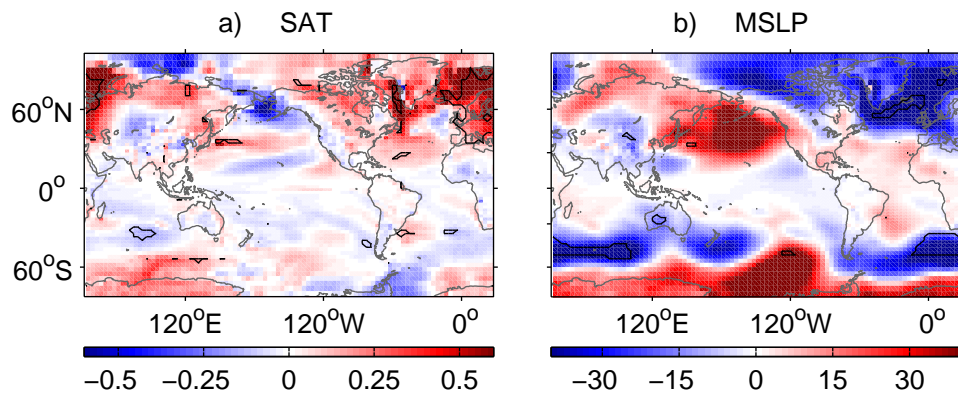


Figure 4.10: Decadal mean anomalies ($EXP1b - control$) for years 31-40: a) surface air temperature (SAT) [$^{\circ}C$]; b) mean sea level pressure (MSLP) [Pa]. Black contours show anomalies significant at the 95 % confidence level.

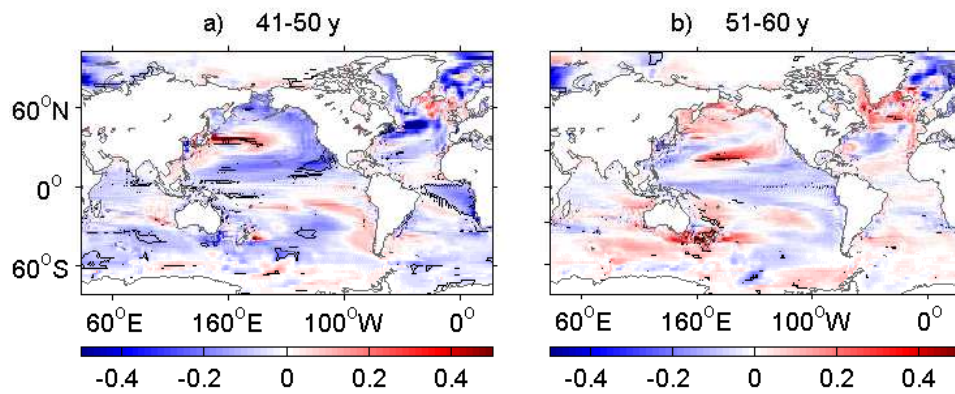


Figure 4.11: Decadal mean sea surface temperature anomalies ($EXP1b - control$) for years a) 41-50, b) 51-60 [$^{\circ}C$]. Black contours show anomalies significant at the 95 % confidence level.

significant at the 95% level, fresh anomalies are found in the North Atlantic and SPG within 20 years. After reaching the NAC within 20 years, fresh anomalies can also be seen progressing northwards into the SPG and GIN Seas. As the simulation progresses, the North Atlantic gradually fills with fresher water as the anomalous water mass recirculates in the STG. For years 41-50, the majority of the Atlantic basin has a reduced salt content (Figure 4.12). Significant freshening is found in the GIN Seas after 50 years, and for years 61-100 there is a significant freshening in the region surrounding the NAC. As fresh anomalies build up north of the NAC, the anomalies are reduced south of $40^{\circ}N$ in the North Atlantic. By the end of the simulation, there is no significant change in salt content between 10 and $40^{\circ}N$, and the salinity sees a slight increase after 70 years (Figure 4.12). This positive salinity anomaly is strongest in the Gulf of Mexico, suggesting that anomalies seen in the rest of the North Atlantic may have originated in this region. A portion of the anomalous AAIW does remain in the South Atlantic. After 100 years, the

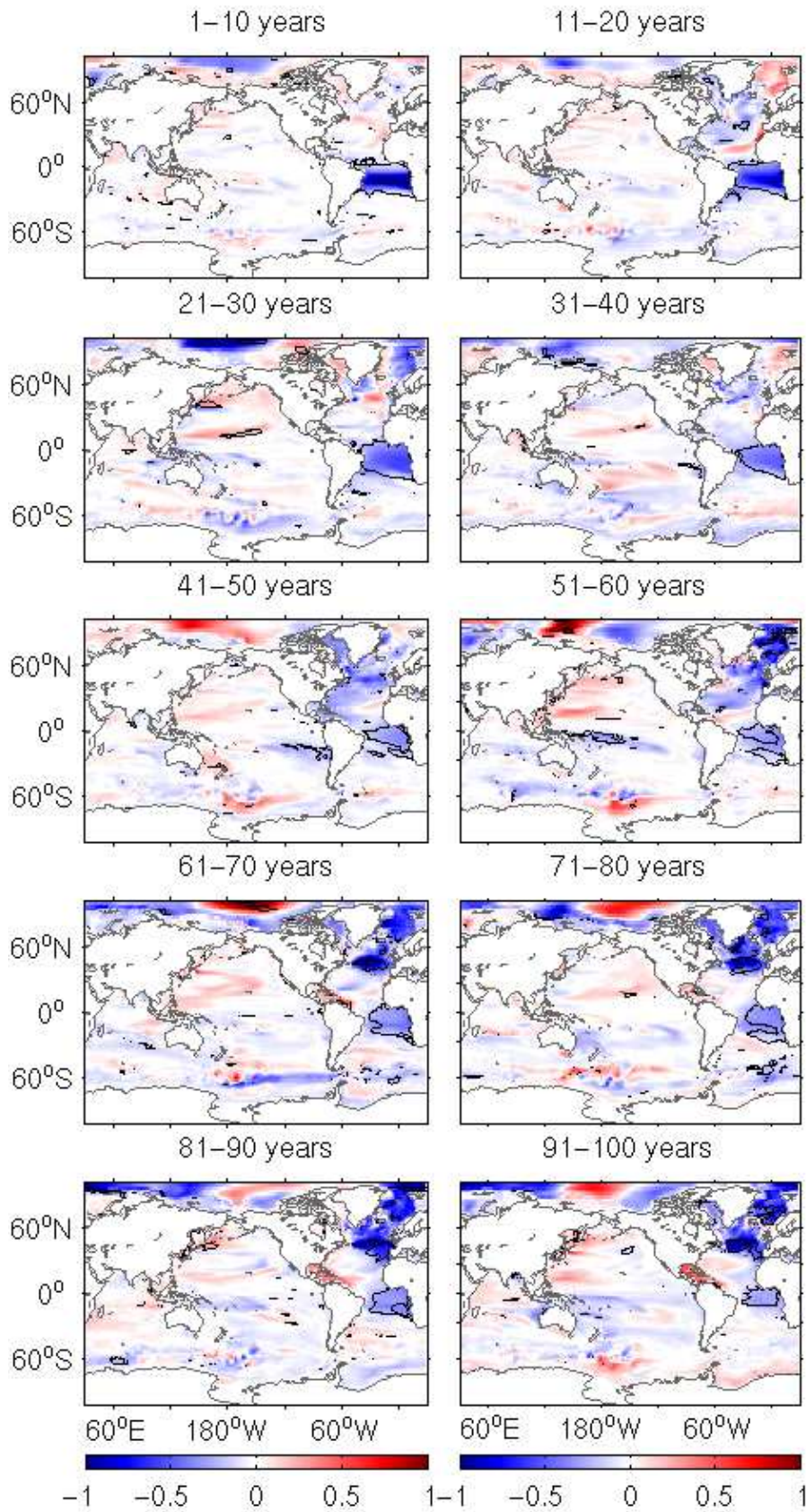


Figure 4.12: Decadal salt content anomalies in columns (EXP2b - control) $[\times 10^2 \text{ kg m}^{-2}]$. Black contours show anomalies significant at the 95% confidence level.

total salt content anomaly in the Atlantic basin, between 30°S and 70°N, is -8.3×10^{14} kg, equivalent to 67% of the initial perturbation. Of this anomaly, -7.6×10^{14} kg is found north of the equator. An anomaly of -1.4×10^{14} kg is also found in the Arctic Ocean ($> 70^\circ\text{N}$), after 100 years.

Figure 4.13 shows the zonally averaged salinity in the Atlantic. For the first 20 years, freshening extends into the upper layers above the initial perturbation, and the surface of the tropical Atlantic. For years 11-20, a freshening is also found in the region of the NAC. This corresponds to the salt anomalies seen in the North Atlantic in Figure 4.12, suggesting that the perturbed water mass reaches this location within 20 years. To be advected north on this timescale requires currents $> 2.1 \text{ cm s}^{-1}$. Along the western boundary of the Atlantic, currents $> 6 \text{ cm s}^{-1}$ are found at a depth of 50 m, and currents $> 2 \text{ cm s}^{-1}$ at ~ 500 m. At greater depth, the anomaly spreads northwards at a slower speed. The majority of the Atlantic, between 30°S and 60°N, is found to be fresher than the control simulation at depths of ~ 200 -1500 m for years 31-40. At 60°N, fresh anomalies are also seen extending from the surface to depths > 3000 m. After 40 years, fresh anomalies are found in the upper 500 m of the GIN Seas, $> 60^\circ\text{N}$. After 50 years, these fresh anomalies extend below the upper layers, with significant anomalies found at depths > 1000 m (level 13 in HadCM3). For years 61-100, the freshening north of 60°N extends from the surface to depths > 2000 m (Figure 4.13). As seen in Figure 4.12, the anomalies in the North Atlantic reduce towards the end of the simulation, with a positive anomaly developing after 60 years. However, the anomalies in the South Atlantic are present up to the end of the simulation, extending to depths > 2000 m.

At the surface, there is a decreased salinity in the South Atlantic for the first 20 years of the simulation (Figure 4.4b,d). This corresponds to the region of surfacing seen in Figure 4.13. The SSS anomalies are strongest along the coast of Africa, where southerly winds result in upwelling along the eastern boundary of the basin. These conditions may bring the perturbed intermediate waters to the surface in this region. For years 11-20, freshening spans the width of the Atlantic from ~ 0 -20°S. In the tropical South Atlantic, there are also negative SST anomalies for the first 10 years, with significant anomalies extending along the path of the North Brazil Current (Figure 4.5b). Positive heat flux anomalies indicate that these changes in the ocean are not forced by a cooler overlying

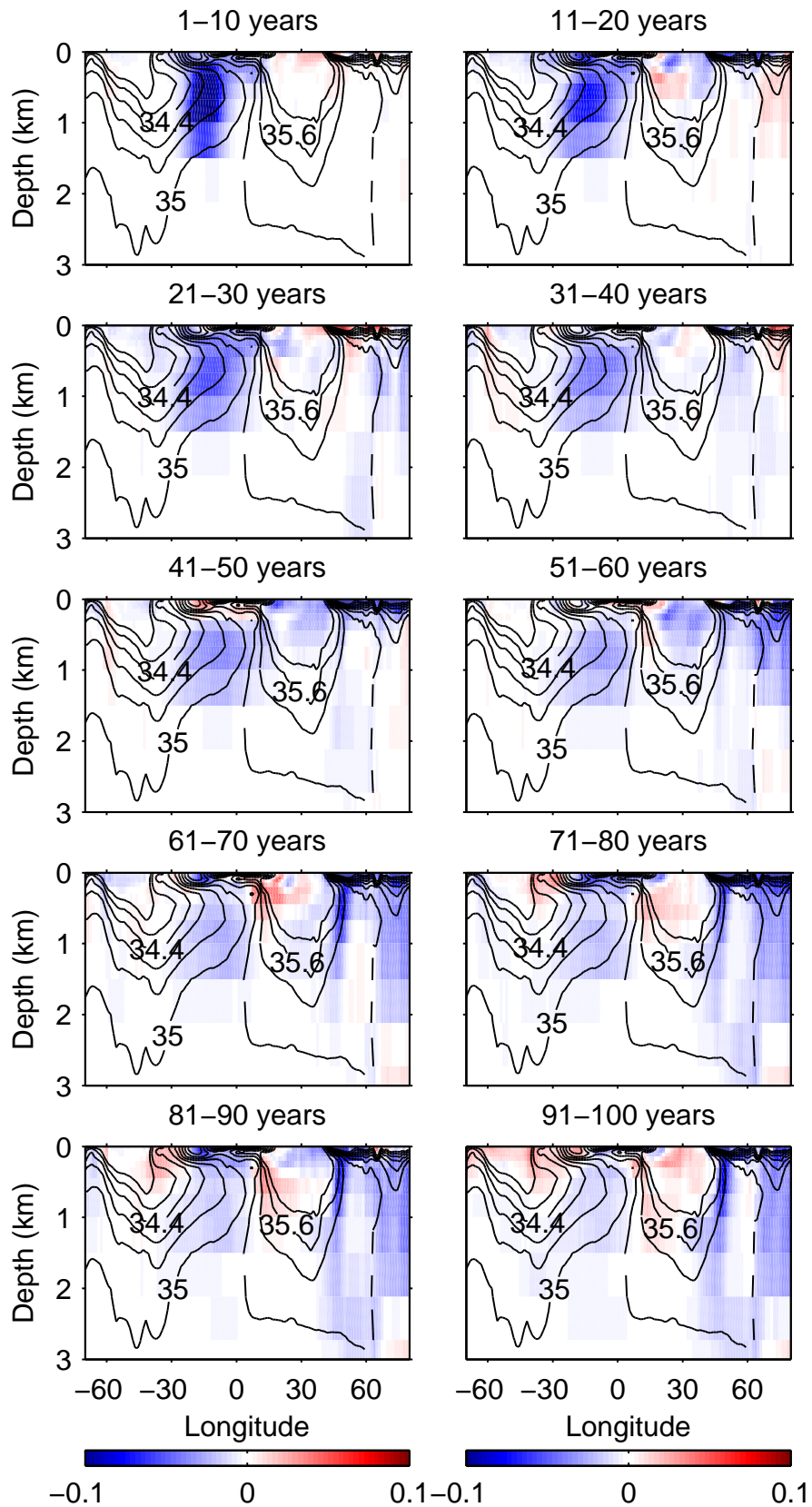


Figure 4.13: Zonally averaged decadal salinity anomalies (EXP2b - control) in the Atlantic for 100 years.

atmosphere (Figure 4.6b). Although this is an indication that the perturbation may be surfacing, the salinity anomalies are not significant on decadal timescales. Also, for years 11-20, the SST anomalies in the tropical Atlantic and along the coast of Africa are not of the same sign as the SSS anomalies. This indicates that although the anomaly may be surfacing in these regions, the heat and salt content anomalies may not be sufficient to cause significant changes compared with the internal variability. On annual timescales, there are significant fresh anomalies in the South Atlantic for years 15-20. However, again there are no SST anomalies of the same sign. Surface heat flux anomalies show that these SST anomalies are predominantly forced by the overlying atmosphere during this decade (Figure 4.6d). For years 11-20, there is a significant cooling in the NAC and around the STG, matching the sign of the SSS anomalies (Figures 4.5d and 4.4d). This supports the suggestion that the cool, fresh anomaly reaches these locations within the first 20 years, as the anomaly travels within the upper layers of the ocean. Few regions of cool, fresh anomalies are found at the Atlantic surface for years 21-40 (Figures 4.4f,h and 4.5f,h). However, for years 41-50, there is a cooling throughout the North and South Atlantic, contributing to a mean cooling seen in the extra-tropical North Atlantic for the first 50 years.

For years 51-100, significant cooling is seen throughout a large area of the North Atlantic, into the SPG and GIN Seas (Figure 4.14a). The cooling is strongest in the path of the NAC, where there are temperature anomalies $< -1^{\circ}\text{C}$, compared with the mean of the control ensemble. The cooling and freshening in this region are persistent for years 61-100 and extend to depths of 2000 m. As seen in Figure 4.13, the anomalies in the GIN Seas also extend below the surface to depths > 2000 m. These regions have deep mixed layer depths (> 300 m), allowing cooler, fresher water to be brought to the surface. The surface heat flux anomalies indicate a heat flux in the atmosphere-to-ocean direction, providing further evidence that the SST anomalies result from the ocean rather than atmospheric forcing (Figure 4.14b).

In the latter half of the simulation there is a significant decrease in the overturning circulation (Figure 4.15). For each of the three indices shown there is a decrease in the decadal-mean streamfunction after 40 years, which persists until the end of the simulation.

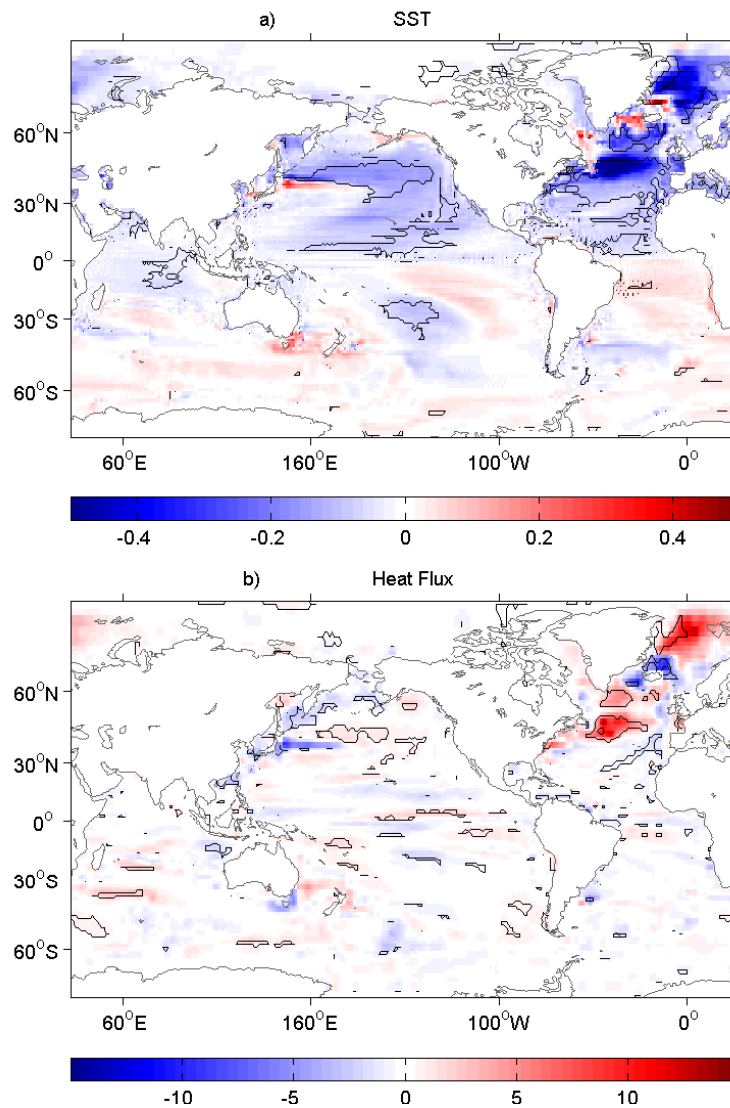


Figure 4.14: 50-year-average anomalies (EXP2b control) for years 51-100 of: a) sea surface temperature (SST) [$^{\circ}\text{C}$]; b) ocean-atmosphere heat flux (positive values indicate flux in atmosphere-to-ocean direction) [W m^{-2}]. Contours show regions significant at the 95% confidence level.

Eight of the nine ensemble members shows a decrease within the latter half of the simulation, when compared with the control (Figures 4.15 and 4.16). Figure 4.16 also shows that the decrease for five of the ensemble members is outside the range control variability during this 500 year simulation. One ensemble member shows an increase during years 71-80. This member had initial conditions from year 250 of the 500 year simulation. Figures 4.1 and 4.16 show that between 250 and 350 years, the control MOC strength oscillates between stronger and weaker states every ~ 30 years. This variable state of the MOC may then have influenced the response of the ensemble member at this time. This decrease is related to the changes in density at 60°N (as described in Chapter 3). Figure

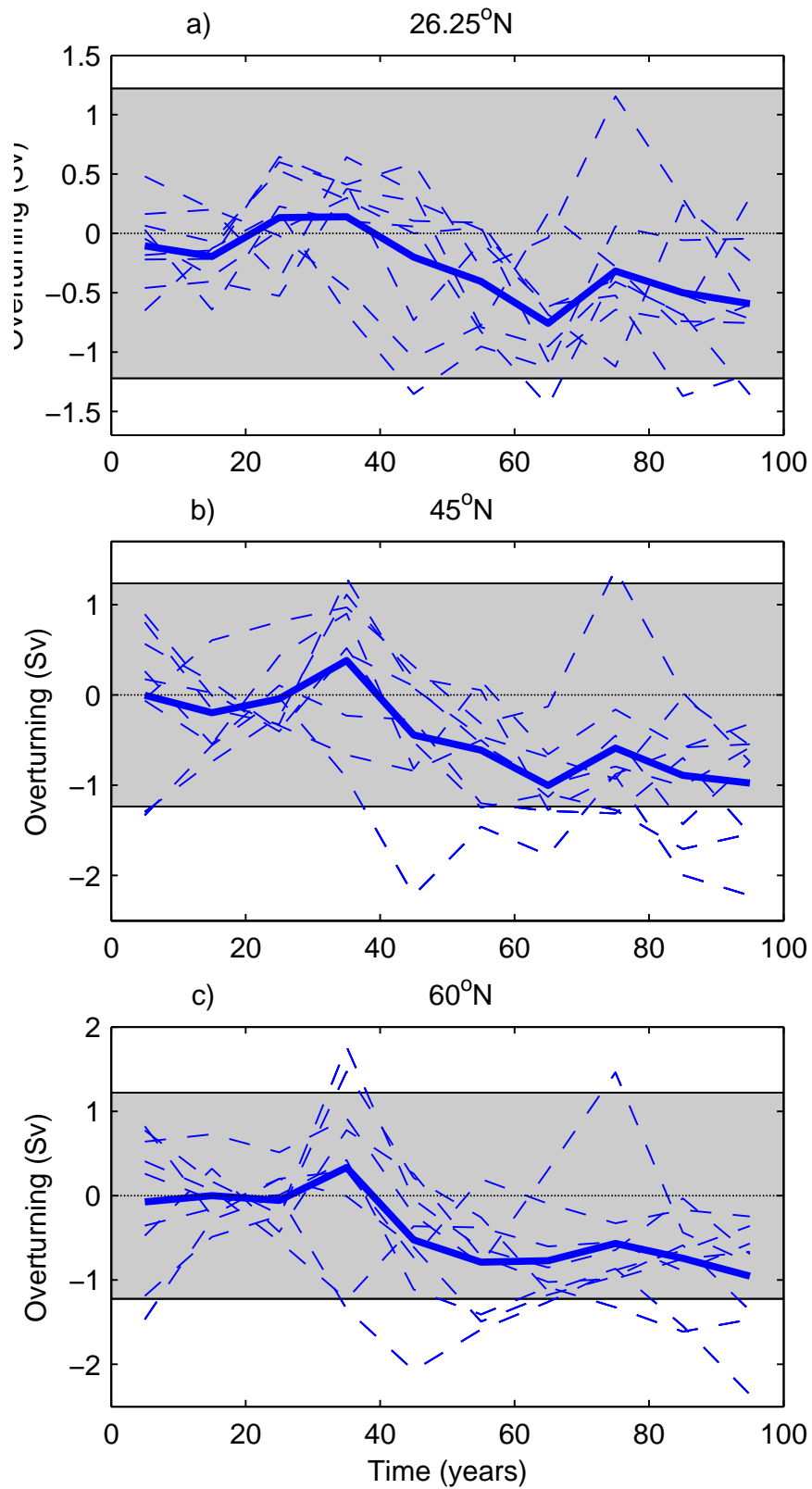


Figure 4.15: Decadal anomalies for three meridional overturning streamfunction indices (EXP2b – control) at: a. 26.5°N; b. 45°N; c. 60°N. Solid lines indicate the anomaly of ensemble mean values (EXP2b – Control); dashed lines show the anomalies of individual EXP2b ensemble members minus mean of the control. Shaded region shows the 95% spread of the control ensemble over the 100 year simulation.

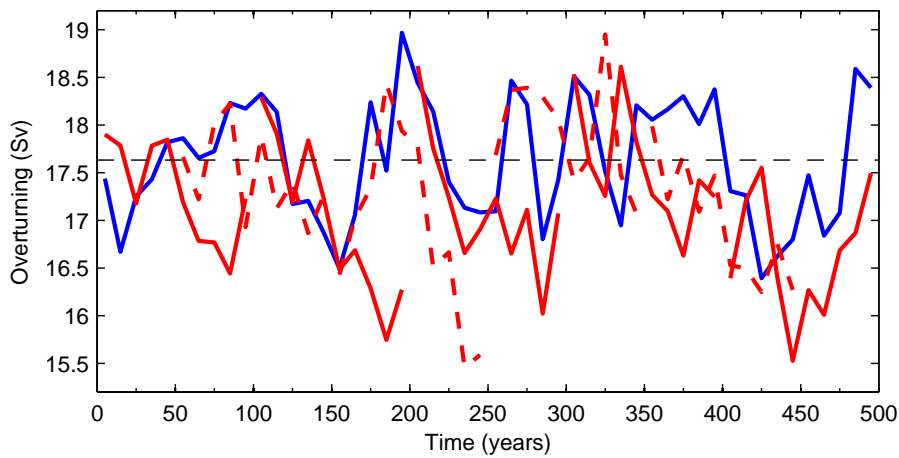


Figure 4.16: Decadal meridional overturning streamfunction index at 45°N , for each ensemble member of EXP2b over 500 years. Blue lines indicate the control values over 500y. Red solid lines show EXP2b ensemble members with start dates 0, 100, 200, 300, 400; red dashed lines show ensemble members with start dates 50, 150, 250, 350. Black dashed line indicates the time-mean of the 500 year control.

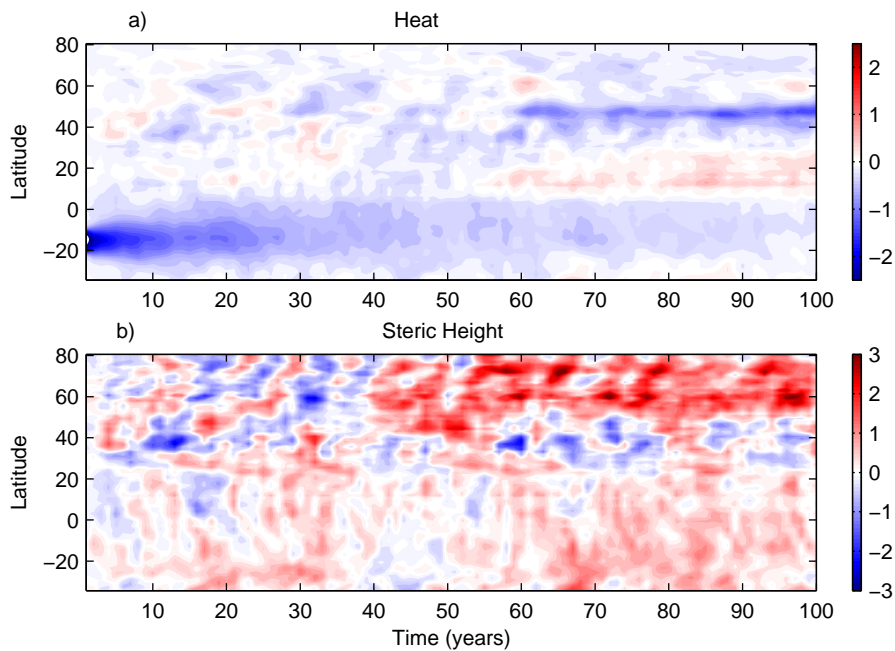


Figure 4.17: Hovmöller plots of a. total heat content anomalies (EXP2b – Control), within 0-3000 m [10^{21} J]; b. zonal mean steric height anomalies (EXP2b – Control) [cm], in the Atlantic.

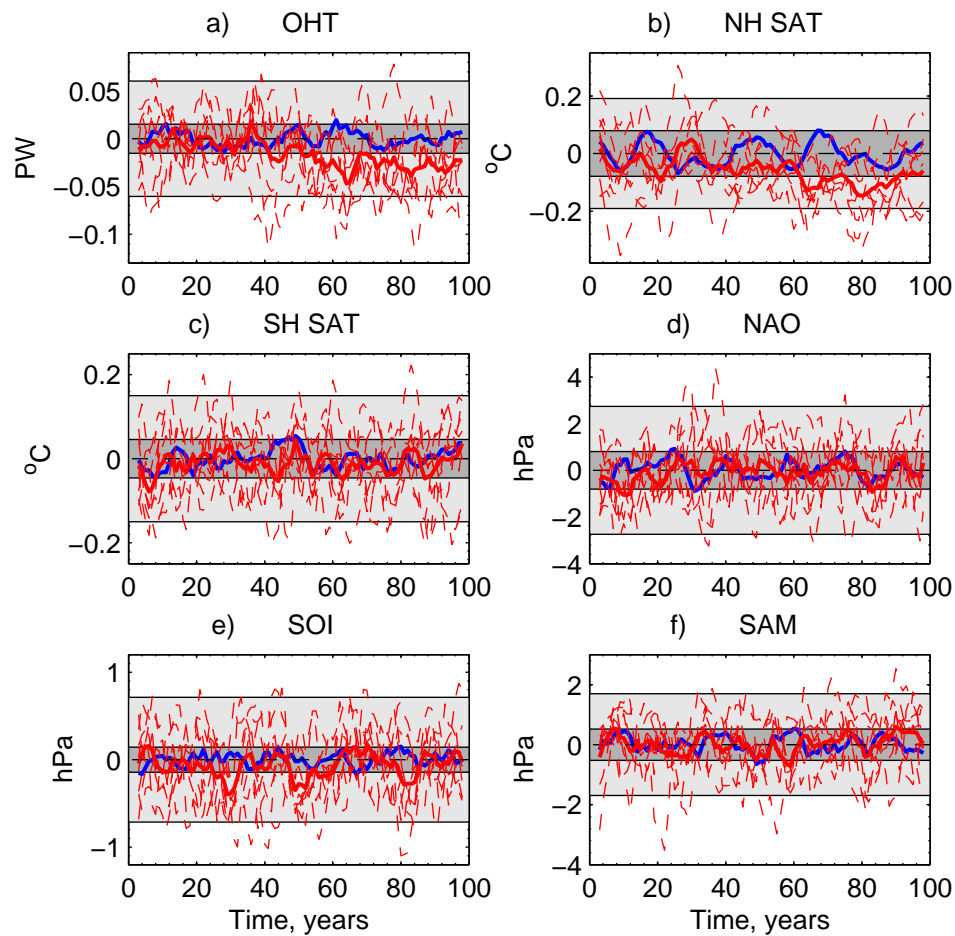


Figure 4.18: Absolute values of climate indices for EXP2b: a) Northward ocean heat transport (OHT) at 26°N in the Atlantic; b) mean Northern Hemisphere (NH) surface air temperature (SAT) c) mean Southern Hemisphere (SH) SAT; d) North Atlantic Oscillation (NAO) index : annual MSLP difference from Gibraltar-Iceland; e) Southern Oscillation Index (SOI) : annual MSLP difference from Tahiti-Darwin; f) Southern Annular Mode (SAM) : annual MSLP difference between 40 and 65°S . Light (dark) shaded area shows the 2σ (95%) spread of the control ensemble (mean) around the 100 year mean. Dashed (solid) red lines show the ensemble (mean) anomalies for EXP2b (EXP2b – time-mean of control). Blue line shows the mean of the control ensemble around the 100 year mean. Data are smoothed using a 5 year running mean. Dashed black line indicates the reference time-mean value for the control ensemble over the 100 year simulation (at zero).

4.17a shows the progression of the cool water mass northwards through the Atlantic. As the anomalous water mass reaches the surface in the North Atlantic and interacts with the atmosphere, it gains heat (reducing the cold anomaly; Figures 4.6 and 4.14b), but remains fresh. This process leads to a reduction in density in the water column, resulting in an increased steric height around 60°N (Figure 4.17b). As the MOC strength decreases, there is a significant reduction in the meridional ocean heat transport (Figure 4.18a). Along with the surfacing of the cooler, fresher AAIW, this contributes to the decreased SST seen in the North Atlantic and GIN Seas.

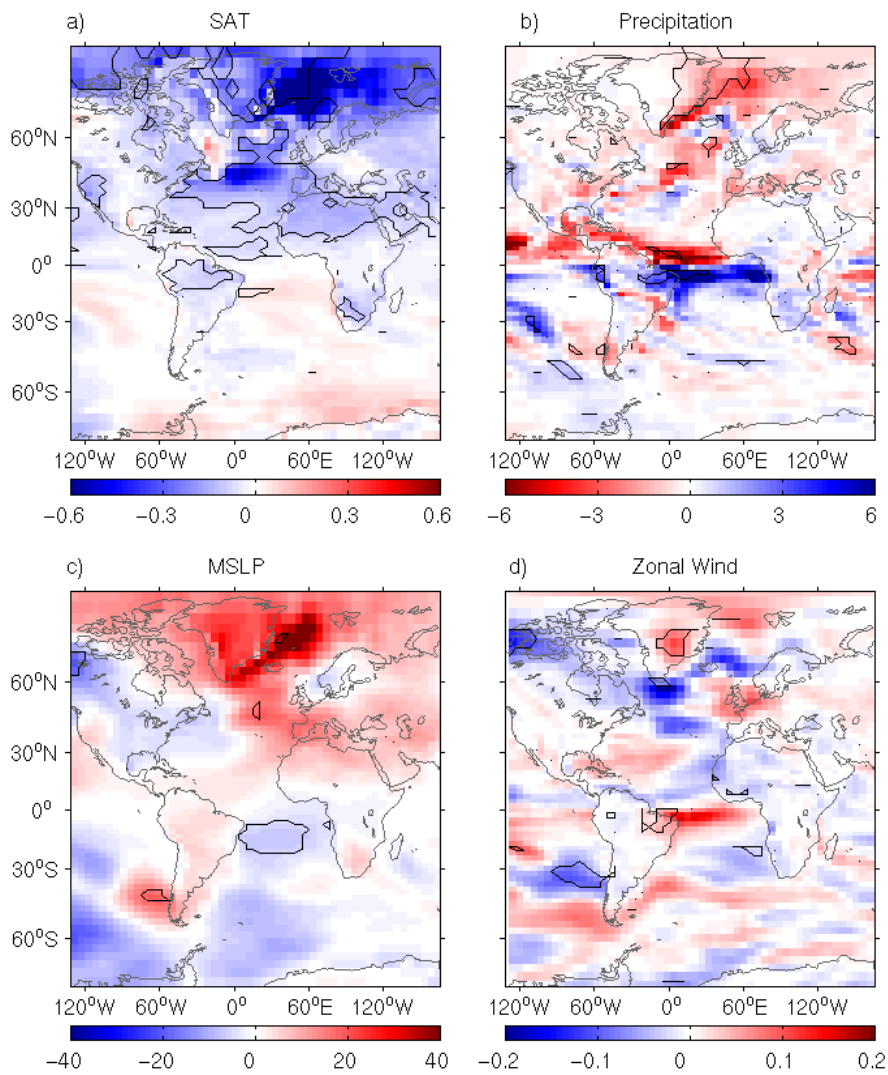


Figure 4.19: Mean atmospheric anomalies for 51-100 years (EXP2b – Control): a. surface air temperature (SAT) [$^{\circ}\text{C}$]; precipitation [cm year^{-1}]; mean sea level pressure (MSLP) [Pa]; zonal wind speed [m s^{-1}]. Black contours show anomalies significant at the 95 % confidence level.

As the negative SST anomalies develop in the North Atlantic, this leads to a significant reduction in the temperature of the overlying atmosphere (Figure 4.19a). As the SST anomalies are strongest over the NAC and GIN Seas, the strongest SAT anomalies are also over these regions. Over the GIN Seas, there is a reduction of up to 2°C during years 71-80. Over the NAC ($45\text{-}53^{\circ}\text{N}$), the strongest anomalies were found during years 91-100, when there is a decrease of 1°C . Although these regions show the strongest anomalies, the cooling is not confined over the oceans (Figure 4.19a). Figure 4.18b shows that there is a cooling over the entire Northern Hemisphere after 40 years, with anomalies of up to 0.2°C around 70 years into the simulation. However, no significant trend is seen in the Southern Hemisphere (Figures 4.19a and 4.18c).

For the latter half of the simulation, significant precipitation anomalies are found over East Greenland and in the Tropical Atlantic (Figure 4.19b). The anomalies in the Tropical Atlantic show a band of increased rainfall to the south of the Equator ($\sim 0-20^{\circ}\text{S}$), and a band of decreased rainfall to the north ($\sim 0-20^{\circ}\text{N}$). This is consistent with a southward shift in the Inter-Tropical Convergence Zone (ITCZ). Vellinga and Wu (2004) have shown that a decrease in MOC strength can result in southward shifts in the ITCZ due to anomalies in the SST gradient in the Tropical Atlantic. The reduced rainfall in the Tropical North Atlantic may account for the increased salinity seen between 0 and 40°N in the North Atlantic after 60 years (Figure 4.13). The anomalies over Greenland coincide with a region of anomalously high mean sea level pressure (MSLP) over Greenland and the GIN Seas (Figure 4.19c). Although there is an increase in MSLP in this region, the anomalies are not significant, and there are no trends in the NAO index (Figure 4.18d). There is a region of decreased wind speed at the southern tip of Greenland, and a region of increased wind speed further north, over the Greenland land mass. However, as the MSLP anomalies show little patterns of significance, there are few significant results for the zonal winds over the region (Figure 4.19). Outside the Atlantic basin, there are no significant MSLP trends relating to the SOI or SAM (Figures 4.18e,f).

4.4 Discussion

For both EXP1b and EXP2b, there are signs of the perturbed water mass surfacing in the tropical Atlantic. Although the response is not significant in both experiments, the salinity anomalies found at the surface (Figure 4.4) extend to the location of the perturbed water mass at intermediate depths. There is a less significant response in SST (Figure 4.5), likely due to the fact that heat can be exchanged rapidly with the overlying atmosphere. The heat content anomaly may not be sufficient to cause changes with respect to the internal variability of the region on decadal timescales.

In Chapter 3, responses in EXP1 and EXP2 were shown to have some similarities, although in general the magnitude of the response in EXP2 is larger. These new ensemble runs have shown that the response in EXP2b is again greater than EXP1b, and significant anomalies are found over a larger area. EXP2b shows a decrease in MOC strength for the latter half of the simulation. This decrease in MOC and the resultant cooling in the North

Atlantic are both greater and significant over a larger area than those seen in EXP2. Given the variety of initial ocean conditions used for EXP2b, this gives greater confidence that these results are not dependent on particular initial ocean states (Figure 4.16).

Contrary to the response seen in EXP1, EXP1b shows no significant long-term trend in climate through the course of the simulation. This suggests that the decreased MOC seen in EXP1 may have been due to the initial ocean conditions used for the ensemble. However, similar to the SSS and SST anomalies seen in EXP1, there are significant anomalies in the first 40 years of the simulation, indicating that the water mass may be surfacing as it moves northwards through the Atlantic. Both experiments show positive heat and salt anomalies in the SPG, and for EXP1b there are also anomalies seen in the GIN Seas. The fact that there is no increased MOC strength shows that these anomalies are driven by the anomalous water mass rather than changes in the overturning heat transport.

Again, it can be seen that overall the responses in these two experiments are not linear (equal and opposite). The significant response in EXP1b is seen in the first half of the simulation, whereas EXP2b sees a response over longer timescales, as the MOC decreases in the latter half of the experiment. As shown in Chapter 3, interaction with the atmosphere leads to opposite density anomalies for the two experiments (Figure 3.32). The fresher AAIW then has a greater tendency to remain in the surface regions, whereas the more saline AAIW will have a tendency to remain at intermediate depths. At the end of the simulation, 47% of the salt anomalies for EXP1b remained at intermediate depths in the Atlantic, whereas for EXP2b, only 14% of the initial salt anomaly remained at intermediate depth levels, with the majority residing in the surface layers, or sinking to deep levels in the north. As the fresher AAIW spends a greater length of time at the surface, the prolonged interaction with the atmosphere results in greater density anomalies. This leads to the significant response in the MOC due to the increase in steric height around 60°N. The MOC index for EXP2b is reduced below the range of the control ensemble for the 500 year simulation. As the warm, saline AAIW spends more time at intermediate depths, the perturbation retains more of the heat anomaly and there are few significant density anomalies. Hence, there is no significant change in the MOC.

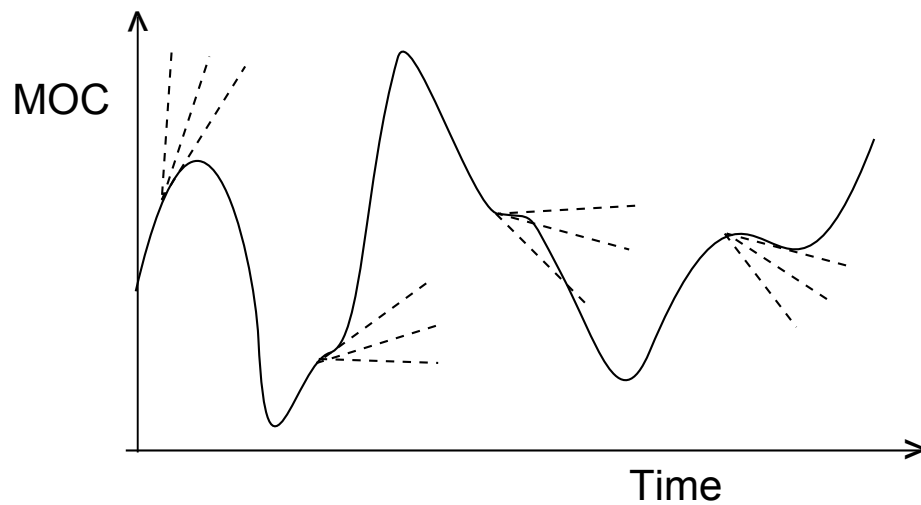


Figure 4.20: Schematic to illustrate possible responses to perturbations for varying initial ocean states. Differing initial states may be predisposed to react in a particular way. Solid line indicates the meridional overturning circulation (MOC) strength for the control simulation. Dashed lines indicate trajectories for perturbed ensembles at varying start dates.

4.5 Summary

The same perturbation experiments as described in Chapter 3 were carried out with ensembles of varying initial conditions in both the atmosphere and ocean. For both perturbations, there were signs of the anomalies surfacing in the tropical North Atlantic within the first 10 years. Anomalies move northwards as they are advected along the western boundary. Significant salt content anomalies are found in the North Atlantic within 20 years. As discussed in Section 3.5, interaction with the atmosphere leads to opposing density anomalies and therefore non-linearity in the results for these two experiments. The warmer, saltier AAIW in EXP1b has a tendency to remain at depth in the ocean, resulting in a less significant response at the ocean surface. There is no decrease in the MOC, suggesting that the response seen in EXP1 may have been due to the initial state in the control run used for the experiment. However, the fresher AAIW in EXP2b spends more time in the surface layers. This results in a significant decrease in density throughout the water column in the North Atlantic, driving a decrease in the MOC strength, greater than that seen for EXP2. Initial states in the ocean may be predisposed to react in a particular way to perturbations (illustrated in Figure 4.20). By choosing an ensemble with varying initial ocean conditions, this effect can be reduced. There is less similarity between the results for EXP1b and EXP2b than there is between EXP1 and EXP2, making it clearer which effects are due to the perturbation rather than variability in the control

climate. This gives us greater confidence in the results presented. Following these results, both styles of ensembles will be used when investigating the response to perturbations in the Indian and Pacific, however the emphasis will be on results from the varying ocean ensemble.

Chapter 5

Response to perturbing AAIW in the Pacific

5.1 Introduction and Methods

Having analysed the response within the Atlantic, we now see what impact a change of properties can have within the other major ocean basins. When considering how to perform the perturbation experiments, the basic principles are kept the same as that used for the previous experiments (Chapters 3 and 4), so that the results can be compared with those from the Atlantic. However, the properties of AAIW vary between the oceans, so the density boundaries used to define the water mass in the Atlantic are not appropriate for experiments in other oceans.

Figure 5.1 shows the temperature-salinity diagram for 10-20°S in the three major ocean basins. From this it can be seen that AAIW in both the Indian and Pacific is fresher than in the Atlantic. The core of the AAIW is defined as the salinity minimum below the surface waters. For the Atlantic we can see a minimum of 34.2 at a potential density of 1028.5 (relative to level 11 in HadCM3). However, the Pacific has a minimum value of 33.9 at 1027.6. As with the Atlantic, the core is typically found in model level 11, but towards the east of the basin, the isopycnals are seen to rise and the core can be found in level 10. As Pacific AAIW is lighter and fresher, the chosen potential density boundaries are then 1027.2 – 1029.1 (Figure 5.2). The temperature is altered by $\pm 1^\circ\text{C}$ within this range, and $\pm 0.5^\circ\text{C}$ in the levels directly above and below. The salinity is then altered

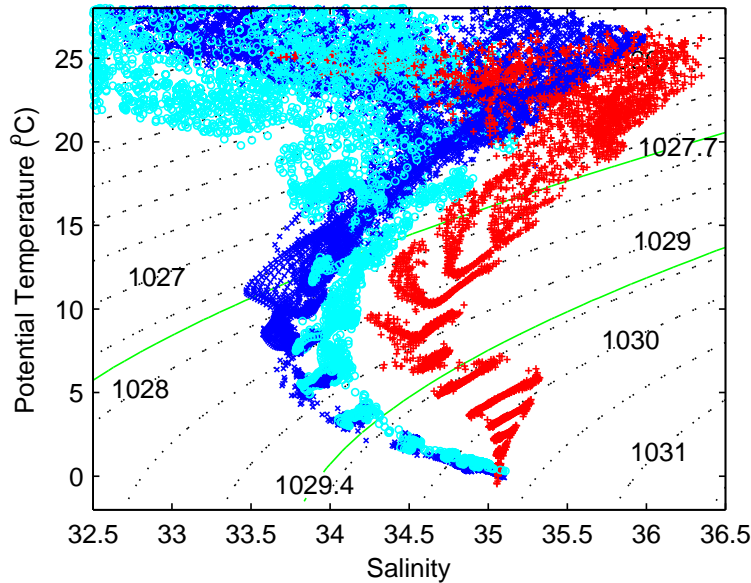


Figure 5.1: Potential temperature (θ) – salinity diagram for the three main ocean basins. Red pluses, blue crosses and cyan circles show the control conditions for the Atlantic, Pacific and Indian oceans respectively, between $10\text{--}20^\circ\text{S}$. Black contours show the corresponding potential density values calculated relative to a depth of ~ 500 m. Green contours show the boundaries of AAIW chosen for the Atlantic, 1027.7 and 1029.4.

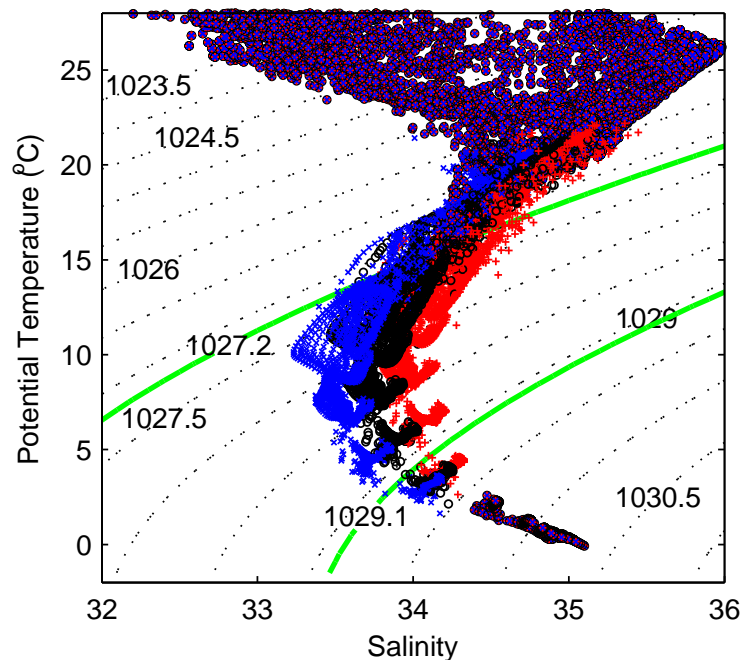


Figure 5.2: θ - S plot for perturbation and control start dumps. Red pluses and blue crosses show the conditions for the $+1^\circ\text{C}$ (EXP3) and -1°C (EXP4) perturbations respectively. Black circles show the control conditions. Black dotted contours show the corresponding potential density values calculated relative to a depth of ~ 500 m. Green contours show the boundaries of AAIW, 1027.2 and 1029.1.

to maintain constant potential density. The Pacific Ocean spans over twice the width of the Atlantic, meaning that our perturbation results in a total heat and salt change that is more than twice that imposed on the Atlantic. For the Pacific, a $+1^{\circ}\text{C}$ perturbation results in an increased heat content of 6.11×10^{22} J, compared with an increase of 2.30×10^{22} J in the Atlantic (for EXP1). The simulations were run for 100 years, with two sets of 9 member ensembles, following the methods described in Sections 3.2 and 4.2. The experiments in this chapter will hereafter be referred to as EXP3 and EXP4 for the $+1^{\circ}\text{C}$ and -1°C perturbations, for the ensembles with the same ocean initial conditions and varying atmosphere; EXP3b and EXP4b denote the $+1^{\circ}\text{C}$ and -1°C ensembles with varying initial conditions in both the atmosphere and ocean (all experiments are listed in Appendix A for reference). Results from the first 40 years will be shown for both types of ensemble, however following the conclusions of Chapter 4, our analysis will focus predominantly on the ensembles with varying ocean initial conditions.

5.2 Response to warmer, saltier AAIW

EXP3 showed a significant response in both the ocean and atmosphere during the first 30 years of the experiment. The following section will discuss this result, before looking at whether the same response is seen in EXP3b in Section 5.2.2.

5.2.1 Response to surfacing in the equatorial Pacific?

For EXP3, there are positive SST and SSS anomalies in the equatorial Pacific during the first 30 years (Figures 5.3 and 5.4). This suggests that the anomalous water mass is surfacing in this region. In the Niño 3.4 climate index region for the central equatorial Pacific (5°N - 5°S , 170 - 120°W), there is an increased SSS throughout the majority of the simulation (Figure 5.5a). The SST in the Niño 3.4 region remains above that of the control simulation for the first ~ 25 years of the experiment (Figure 5.5b). From the initial perturbation region, the anomaly is advected into the equatorial region, where upwelling and shoaling isopycnals to the east can allow the warmer, saltier waters to reach the surface layers (Figure 5.6). For years 11-20, warmer surface waters are also found around the Southern Ocean, however for years 21-30 a significant cooling and freshening is then found in this surface region. Integrated throughout the water column, there is an increased

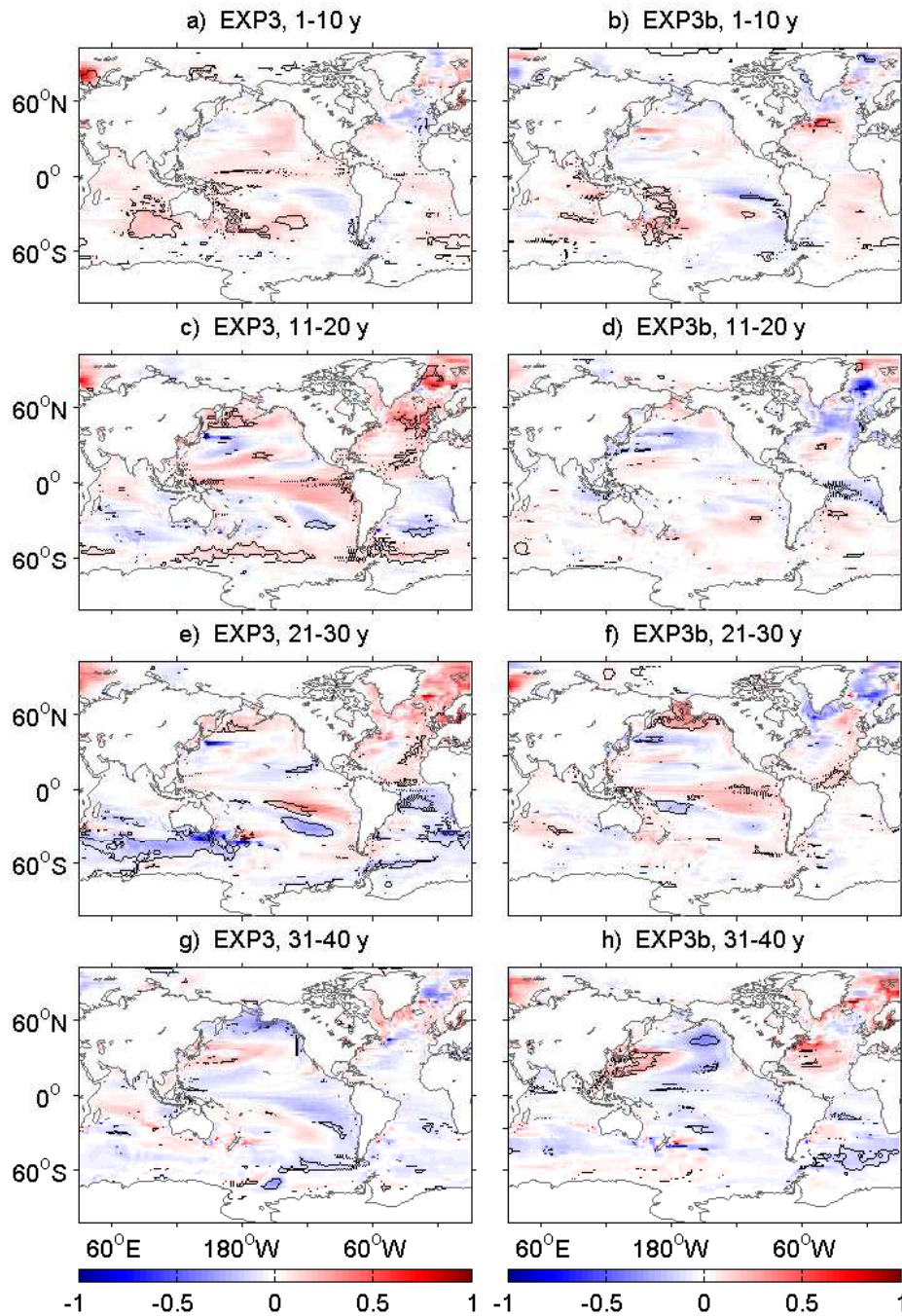


Figure 5.3: Decadal sea surface temperature anomalies ($EXP - control$) for the first 40 years [$^{\circ}C$]. Figures a, c, e and g show anomalies for EXP3; b, d, f and h show anomalies for EXP3b. Contours show regions significant at the 95% confidence level.

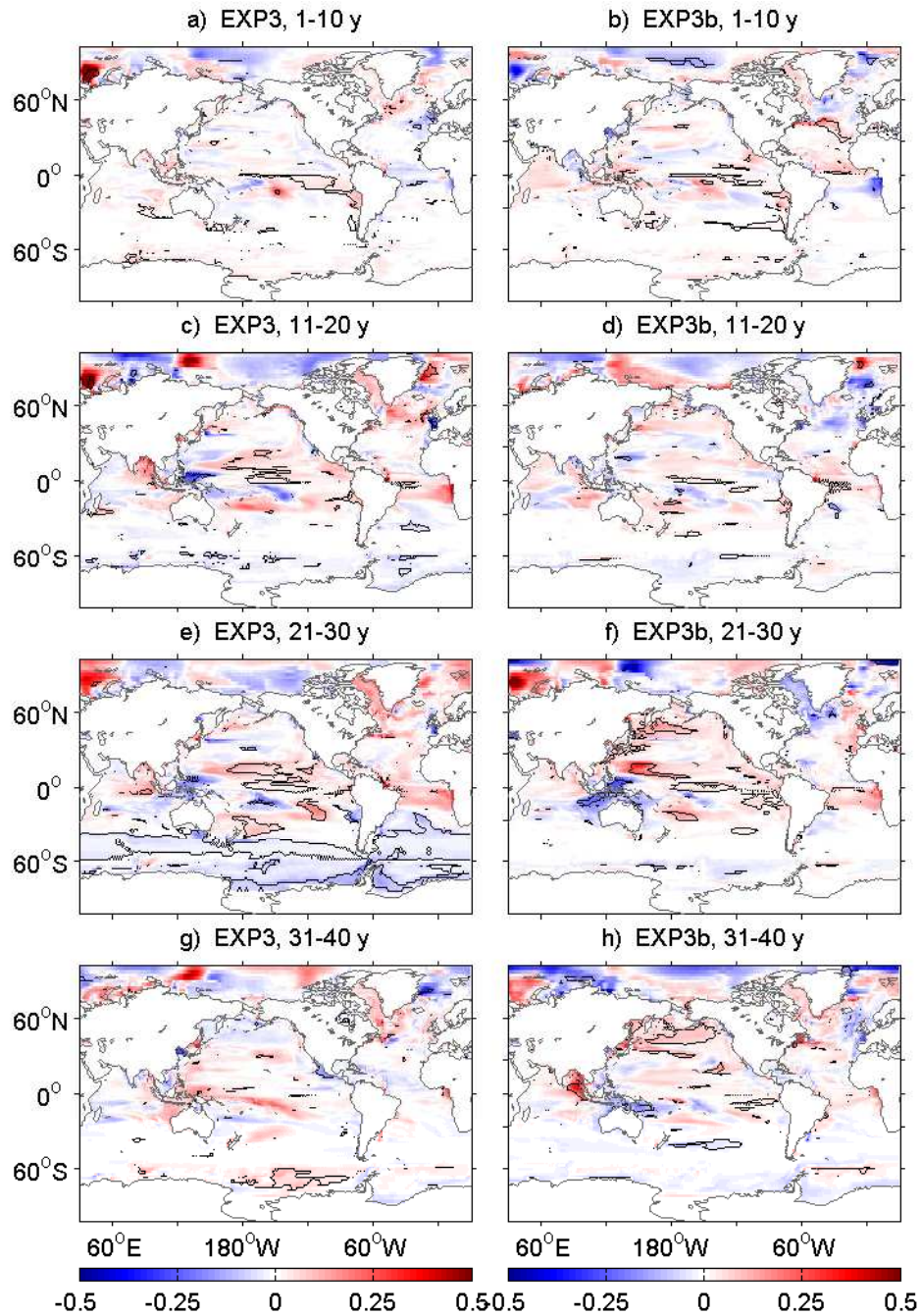


Figure 5.4: Decadal sea surface salinity anomalies (EXP – control) for the first 40 years. Figures a, c, e and g show anomalies for EXP3; b, d, f and h show anomalies for EXP3b. Contours show regions significant at the 95% confidence level.

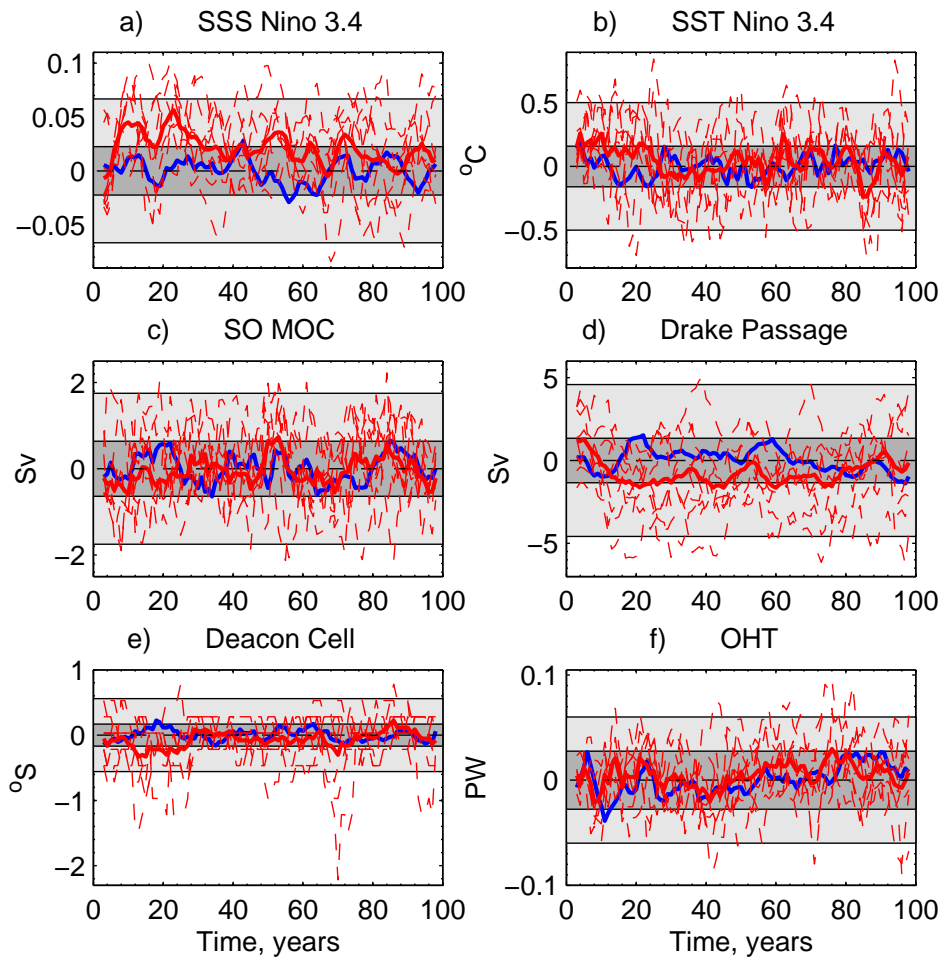


Figure 5.5: Absolute values of climate indices for EXP3: a) mean sea surface salinity (SSS) in the Niño 3.4 index region (5°N - 5°S , 170 - 120°W); b) mean sea surface temperature (SST) in the Niño 3.4 index region; c) strength of Southern Ocean meridional overturning circulation (SO MOC) : maximum overturning south of 30°S ; d) volume transport through Drake Passage; e) latitude of Deacon Cell (SO MOC); f) Northward ocean heat transport (OHT) at 26°N in the Atlantic. Light (dark) shaded area shows the 2σ (95%) spread of the control ensemble (mean) around the 100 year mean. Dashed (solid) red lines show the ensemble (mean) anomalies for EXP3 (EXP3 – time-mean of control). Blue line shows the mean of the control ensemble around the 100 year mean. Data are smoothed using a 5 year running mean. Dashed black line indicates the reference time-mean value for the control ensemble over the 100 year simulation (at zero).

salinity north of 60°S , and a decreased salt content from 60°S to the Antarctic coast (Figure 5.7).

During years 11-20, there are regions of significant MSLP anomalies in the SH. The MSLP decreases over the mid-latitudes in the SH and increases over Antarctica. This corresponds to a decrease in the Southern Annular Mode (SAM) index, with a minimum at ~ 20 years (Figure 5.8a). These MSLP anomalies lead to changes in the wind stress around the Southern Ocean, with a northward shift and weakening of the SH jet stream. The ACC then also weakens and shifts northwards, along with the overturning Deacon

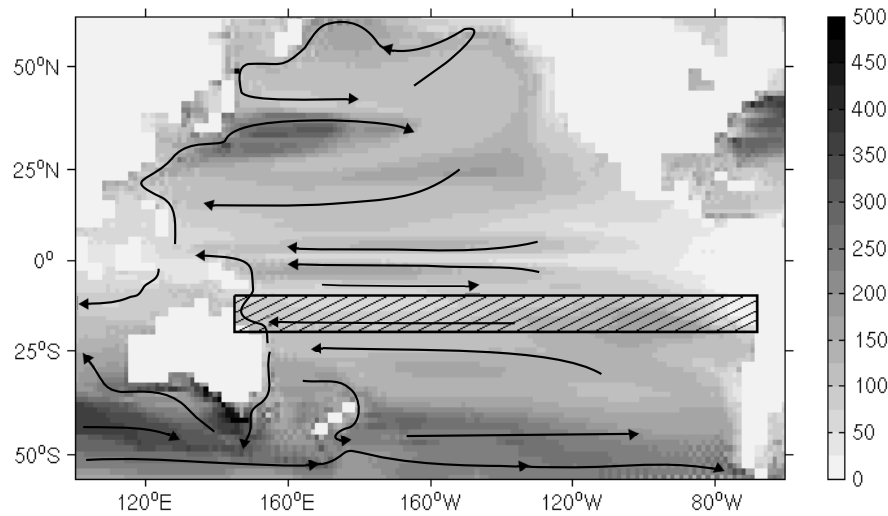


Figure 5.6: Schematic of the perturbed region of the Pacific in HadCM3, 10–20°S (hatched box). Arrows show the mean locations of the strongest currents ($> 1 \text{ cm s}^{-1}$) at $\sim 500 \text{ m}$ (level 11 in HadCM3, the depth of the salinity minimum in the perturbed region). Shading shows the mean maximum mixed layer depth for 100 years of the control ensemble [m]. Resolution of the coastline is $2.5^\circ \times 3.75^\circ$, matching the resolution of the atmospheric component.

Cell (Figures 5.5c-e). These changes are consistent with atmosphere-ocean coupling associated with the SAM (e.g. Thompson and Wallace, 2000; Hall and Visbeck, 2002; Sen Gupta and England, 2006) and are illustrated in Figure 5.9. During a negative phase of the SAM, the westerly winds weaken and shift northwards. This leads to easterly wind anomalies in the south, and westerly wind anomalies in the north of the Southern Ocean. As the wind stress patterns are altered, the resultant change in ocean circulation may account for changes in salt content, as there is a reduction in Ekman transport of fresh Antarctic Surface Water to the north, and a reduced upwelling of warm, salty deep waters in the south.

Marshall and Connolley (2006) and Sen Gupta and England (2007a) show that changes in the Southern Ocean can also lead to changes in the overlying atmosphere. Marshall and Connolley (2006) show that as the meridional SST gradient decreases around the Southern Ocean, this may weaken the SAM index. The thickness of layers in the atmosphere is dependent on their temperature. Warmer SSTs then lead to an increased geopotential height in the atmosphere, and as the meridional SST gradient is altered this will lead to a change in geopotential height gradient. As the SSTs increase around Antarctica, this leads to increased MSLP over the continent. For years 11-20 the increased SST south of $\sim 45^\circ\text{S}$, along with decreased SST further north, may then be a contributing cause of the

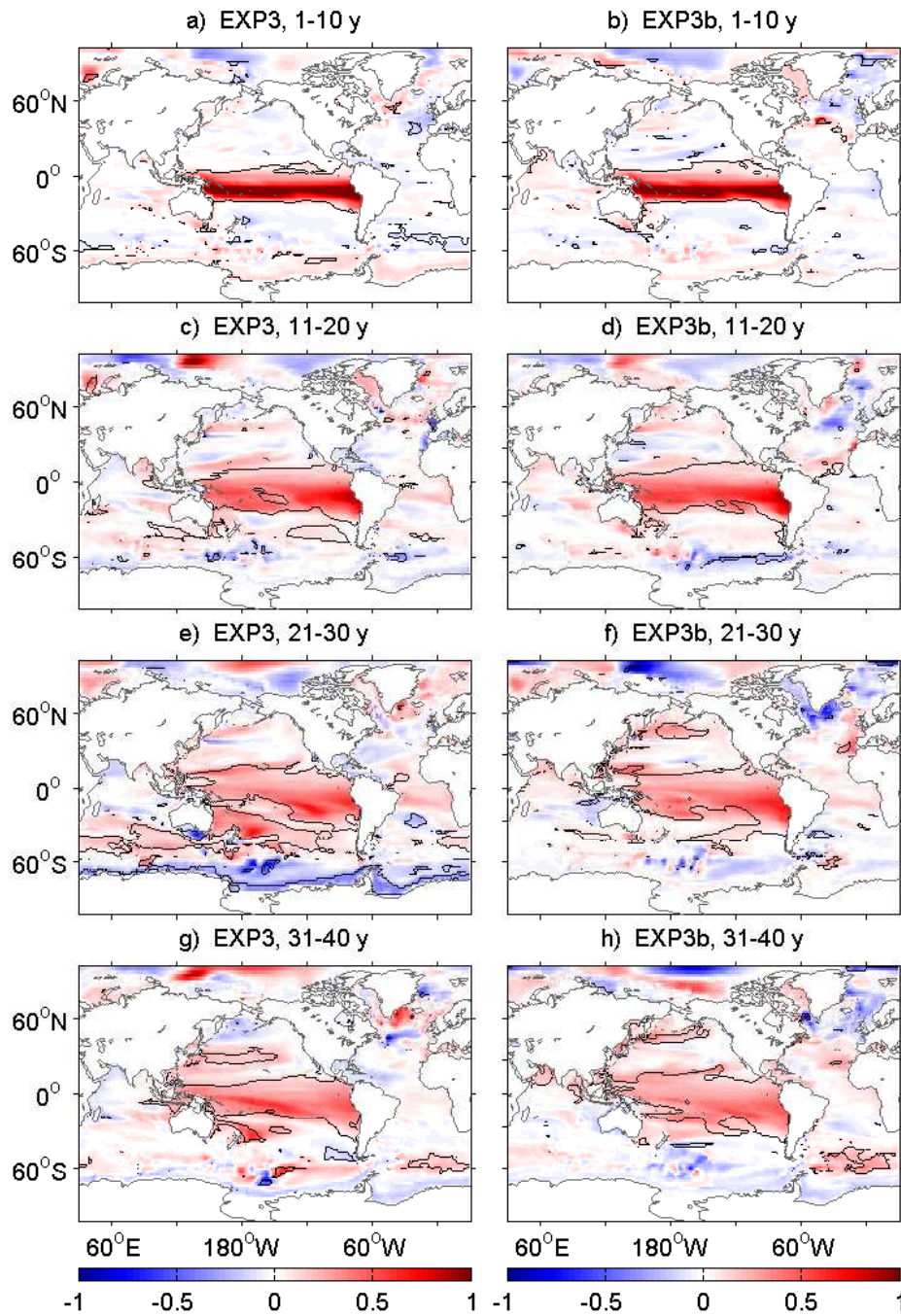


Figure 5.7: Decadal salt content anomalies (EXP - control) for the first 40 years [10^2 kg m^{-2}]. Figures a, c, e and g show anomalies for EXP3; b, d, f and h show anomalies for EXP3b. Contours show regions significant at the 95% confidence level.

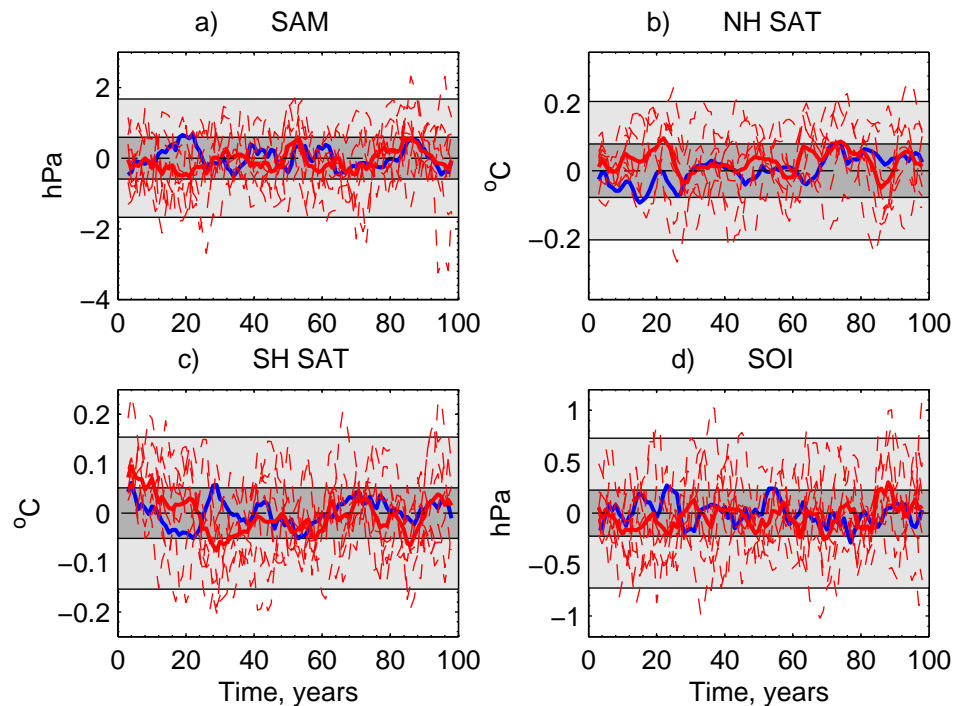


Figure 5.8: Absolute values of climate indices for EXP3: a) Southern Annular Mode (SAM) : annual MSLP difference between 40 and 65°S; b) mean Northern Hemisphere (NH) surface air temperature (SAT) c) mean Southern Hemisphere (SH) SAT; d) Southern Oscillation Index (SOI) : annual MSLP difference from Tahiti-Darwin. Light (dark) shaded area shows the 2σ (95%) spread of the control ensemble (mean) around the 100 year mean. Dashed (solid) red lines show the ensemble (mean) anomalies for EXP3 (EXP3 – time-mean of control). Blue line shows the mean of the control ensemble around the 100 year mean. Data are smoothed using a 5 year running mean. Dashed black line indicates the reference time-mean value for the control ensemble over the 100 year simulation (at zero).

reduced SAM index, rather than just a result. Zhou and Yu (2004) also show that there is a negative correlation between SST in the tropical Pacific and the SAM index. This indicates that the negative phase of the SAM may have been triggered through the surfacing of warmer intermediate waters in the tropical Pacific (Figures 5.3 and 5.5b).

Although the mechanisms described here, and shown in previous work, may account for the negative SAM index anomalies, it is also worth considering the state of the control climate. During years 11-30 the control simulation shows a strong positive phase for the SAM. The control SAM index peaks at ~ 20 years, when t -test analysis suggests that anomalies for EXP3 are significant. The strong negative anomalies seen for this experiment will then be influenced by the strong SAM in the control. For year 20, 8 out of 9 of the ensemble members show an increased pressure over Antarctica. SST anomalies in the tropical Pacific are positive in 6 out of 9 of the ensemble members at this same time. In the following section we show the results for the experiments with the varying

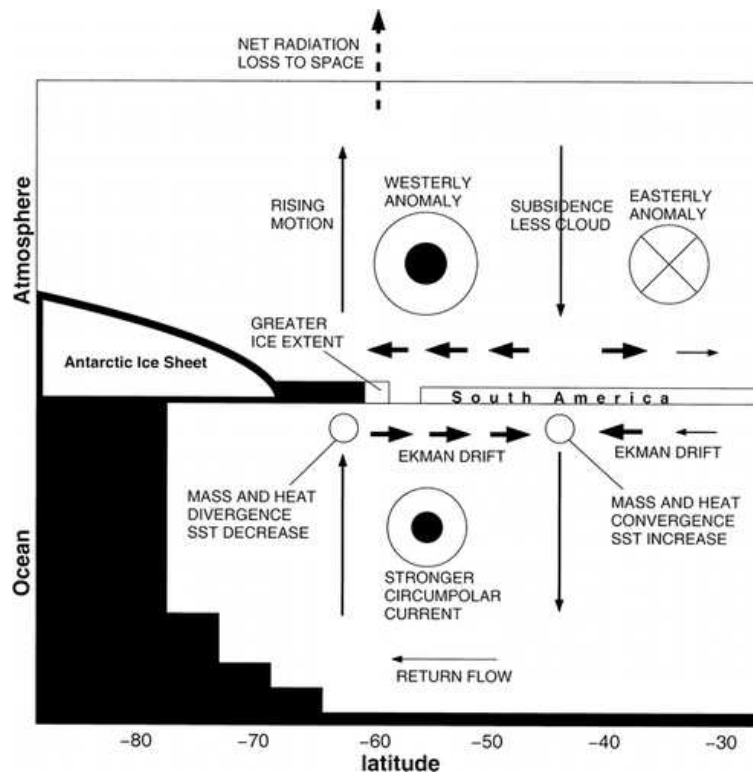


Figure 5.9: Schematic to illustrate the coupled ocean-atmosphere response to a positive phase of the SAM (Hall and Visbeck, 2002). For a negative phase of the SAM, the response pattern is the same, but with anomalies of the opposite sign and circulation patterns acting in the opposite direction.

initial ocean states. This alternative ensemble method does not show the same SAM response, supporting the suggestion that the response described here, although statistically significant, is likely due to the state of the control.

5.2.2 Response when varying initial ocean states

5.2.2.1 Where does the anomalous water go?

Within the first 10 years of EXP3b, the saline anomaly has spread to both the north and south of the initial perturbation region through advection and diffusion (Figure 5.7b). To the north, the anomaly is carried along the western boundary to the equatorial Pacific, where currents allow the warm, salty water to spread throughout the equatorial region. To the south, significant anomalies extend along the east coast of Australia. The anomaly is carried by the East Australian Current, from where it can then travel around the south of Australia. The location of these currents at the core AAIW depth (level 11 in HadCM3) is illustrated in Figure 5.6. As coastal Kelvin waves travel polewards along the eastern

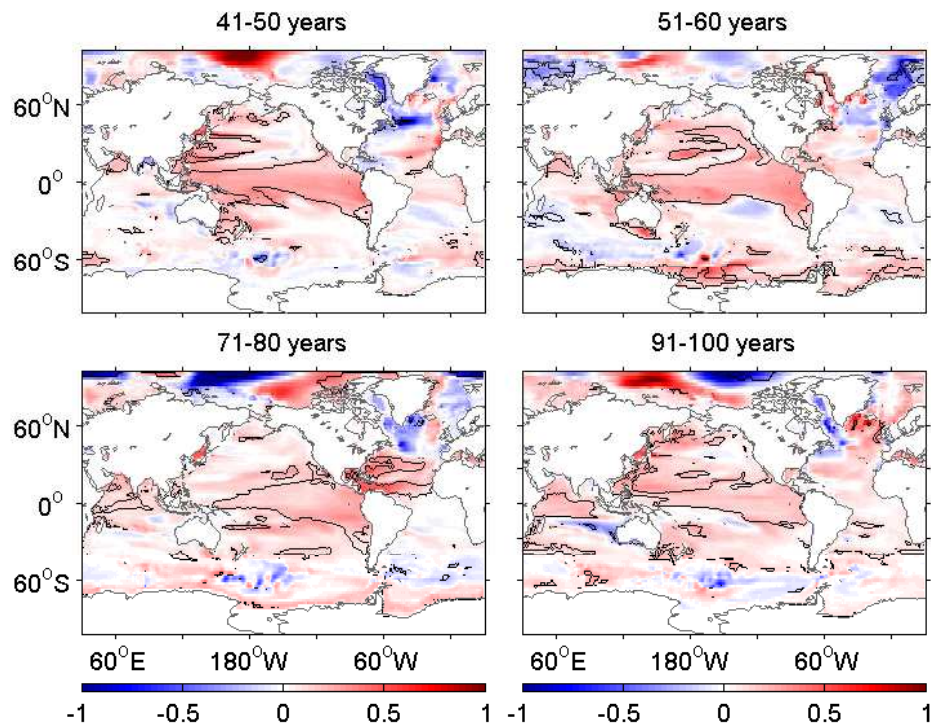


Figure 5.10: Decadal salt content anomalies (*EXP3b* – control) for years 41-50, 51-60, 71-80 and 91-100 [10^2 kg m^{-2}]. Contours show regions significant at the 95% confidence level.

boundaries of the ocean, positive anomalies also extend southwards along the coast of South America (Figure 5.7b).

As the simulation continues, the water mass spreads further north, and within 30 years, anomalies are seen extending along the western boundary of the North Pacific and in the region of the subpolar gyre (SPG) (Figure 5.7f). Anomalies persist in the North Pacific throughout the remainder of the simulation (Figure 5.10). For years 51-60, increased salt anomalies follow paths of recirculation in the subtropical gyre (STG). The anomaly also continues to recirculate in the South Pacific, however the largest area of significant anomalies remains in the tropical regions. By the end of the simulation, the vast majority of the Pacific basin has an increased salt content.

As well as spreading throughout the Pacific, both the Indian and Atlantic oceans have increased salt contents at the end of the simulation (Figure 5.10). The more saline water mass can enter the Indian Ocean from either the Indonesian Through-Flow or from the south of Australia (Figure 5.6). During the first 10 years, increased salt content can be found around both these entrance routes. The spread of water from the ITF into the Indian Ocean is most significant on levels 12-13 in HadCM3 (not shown). Significant salt

anomalies are found in the northwest section of the Indian basin for years 31-40 (Figure 5.7h) and persist in this region for the remainder of the simulation (Figure 5.10).

From the Indian Ocean, anomalies can enter the Atlantic around Cape Agulhas. Tracer release experiments carried out by Sen Gupta and England (2007b) show that anomalies in the southwest Pacific can rapidly be carried throughout the southern hemisphere basins, with the signal travelling westwards in to the Indian Ocean and then on to the Atlantic to the south of South Africa (see their Fig. 10e). Alternatively, as the anomalies spread in to the Southern Ocean, they can also be carried through Drake Passage with the ACC. Significant anomalies are found in the Atlantic sector of the Southern Ocean within 40 years (Figure 5.7h). After 50 years the majority of the Atlantic has an increased salt content, with positive anomalies extending in to the GIN Seas by the end of the simulation (Figure 5.10).

Figure 5.11 shows the total salt content at upper, intermediate and deep levels of the Pacific basin. Throughout the simulation, the upper levels of the Pacific have an increased salt content. At the same time, the salt content in the intermediate depths continues to decrease. This supports the suggestion that the anomalous water mass is upwelling to shallower depths through the course of the experiment, as well as being advected out of the Pacific. At the end of the simulation the upper and intermediate depths have salt content anomalies of 5.6×10^{14} kg and 1.18×10^{15} kg, equivalent to 18 % and 39 % of the initial perturbation (3.08×10^{15} kg), respectively. Just 4 % of the initial anomaly enters the deep levels of the basin. It is also worth noting that the spread seen in the ensemble members for the deep levels (14-20) arises from the drift in the model. In these deep levels, the drift leads to an increasing salinity with time. In total, 61 % of the initial salt perturbation remains in the Pacific after 100 years. This supports the fact that a significant proportion of the anomaly has spread to other regions of the world ocean. Globally, 78 % of the initial heat anomaly remains in the ocean after 100 years. This suggests that ~ 22 % may have been lost through contact with the atmosphere.

5.2.2.2 Anomalies at the sea surface

Throughout the experiment, there is an increased SSS in the equatorial Pacific (Figures 5.4 and 5.12). In the central equatorial Pacific, the mean SSS in the Niño 3.4 region (5° S-

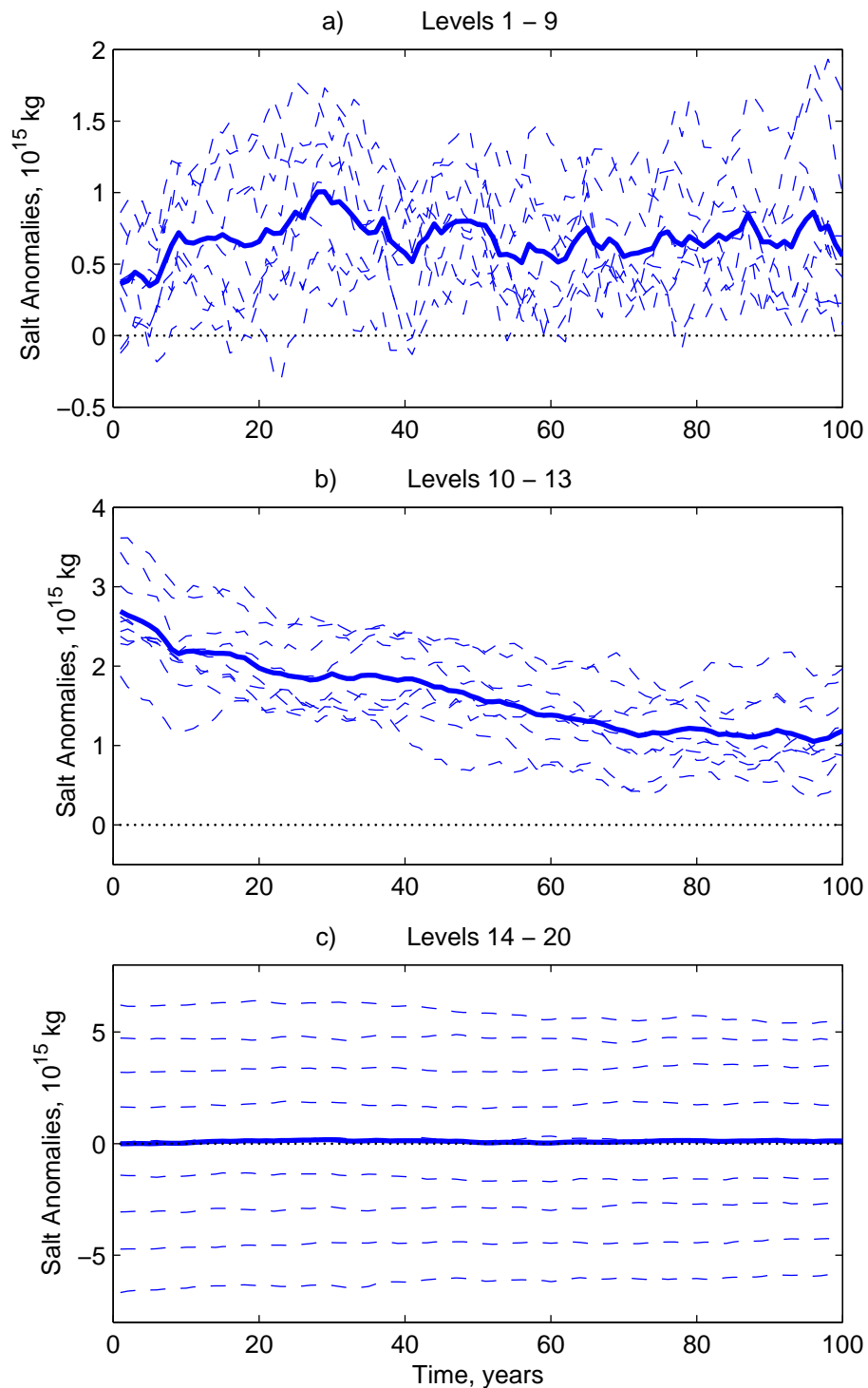


Figure 5.11: Total salt content anomalies in the Pacific, between $\sim 36^{\circ}\text{S}$ and 65°N , for depth levels (a) 1 – 9, $\sim 0 - 300$ m; (b) 10 – 13, $\sim 300 - 1500$ m; (c) 14 – 20, $\sim > 1500$ m. Solid lines show the ensemble mean anomalies (EXP3b – control); dashed lines show anomalies of individual EXP3b ensemble members minus the mean of the control ensemble.

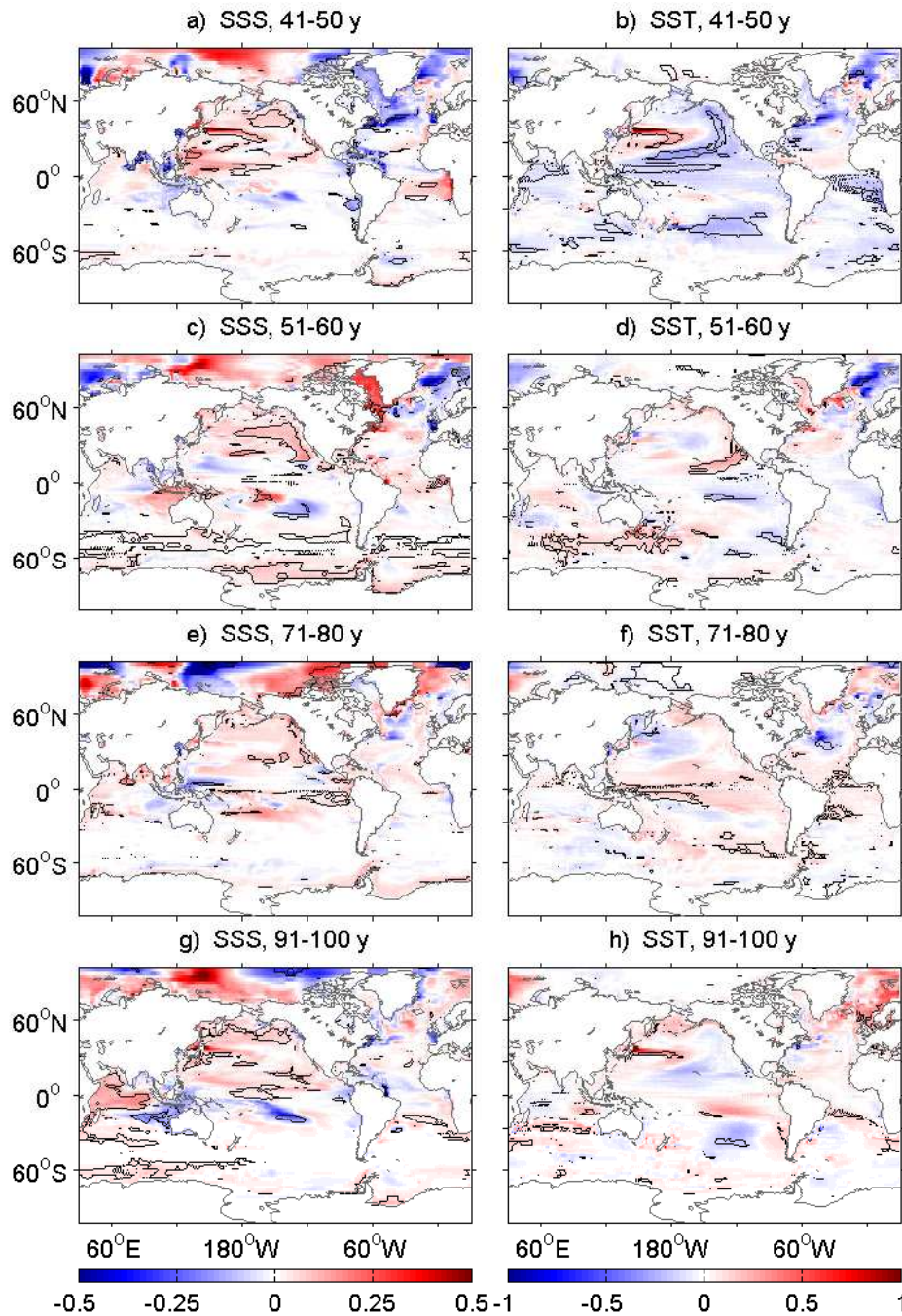


Figure 5.12: Decadal anomalies (EXP3b – control) for years 41-50, 51-60, 81-90 and 91-100. Figures a, c, e and g show sea surface salinity (SSS); b, d, f and h show sea surface temperature (SST) [$^{\circ}\text{C}$]. Contours show regions significant at the 95% confidence level.

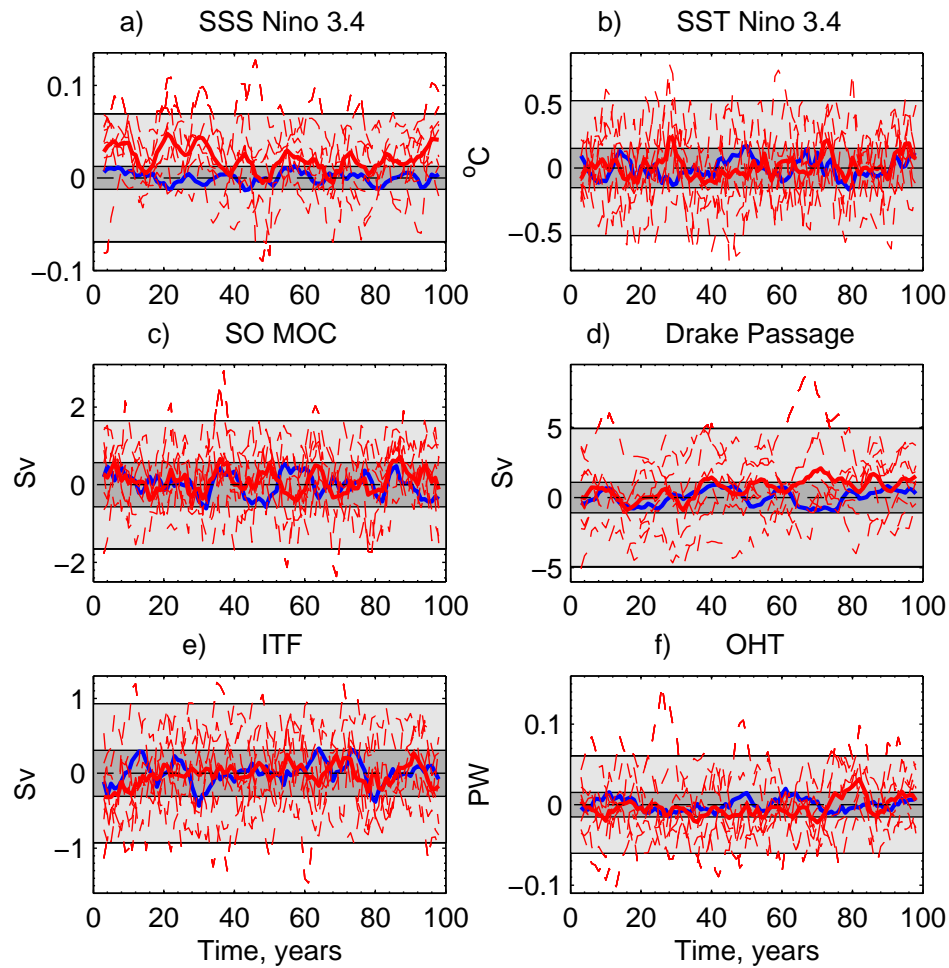


Figure 5.13: Absolute values of climate indices for EXP3b: a) mean sea surface salinity (SSS) in the Niño 3.4 index region (5°N - 5°S , 170°W - 120°W); b) mean sea surface temperature (SST) in the Niño 3.4 index region; c) strength of Southern Ocean meridional overturning circulation (SO MOC) : maximum overturning south of 30°S ; d) volume transport through Drake Passage; e) volume transport through the Indonesian Through-Flow (ITF); f) Northward ocean heat transport (OHT) at 26°N in the Atlantic. Light (dark) shaded area shows the 2σ (95%) spread of the control ensemble (mean) around the 100 year mean. Dashed (solid) red lines show the ensemble (mean) anomalies for EXP3b (EXP3b – time-mean of control). Blue line shows the mean of the control ensemble around the 100 year mean. Data are smoothed using a 5 year running mean. Dashed black line indicates the reference time-mean value for the control ensemble over the 100 year simulation (at zero).

5°N , 170° - 120°W) is increased throughout the simulation (Figure 5.13a). The anomalies in this region extend from the surface to depths of ~ 1500 m, showing that the anomalies may arise from the surfacing of AAIW. Along the equator, easterly winds lead to poleward Ekman transport of the surface layer, resulting in the upwelling of deeper waters.

Away from the equatorial regions, significant SSS anomalies are also found in the North Pacific (Figures 5.4 and 5.12). Significant anomalies are found along the western boundary and in the SPG within 30 years, corresponding with the arrival of significant

salt anomalies in these regions (Figure 5.7). From Figure 5.6, it can be seen that the MLD increases along the western boundary and into the Kuroshio Extension, allowing the perturbed AAIW to be brought to the surface as it is advected northwards. Isopycnals also begin to shoal to the north, allowing AAIW to move closer to the surface as it enters the SPG. As the water mass spreads throughout the basin, the surface salinity of the North Pacific remains increased to the end of the simulation (Figure 5.12). Upwelling is also known to occur along the eastern boundaries of ocean basins. In the North Pacific, the salinity anomalies along the eastern boundary extend from the surface to depths of 300 m, however few increased salinity anomalies are found along the eastern boundary of the South Pacific. As the anomalous water mass circulates in the South Pacific STG, and portions are lost to the south of Australia or through Drake Passage with the ACC, this reduces the volume of anomalous water that returns northwards along the eastern boundary.

Although it has been shown that upwelling of the perturbed water mass occurs in a number of regions, the anomalous heat content does not appear to result in significant SST anomalies (Figures 5.3 and 5.12). Figure 5.13b shows the mean SST for the Niño 3.4 index region. Unlike the SSS, there is no significant shift in temperature through the experiment. This is contrary to the results seen for EXP3, which saw a shift in the SST for the first 30 years of the experiment. For the first 10 years of EXP3b, there is an increased SST for the Niño 3.4 region, which is accompanied by a decreased heat flux in the atmosphere-to-ocean direction (Figures 5.13b and 5.14). However, there is no trend in the heat flux anomalies that persists through the course of the simulation. Therefore, although the warmer water mass may be surfacing, the anomalous heat content may not be great enough to overcome the internal variability and cause a significant change in the ocean-atmosphere heat flux on decadal timescales.

In the extra-tropical Pacific, some SST anomalies coincide with SSS anomalies of the same sign, however this is not always the case. For years 31-50, there is an increased SSS throughout the majority of the North Pacific (Figures 5.4h and 5.12a), however the SST field shows large regions of cooling surrounding warm centres in the western side of the North Pacific (Figures 5.3h and 5.12b). This SST pattern is characteristic of the Pacific Decadal Oscillation, with anomalies of this sign corresponding to the negative phase

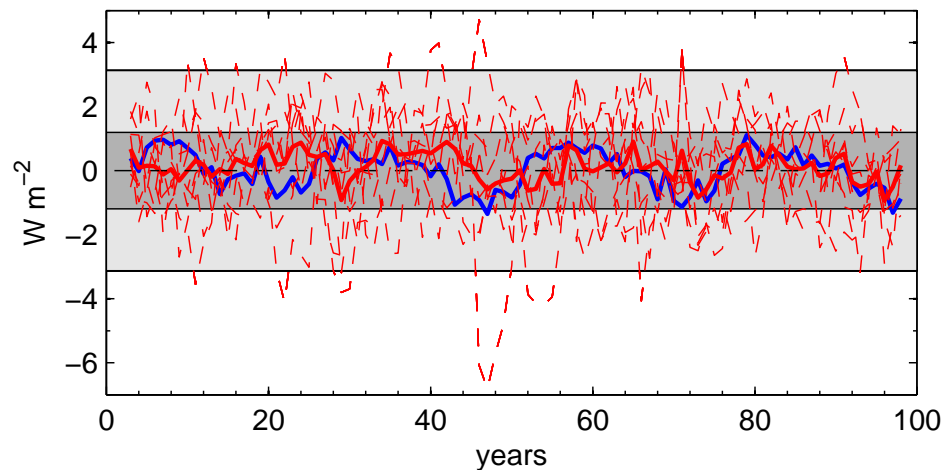


Figure 5.14: Mean ocean-atmosphere heat flux in the Niño 3.4 index region (5°N - 5°S , 170 - 120°W). Positive values indicate heat flux in the atmosphere-to-ocean direction. Light (dark) shaded area shows the 2σ (95%) spread of the control ensemble (mean) around the 100 year mean. Dashed (solid) red lines show the ensemble (mean) anomalies for EXP3b (EXP3b – time-mean of control). Blue line shows the mean of the control ensemble around the 100 year mean. Data are smoothed using a 5 year running mean. Dashed black line indicates the reference time-mean value for the control ensemble over the 100 year simulation (at zero).

(Mantua *et al.*, 1997). While some of the increased SSTs may be due to warmer waters surfacing, surface fluxes show that the cooling is driven by the overlying atmosphere, and not a result of internal ocean processes. These SST anomalies will be discussed in further detail in Section 5.2.2.3.

Outside the Pacific, significant SSS anomalies are found in the Southern Ocean during the latter years of the experiment, in particular for years 51-60 and 91-100 (Figures 5.12c,g). Regions of increased SST can also be found during this time (Figure 5.12d,h). As isopycnals shoal towards the south, anomalous AAIW may be brought to the surface in the Southern Ocean. The warm region found south of Australia for years 51-60 coincides with regions of deep MLD (Figure 5.6), where anomalies may be brought to the surface from depths > 300 m. As described for EXP3 (Section 5.2.1), changes in SST around the Southern Ocean may also be attributed to the Southern Ocean (SO) meridional overturning circulation. Prior to year 50, there is an increased SO MOC strength, followed by a decrease after year 50 (Figure 5.13c). For years 40-60 there is also a shift from positive to negative phase in the SAM index, indicating a changes in wind stress over the Southern Ocean (Figure 5.15a). For years 80-100, there is also an increase in both the SO MOC strength and SAM index. During the positive phase of the SAM, the increased wind stress

leads to a increased Ekman transport of fresh AASW to the north (Figure 5.9). An increased SO MOC will also result in greater volumes of warm, salty deep waters moving polewards and upwelling in the Southern Ocean. Both these effects will contribute to the increased salinity found south of 60°N , around the Antarctic coast (Figure 5.12). The increased poleward transport of deep waters also results in salt content anomalies in the Southern Ocean (Figure 5.10). The resulting density changes leads to an increased tilt in isopycnals towards the south. Along with the increased wind stress, this leads to an increased Drake Passage transport (DPT) during the latter half of the simulation (Figure 5.13d). The atmospheric anomalies mentioned here will be discussed further in Section 5.2.2.3.

In the Indian Ocean, a large area of significant anomalies is found at the surface at the end of the simulation (Figure 5.12g,h). Anomalies around 30°S show the same sign for both SSS and SST, and extend from the surface to > 300 m depth. However, the stronger salinity anomalies further north do not coincide with SST anomalies of the same sign, suggesting that they do not result from surfacing AAIW. Patterns of warm, fresh anomalies in the east and cool, salty water in the northwest are characteristic of the Indian Ocean Dipole (IOD) (Saji *et al.*, 1999). This pattern of climate variability is associated with changes in atmospheric circulation over the basin and will be described in further detail in Section 5.2.2.3. The large region of significance for SSS anomalies results from 7 out of the 9 ensemble members being in the same (negative) phase of the IOD, when compared with the mean of the control ensemble. There does not appear to be a relation with anomalous ITF transport from the Pacific (Figure 5.13e).

In the Atlantic, there is an increased SST and SSS through the basin towards the end of the simulation (5.12), coinciding with the increased salt content seen in Figure 5.10. As the warm, saline AAIW moves northwards through the Atlantic, there is a mean increase in the meridional ocean heat transport (OHT) after 70 years (Figure 5.13f). However, there is no significant increase in the Atlantic MOC when compared with the control ensemble (not shown).

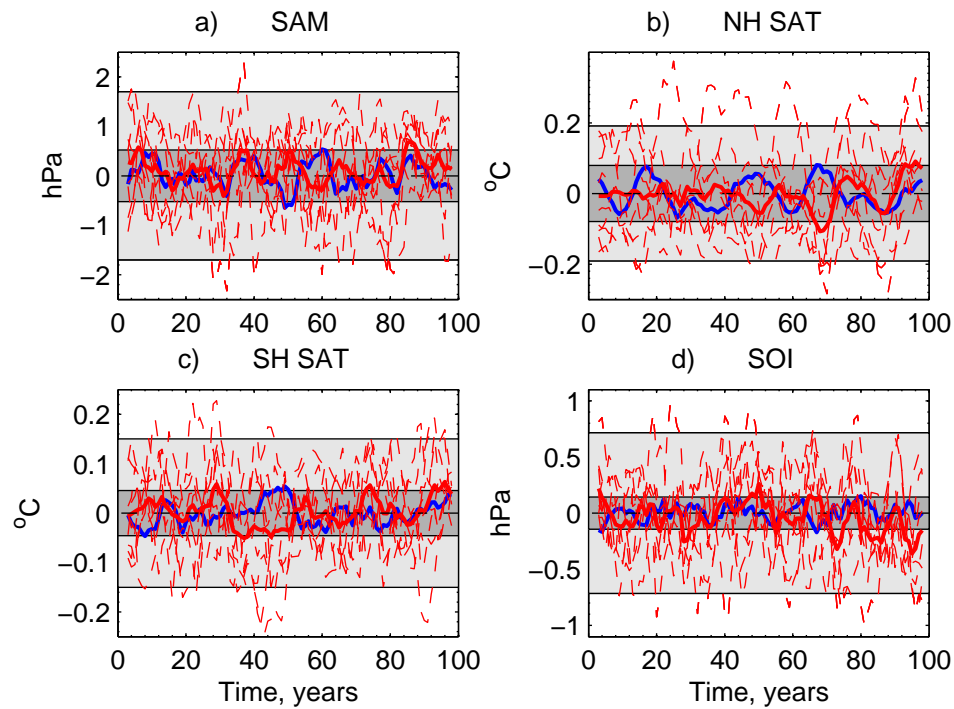


Figure 5.15: Absolute values of climate indices for EXP3b: a) Southern Annular Mode (SAM) : annual MSLP difference between 40 and 65°S; b) mean Northern Hemisphere (NH) surface air temperature (SAT) c) mean Southern Hemisphere (SH) SAT; d) Southern Oscillation Index (SOI) : annual MSLP difference from Tahiti-Darwin. Light (dark) shaded area shows the 2σ (95%) spread of the control ensemble (mean) around the 100 year mean. Dashed (solid) red lines show the ensemble (mean) anomalies for EXP3b (EXP3b – time-mean of control). Blue line shows the mean of the control ensemble around the 100 year mean. Data are smoothed using a 5 year running mean. Dashed black line indicates the reference time-mean value for the control ensemble over the 100 year simulation (at zero).

5.2.2.3 Atmospheric response

Unlike EXP3, there is no significant response in the SAM index for EXP3b (Figure 5.15a). This can be attributed to the lack of significant SST anomalies in both the tropical and extra-tropical Pacific during the first 20 years (Figure 5.3). Although there is little significance in the SST anomalies, there are positive SAT anomalies for both the NH and SH during the first 10 years (Figures 5.15b,c). The SAT anomalies correlate predominantly with the changes in SST. Positive SAT anomalies are found for years 1-30, however after this time, the SH SAT decreases, and after 40 years both the NH and SH have a decreased mean SAT. For the same period there is a reduction in SST, with a negative phase of the PDO shown in the North Pacific (Mantua *et al.*, 1997). The PDO pattern resembles the extra-tropical response to ENSO, with the atmospheric bridge causing anomalous heat fluxes due to changes in the Aleutian Low. It has been shown that anomalies can persist on

decadal time scales due to the 'reddening' of ENSO variability, through the re-emergence of SST anomalies in subsequent winters (Newman *et al.*, 2003). Collins *et al.* (2001) also show that in HadCM3, the power spectrum for PDO variability gives no indication of cyclic variability, and anomalies in the North Pacific are correlated with tropical Pacific variability. The surface flux anomalies for this experiment show that the warm region in the northwest Pacific is partly forced by the overlying atmosphere, and regions of cooler SST are releasing more heat to the atmosphere. Therefore, the SST pattern during this decade may be a result of changes in overlying atmosphere rather than oceanic processes.

For years $\sim 42-52$ there is a positive phase of the SAM, with significant anomalies around year 50. This is followed by a negative phase during years $\sim 52-60$. As mentioned in Section 5.2.1, changes in the SAM may be triggered by SST anomalies in the tropical Pacific, so the MSLP anomalies seen over the Southern Ocean may be a response to SST anomalies during years 40-60 (Figure 5.23). These SAM anomalies lead to corresponding anomalies in the Deacon Cell (SO MOC) for years 40-60 (Figure 5.13c), however they are not significant.

Towards the end of the simulation, there is a mean increase for the SAM index, NH SAT and SH SAT, corresponding with an average increase in SST (Figures 5.15 and 5.12). As there is an increased SST around the extra-tropical SH, this may lead to the increased SAM index. This change in mean sea level pressure (MSLP) and resulting wind patterns contributes to the increased DPT towards the end of the simulation (Figure 5.13d).

The Southern Oscillation Index (SOI) is related to ENSO variability in the Pacific, with a negative (positive) SOI corresponding to El Niño (La Niña) events. For EXP3b there is little significance in the SOI anomalies (Figure 5.15d), consistent with the lack of significant anomalies for the Niño 3.4 SST index (Figure 5.13b). However, there is a tendency for more negative SOI phases towards the end of the simulation, corresponding with warmer temperatures in the equatorial Pacific - El Niño events.

For years 91-100, the strong SSS anomalies in the Indian Ocean (Figure 5.12g) are consistent with a negative phase of the IOD. Saji *et al.* (1999) describe the IOD as a pattern of ENSO-like variability in the Indian Ocean, where a difference in SST between the east and west of the basin is driven by coupled air-sea interactions. These SST anomalies are shown to be linked with anomalies in precipitation and wind stress, leading to

changes in the thermocline and resultant ocean circulation patterns. The Indian Ocean is known to be strongly influenced by ENSO variability, however this mode is shown to vary independently (Saji *et al.*, 1999). In the case observed here for years 91-100, there is a region of warmer, fresher water in the eastern side of the basin, and cooler, saltier water to the west (Figure 5.12g-h). Although the IOD is defined by SST variability, here the SSS anomalies are stronger and more significant. SSS anomalies persist throughout this decade, however significant SST anomalies do not, with years 97-99 being dominated by ENSO variability (Figure 5.15d). As a result, the pattern of atmospheric anomalies is not completely consistent with those observed (Saji *et al.*, 1999). Anomalous easterly wind stress anomalies are observed over the region of warmer, fresher ocean in the south Indian basin, however positive (westerly) wind stress anomalies are seen along the equator for this decadal mean (not shown). Spencer *et al.* (2005) show that while HadCM3 does reproduce the key features of SST variability for the IOD, the poor vertical resolution of the ocean model leads to anomalies persisting and reinvigorating in following years. Therefore, the SSS anomalies seen in the Indian Ocean for this simulation are not likely to be a realistic response.

5.3 Response to cooler, fresher AAIW

5.3.1 Where does the anomalous water go?

Within the first 10 years, the fresher AAIW is seen to have spread to both the north and south in the Pacific (Figure 5.16). Figure 5.6 shows the major currents at the core AAIW depth. To the south, the anomaly is carried with the East Australian Current. As seen in the Atlantic (Chapter 3), the speed of transport can be accounted for by advective timescales, due to currents of $> 1 \text{ cm s}^{-1}$ at depths $\sim 500 \text{ m}$ (core depth of AAIW). North of the perturbed region, AAIW is carried to the equatorial regions as it travels with the western boundary current and circulates in the South Equatorial Gyre. Along the eastern boundary of the South Pacific, coastal Kelvin Waves also allow a southward spread of the fresh anomaly.

As the simulation continues, the fresher water mass continues to spread northwards as it is carried with the North Pacific STG. Fresh anomalies are found in the STG through

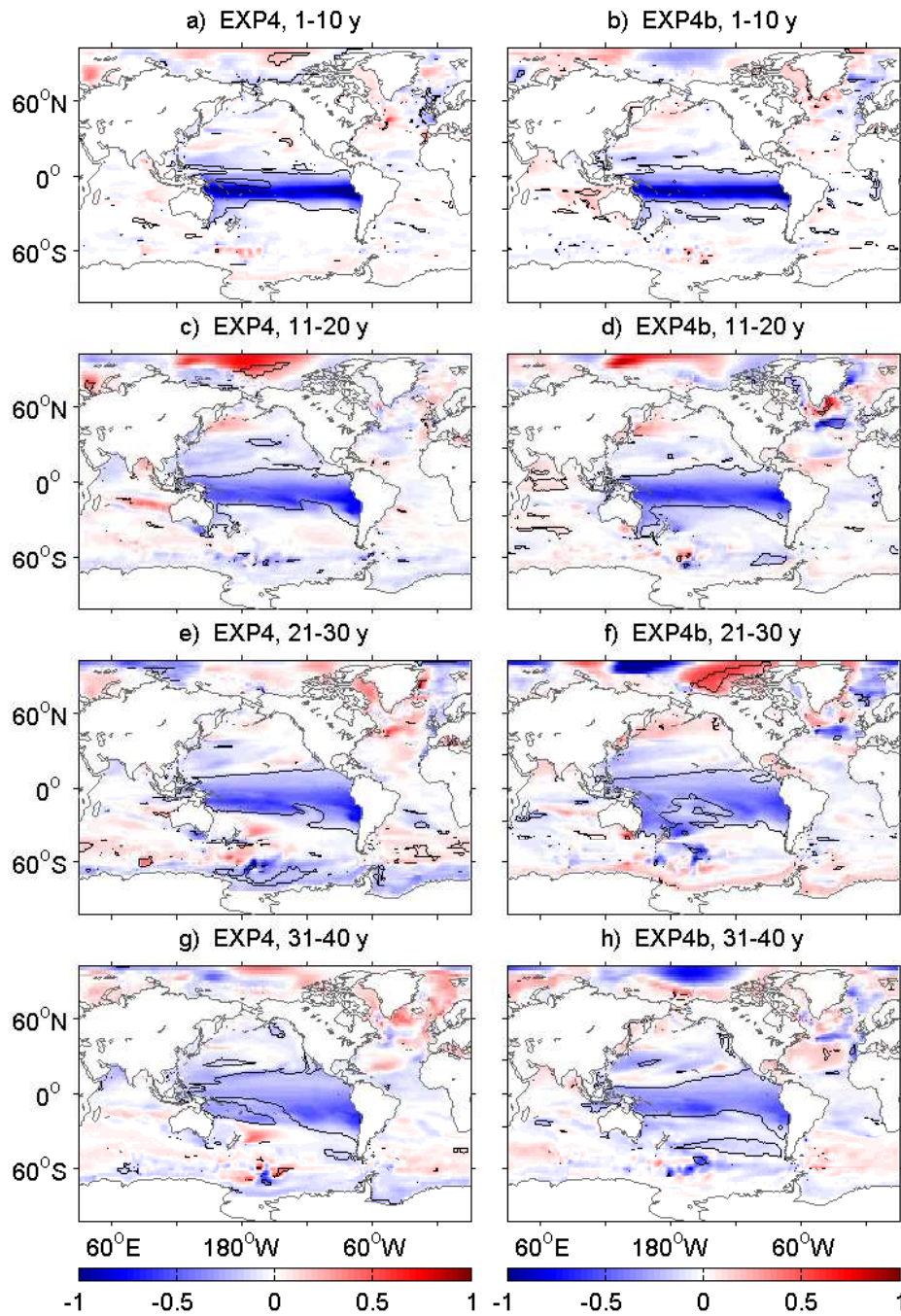


Figure 5.16: Decadal salt content anomalies ($EXP - control$) for the first 40 years [10^2 kg m^{-2}]. Figures a, c, e and g show anomalies for EXP4; b, d, f and h show anomalies for EXP4b. Contours show regions significant at the 95% confidence level.

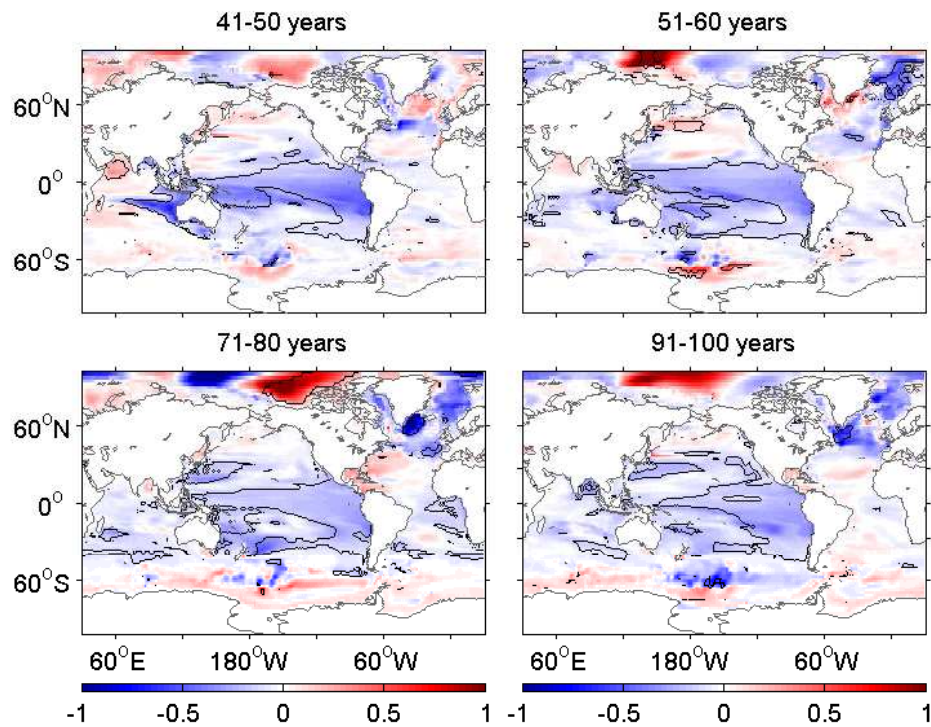


Figure 5.17: Decadal salt content anomalies (*EXP4b* – control) for years 41-50, 51-60, 71-80 and 91-100 [10^2 kg m^{-2}]. Contours show regions significant at the 95% confidence level.

the experiment, however there are few regions of significance in the early stages of the experiment (Figure 5.16). However, after 70 years there is a region of significantly decreased salt content in the western side of the North Pacific basin and for years 91-100 the significant anomalies follow the Kuroshio Extension and the path of recirculation within the gyre (Figure 5.17). Few fresh anomalies are found north of the Kuroshio Extension, suggesting that little of the water mass is carried further north in to the subpolar gyre. Although some fresh anomalies can be seen to extend along the western coast of North America, for example in years 51-60 of Figure 5.17.

To the south, significant salt content anomalies remain in the South Pacific as the fresher AAIW recirculates in the STG. However, as AAIW is carried south with the East Australian Current, a portion of the anomalous water mass is carried eastwards in to the Indian Ocean. This can be seen for both *EXP4* and *EXP4b* in years 31-40 (Figure 5.16). For years 41-50, a region of significant freshening is found in the Indian Ocean. The anomalous water mass can also be seen to enter through the ITF. From years 11-20, the anomalous salt content can be seen passing through this channel (Figure 5.16d). By the end of the simulation, the majority of the Indian Ocean has a reduced salt content (Figure

5.17d), and the anomalous water mass has spread through to the Atlantic.

Figure 5.18 shows the total salt content at upper, intermediate and deep levels of the Pacific basin (from $\sim 45^{\circ}\text{S}$ - 65°N) for EXP4b. As the water mass spreads within the Pacific it can be seen that whilst a portion of the anomaly enters the upper 9 levels of the ocean, the majority of the water mass remains at intermediate depths. At the end of the simulation, there is a salt content anomaly of -1.51×10^{15} kg in levels 10-13 of HadCM3, equivalent to 53% of the initial perturbation. Although the mean salt content in the upper levels remains lower than the control simulation, the remaining anomaly after 100 years is equivalent to just 8% of the initial perturbation, and 12% enters the deep levels of the ocean. In total, the Pacific has a salt and heat anomaly of -2.10×10^{15} kg and -3.82×10^{22} J at the end of the simulation, equivalent to 73 % and 63 % of the initial perturbation respectively. This suggests that 27% of the anomaly has been lost to other regions of the world ocean. The lower heat content anomaly is also consistent with ~ 10 % of the anomaly coming into contact with the atmosphere (Figure 5.11), and gaining heat through anomalous heat fluxes.

In general, the spread of anomalous AAIW in the Pacific is similar for EXP4 and EXP4b (Figure 5.16). The major region where differences occur is the Southern Ocean. For EXP4 there is a region of decreased salt content around Antarctica, however EXP4b sees an increased salt content in this region. These anomalies will be discussed in further detail in Section 5.3.3.

5.3.2 Anomalies at the ocean surface

Significant sea surface salinity (SSS) anomalies can be found in the equatorial Pacific during the first 10 years of EXP4b (Figure 5.19b). These negative anomalies extend from the surface to intermediate depths, suggesting that the anomalous AAIW is surfacing in this region. Along the Equator, upwelling occurs as a result of easterly winds driving Ekman transport away from the Equator. As more AAIW spreads into the equatorial regions, this allows cooler, fresher water to continue to surface. For the first 50 years, significant fresh anomalies are found in the equatorial regions for EXP4b, and for EXP4, significant anomalies can also be found for years 21-40 (Figure 5.19). For the central equatorial Pacific, the Niño 3.4 index region shows a decreased mean SSS throughout the

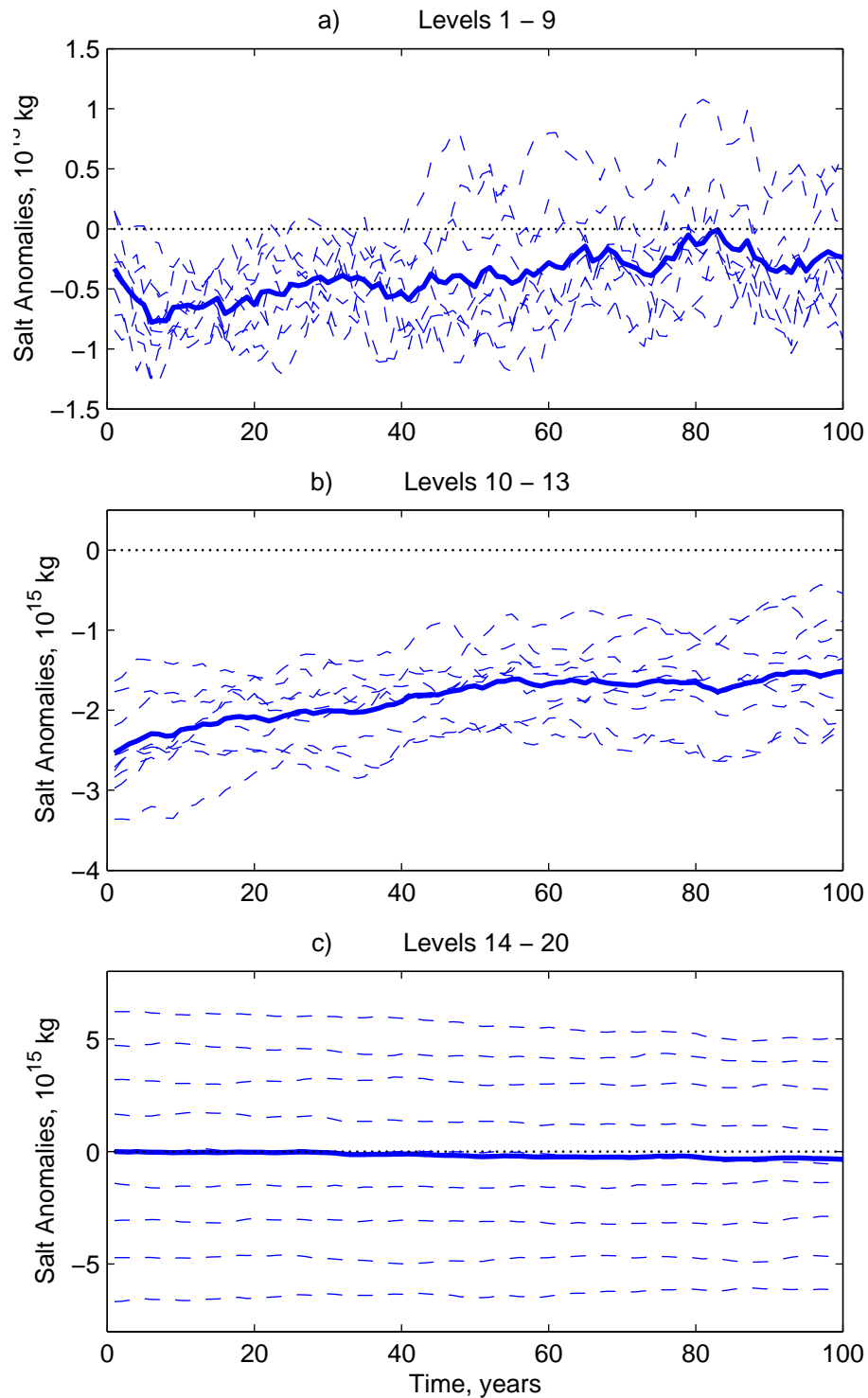


Figure 5.18: Total salt content anomalies in the Pacific, between $\sim 36^{\circ}\text{S}$ and 65°N , for depth levels (a) 1 – 9, $\sim 0 - 300$ m; (b) 10 – 13, $\sim 300 - 1500$ m; (c) 14 – 20, $\sim > 1500$ m. Solid lines show the ensemble mean anomalies (EXP4b – control); dashed lines show anomalies of individual EXP4b ensemble members minus the mean of the control ensemble.

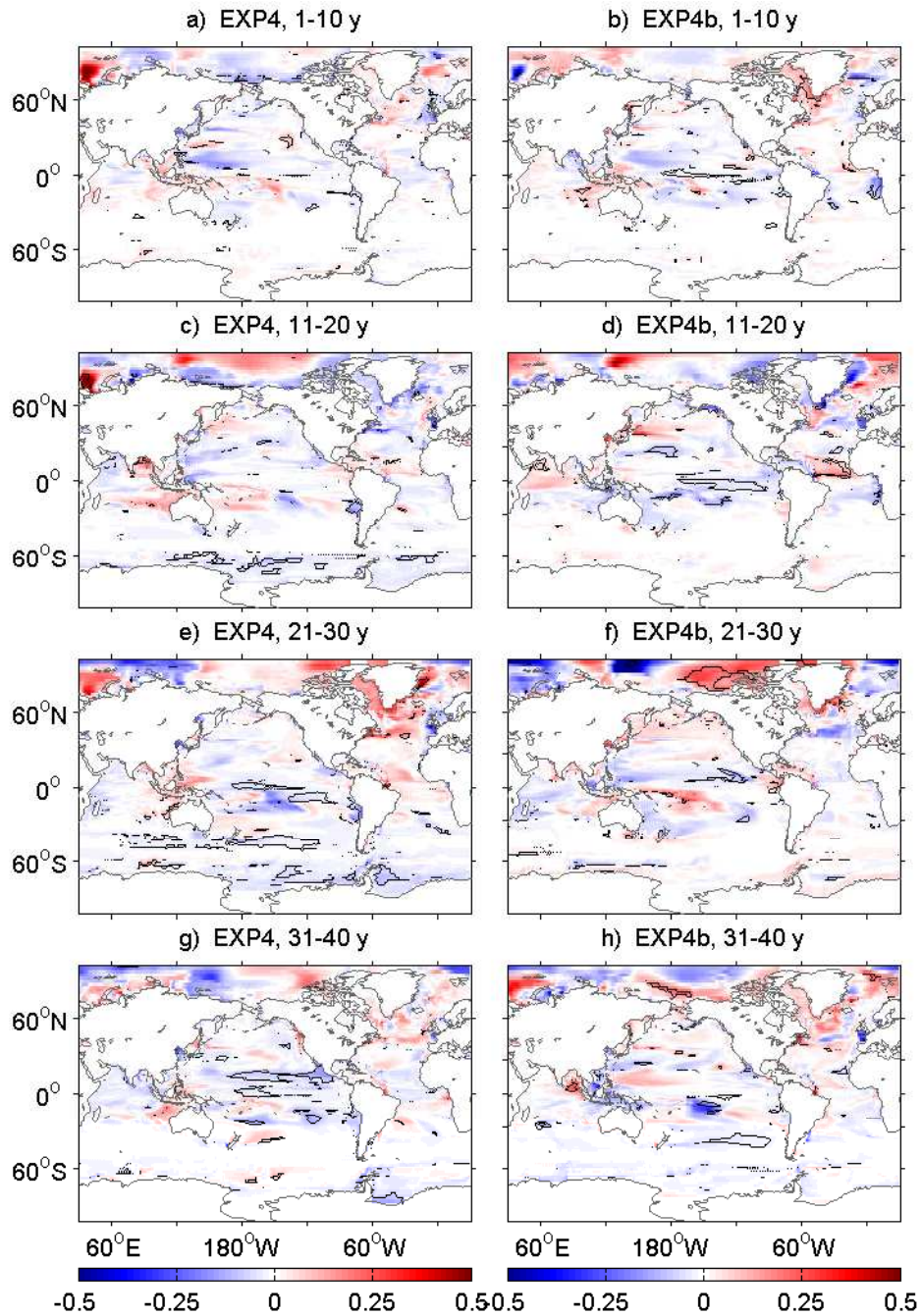


Figure 5.19: Decadal sea surface salinity anomalies (EXP – control) for the first 40 years. Figures a, c, e and g show anomalies for EXP4; b, d, f and h show anomalies for EXP4b. Contours show regions significant at the 95% confidence level.

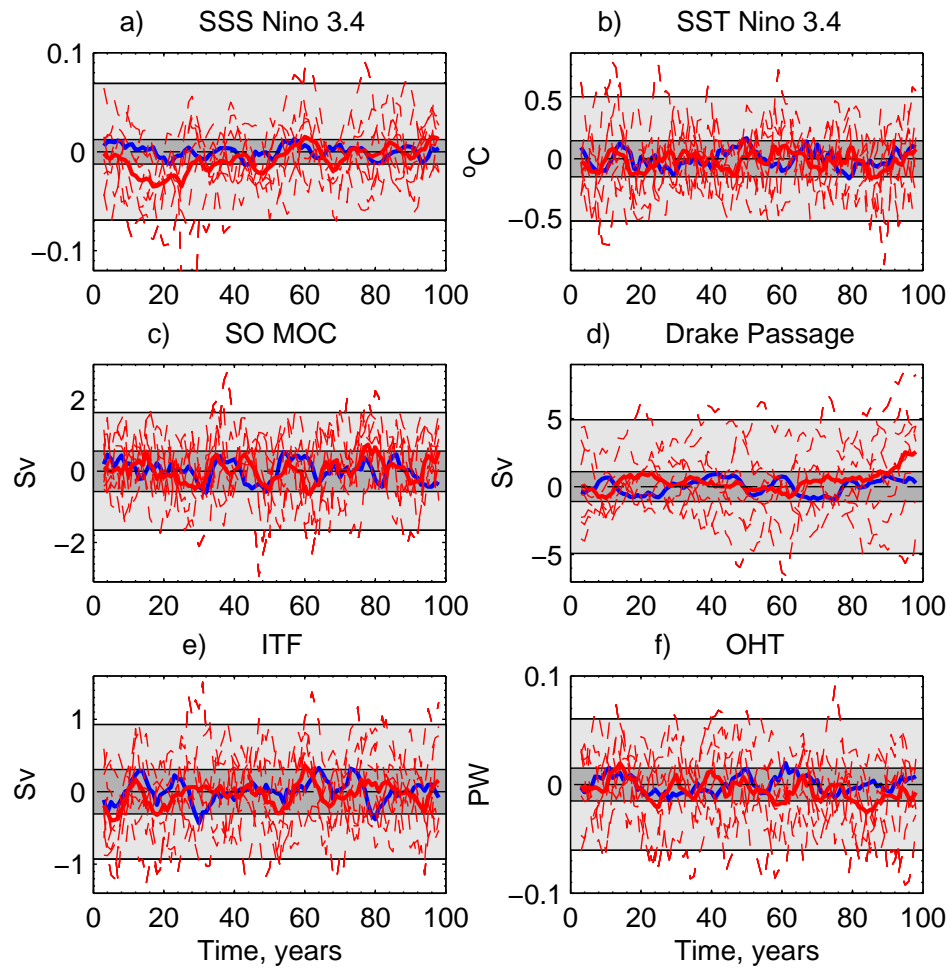


Figure 5.20: Absolute values of climate indices for EXP4b: a) mean sea surface salinity (SSS) in the Niño 3.4 index region (5°N - 5°S , 170 - 120°W); b) mean sea surface temperature (SST) in the Niño 3.4 index region; c) strength of Southern Ocean meridional overturning circulation (SO MOC) : maximum overturning south of 30°S ; d) volume transport through Drake Passage; e) volume transport through the Indonesian Through-Flow (ITF); f) Northward ocean heat transport (OHT) at 26°N in the Atlantic. Light (dark) shaded area shows the 2σ (95%) spread of the control ensemble (mean) around the 100 year mean. Dashed (solid) red lines show the ensemble (mean) anomalies for EXP4b (EXP4b – time-mean of control). Blue line shows the mean of the control ensemble around the 100 year mean. Data are smoothed using a 5 year running mean. Dashed black line indicates the reference time-mean value for the control ensemble over the 100 year simulation (at zero).

first 40 years in EXP4b, however after this time the salinity recovers and there is no trend in the sign of anomalies towards the end of the simulation (Figure 5.20a). Upwelling is also known to occur along eastern boundaries of ocean basins. Near the coast of South America, regions of decreased salinity can be found for both EXP4 and EXP4b throughout the majority of the simulation, albeit not significant (Figures 5.19 and 5.23).

Although it is clear that the anomalous water mass is surfacing in these regions, there are few significant SST anomalies. In the equatorial Pacific there is a reduced SST during

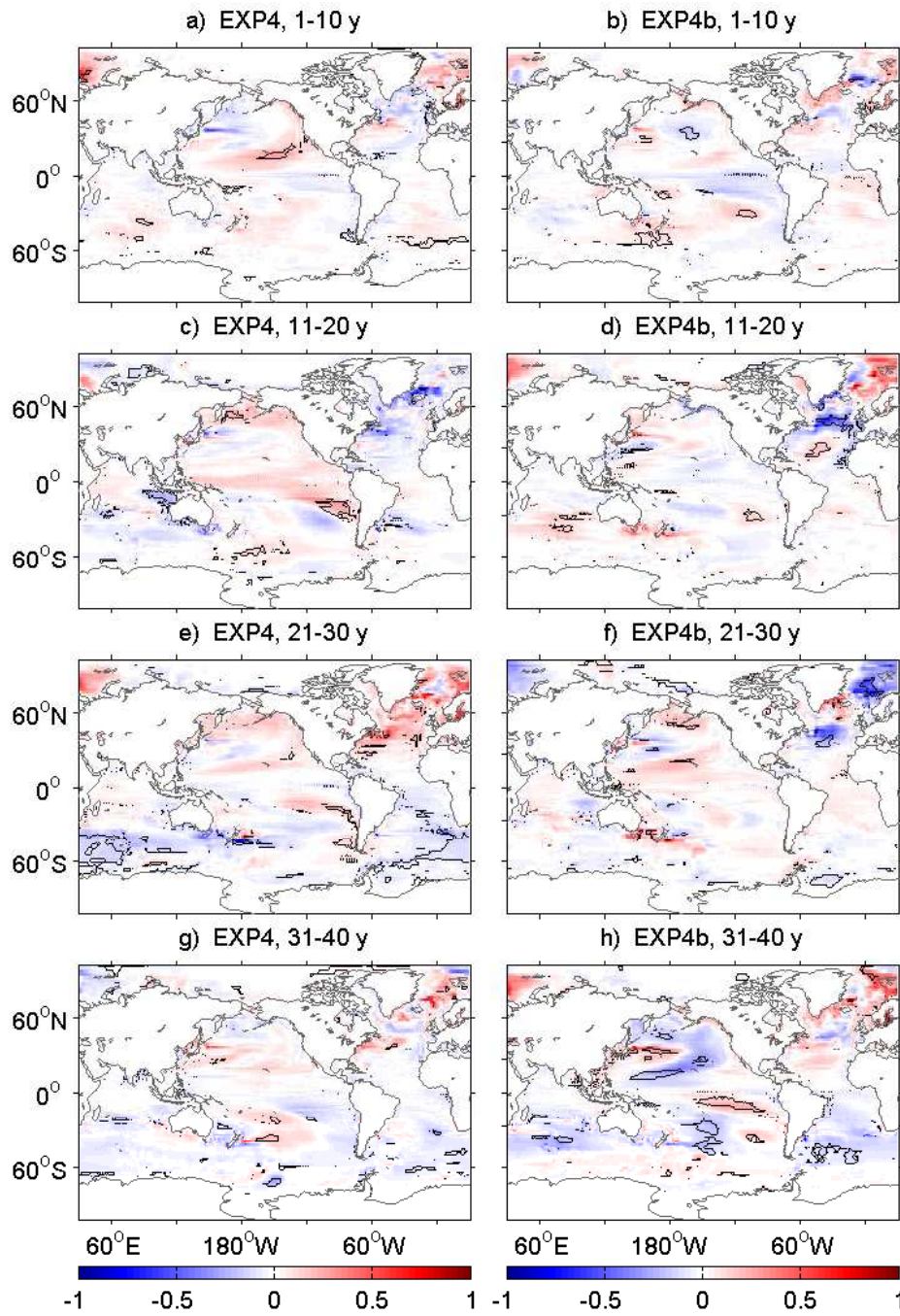


Figure 5.21: Decadal sea surface temperature anomalies ($EXP - control$) for the first 40 years [$^{\circ}C$]. Figures a, c, e and g show anomalies for EXP4; b, d, f and h show anomalies for EXP4b. Contours show regions significant at the 95% confidence level.

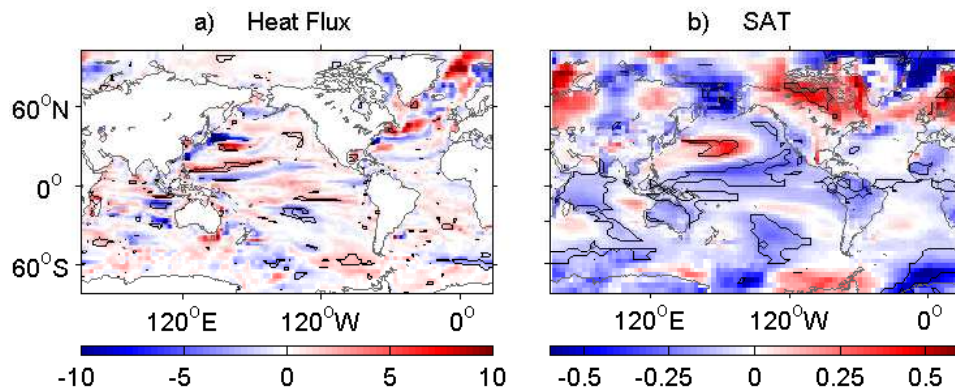


Figure 5.22: Decadal mean anomalies (*EXP4b* – control) for years 41-50: a) ocean-atmosphere heat flux (positive anomalies indicate heat flux in the atmosphere-to-ocean direction) [W m^{-2}]; b) surface air temperature (SAT) [$^{\circ}\text{C}$]. Black contours show anomalies significant at the 95 % confidence level.

the first 10 years, however there are few regions of significance (Figure 5.21). Figure 5.20b also shows that although the mean SST for the Niño 3.4 region shows an initial decrease, there is no trend in the sign of anomalies as the simulation continues. This is likely due to the large internal variability in the equatorial Pacific for the model.

Significant SST anomalies can be found in the extratropical Pacific for years 31-40, 41-50 and 91-100. The patterns of anomalies found during these decades are characteristic of the PDO, with the negative anomalies surrounding a warm centre in the west corresponding to a negative phase of the oscillation (Mantua *et al.*, 1997). These temperature anomalies are confined to the upper layers of the ocean (~ 500 m) and do not coincide with salinity anomalies of the same sign. Surface heat flux anomalies also suggest that the SST is partly forced by the overlying atmosphere, with positive anomalies coinciding with warm SST in the west (Figure 5.22a). These anomalies will then be discussed further in Section 5.3.3.

Outside the Pacific, a significant cooling and freshening is found in the Southern Ocean for years 21-30 in *EXP4* (Figures 5.19e and 5.21e), suggesting surfacing of anomalous AAIW. However, the significant anomalies do not always coincide and are similar to those seen in *EXP3* for the negative phase of the SAM (Section 5.2.1). These anomalies are then likely to be influenced by the initial conditions used in this experiment. For *EXP4b*, a reduction in SSS and SST is seen after 30 years, with significant SSS anomalies in the Pacific sector (Figures 5.19h and 5.21h). Shoaling of isopycnals to the south can allow the cooler, fresher water to be brought to the surface layers as it is advected into the

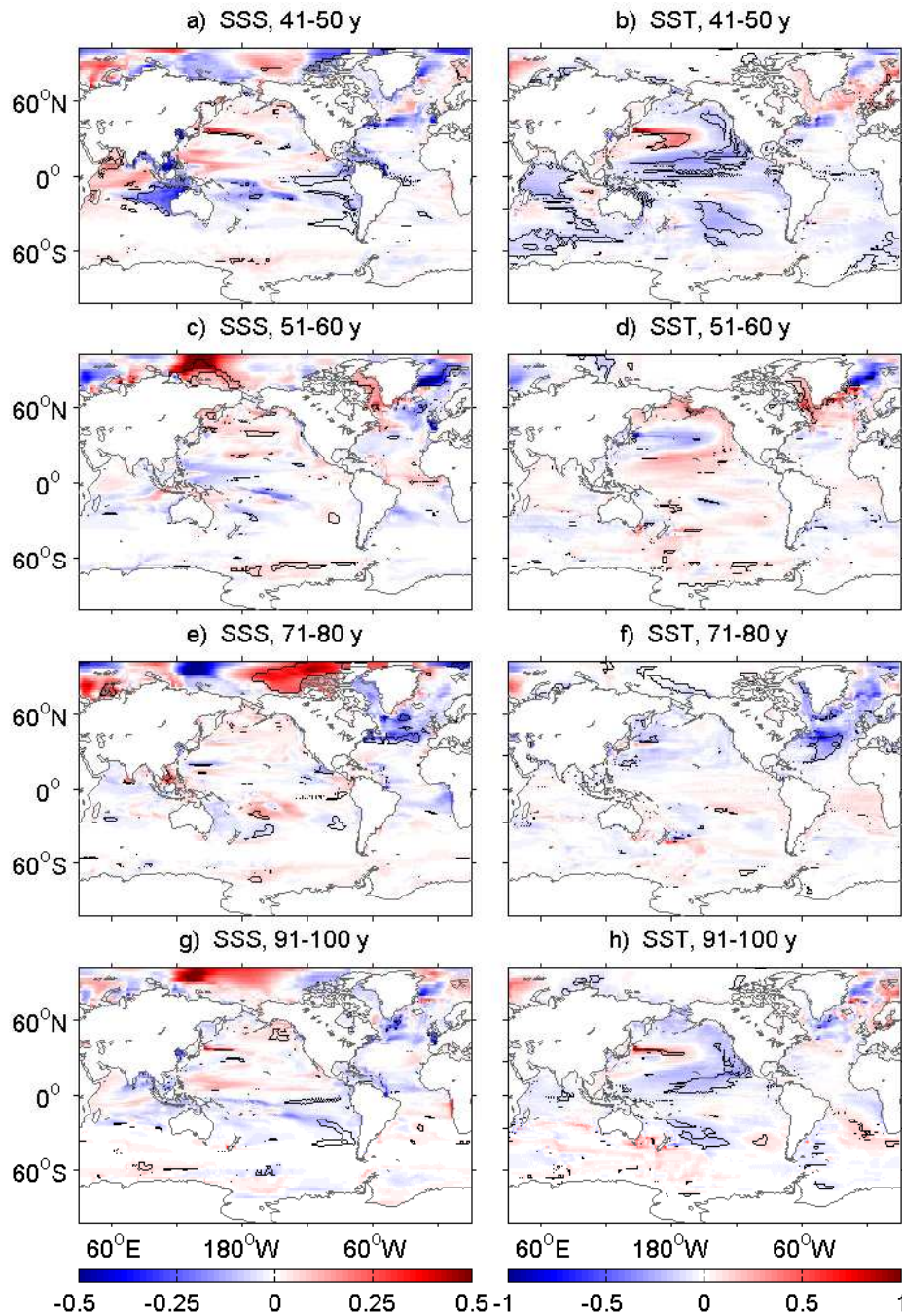


Figure 5.23: Decadal anomalies (EXP4b – control) for years 41-50, 51-60, 81-90 and 91-100. Figures a, c, e and g show sea surface salinity (SSS); b, d, f and h show sea surface temperature (SST) [$^{\circ}\text{C}$]. Contours show regions significant at the 95% confidence level.

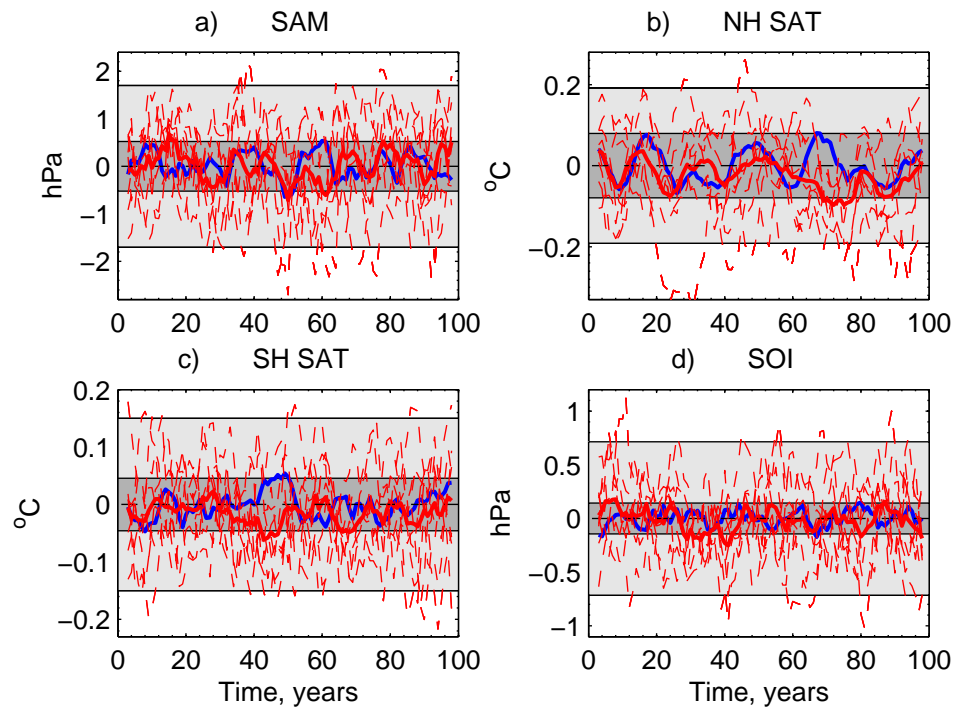


Figure 5.24: Absolute values of climate indices for EXP4b: a) Southern Annular Mode (SAM) : annual MSLP difference between 40 and 65°S; b) mean Northern Hemisphere (NH) surface air temperature (SAT) c) mean Southern Hemisphere (SH) SAT; d) Southern Oscillation Index (SOI) : annual MSLP difference from Tahiti-Darwin. Light (dark) shaded area shows the 2σ (95%) spread of the control ensemble (mean) around the 100 year mean. Dashed (solid) red lines show the ensemble (mean) anomalies for EXP4b (EXP4b – time-mean of control). Blue line shows the mean of the control ensemble around the 100 year mean. Data are smoothed using a 5 year running mean. Dashed black line indicates the reference time-mean value for the control ensemble over the 100 year simulation (at zero).

Southern Ocean. Negative SSS anomalies continue to be found around the SH oceans as the simulation progresses (Figure 5.23). Again it is worth noting that the SST anomalies are partly forced by the overlying atmosphere, as MSLP anomalies (along with resulting wind stress anomalies) develop over the Southern Ocean (Figure 5.24a).

In the Indian ocean, a region of significant freshening is found in the eastern basin for years 41-50 (Figure 5.23a). This region of fresher water appears to be isolated in the upper layers of the ocean, separate from the anomalous AAIW at intermediate depths. As fresher water is found in the western Pacific, this suggests that the anomaly may arrive through the ITF. However, rather than bringing an increased volume of water from the Pacific, the ITF has a decreased transport during this decade (Figure 5.20e). The surface freshening in the Indian Ocean is also accompanied by an increased SST, with decreased SST found in the west of the basin (Figure 5.23b). This supports the suggestion that surfacing AAIW is not the cause of this anomaly. This pattern of SST in the Indian basin

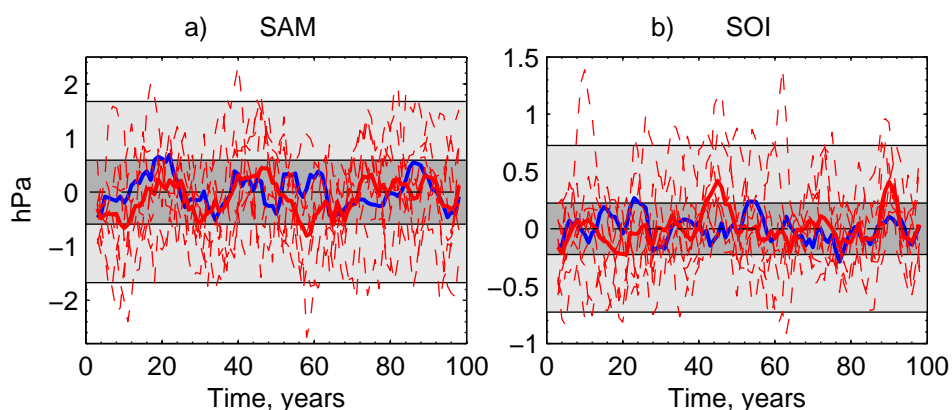


Figure 5.25: Absolute values of atmospheric climate indices for EXP4: a) Southern Annular Mode (SAM) : annual MSLP difference between 40 and 65°S; b) Southern Oscillation Index (SOI) : annual MSLP difference from Tahiti-Darwin. Light (dark) shaded area shows the 2σ (95%) spread of the control ensemble (mean) around the 100 year mean. Dashed (solid) red lines show the ensemble (mean) anomalies for EXP4 (EXP4 – time-mean of control). Blue line shows the mean of the control ensemble around the 100 year mean. Data are smoothed using a 5 year running mean. Dashed black line indicates the reference time-mean value for the control ensemble over the 100 year simulation (at zero).

is characteristic of the IOD (Saji *et al.*, 1999).

In the Atlantic, significant cool, fresh anomalies can be found in the north towards the end of the simulation (Figure 5.23). As the water mass spreads into the Atlantic basin, the decreased salt content can lead to a reduction in the overturning circulation. This results in a decreased meridional OHT towards the end of the simulation (Figure 5.20f). At the end of EXP4b, the Atlantic MOC has a reduced strength when compared with the control simulation, with an anomaly of -0.48 Sv. This, along with the cooler AAIW moving northwards through the basin, can account for the decreased heat and salt content in the North Atlantic. However, it is worth noting that this decrease in MOC strength and OHT is not significant.

5.3.3 Atmospheric response

Although there is a significant SSS and SST change for years 21-30 in EXP4, there is no significant SAM response, as was seen for EXP3 (Figure 5.25a). Rather than seeing an equal and opposite response to that for EXP3, the SAM index is again reduced, when compared with the mean of the control ensemble. There is also a decrease in the SOI, corresponding to El Niño, conditions in the Pacific (Figure 5.25b). With varying initial ocean conditions, Figure 5.24a shows that there is no significant trend in the SAM index

for the initial decades of EXP4b. As reduced SST is found in the equatorial Pacific for the first 10 years, positive anomalies are found for the SOI (Figures 5.21b and 5.24d). However, as no significant trends were seen for the SST index, there are no significant trends in the SOI for the duration of the simulation.

There is a period of weakened SAM index for years 50-65 of EXP4b (Figure 5.24a). As described in Section 5.2.1, a decrease in the SAM index leads to changes in wind stress that result in a mean decrease in the strength of the SO MOC (Figure 5.20c). The SAM is also linked with changes in the meridional SST gradient. For years 51-60, decreased SST is found between 30 and 50°S in the Atlantic and Indian Ocean, along with increased SST found further south (Figure 5.23d). Around year 60, the mean DPT also decreases, however following this there is an increased DPT which persists until the end of the simulation (Figure 5.20d). During this time, the fresh AAIW can be found on the northern side of the ACC, in each of the three major ocean basins (Figure 5.17). In control conditions, isopycnals shoal towards the south in the SO. The presence of fresher (less dense) water to the north, then leads to an increased slope of isopycnals, and hence an increased DPT.

Patterns of SAT anomalies correspond mainly with SST anomalies. The largest anomalies in the northern hemisphere (NH) occur during years ~ 60-80 (Figure 5.24b), when there is a reduced SST in both the Pacific and Atlantic basins (Figure 5.23f). SAT is also reduced during years 41-50 (Figure 5.22b), during which there is the strongest decrease in SH SAT (Figure 5.24c). This coincides with negative phases of both the PDO and IOD. As described in Section 5.2.2.3, the PDO has been shown to occur through 'reddening' of ENSO events, and there is no sign of cyclic variability in HadCM3. The IOD is also known to show greater persistence in HadCM3, than seen in observations (Spencer *et al.*, 2005). Therefore, the anomalies in the Indian Ocean, and hence the large decrease in SH SAT for this time, may not be a realistic response.

5.4 Discussion

For both the perturbations in the Pacific, $\pm 1^\circ\text{C}$, the anomaly is seen to surface in the equatorial Pacific. For EXP3, the warmer surface waters trigger a negative phase of the SAM for years 11-30, and significant changes in the Southern Ocean circulation. However, the same response was not seen in EXP3b, when varying the initial ocean conditions. This

suggests that the response in EXP3 is influenced by the initial state of the control ensemble. Also, no equal and opposite response is seen for EXP4 or EXP4b. As with the previous experiments, we find that response to the two perturbations, $\pm 1^\circ\text{C}$ is non-linear.

In the Pacific, the warmer, saltier AAIW appears to spend more time in the surface layers, with 18 % of the salt perturbation remaining in model levels 1-9 of the Pacific after 100 years. The cooler, fresher AAIW remains predominantly at intermediate depths, with 53 % of the salt anomaly being found in levels 10-13 at the end of the simulation, and just 8 % in the upper levels. As the warm, saline AAIW spreads in the upper levels of the ocean, a greater portion of the anomalous water mass spreads outside the Pacific, as it is advected with more rapid currents at shallower depths. The cooler, fresher AAIW has a tendency to remain in the Pacific, and extends less far to the north, with little evidence of it reaching the SPG (Figure 5.17). In total, 61 % and 73 % of the warmer and cooler AAIW, respectively, remains between $\sim 36^\circ\text{S}$ and 65°N in the Pacific after 100 years.

This result is contrary to that found for the Atlantic, where the cooler, fresher AAIW spends more time in surface layers (Figure 3.32). The circulation in the Pacific is fundamentally different to the Atlantic, with no sinking of deep waters in the north. The main overturning cells for the upper layers of the ocean occur in the subtropical gyres, with upwelling along the Equator, driven by surface wind stress. SSS anomalies are found in this region for both experiments, however the persistence of anomalies in upper layers for EXP3b may be related to an increase in the overturning gyre in the North Pacific (Figure 5.26). A combination of advection and diffusion allow the perturbed water masses to spread northwards through the basin. For EXP4b, the overturning circulation decreases during years 50-80, due to wind stress anomalies over the equatorial region (not shown).

Although the water masses are seen to reach the surface layers of the ocean in the tropical Pacific, the SST response is less significant. This may be due to the large internal variability in this region, due to the ENSO. Significant SST anomalies are found in the extra-tropical Pacific that resemble the PDO. However, Collins *et al.* (2001) and Newman *et al.* (2003) show that this variability in the Pacific is linked to SST in the tropics and is likely a result of ENSO variability, along with the re-emergence of SST anomalies from previous winters. Therefore these anomalies may be due to internal variability in the model rather than a result of the perturbations.

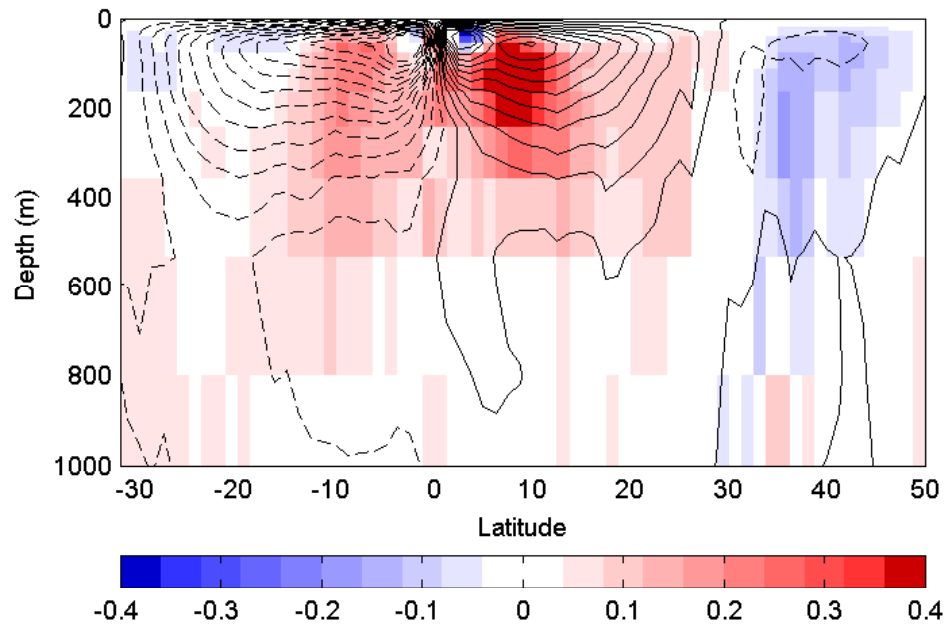


Figure 5.26: Mean overturning streamfunction anomaly in the top 1000 m of the Indo-Pacific for 100 years of EXP3b (EXP3b-Control) [Sv]. Contours show the mean overturning streamfunction in the control ensemble, with solid (dashed) lines indicating positive (negative) values and clockwise (anti-clockwise) circulation. Contours are drawn at intervals of 3 Sv.

As the perturbed water mass leaves the Pacific, the large heat and salt perturbations made in these experiments allow heat and salt anomalies to be seen throughout the world ocean by the end of the experiment. Heat and salt enter the Indian Ocean through either the ITF or from the south of Australia. The majority of the anomalies in the Atlantic enter from the south of South Africa. The representation of the Agulhas Current and retroflection in HadCM3 is poor due to the lack of eddy resolution. However, this path of transport is consistent with previous modelling studies and observations (e.g. Sen Gupta and England, 2007b; McCarthy *et al.*, 2011). As the anomaly spreads south, into the Southern Ocean, both perturbations show an increased DPT towards the end of the simulation. For the cooler, fresher AAIW, anomalous surface heat fluxes allow the water mass to gain heat, but remain fresh. This leads to a reduction in density north of the ACC, and an increase in the meridional density gradient (illustrated in Figure 5.27). However, the DPT response to the warm, saline perturbation is not opposite, and instead may be linked to changes in wind stress over the Southern Ocean. As the warmer water surfaces, this leads to an increase in the meridional temperature gradient. This may be a cause of the increased mean SAM index in the latter years of the simulation (Marshall and Connolly, 2006; Sen Gupta and England, 2007a). As the wind stress over the Southern Ocean

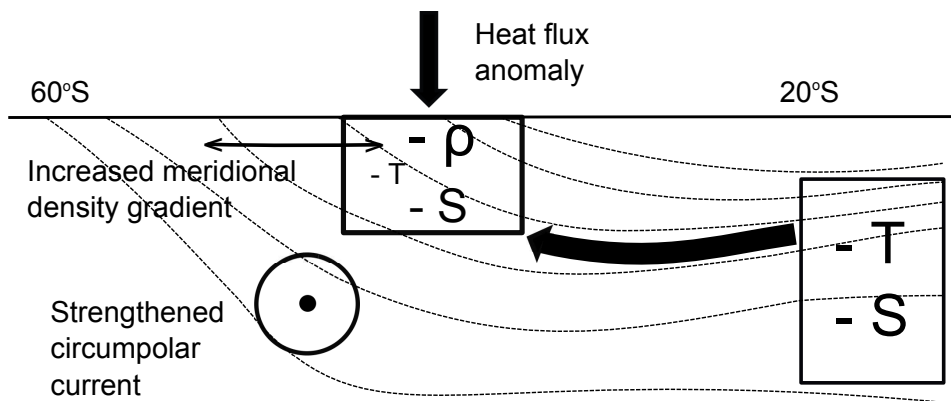


Figure 5.27: Schematic to demonstrate the response to a cold, fresh (density-compensating) perturbation, as seen in EXP4b. Dashed lines illustrate isopycnals in the ocean. As isopycnals shoal towards the south, the anomalous water mass comes into contact with the atmosphere. Heat flux anomalies into the ocean result in a negative density anomaly as the fresh anomaly remains. This increases the north-south density gradient across the Polar Frontal Zone, strengthening the ACC.

increases, this can then drive the increased ACC and DPT (Figure 5.9).

It is worth noting that although the nonlinear response in the Pacific is somewhat different to that observed for the Atlantic experiments, as the anomalous water mass enters the Atlantic, a similar response to EXP1b and EXP2b can be seen. As the cooler, fresher AAIW moves northwards, a greater proportion is found in the upper layers, and there is a reduction in the MOC towards the end of the simulation.

Chapter 6

Response to perturbing AAIW in the Indian Ocean

6.1 Introduction and Methods

We now see what impact a change of properties can have within the Indian Ocean. The basic principle is again kept the same as that used for the previous experiments (Chapters 3 and 4), so that the results can be compared with those for the Atlantic and Pacific. Figure 5.1 showed the temperature-salinity diagram for 10-20°S in each of the three major ocean basins. In the Indian Ocean, the salinity minimum occurs around the same isopycnal range as that for the Atlantic, with a minimum of 33.8 at a potential density of 1028.5 (relative to level 11 in HadCM3). In the Indian Ocean, the core is found at a greater depth than in Atlantic or Pacific, in level 12 of the model. The potential density boundary for AAIW in the Indian Ocean is then chosen to be 1027.5 – 1029.1 (Figure 6.1). The temperature is altered by $\pm 1^\circ\text{C}$ within this density range, and $\pm 0.5^\circ\text{C}$ in the model levels directly above and below. The salinity is then altered to maintain constant density. The location of the perturbed region, between 10 and 20°S in the basin, is illustrated in Figure 6.2.

The experiments in this chapter will hereafter be referred to as EXP5 and EXP6 for the $+1^\circ\text{C}$ and -1°C perturbations, for the ensembles with the same ocean initial conditions and varying atmosphere; EXP5b and EXP6b denote the $+1^\circ\text{C}$ and -1°C ensembles with varying initial conditions in both the atmosphere and ocean (experiments are listed in Appendix A for reference). Analysis of results will focus predominantly on the ensembles

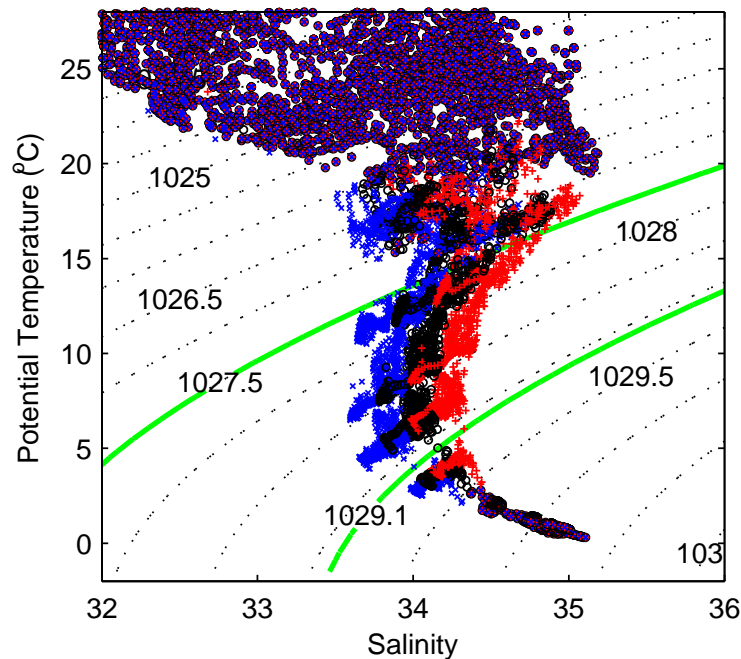


Figure 6.1: θ - S plot for perturbation and control start dumps. Red pluses and blue crosses show the conditions for the $+1^\circ\text{C}$ (EXP5) and -1°C (EXP6) perturbations respectively. Black circles show the control conditions. Black dotted contours show the corresponding potential density values calculated relative to a depth of ~ 500 m. Green contours show the boundaries of AAIW, 1027.5 and 1029.1.

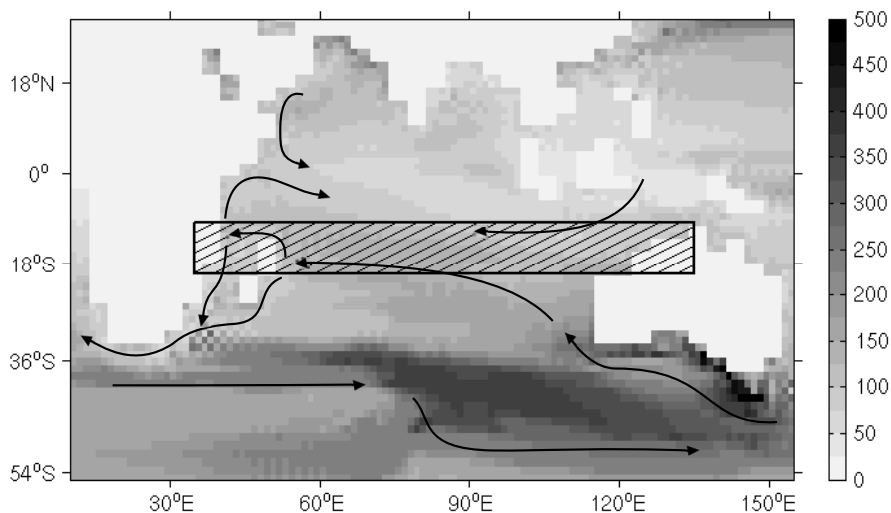


Figure 6.2: Schematic of the perturbed region of the Indian in HadCM3, 10 – 20°S . Arrows show the mean locations of the strongest currents ($> 1 \text{ cm s}^{-1}$) at ~ 500 m (level 11 in HadCM3). Shading shows the mean maximum mixed layer depth for 100 years of the control ensemble [m]. Resolution of the coastline is $2.5^\circ \times 3.75^\circ$, matching the resolution of the atmospheric component.

with varying ocean initial conditions.

6.2 Results

6.2.1 Warmer, saltier AAIW

6.2.1.1 Where does it go?

The anomaly spreads away from the initial perturbation region due to a combination of advection and diffusion. Within the first 10 years, the majority of the Indian Ocean has an increased salt content (Figure 6.3). To the north, significant anomalies extend along the coast of Africa as the anomalous water mass is carried with the Somali Current. The location of the major currents ($> 1 \text{ m s}^{-1}$) at intermediate depths in the Indian Ocean are shown in relation to the perturbed region in Figure 6.2. The anomaly spreads predominantly at intermediate depth levels, and significant anomalies can be found in the north of the basin on levels 10-14 of HadCM3 within the first 40 years (not shown). In the latter half of the simulation, there are fewer significant anomalies in the South Indian Ocean, however significant anomalies persist north of the equator and particularly in the western side of the basin (Figure 6.3).

After 100 years, the Indian Ocean in EXP5b contains 2.2×10^{14} kg more salt than the control simulation, corresponding to just 13% of the initial perturbation. The majority of the anomaly is found at intermediate depths, with Figure 6.4a showing that there is an increased zonal-mean salinity from ~ 300 -2000 m throughout the Indian Ocean for years 91-100. A portion of the anomaly enters the deep levels, however a fresh anomaly is found in the upper levels at the end of the simulation. As only 13% of the salt anomaly remains in the Indian Ocean, this shows that the vast majority has spread in to other regions of the world ocean.

To the south of the initial perturbation, the Mozambique Current carries the anomalous water mass along the western boundary of the basin (Figure 6.2). From here, AAIW can then be carried into the Atlantic with the Agulhas and Benguela Currents. The representation of the Agulhas Current and retroflexion in HadCM3 is poor due to the lack of eddy resolution. Although this error may lead to larger volumes of AAIW entering the

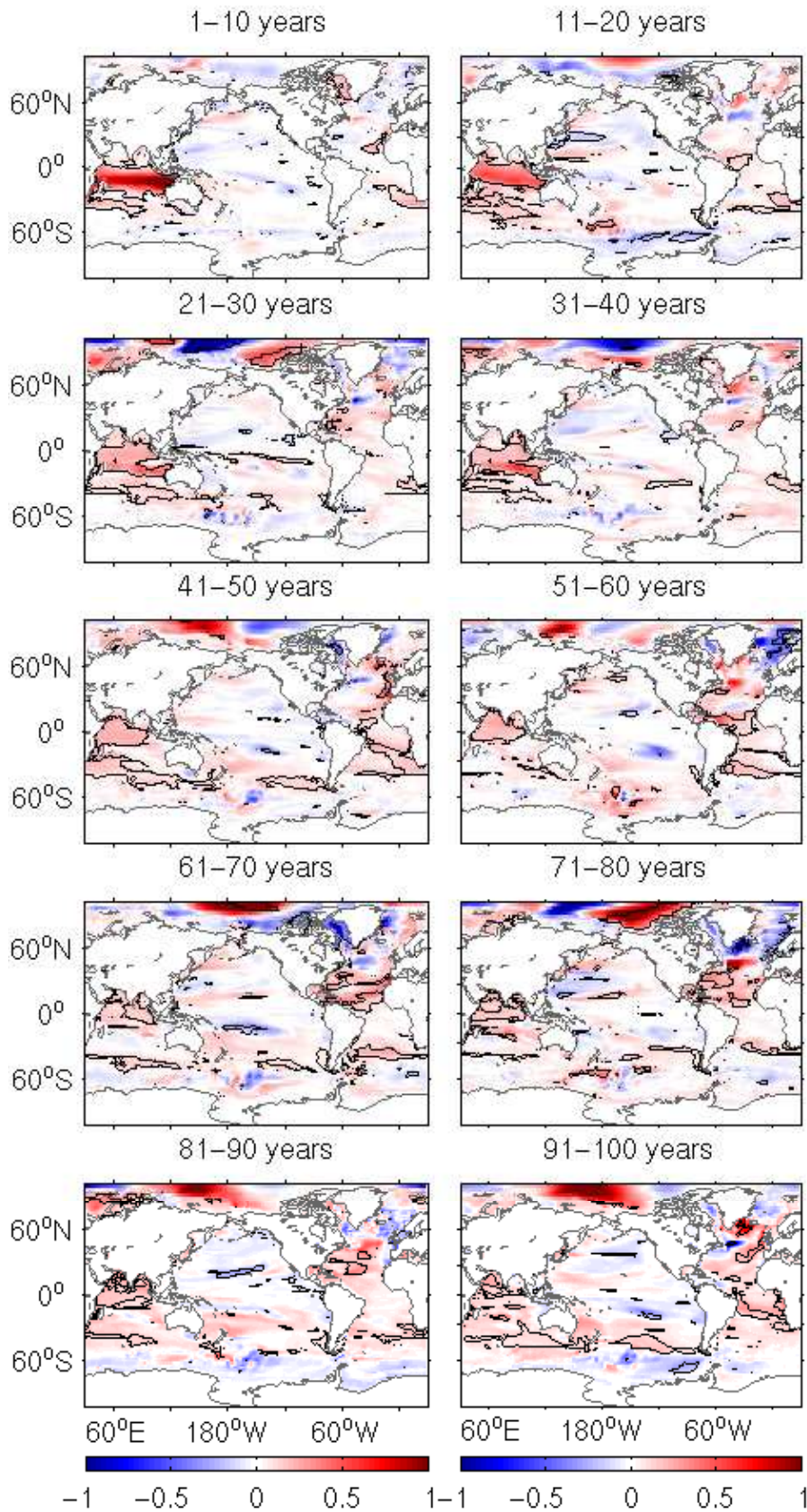


Figure 6.3: Decadal salt content anomalies (EXP5b - control) [10^2 kg m^{-2}]. Contours show regions significant at the 95% confidence level.

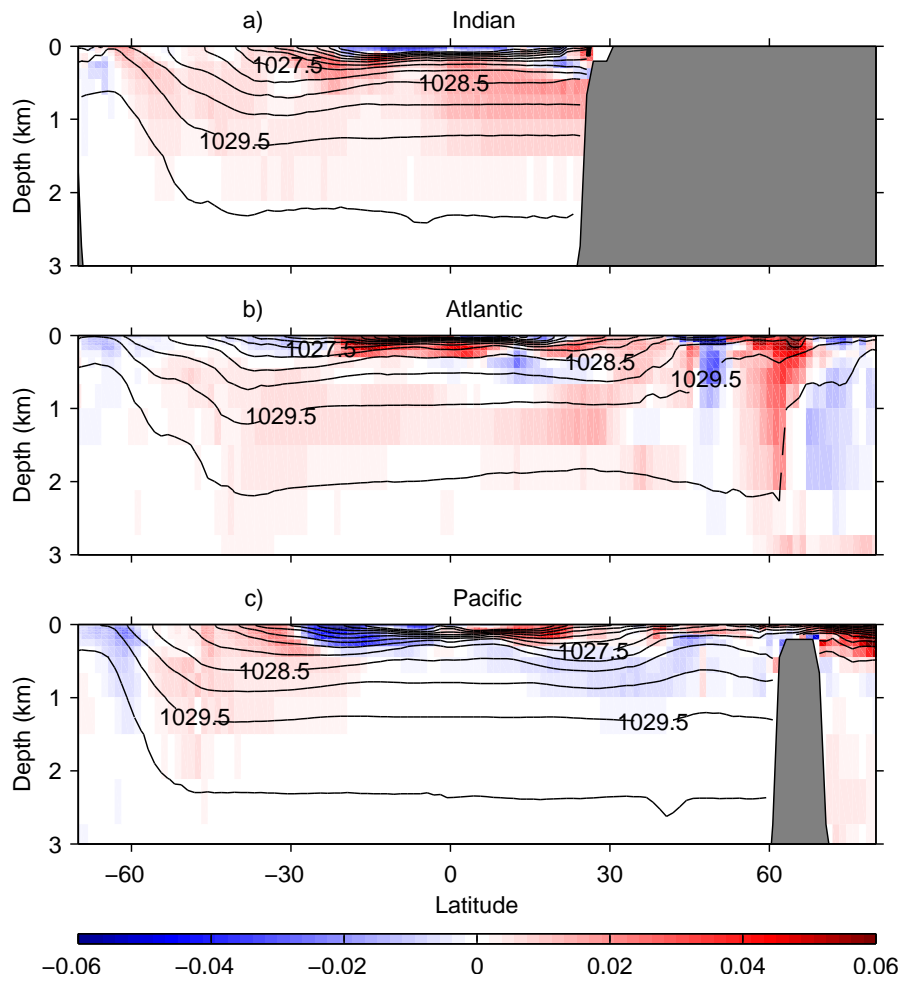


Figure 6.4: Zonally averaged decadal salinity anomalies (*EXP5b* – control) for years 91-100 in the: a) Indian; b) Atlantic; c) Pacific oceans. Contours show mean potential density (relative to level 11 in *HadCM3*) for years 91-100 of the control ensemble.

Atlantic through this route, than would be seen in reality, this path of transport is consistent with previous modelling studies and observations (e.g. Sen Gupta and England, 2007b; McCarthy *et al.*, 2011). Significant salt anomalies can be found in the South Atlantic within 10 years (Figure 6.3). After the anomalies reach the Atlantic, the path of circulation is similar to that observed in the Atlantic experiments (Figure 3.7). Within 20 years, significant anomalies are found in the tropical North Atlantic, and within 30 years, significant anomalies extend along the path of the Gulf Stream (Figure 6.3). After 100 years, the majority of the Atlantic basin and SPG have an increased salinity (Figure 6.4b) and the total salt anomaly for the basin is 6.0×10^{14} kg, equivalent to 36% of the original perturbation.

As well as spreading into the Atlantic, a portion of the anomaly that moves southwards enters the Southern Ocean. The water mass is carried eastwards with the ACC, from which

it can enter the South Pacific sub-tropical gyre (Figure 6.3). Regions of significant salt anomalies are found in the southwest and southeast Pacific within 20 years. For years 21-30, significant anomalies can also be found in the tropical Pacific. Positive anomalies remain in the sub-tropical South Pacific for the remainder of the simulation, however there are few significant anomalies, and less northward transport than is seen in the Atlantic (Figure 6.3 and 6.4). In total, the salt anomaly in the Pacific at the end of the simulation is 14% of the original perturbation. As seen in EXP3b, the majority of this warm, saline anomaly can be found in the upper layers (< 300 m).

This leaves a large portion (37%) of the anomaly outside the 3 major ocean basins. Significant salt content anomalies remain in the Southern Ocean to the end of the simulation (Figure 6.3). Figure 6.4 shows that there is an increased salinity south of 30°S in each of the zonal mean sections. South of the Indian Ocean, this anomaly extends to the surface at 60°S .

6.2.1.2 Anomalies seen at the surface

For the first 40 years, positive SSS anomalies can be found in the South Indian Ocean, in particular on the eastern side of the basin (Figures 6.5a,c). These anomalies extend from the surface to depths greater than 500 m, suggesting that the anomalous water mass is surfacing in these regions. There is also a warming in the surface Indian Ocean during this time, although the significant SST anomalies are found further west and are not consistent with the locations of the strongest salinity anomalies (Figures 6.5b,d). Negative heat flux anomalies along the eastern boundary of the South Indian Ocean show that there is an increased heat loss from the ocean (not shown). This indicates that the excess heat may be lost to the atmosphere, and not be sufficient to cause significant SST anomalies in this region.

For years 11-20, positive salinity anomalies are found in the north of the basin, however there is a cooling in this region (not shown). Positive SST anomalies are confined to $\sim 30^{\circ}\text{S}$. At this latitude, deeper mixed layers may allow anomalies to be brought to the surface from depths greater than 300 m (Figure 6.2).

Fresh anomalies develop in the equatorial region for years 21-30 (Figure 6.5c), and

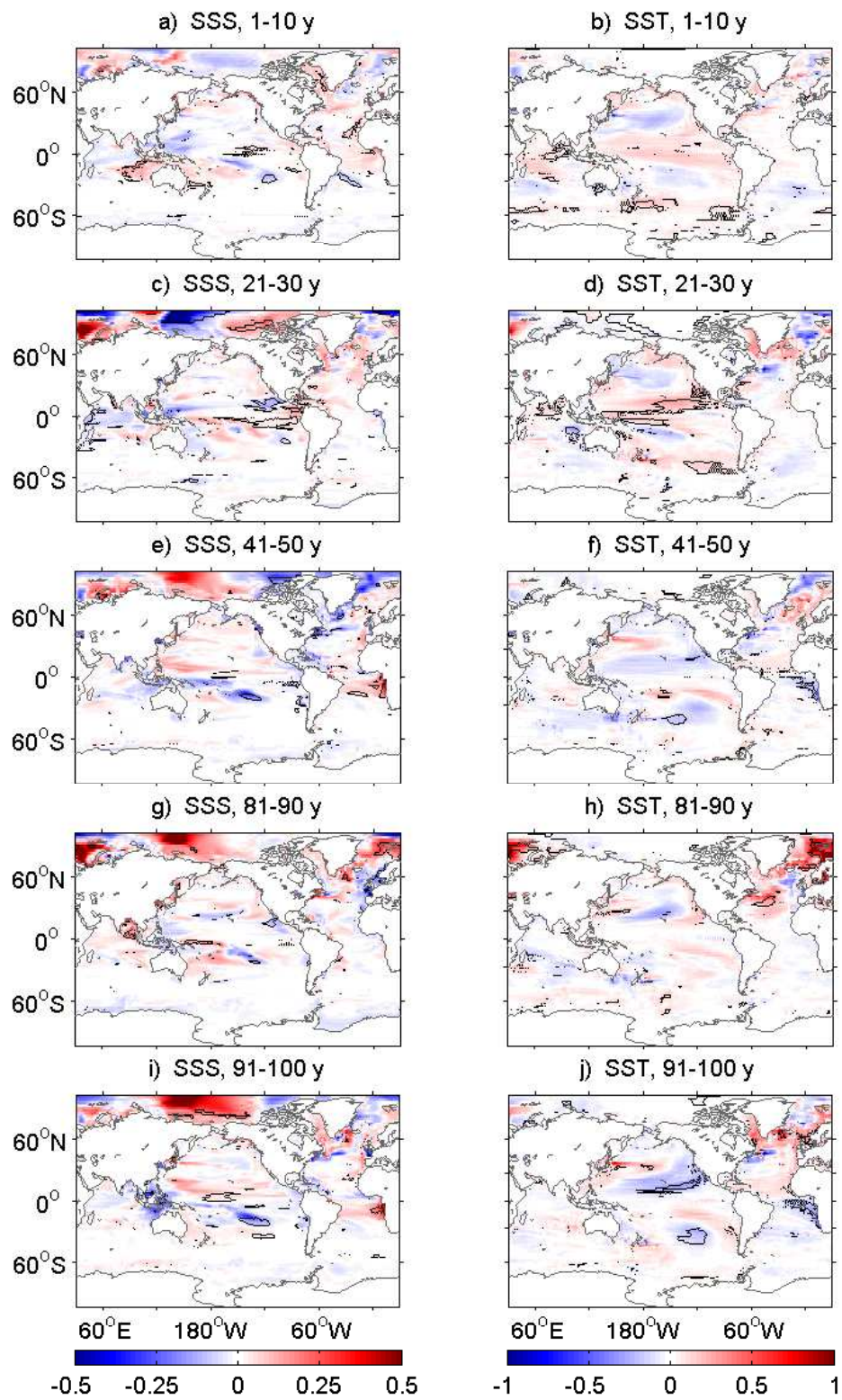


Figure 6.5: Decadal anomalies (*EXP5b* – control) for years 1-11, 21-30, 41-50, 81-90 and 91-100. Figures a, c, e, g and i show sea surface salinity (SSS); b, d, f, h and j show sea surface temperature (SST) [$^{\circ}\text{C}$]. Contours show regions significant at the 95% confidence level.

extend into the Arabian Sea for years 31-40 (not shown). During these decades, the positive SSS anomalies are confined to the coast of India (Figure 6.5c), and for years 31-40, can still be found in the Bay of Bengal. The fresh anomalies are found only in the upper 8 levels of the ocean, showing that surface freshwater fluxes are likely to cause this variability. For years 21-30, significant SST anomalies are found in the southeast and northwest of the basin (Figure 6.5d). This pattern is consistent with the IOD (Saji *et al.*, 1999; Spencer *et al.*, 2005), and occurs as a result of wind stress variability over the Indian Ocean (this will be discussed in further detail in Section 6.2.1.3). There is also a warming in the tropical Pacific during this time. Such anomalies are known to affect the atmospheric circulation over the Indian Ocean, and hence the surface properties of the ocean (e.g. Bjerknes, 1969; Tourre and White, 1995). There are no significant SST anomalies in these regions for years 31-40, however there is a warming in the Bay of Bengal that extends to intermediate depths (not shown), suggesting that anomalies in this region may be due to the surfacing warmer, saltier water.

For the latter half of the simulation, there are few significant temperature and salinity anomalies, except for a region of increased salinity in the northeast of the basin for years 81-90 (Figure 6.5g). However, the anomaly is only significant in the upper layers of the ocean and there are only weak anomalies in SST (Figure 6.5h). At the end of the simulation, although an increased salinity remains at depth, the average salinity in the surface layer of the Indian Ocean sees no significant change, and is actually fresher than the control simulation (Figures 6.4a and 6.5i). The upper Indian Ocean remains warmer than the control (Figure 6.5j), but the anomaly in the heat content is only equivalent to 4% of the original perturbation.

As the anomalous water mass is advected away from the perturbation region, stronger and more significant anomalies are found outside the Indian Ocean (Figure 6.3). In the North Atlantic and GIN Seas, there are regions of significant warming during years 81-90 (Figure 6.5h). Although less significant, there is also an increased surface salinity in these regions (Figure 6.5g). In the North Atlantic, the anomalies extend from the surface to depths > 2000 m, suggesting that the warmer, saltier water mass may be surfacing as it progresses northwards (Figure 6.4b). Surface heat flux anomalies also show that the warm ocean is losing heat to the atmosphere, rather than being atmospherically forced

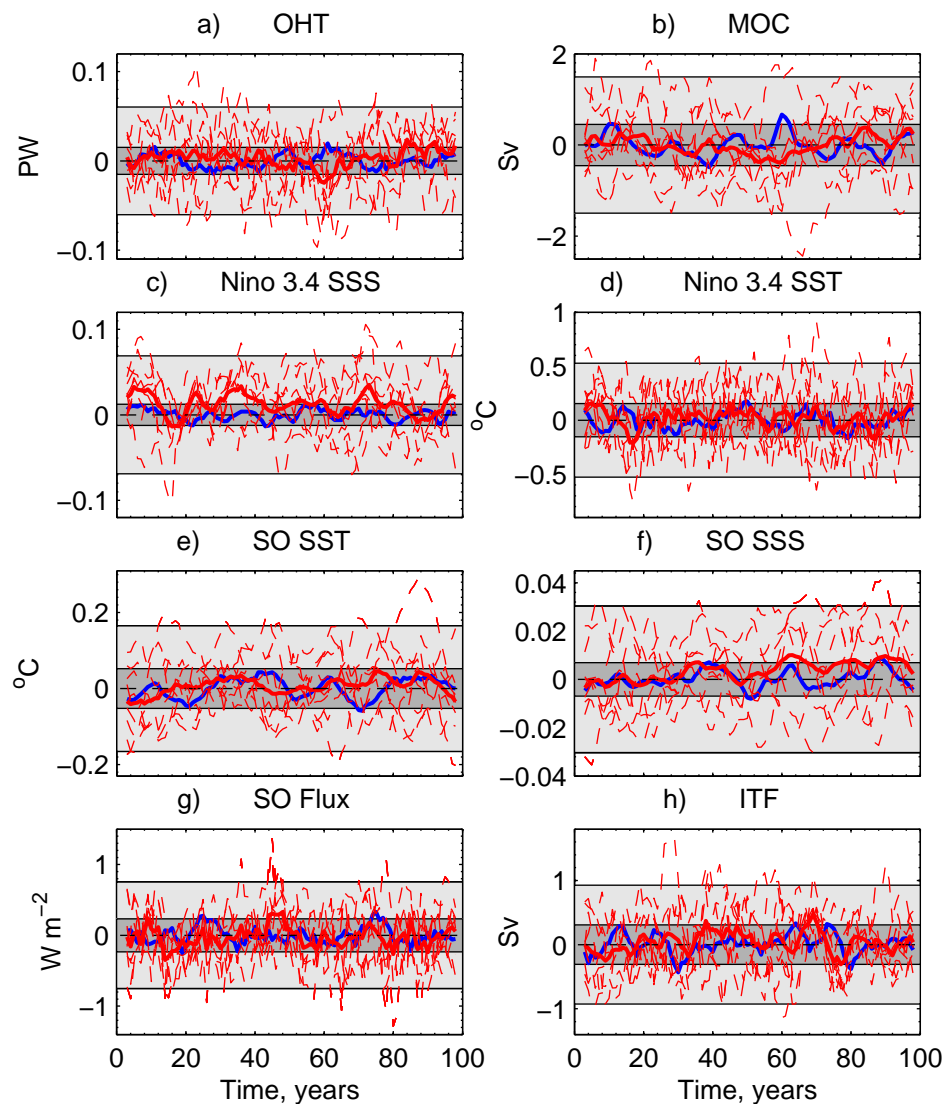


Figure 6.6: Absolute values of climate indices for EXP5b: a) Total global northward ocean heat transport (OHT) at 26°N ; b) Atlantic meridional overturning streamfunction (MOC) index : maximum overturning at 45°N ; c) mean sea surface salinity (SSS) in the Niño 3.4 index region (5°N - 5°S , 170 - 120°W); d) mean sea surface temperature (SST) in the Niño 3.4 index region; e) mean SST in the Southern Ocean (SO), 30 - 50°S ; f) mean SSS in the SO, 30 - 50°S ; g) mean atmosphere-ocean heat flux in the SO, 30 - 50°S : positive values indicate heat flux in the atmosphere to ocean direction; h) volume transport through the Indonesian Through-Flow (ITF). Light (dark) shaded area shows the 2σ (95%) spread of the control ensemble (mean) around the 100 year mean. Dashed (solid) red lines show the ensemble (mean) anomalies for EXP5b ($\text{EXP5b} - \text{time-mean of control}$). Blue line shows the mean of the control ensemble around the 100 year mean. Data are smoothed using a 5 year running mean. Dashed black line indicates the reference time-mean value for the control ensemble over the 100 year simulation (at zero).

(not shown).

In Chapter 3, the density in the North Atlantic was shown to cause changes in the meridional OHT. As the saltier water mass arrives in the SPG, and sinks around 60°N , there is an increased density and decreased steric height at this latitude. For this experi-

ment, there is an increased OHT towards the end of the simulation, as there is an increase in the MOC strength (Figures 6.6a,b). However, for years 91-100 years the MOC strength returns to control values. This increased MOC strength and OHT will contribute to the increased SST in the North Atlantic (Figures 6.5h,j).

In the Pacific, there is a sign that the anomaly may be surfacing in the equatorial regions. For the Niño 3.4 index region, in the central Pacific, there is an increased SSS throughout the majority of the simulation (Figures 6.5 and 6.6c). However, there is no significant change in SST in this region (Figure 6.6d). Around year 30, there is an anomalous heat flux from the ocean to the atmosphere, indicating that some of the increased heat content has been lost to the atmosphere. However, there is no longterm trend in the heat flux anomalies during the simulation. Some of the increased heat may be lost through transit to the Pacific via the Southern Ocean. At the end of the simulation, the majority of the anomalous heat and salt which remains in the Pacific is found in the upper layers of the ocean (Figure 6.4c). The salt anomaly in the upper 9 model levels is equivalent to 9 % of the original perturbation, whereas a total of 5 % is found in the levels below. This is similar to the results seen for EXP3b (Chapter 5).

Although there is a lack of significant SST signals in the equatorial regions, they can be found further south. In the first 10 years, regions of significant warming can be found around the Southern Ocean, $\sim 40-60^{\circ}\text{S}$ (Figure 6.5b). Warming is also seen for years 11-20 (not shown). Figure 6.6e shows the mean SST for the Southern Ocean between 30 and 50°S during the simulation. Some negative anomalies can be found during the first half of the simulation, however the mean SST for EXP5b remains above the control simulation for years $\sim 10-30$, and there is a greater warming during years $\sim 65-80$. The mean SSS also increases for the latter half of the simulations, with the mean of EXP5b outside the 95% range of the mean of the control (Figure 6.6f). Figure 6.6g shows the mean surface flux over $30-50^{\circ}\text{S}$ in the Southern Ocean. The sign of the surface heat flux anomalies is not consistent throughout warm periods, showing that the warming may be partly due to atmospheric forcing. This will be discussed further in the following section (Section 6.2.1.3). However, for years 11-30 and 71-80, increases in SST and SSS are accompanied by negative flux anomalies. As this indicates that the ocean is losing more heat to the atmosphere, this suggests that warmer water is surfacing in the Southern Ocean during

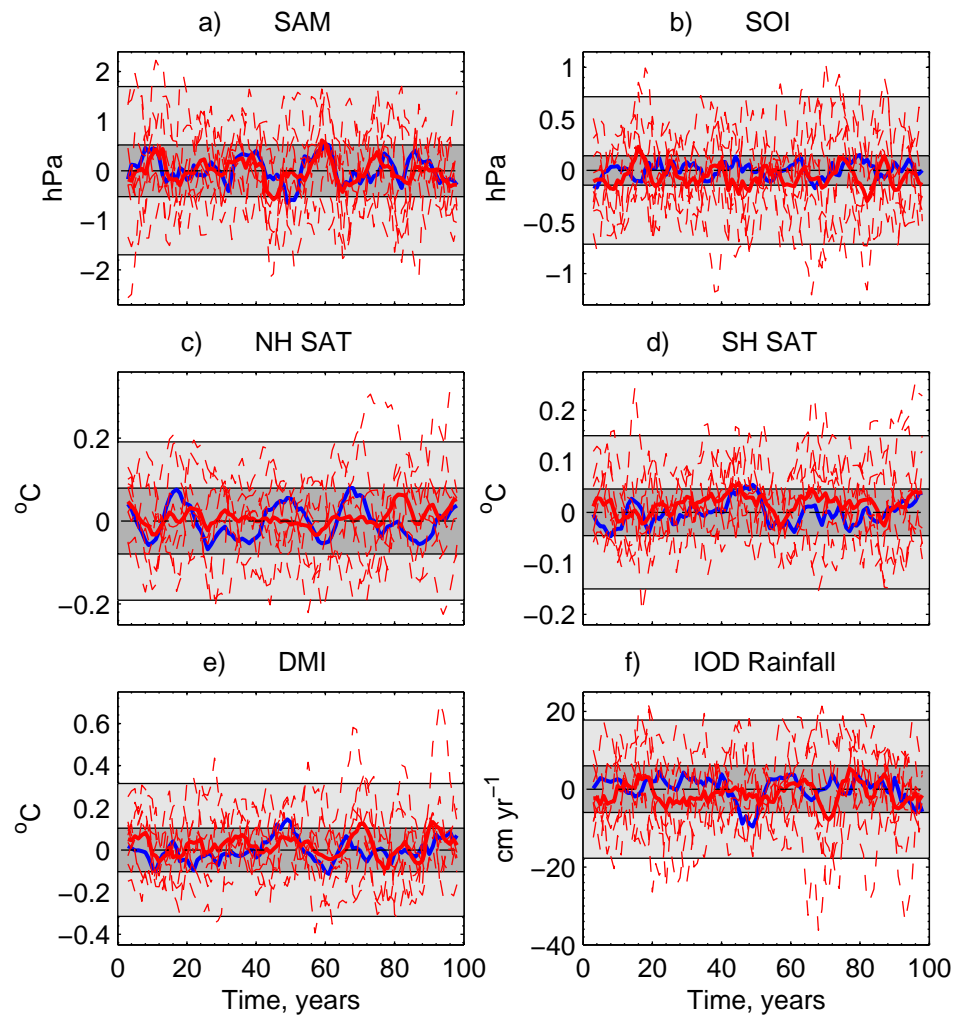


Figure 6.7: Absolute values of climate indices for EXP5b: a) Southern Annular Mode (SAM) : annual MSLP difference between 40 and 65°S ; b) Southern Oscillation Index (SOI) : annual MSLP difference from Tahiti-Darwin c) mean Northern Hemisphere (NH) surface air temperature (SAT) d) mean Southern Hemisphere (SH) SAT; e) Dipole Mode Index (DMI) : mean SST difference between west and east of Indian Ocean (10°N - 10°S , 60 - 80°E – 0 - 10°S , 90 - 110°E); f) Rainfall response to the Indian Ocean Dipole (IOD) : mean precipitation in tropical eastern Indian Ocean (0 - 30°S , 90 - 120°E). Light (dark) shaded area shows the 2σ (95%) spread of the control ensemble (mean) around the 100 year mean. Dashed (solid) red lines show the ensemble (mean) anomalies for EXP5b (EXP5b – time-mean of control). Blue line shows the mean of the control ensemble around the 100 year mean. Dashed black line indicates the reference time-mean value for the control ensemble over the 100 year simulation (at zero).

this time.

6.2.1.3 Atmospheric response

There are no significant trends in the SAM or SOI (Figures 6.7a,b). However, particular phases of variability can account for temperature anomalies seen in the ocean and atmosphere. During the first 10 years, positive SST and SAT anomalies are found around the

Southern Ocean, between ~ 50 and 60°S (Figures 6.5b and 6.6e). However, surface flux anomalies show that the ocean temperature is being forced by the overlying atmosphere (Figure 6.6g). During this time, there is a negative SOI anomaly, corresponding to an El Niño event in the Pacific (Figures 6.7b and 6.6d). There is also a negative phase of the SAM (albeit not significant; Figure 6.7a). Negative phases of the SOI and SAM can be associated with increased SST in the Southern Ocean (e.g. Deser and Blackmon, 1995; Hall and Visbeck, 2002; Zhou and Yu, 2004).

For years 21-30, significant SAT anomalies are found over the Pacific and Indian Oceans, consistent with the location of SST anomalies (Figure 6.5d). These SST anomalies show patterns associated with El Niño and the IOD. Although some warmer, saltier water is believed to surface in the equatorial regions of the Indo-Pacific, the location of the salinity anomalies is not consistent with SST anomalies of the same sign (Figure 6.5c). This suggests that atmospheric variability is responsible for the SAT anomalies in these regions.

The IOD is described by Saji *et al.* (1999) as a coupled mode of variability, involving changing wind, precipitation and SST patterns over the equatorial Indian Ocean. During a Dipole Mode event, cool anomalies develop off the coast of Sumatra. Reduced convection in the region and surface pressure anomalies then lead to a change in the surface wind field. The westerly winds, usually found in the equatorial region, weaken and reverse direction. Easterly wind anomalies are then characteristic of these events. Increased convergence and moisture supply in the west then lead to increased precipitation over East Africa, along with the warm SST anomalies. In the eastern side of the basin, there is reduced precipitation over Indonesia and Western Australia. The Dipole Mode Index (DMI) defined for the IOD calculates the difference in SST between the west and east of the Indian Ocean (10°N - 10°S , 60 - 80°E – 0 - 10°S , 90 - 110°E). For EXP5b the mean DMI remains above that for the control ensemble for years 21-40 (Figure 6.7e). During this time, there is a significant easterly anomaly in the zonal wind stress (not shown). Figure 6.7f also shows that the mean precipitation over the eastern Indian basin, Indonesia and northwestern Australia (0 - 30°S , 90 - 120°E) is decreased for years ~ 20 -40.

For years ~ 30 -60, there is a mean increase in the ITF, from the Pacific into the Indian Ocean (Figure 6.6h). Godfrey's island rule states that the circulation around an island

can be determined purely from the windstress curl across the ocean (Godfrey, 1989). Banks (2000a) use this theory to show that the ITF transport in HadCM3 is composed of an upper and lower level, with the upper level (< 250 m) driven predominantly by the wind stress, and the lower level (> 250 m) by bottom pressure torques. Observations and modelling studies have also shown that the transport volume varies in phase with the SOI (e.g. Meyers, 1996; England and Huang, 2005). For EXP5b, this relationship holds true for the first ~ 30 years, with increased transport being found during La Niña periods (positive SOI), and decreases during El Niño (negative SOI index; Figures 6.6h and 6.7b). However, after this time, there is no prolonged La Niña state to account for the increased transport from the Pacific.

This slight increase in the ITF suggests an increased transport of either warm, saline thermocline waters in the upper level, or fresher intermediate waters in the lower level, from the Pacific. As the increase is not shown to be driven by the ENSO, this suggests that the increase may be predominantly in the lower level, leading to an increased volume of Pacific intermediate waters entering the Indian Ocean. Analysis of the total transport across 32°S in the Indian basin shows that there is an increased southward flux of intermediate waters during the course of the experiment (not shown). This may account for the decreased significance of saline anomalies in the southern Indian Ocean in the second half of the simulation (Figure 6.3). The southward flux of surface and deep waters also increases, when compared with the control ensemble.

Towards the end of the simulation there is an increase in the meridional OHT, leading to an increased mean SAT over the northern hemisphere after 70 years (Figure 6.7c). The increased SST in the North Atlantic (Figure 6.5) leads to a significant increase in the SAT over the GIN Seas, Scandinavia and eastern Europe. Although not significant, the mean southern hemisphere SAT remains warmer throughout the majority of the simulation (Figure 6.7d).

6.2.2 Cooler, fresher AAIW

6.2.2.1 Where does it go?

The cool, fresh anomaly spreads through the Indian Ocean by a combination of advection and diffusion, along similar paths to those seen for EXP5b. To the north, the anomaly

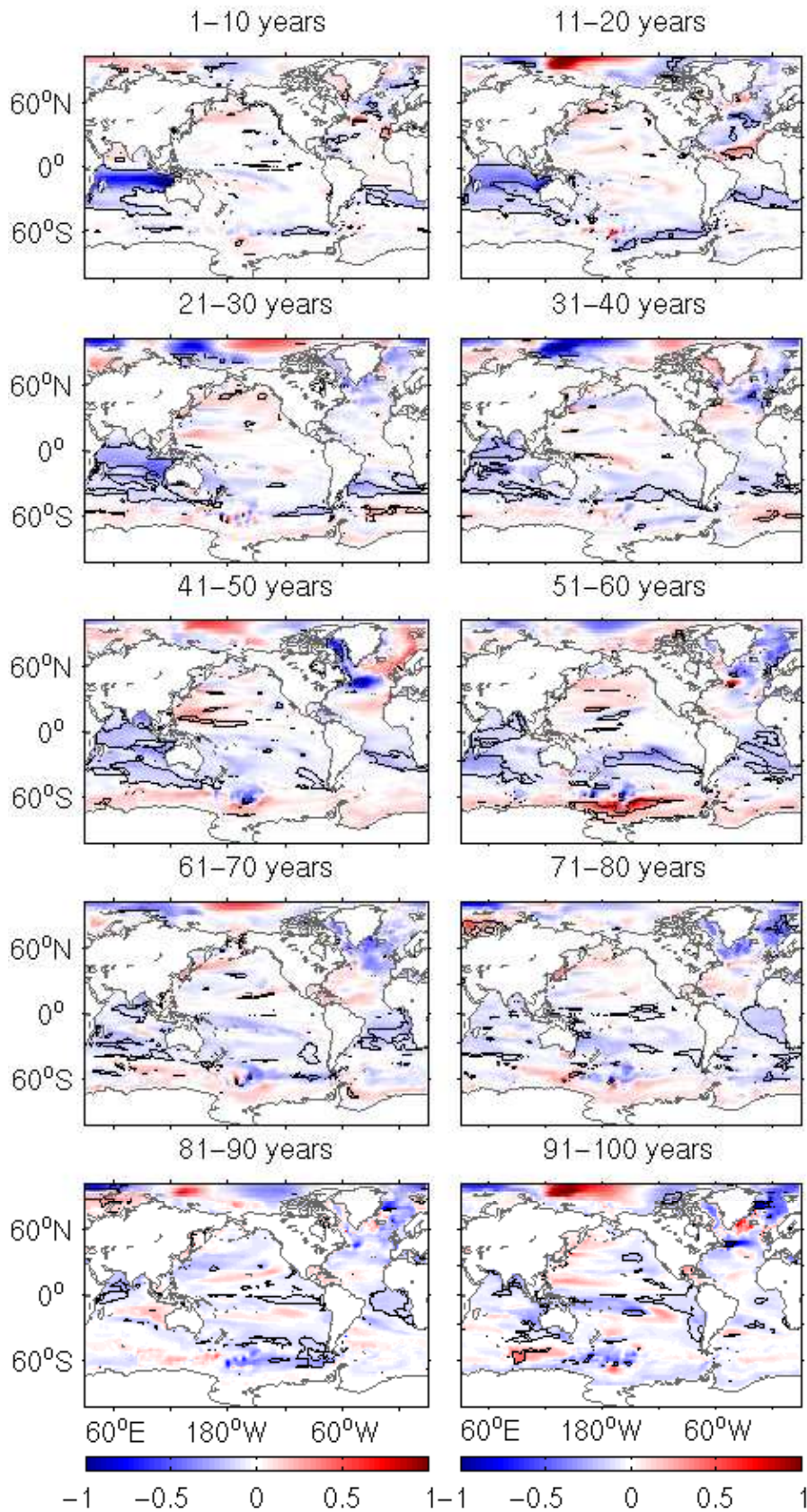


Figure 6.8: Decadal salt content anomalies (EXP6b - control) [10^2 kg m^{-2}]. Contours show regions significant at the 95% confidence level.

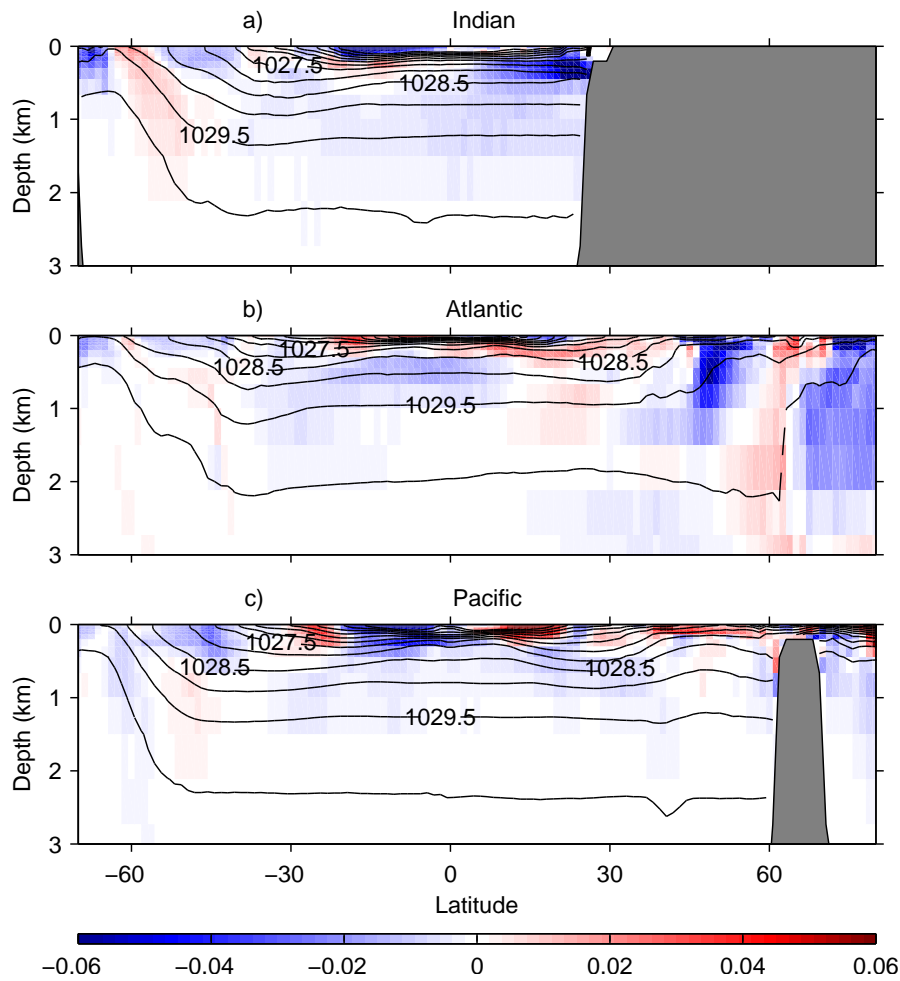


Figure 6.9: Zonally averaged decadal salinity anomalies (*EXP6b* – control) for years 91-100 in the: a) Indian; b) Atlantic; c) Pacific oceans. Contours show mean potential density (relative to level 11 in *HadCM3*) for years 91-100 of the control ensemble.

spreads up the coast of Africa with the Somali Current (Figures 6.2 and 6.8). The core of AAIW in the Indian Ocean lies between levels 11-12 (~ 400 -800 m). At these depths, significant anomalies extend into the Arabian Sea and the Bay of Bengal within 20 years (not shown). The majority of the Indian Ocean then has a reduced salt and heat content, with significant salt anomalies extending from $\sim 40^{\circ}\text{S}$ - 10°N . Significant negative anomalies persist throughout the Indian Ocean for the first 70 years of the experiment, however after this point the significance decreases and positive anomalies can be found in the South Indian Ocean for years 81-90 (Figure 6.8). Cold, fresh anomalies remain north of the equator up to the end of the simulation (Figure 6.9a).

After 100 years a salt anomaly of -6.0×10^{14} kg remains in the Indian, equivalent to 38 % of the original perturbation. This salt anomaly is relatively evenly spread between the upper and intermediate levels of the basin (Figure 6.9a), with -2.9×10^{14} kg in the

upper levels and -2.6×10^{14} kg at intermediate depths. Little of the anomaly enters the deep levels of the Indian Ocean, with just 3 % of the total anomaly at levels 14 and below after 100 years. After 100 years, the majority of the initial anomaly has spread into the other ocean basins.

Within the first 10 years, the anomaly has spread south of South Africa and into the South Atlantic, with the Agulhas and Benguela Currents (Figure 6.8). As the anomaly enters the Atlantic, it is carried rapidly northwards and significant negative anomalies are found in the north within the first 20 years of the experiment. The anomaly spreads north in the Atlantic at intermediate depths (< 1500 m), before entering the deep levels (> 1500 m) north of the NAC. Figure 6.9b shows that by the end of the simulation, the fresh anomalies in the NAC and GIN Seas extend from the surface to depths greater than 2000 m. Of the original perturbation, 27% remains in the Atlantic after 100 years, with the largest reduction in salt content being found in the upper and intermediate depths.

In the Pacific Ocean, there is less progression of the anomaly northwards than is seen in the Atlantic (Figure 6.8). After 10 years, significant fresh anomalies can be seen in the ACC, west of Drake Passage. From here, a portion of the anomaly can enter the South Pacific STG. Fresh anomalies can then be found in the South Pacific within 30 years, however only in the latter half of the simulation can significant anomalies be found in the north (Figure 6.8). After 100 years, the total salt anomaly in the Pacific is -5.5×10^{14} kg, equivalent to 36% of the original perturbation. However, the surface layer of the North Pacific remains more saline, with the fresh anomaly remaining predominantly at intermediate depths (~ 300 -1500 m; Figure 6.9c).

6.2.2.2 Anomalies seen at the surface

During years 1-10, negative SSS anomalies are found between ~ 30 - 40° S in the Indian and Atlantic oceans (Figure 6.10a). These correspond to the locations of salt anomalies seen in Figure 6.8 and extend to depths greater than 1000 m (level 13 in HadCM3). The path of these anomalies can be traced back to the original perturbation region, suggesting that the anomalous water mass is surfacing in these regions. Figure 6.2 also shows that south of 30° S in the Indian Ocean, there are regions of deep mixed layer depth (> 300 m),

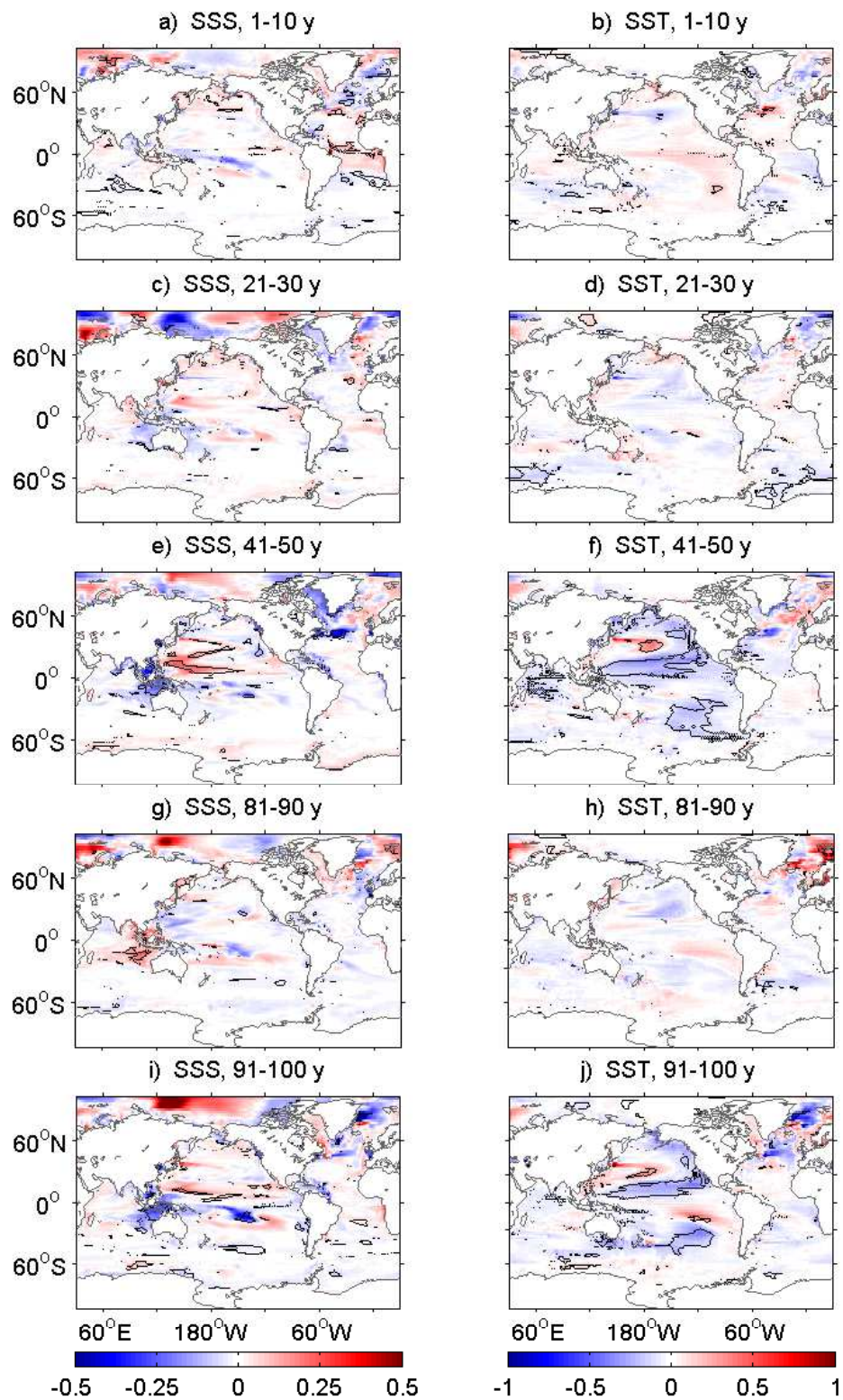


Figure 6.10: Decadal anomalies (EXP6b – control) for years 1-11, 21-30, 41-50, 81-90 and 91-100. Figures a, c, e, g and i show sea surface salinity (SSS); b, d, f, h and j show sea surface temperature (SST) [$^{\circ}$ C]. Contours show regions significant at the 95% confidence level.

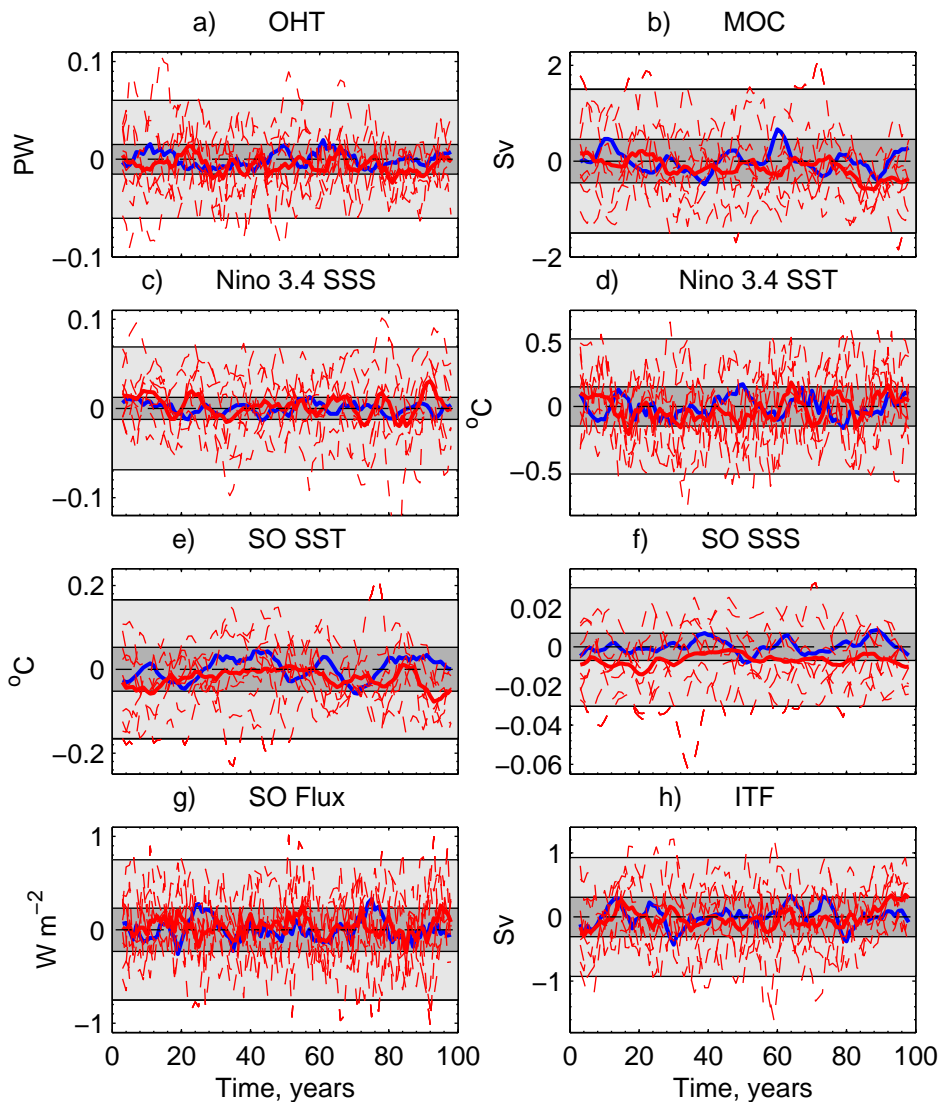


Figure 6.11: Absolute values of climate indices for EXP6b: a) Total global northward ocean heat transport (OHT) at 26°N ; b) Atlantic meridional overturning streamfunction (MOC) index : maximum overturning at 45°N ; c) mean sea surface salinity (SSS) in the Niño 3.4 index region (5°N - 5°S , 170 - 120°W); d) mean sea surface temperature (SST) in the Niño 3.4 index region; e) mean SST in the Southern Ocean (SO), 30 - 50°S ; f) mean SSS in the SO, 30 - 50°S ; g) mean atmosphere-ocean heat flux in the SO, 30 - 50°S : positive values indicate heat flux in the atmosphere to ocean direction; h) volume transport through the Indonesian Through-Flow (ITF). Light (dark) shaded area shows the 2σ (95%) spread of the control ensemble (mean) around the 100 year mean. Dashed (solid) red lines show the ensemble (mean) anomalies for EXP6b (EXP6b – time-mean of control). Blue line shows the mean of the control ensemble around the 100 year mean. Data are smoothed using a 5 year running mean. Dashed black line indicates the reference time-mean value for the control ensemble over the 100 year simulation (at zero).

allowing anomalies to surface as isopycnals shoal to the south. For the first 10 years, negative SST anomalies can also be found in these regions, however they are less significant than the SSS anomalies (Figure 6.10b).

For years 11-50 there is a decrease in the mean SST between 30 and 50°S , in the

Southern Ocean (Figures 6.10d,f and 6.11e). There is also persistent SSS decrease (Figure 6.11f). However the mean ocean-atmosphere heat flux in the region also shows some negative anomalies, indicating that some of the SST anomalies may be forced by the overlying atmosphere rather than just the surfacing cooler AAIW (Figure 6.11g).

Around year 50, there are significant anomalies for both SSS and SST in the Indian, Pacific and Southern Oceans (Figures 6.10 and 6.11). The pattern in the North Pacific is consistent with the PDO. However, at this time the control climate sees a significant change from the long-term mean. For example, the mean of the control ensemble is warmer in the equatorial Pacific and fresher in the Southern Ocean (Figures 6.11d,f). The stronger anomalies for the experiments at this point in the simulation may then be due to the shift in the control ensemble. The SST anomalies seen for years 41-50 are similar to those seen for this same time period in EXP3b and EXP4b (Figures 5.12 and 5.23).

After 50 years, there is a decrease in the mean SSS in the Southern Ocean, although the mean SST does not show this persistent trend, and becomes a little more variable than seen for the earlier half of the experiment (Figures 6.11e,f). Again the SST anomalies may be partly forced by the overlying atmosphere, with negative heat flux anomalies for years 70-80 (Figure 6.11g). However, the reduction in SST towards the end of the simulation is accompanied by an increased atmosphere-to-ocean heat flux. This, along with the decreased SSS, suggests that cooler, fresher water is surfacing in the region.

In the North Atlantic and GIN Seas there is also a decrease in the SSS through to the end of the simulation (Figure 6.10i). As the fresher water mass spreads northwards through the Atlantic it reaches the surface in the NAC, SPG and GIN Seas, as described in Chapters 3 and 4. As seen for EXP2(b), we find that the majority of the anomalous water mass is found in the upper 300 m of the Atlantic after 100 years (12% of the original salt perturbation). A portion also sinks into deep levels (> 1500 m) as it reaches the deep water formation regions (Figure 6.9b). As the density decreases in the North Atlantic, there is a decline in the MOC strength towards the end of the simulation (Figure 6.11b). This results in a decrease in the mean meridional OHT after ~ 80 years (Figure 6.11a), however due to the smaller volume of anomalous water, the effect in EXP6b is less strong than that for EXP2b. The SST decreases in the North Atlantic and GIN Seas as a result of surfacing AAIW anomalies and a decrease in meridional OHT.

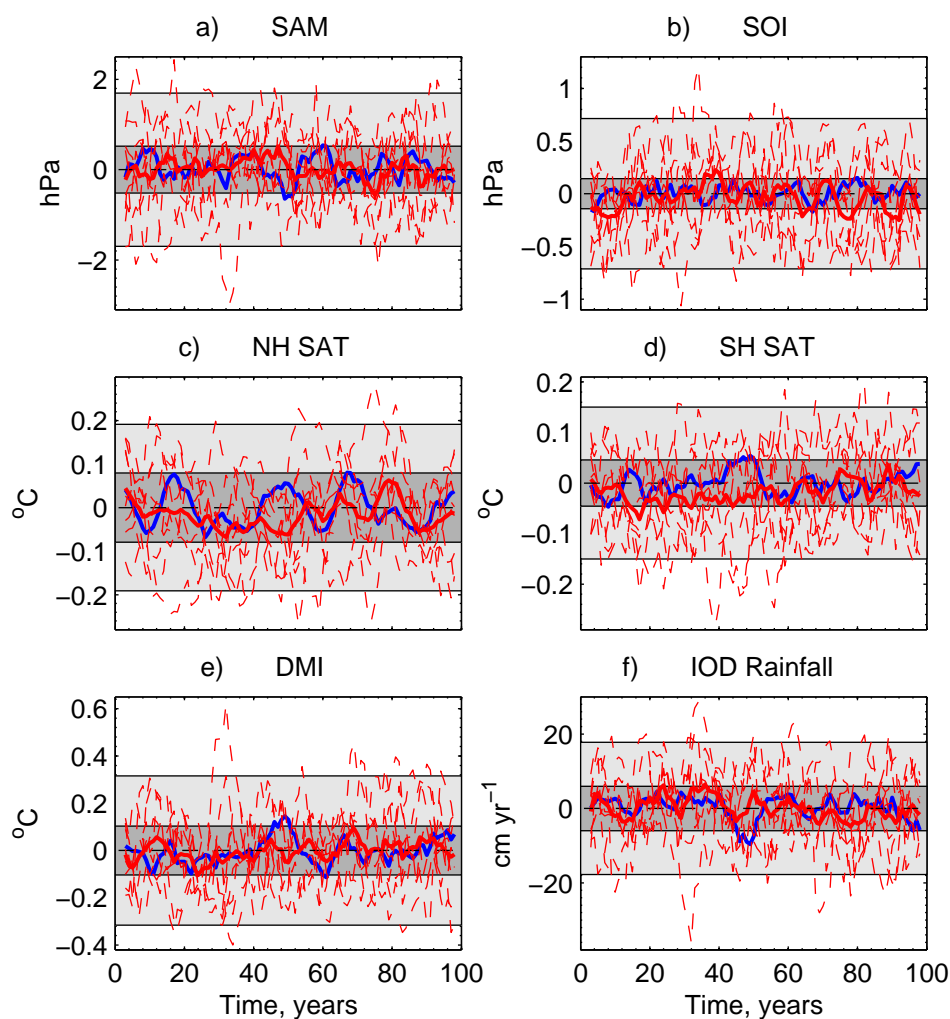


Figure 6.12: Absolute values of climate indices for EXP6b: a) Southern Annular Mode (SAM) : annual MSLP difference between 40 and 65°S; b) Southern Oscillation Index (SOI) : annual MSLP difference from Tahiti-Darwin c) mean Northern Hemisphere (NH) surface air temperature (SAT) d) mean Southern Hemisphere (SH) SAT; e) Dipole Mode Index (DMI) : mean SST difference between west and east of Indian Ocean (10°N-10°S, 60-80°E – 0-10°S, 90-110°E); f) Rainfall response to the Indian Ocean Dipole (IOD) : mean precipitation in tropical eastern Indian Ocean (0-30°S, 90-120°E). Light (dark) shaded area shows the 2σ (95%) spread of the control ensemble (mean) around the 100 year mean. Dashed (solid) red lines show the ensemble (mean) anomalies for EXP6b (EXP6b – time-mean of control). Blue line shows the mean of the control ensemble around the 100 year mean. Dashed black line indicates the reference time-mean value for the control ensemble over the 100 year simulation (at zero).

6.2.2.3 Atmospheric response

During the first 50 years, there is a decrease in the Northern and Southern Hemisphere SAT (Figures 6.12c,d). This coincides with the decreased SST around the Southern Ocean, as well as negative phases of the PDO and surfacing anomalies in the North Atlantic (Figures 6.10 and 6.11e). Surface heat flux anomalies show that the SST anomalies in the Southern Ocean may be partly due to atmospheric forcing (Figure 6.11g). During

years \sim 1-10 and 20-30, negative anomalies indicate that the ocean is losing more heat to the overlying atmosphere, when compared with the control ensemble.

There is little trend in the SAM, however during years 10-30 and 40-50, the mean of EXP6b remains above that of the control ensemble (Figure 6.12a). This indicates stronger winds around the Southern Ocean. As discussed in Chapter 5, SST anomalies in either the Pacific or Southern Ocean can be associated with MSLP anomalies over the Southern Ocean and Antarctic continent. For years 30-50, there is a decrease in the Niño 3.4 SST index (Figure 6.11d), coinciding with the PDO event in the North Pacific (Figure 6.10f). Unlike EXP4b, there is no significant shift in SSS in the equatorial Pacific (Figure 6.10 and 6.11c), showing that this effect is likely due to the atmospheric variability rather than surfacing ocean anomalies. For years \sim 30-40, there is an increased SOI, corresponding with a cool, La Niña anomaly in the tropical Pacific (Figure 6.12b). For the PDO event, there is also a significantly increased MSLP over the North Pacific (not shown). This may lead to a change in wind circulation over the Pacific, bringing cooler air down over the eastern boundary and cooling the surface ocean in this region. Although the anomalies are not significant, the surface fluxes show that the northeast Pacific is losing more heat to the atmosphere during years 41-50 (not shown).

For years \sim 35-80, there is a mean decrease in the ITF, from the Pacific into the Indian Ocean (Figure 6.11h). Previous studies have shown that the ITF varies in phase with the SOI (e.g. Meyers, 1996; England and Huang, 2005). On shorter timescales (annual-decadal) the relationship between the ITF and the SOI does appear to hold in this model, however there is no shift in the SOI to account for the decreased transport in this experiment (Figure 6.12b). For HadCM3, Banks (2000a) shows that while the upper 250 m of the ITF is forced by wind stress, at depths greater than 250 m, water mass properties may play a more important role. The lower core of the through-flow is shown to be correlated with the bottom pressure torque at the western boundary of the South Pacific. As the transport anomaly seen here occurs predominantly in the lower core of the flow, it is then likely a result of anomalous heat or salt contents in the southwest Pacific. The control state of the Indian Ocean has a net southward flow of intermediate waters (\sim 300-1500 m) across 32° S, which decreases (or reverses) when the ITF decreases (or reverses) (Banks, 2000a). As the flow of intermediate waters from the Pacific (lower level of the

ITF) decreases through this experiment, this may account for the persistence of anomalies in the southern Indian Ocean, as the transport out of the Indian Ocean decreases. After 80 years, the ITF increases, and the significant salt anomalies are then lost from this region (Figures 6.11h and 6.8). This increase occurs predominantly in the upper 250 m of the ocean, therefore is likely due to wind stress variability.

6.3 Discussion

Both the warming and cooling experiments show a large transport of the anomalous intermediate water out of the Indian Ocean. After 100 years, just 13% and 38% of the original salt anomalies are still present in the Indian Ocean in EXP5b and EXP6b, respectively. This difference may be accounted for by an increased ITF for EXP5b, and a decreased ITF for EXP6b. As the through-flow increases, an increased volume of Pacific intermediate waters enters the Indian Ocean, and the volume of intermediate water leaving the Indian Ocean increases. Banks (2000a) shows that the control overturning in the Indian Ocean for HadCM3 has a net out-flow of intermediate waters (1000-2000 m), which decreases as the ITF decreases. The decreased ITF in EXP6b is likely due to bottom pressure torque anomalies in the western boundary of the South Pacific, related to an increased transport in the East Australian Current. However, Banks (2000a) also note that the resolution of the model topography (Figure 2.4) may mean that this response is not entirely realistic.

As the anomalous water mass leaves the Indian Ocean, EXP6b shows a relatively even spread within each of the 3 major ocean basins. However, for EXP5b, there is less transport into the Pacific, and more into the Atlantic and Southern Ocean. The majority of the anomaly remains at intermediate depths (~ 300 -1500 m, model levels 10-13). For EXP5b, 47% of the salt anomaly remains in levels 10-13, with the remainder spread relatively evenly between the upper (< 300 m, levels 1-9) and deep (> 1500 m, levels 14-20) levels of the model. Contrary to the mechanisms proposed in Chapter 3, a larger portion (65%) of the fresh anomaly remains at intermediate depths for EXP6b, than the salt anomaly in EXP5b. Both experiments see a similar portion enter the deep levels. Less of the anomalous water mass enters the upper 300 m of the ocean in EXP6b, than in EXP5b. Given this difference in spread between the two experiments, within the water columns and world oceans, the question arises as to what causes this non-linear response

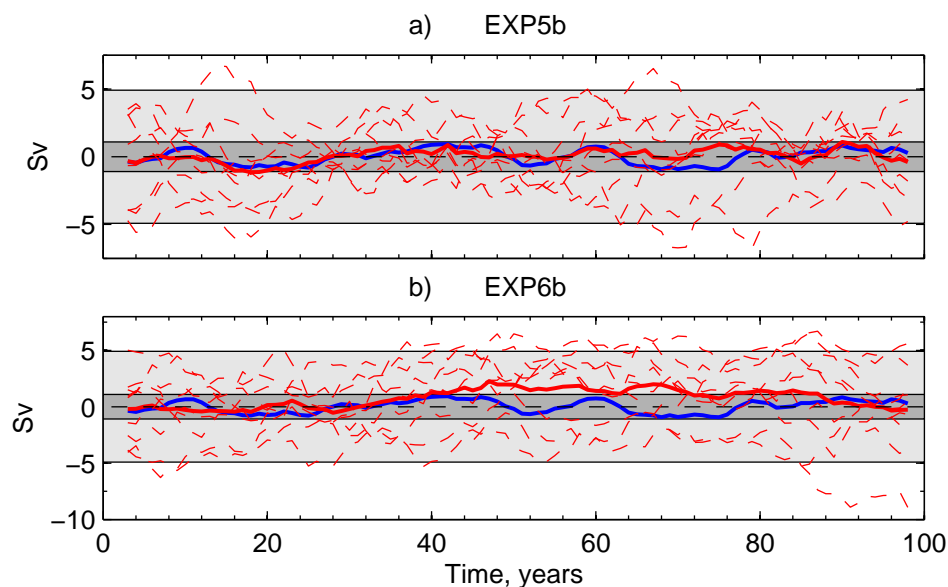


Figure 6.13: Drake Passage transport anomalies for: a) EXP5b; b) EXP6b. Light (dark) shaded area shows the 2σ (95%) spread of the control ensemble (mean) around the 100 year mean. Dashed (solid) red lines show the ensemble (mean) anomalies for each experiment (EXP – time-mean of control). Blue line shows the mean of the control ensemble around the 100 year mean. Data are smoothed using a 5 year running mean. Dashed black line indicates the reference time-mean value for the control ensemble over the 100 year simulation (at zero).

to the anomalies? Could it be that the presence of greater anomalies at depth leads to more of the cooler fresher, water remaining within the Indian and Pacific basins? Or does the spread within the different basins lead to spread at different depths?

As the anomalous water mass spreads southwards, density anomalies occur as the AAIW shoals towards the surface mixed layers. For the cooler, fresher AAIW, surfacing leads to a reduced density as heat is gained from the atmosphere. As this anomaly develops, the meridional density gradient increases in the Southern Ocean, strengthening the ACC (process illustrated in Figure 5.27). For years 40-90 this leads to an increased transport through Drake Passage (Figure 6.13b). The strengthened ACC may then account for greater eastward transport, leading to increased anomalies in the Pacific. The response to a warm, saline anomaly can be opposite, with the increased density reducing the meridional density gradient. The strength of the currents may be decreased in parts of the Southern Ocean for EXP5b, however the impact does not extend as far as that seen in EXP6b, with no significant change in Drake Passage (Figure 6.13a). Non-linearity arises as the change in current strength affects the distribution of the anomalous water mass in the world ocean. For EXP5b, a greater portion of the anomaly then moves westwards,

into the Atlantic basin. This difference in global spread can then account for the difference in vertical distribution of the anomaly. For example, as more of the warm, saline water moves northward in the Atlantic, a greater portion enters the deep levels (levels 14-20 of HadCM3; > 1500 m).

Some surface responses do appear to be opposite (linear) between the experiments. As anomalies surface in the Southern Ocean, SST anomalies lead to SAT anomalies in the Southern Hemisphere for both experiments. There is also a similar response in the northern hemisphere Atlantic to that seen in Chapter 3. As the water mass moves northwards, surfacing anomalies and resulting changes in the MOC lead to SST anomalies in the subtropical North Atlantic, SPG and GIN Seas. However, unlike EXP1b, an increased MOC strength can be seen for EXP5b. As the anomalous AAIW from the Indian Ocean is advected southwards before entering the Atlantic, shoaling isopycnals allow the water mass to have greater contact with the atmosphere than in EXP1b. This leads to greater density anomalies in the intermediate waters, which then move northwards through the Atlantic. The salt anomaly also moves northwards at greater depth in the Atlantic for EXP5b than for EXP6b, due to the non-linear response mechanism described in Section 3.5 (illustrated in Figure 3.32).

Over the Indian Ocean, the atmospheric response to both experiments showed signs of IOD variability. Spencer *et al.* (2005) show that while HadCM3 does reproduce the key features of SST variability, the poor vertical resolution of the ocean model leads to the anomalies persisting and reinvigorating in following years. In models with increased vertical resolution, surface anomalies are able to separate from the anomalies in the sub-surface thermocline, preventing this unrealistic response. Therefore, the peaks in the DMI seen for these simulations are not likely to be a realistic response. The PDO response in the Pacific is also similar to that seen in Chapter 5. As a similar response is seen in both experiments, these anomalies may be due to the state of the Control ensemble at these times.

Chapter 7

Discussion

7.1 Does perturbing AAIW affect climate?

The aim of this thesis has been to investigate whether changes in AAIW can have an impact on the climate system. For changes in the ocean to have an impact on the atmosphere, temperature or heat flux anomalies must develop at the surface. From these experiments, it has been shown that there is a surface response to changing properties at intermediate depths in each of the three major ocean basins. The key regions where AAIW is found to reach the sea surface are shown in Figure 7.1. They are:

- equatorial regions, through wind-driven upwelling.
- eastern boundaries, through wind-driven upwelling.
- in the southern hemisphere, $\sim 30\text{-}50^\circ\text{S}$, due to shoaling isopycnals and/or deep mixed layer.
- in the northern hemisphere, the Kuroshio Extension, NAC, North Atlantic SPG and GIN Seas, due to shoaling isopycnals and/or regions of deep mixed layers.

Although SSS anomalies are found in each of these regions, they are not always accompanied by SST anomalies. As the anomalous water mass reaches the surface, anomalous heat fluxes lead to heat anomalies being lost to the atmosphere. In equatorial regions, heat fluxes and the large range of internal variability lead to few significant SST anomalies developing. However, the salinity anomaly leads to no atmospheric response. Significant

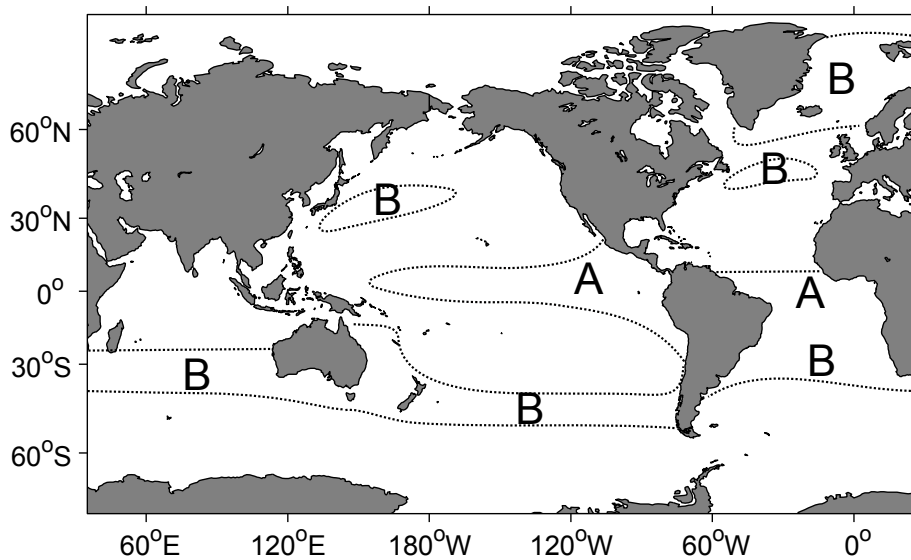


Figure 7.1: Map to show key regions where AAIW reaches the surface layers, leading to surface temperature and salinity anomalies. Regions are labelled with A or B, to indicate the mechanisms responsible for surfacing: A: equatorial or coastal upwelling, due to wind stress; B: shoaling of isopycnals and/or deep mixed layer depths.

SSS anomalies are found in equatorial regions, and persist for the entire simulation in EXP3b.

Perturbing AAIW does have an impact on the climate system. On decadal timescales, anomalies in atmospheric temperature are found to be predominantly driven by the ocean, and linked with SST anomalies of the same sign. Therefore, regions where the warmer or cooler AAIW comes to the surface may be associated with warmer or cooler SAT. The atmospheric response to AAIW will be discussed further in Section 7.3.

7.2 Non-linear responses

Although the experiments carried out here were initially density-compensating, interaction with the atmosphere leads to heat flux anomalies, but no direct response to surface salinity anomalies. This results in opposing density anomalies for the warming and cooling experiments. The depth distributions of salt anomalies at the end of each experiment are illustrated in Figure 7.2. In the Atlantic Ocean, opposing density anomalies lead to the fresher water spending a greater time in the surface layers (< 300 m; Figure 3.32). The lighter water mass then leads to a reduction of the Atlantic MOC as it reaches the SPG and GIN Seas. The denser, saltier water mass spends more time at intermediate

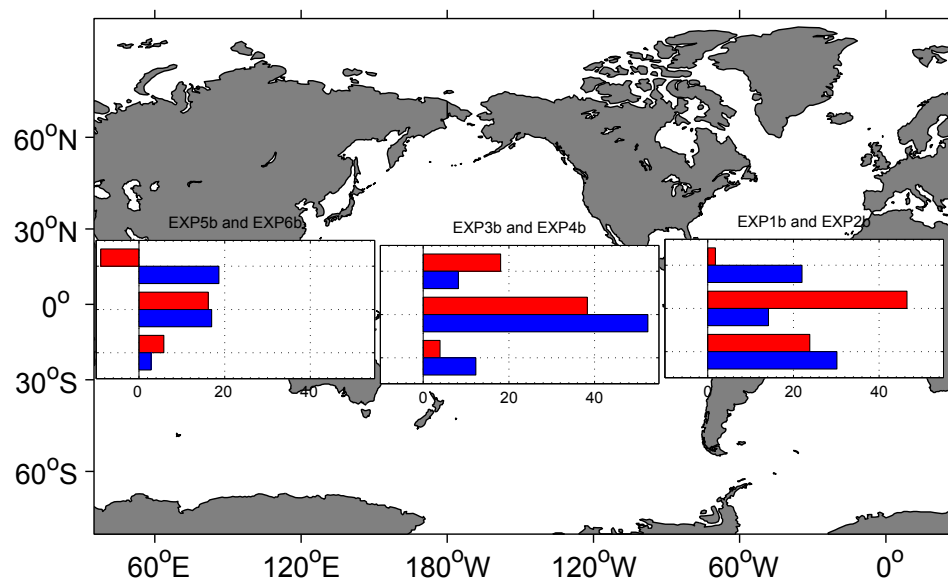


Figure 7.2: Percentage of the initial salt perturbation left at: upper (< 300 m; top 2 bars), intermediate (300 – 1500 m; middle 2 bars) and deep (> 1500 m; bottom 2 bars) levels, after 100 years. Results refer to totals left in the initially perturbed basin: EXP1b and EXP2b for the Atlantic; EXP3b and EXP4b for the Pacific; EXP5b and EXP6b for the Indian Ocean. Red bars refer to warm, salty perturbations; blue bars refer to cool, fresh perturbations. Note that values for each experiment do not sum to 100% when anomalies are advected out of the originally perturbed basin.

depths, leading to less interaction with the atmosphere, and hence less response in the MOC. However, for warm, salty perturbations made in the Pacific and Indian Oceans, the perturbed water mass that subsequently enters the Atlantic does lead to an increased MOC strength. As the anomalous water is advected towards the Atlantic in the Southern Ocean, it spends a greater time in the surface layers, leading to greater density anomalies, when compared with EXP1b. As meridional OHT is correlated with the MOC, these changes in ocean circulation contribute to basin-wide SST anomalies. This effect is seen most clearly for EXP2b (Figure 4.14).

In the Pacific Ocean, the final depth distribution of the anomaly is not the same as that in the Atlantic (Figure 7.2). An increased proportion of salty water is found in the upper 300 m (Figure 7.2, EXP3b). This is likely due to the increased shallow, wind-driven overturning during EXP3b, compared with EXP4b. As the MSLP (and hence large-scale wind patterns) in the Pacific are influenced by the PDO, this result may be due to internal climate variability rather than a response to the perturbations. In the Indian Ocean, the surface layer becomes fresher during EXP5b. The distribution of heat and salt in this ocean is influenced by the strength of the ITF, which increases during EXP5b,

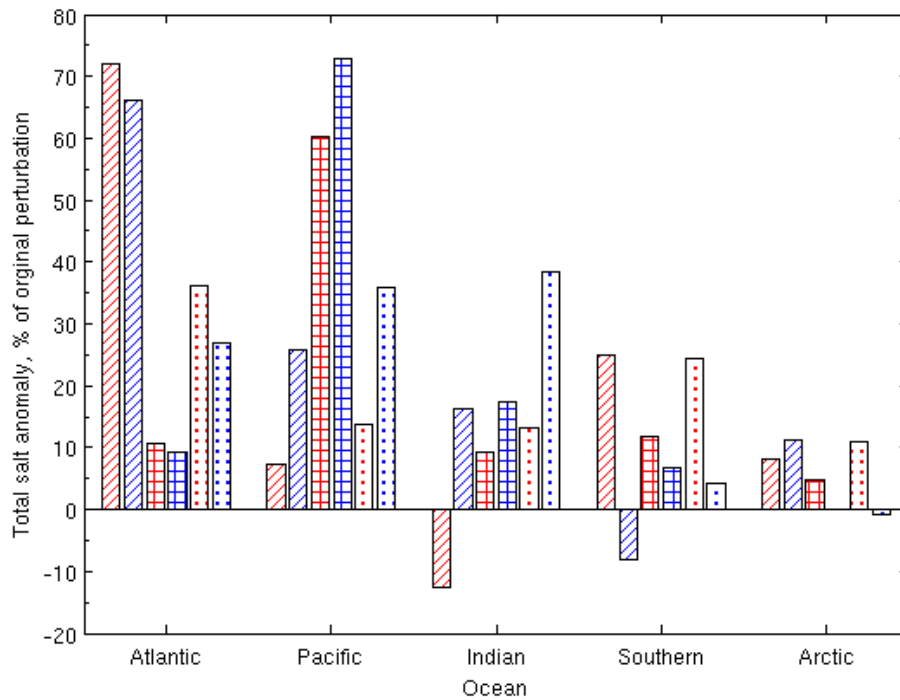


Figure 7.3: Percentage of original salt perturbation found in each ocean basin after 100 years, for each experiment. Red bars indicate warm, salty initial perturbations; blue bars indicate cool, fresh initial perturbations. For each basin, hatched bars refer to EXP1b and EXP2b; cross-hatched bars refer to EXP3b and EXP4b; dotted bars refer to EXP5b and EXP6b.

and decreases during EXP6b. The ITF can be influenced by either wind stress (ENSO) or bottom pressure anomalies in the Pacific. The long term trends in these experiments occur in the lower level of the flow (> 250 m), which is driven by bottom pressure anomalies in the Pacific.

The surfacing of the anomalous water mass also leads to non-linear responses in the Southern Ocean (Figure 5.27). Changes in the meridional density gradient in the ocean lead to differing responses in the ACC transport, and hence differing global distributions of the salt anomaly (Figure 7.3). As the ACC transport increases when the fresh anomalies reach the Southern Ocean, this may account for the greater proportion of the salt anomaly entering the Indian and Pacific Oceans. In the Atlantic, the decreased MOC in the case of fresh anomalies (initiated in each basin) also leads to less meridional transport into the basin. For saline anomalies, there is less eastward transport into the Indian and Pacific Oceans, and more northward transport into the Atlantic with an increased MOC. Changes in the MOC can also account for the spread of salt anomalies in the Arctic Ocean (Figure 7.3).

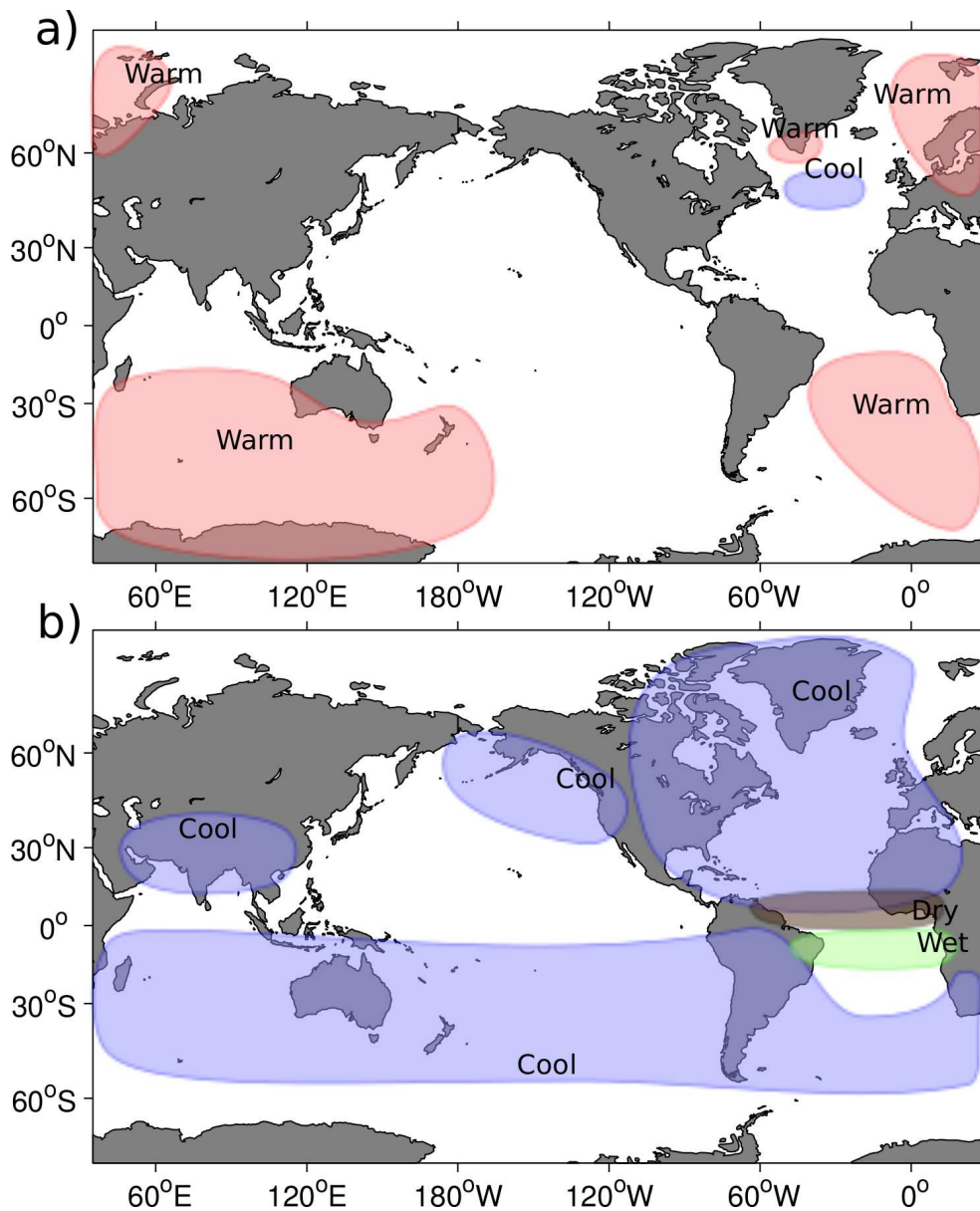


Figure 7.4: Schematic to illustrate global atmospheric responses to perturbations in Antarctic Intermediate Water: a) warming, salting (EXPIb,3b,5b); b) cooling, freshening (EXP2b,4b,6b). Figure summarises the major long-term responses throughout the course of each simulation, for surface air temperature and precipitation.

7.3 Atmospheric responses

Figure 7.4 summarises the major atmospheric responses to either a warming or cooling of AAIW. The majority of signals occur within the Atlantic and Southern Ocean. In the North, surfacing of warm/cool anomalies in the North Atlantic STG, SPG and GIN Seas leads to warming/cooling of the overlying atmosphere. The response is significant over a larger area for the cool, fresh perturbation due to a greater proportion of the fresher water remaining at the surface, and the Atlantic MOC decreasing. Sutton and Hodson

(2005) show that basin-wide changes in SST can lead to MSLP and precipitation anomalies over the surrounding continents. Evidence of this same response was found for EXP2. However, despite the stronger SST response for EXP2b, the MSLP and precipitation responses over North America and Africa were less significant in EXP2b than EXP2. The precipitation anomalies in the tropical Atlantic for the cooling experiments are consistent with a southward shift of the ITCZ due to the decreased MOC and change in meridional temperature gradient (Vellinga and Wu, 2004).

For both the warming and cooling experiments, there is a cooling in the NAC (Figure 7.4). In Section 3.3.2.1, this was shown to result from a divergence of OHT, with an increased SPG transport bringing cooler, fresher water into the NAC. For EXP2, this anomaly persists from year 30, to the end of the entire simulation. The reduced SST forces an increased MSLP in the region, causing wind stress anomalies that act to strengthen the SPG. This results in a feedback loop, with the increased SPG transport then bringing cooler, fresher water into the NAC, leading to a more significant response to the perturbation. The response is less persistent for EXP2b. However, there is a decreased SST and divergence of OHT in the NAC, which lasts from year 60 to the end of the simulation. For the warming experiments, the cool anomalies may initially result due to reduced MSLP over Greenland, caused by increased SST in the region. This leads to wind stress anomalies over the Labrador Sea and SPG.

In the Pacific, SST and SAT anomalies appear to be predominantly associated with the ENSO and PDO. It is therefore unclear whether this result is a response to the perturbation, or internal variability of the model climate. EXP1b-6b all show a cool phase of the PDO for years 41-50. During this time, the mean of the control ensemble is in a strong warm phase of the PDO. This shows that whilst varying the initial ocean conditions does improve confidence in our results, there is still an influence from the control state of the simulation. Increasing the ensemble size of the experiments, or adding a passive tracer to the perturbed AAIW may have helped to address this issue. For EXP3, surfacing warm anomalies in the equatorial Pacific were shown to cause a negative phase of the SAM. This response was likely sensitive to the initial ocean conditions, as the same response was not seen for EXP3b.

As the anomalies surface in the Southern Ocean, SAT anomalies occur for both the

warming and cooling experiments (Figures 7.1 and 7.4). SST anomalies in the Southern Ocean have been shown to cause shifts in the SAM (due to the meridional SST gradient; Marshall and Connolley, 2006; Sen Gupta and England, 2007a), however there was no long term trend in MSLP over the Southern Ocean in these experiments. The SAT response over the Southern Ocean was strongest in the case of the Indian Ocean perturbations, due to the net southward transport of intermediate waters in Indian Ocean. The surface response over the Indian Ocean also showed patterns associated with the IOD. The IOD in HadCM3 is known to not be realistic, showing greater persistence than seen in observations (Spencer *et al.*, 2005). Therefore, it is unlikely that this is a realistic response to changes in AAIW.

7.4 What response can we expect in reality?

Climate projections suggest that AAIW will change in our warming climate, with a warming of the salinity minimum at depth, and cooling and freshening on isopycnals (e.g. Banks, 2000b; Sen Gupta *et al.*, 2009; Downes *et al.*, 2011). Figure 7.5 illustrates how a warming of the water column can be observed as a decreased temperature and salinity, for isopycnals initially above the salinity minimum. In the case of a cooling and freshening on isopycnals, our results from the cooling and freshening experiments may be most useful for understanding potential climate responses. A decreasing MOC is consistent with climate projections (Gregory *et al.*, 2005), and may contribute to reduced warming in the North Atlantic (i.e. negative feedback), in particular in the region of the NAC. The positive feedback mechanism proposed for cooling in the NAC (Section 3.3.2.1) may also be applicable for climate projections, as an increased occurrence of positive NAO phases has been suggested in future climate scenarios (Meehl *et al.*, 2007).

Recent observations have shown a warming of the AAIW core (McCarthy *et al.*, 2011; Schmidtko and Johnson, 2011), and along isopycnals initially below the salinity minimum this can lead to an increased temperature and salinity (Figure 7.5). Lessons should then also be learned from the warming perturbations presented here. These experiments have shown that additional heat content in the ocean does not cause significant changes in the equatorial regions, but may contribute to a warming at higher latitudes, in particular in the GIN Seas and the Southern Ocean. This suggests that warmer AAIW could lead to a

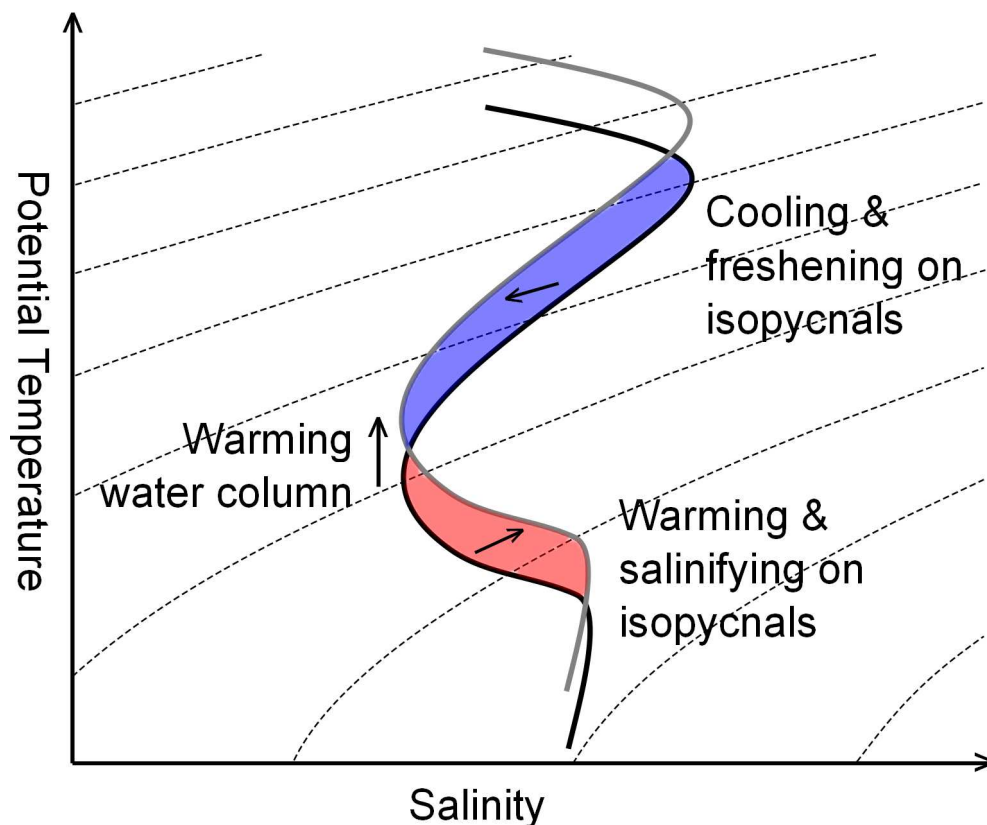


Figure 7.5: Schematic to illustrate changes on isopycnals for AAIW in the case of a warming water column. The solid black (grey) line indicates the potential temperature-salinity profile of the water column before (after) warming. Dashed lines show isopycnal surfaces. For isopycnals initially above the salinity minimum, AAIW is observed to cool and freshen (blue shading). For isopycnals initially below the salinity minimum, AAIW is observed to have an increased temperature and salinity (red shading). This principal is discussed fully by Bindoff and McDougall (1994).

positive feedback at high latitudes. Our perturbations were much larger than the observed heat changes in the ocean for the past century, however climate models suggest warming of up to 1°C over the next century (e.g. Sen Gupta *et al.*, 2009), therefore the magnitude of changes in our experiment may not be entire unrealistic.

It is worth remembering that as AAIW is formed in the Southern Ocean, the Southern Ocean responses seen here may not be applicable to real-world changes in AAIW. However, they do illustrate how changes in individual ocean basins can spread to other regions of the global ocean. Changes in the Southern Ocean and ACC transport can lead to variations in the global spread of AAIW, along with its heat and salt variations.

7.5 Possibilities for future work?

From this thesis, I feel that there are a number of key areas for future work:

- Further perturbation experiments
 - using different coupled models, with more realistic representations of AAIW (e.g. Sloyan and Kamenkovich, 2007).
 - using varying magnitudes of perturbations - sensitivity tests and increased signal to noise ratio.
 - increased ensemble sizes of previous experiments.
 - addition of passive tracer to the perturbed region.
- Continued analysis of AAIW control states, using both models and observations
 - What is the range of internal variability, and what are the causes?
 - Are trends in observations outside this range of variability?

Whilst it would have been interesting to perform a sensitivity analysis for this thesis, with varying control conditions and magnitudes of perturbations, time and computer power were not available. Using ensembles with varying initial states in the ocean and atmosphere gave greater confidence in the results, however it is still clear that the state of the control runs can influence the results. Increasing the ensemble size of the previous experiments would address this issue. Whilst the perturbations performed here were large with respect to the observed changes, performing larger perturbations may also allow for a greater signal to noise ratio. The inclusion of a passive tracer in the perturbed region would also allow for clearer tracking of the path of the anomalous water, and would be a useful addition to future experiments.

Performing further experiments with various models would provide greater insight into the influence of AAIW on the climate system. For HadCM3, it is clear that the North Atlantic and MOC are sensitive to changes in AAIW. Experiments with various ocean models may show whether this is a real response, or whether HadCM3 is overly sensitive in this region. The persistence of anomalies in the NAC is also an interesting response that may warrant further study, and give us further insight into the ocean-atmosphere interactions responsible for North Atlantic climate variability.

Other climate models have shown more realistic representations of AAIW (Sloyan and Kamenkovich, 2007). It would then be interesting to see whether they respond in a

different manner to the results shown here. Sloyan and Kamenskovich (2007) show that AAIW in HadCM3 lies at shallower depths than seen in observations. This may affect the transport of heat and salt into the surface layers of the ocean. CHIME is a version of HadCM3 that includes a hybrid coordinate ocean model (Megann *et al.*, 2010). In this model, the ocean is observed to be less diffusive, allowing water masses such as AAIW to extend further through the ocean before their core properties are eroded. This may have consequences for how heat and salt anomalies are transported northwards the ocean, away from AAIW formation regions. It is also worth noting that HadCM3 is not resolve eddies in the ocean. More recently, higher resolution coupled models have been developed, which are eddy permitting. HiGEM is a higher resolution version of the Hadley Centre coupled model, with a resolution of $1/3^\circ$ in the ocean (Shaffrey *et al.*, 2009). As eddies have been shown to play a key role in the formation and subduction of AAIW (e.g. Marshall, 1997; Sørensen *et al.*, 2001; Sloyan *et al.*, 2010), it would be interesting to see the impact of perturbation experiments in such higher resolution models.

As surface anomalies have been shown to develop on decadal timescales, these results also emphasize the importance of observations at intermediate depths for decadal predictions. The growing density of Argo floats in the global ocean are helping to improve our knowledge of the ocean state to depths of up to 2000 m and projects such as the Southern Ocean Observing System (SOOS) are now focusing on long term observational time series. Much work is still to be done, and the results presented here show that it is worthwhile pursuing.

7.6 Summary

This thesis has shown that there is a surface response to changes in AAIW at depth in each of the three major ocean basins. When the water mass surfaces in the equatorial regions, there is no significant change in SST. There is a greater response when the anomalies surface in higher latitudes. Anomalous sea-to-air heat fluxes leave density anomalies in the ocean. Resulting changes in ocean circulation then cause the responses to warm and cool perturbations to not be equal and opposite. The North Atlantic appears to be particularly sensitive to cool, fresh perturbations, with the density anomalies leading to changes in the MOC, outside the range of internal variability for the control. Surfacing anomalies and

changes in OHT cause basin-wide changes in surface ocean and overlying atmosphere on multi-decadal timescales. Some results from the Pacific Ocean experiments are less certain. Further model runs are needed to establish whether the patterns seen are due to internal variability or are a real response to the perturbations.

Appendix A

List of Experiments

For each experiment, perturbations were made in the latitude band of 10-20°S, within the density boundaries of Antarctic Intermediate Water for that particular ocean basin. The chosen density boundaries were: Atlantic = 1027.9–1029.4; Pacific = 1027.2–1029.1; Indian = 1027.5–1029.1. Further details can be found in Section 3.2.

Table A.1: List of perturbation experiments carried out.

Label	Ensemble Type ¹	Perturbation ²
EXP1	A	Atlantic, +1°C
EXP1b	B	Atlantic, +1°C
EXP2	A	Atlantic, -1°C
EXP2b	B	Atlantic, -1°C
EXP3	A	Pacific, +1°C
EXP3b	B	Pacific, +1°C
EXP4	A	Pacific, -1°C
EXP4b	B	Pacific, -1°C
EXP5	A	Indian, +1°C
EXP5b	B	Indian, +1°C
EXP6	A	Indian, -1°C
EXP6b	B	Indian, -1°C

¹ Ensemble types: A = Ocean: 1/12/2789, Atmosphere: (1-9)/12/2789; B = Ocean and atmosphere: 1/12/(2789, 2839, 2889, 2939, 2989, 3039, 3089, 3139, 3189). Dates given refer to the date of the start dump used for the initial conditions, in model years.

² For each temperature perturbation, a density compensating change in salinity was also made.

References

- Aoki, S., N. L. Bindoff, and J. A. Church (2005), Interdecadal water mass changes in the Southern Ocean between 30 degrees E and 160 degrees E, *Geophys Res Lett*, 32(7).
- Arbic, B., and W. Owens (2001), Climatic warming of Atlantic intermediate waters, *J Clim*, 14(20), 4091–4108.
- Baehr, J., K. Keller, and J. Marotzke (2008), Detecting potential changes in the meridional overturning circulation at 26 degrees N in the Atlantic, *Clim Change*, 91(1-2), 11–27.
- Banks, H. (2000a), Indonesian Throughflow in a coupled climate model and the sensitivity of the heat budget and deep overturning, *J Geophys Res*, 105(C11), 26,135–26,150.
- Banks, H. (2000b), Ocean heat transport in the South Atlantic in a coupled climate model, *J Geophys Res*, 105(C1), 1071–1092.
- Banks, H. T., and N. L. Bindoff (2003), Comparison of observed temperature and salinity changes in the Indo-Pacific with results from the coupled climate model HadCM3: Processes and mechanisms, *J Clim*, 16(1), 156–166.
- Banks, H. T., S. Stark, and A. B. Keen (2007), The adjustment of the coupled climate model HadGEM1 toward equilibrium and the impact on global climate, *J Clim*, 20(23), 5815–5826.
- Bindoff, N., J. Willebrand, V. Artale, A. Cazenave, J. Gregory, S. Gulev, K. Hanawa, C. Le Quéré, S. Levitus, Y. Nojiri, C. Shum, L. Talley, and A. Unnikrishnan (2007), Observations: Oceanic Climate Change and Sea Level, in: *Climate Change 2007: The Physical Science Basis. Contribution of Working Group I to the Fourth Assessment Report of the Intergovernmental Panel on Climate Change* (Solomon, S., D. Qin, M. Manning, Z. Chen, M. Marquis, K. Averyt, M. Tignor, and H. Miller, eds.), Cambridge University Press, Cambridge, United Kingdom and New York, NY, USA.
- Bindoff, N. L., and T. J. McDougall (1994), Diagnosing climate change and ocean ventilation using hydrographic data, *J Phys Oceanogr*, 24(6), 1137–1152.
- Bindoff, N. L., and T. J. McDougall (2000), Decadal changes along an Indian Ocean section at 32 degrees S and their interpretation, *J Phys Oceanogr*, 30(6), 1207–1222.
- Bjerknes, J. (1969), Atmospheric teleconnections from the equatorial Pacific, *Mon Wea Rev*, 97, 163–172.
- Bryan, K. (1969), Climate and ocean circulation .3. Ocean model, *Mon Wea Rev*, 97(11), 806–&.
- Bryden, H. L., E. L. McDonagh, and B. A. King (2003), Changes in ocean water mass properties: Oscillations or trends?, *Science*, 300(5628), 2086–2088.

- Cattle, H., and J. Crossley (1995), Modeling Arctic climate change, *Philosophical Transactions of the Royal Society of London Series a-Mathematical Physical and Engineering Sciences*, 352(1699), 201–213.
- Clarke, A., J. Church, and J. Gould (2001), Ocean Processes and Climate Phenomena, in: *Ocean Circulation and Climate*.
- Collins, M., S. F. B. Tett, and C. Cooper (2001), The internal climate variability of HadCM3, a version of the Hadley Centre coupled model without flux adjustments, *Clim Dyn*, 17(1), 61–81.
- Cooper, C., and C. Gordon (2002), North Atlantic oceanic decadal variability in the Hadley Centre coupled model, *J Clim*, 15(1), 45–72.
- Cox (1984), *A primitive equation, 3-dimensional model of the ocean*, Technical Rep 1, GDFL Ocean Group, Princeton NJ, USA.
- Cox, P. M., R. A. Betts, C. B. Bunton, R. L. H. Essery, P. R. Rowntree, and J. Smith (1999), The impact of new land surface physics on the GCM simulation of climate and climate sensitivity, *Clim Dyn*, 15(3), 183–203.
- Cunningham, S. A., T. Kanzow, D. Rayner, M. O. Baringer, W. E. Johns, J. Marotzke, H. R. Longworth, E. M. Grant, J. J. M. Hirschi, L. M. Beal, C. S. Meinen, and H. L. Bryden (2007), Temporal variability of the Atlantic meridional overturning circulation at 26.5 degrees N, *Science*, 317(5840), 935–938.
- Curry, R., B. Dickson, and I. Yashayaev (2003), A change in the freshwater balance of the Atlantic Ocean over the past four decades, *Nature*, 426(6968), 826–829.
- Curry, W., and D. Oppo (2005), Glacial water mass geometry and the distribution of delta C-13 of Sigma CO2 in the western Atlantic Ocean, *Paleoceanography*, 20(1).
- Cusack, S., A. Slingo, J. M. Edwards, and M. Wild (1998), The radiative impact of a simple aerosol climatology on the Hadley Centre atmospheric GCM, *Q J R Meteorol Soc*, 124(551), 2517–2526.
- Deacon, G. E. R. (1937), The hydrology of the Southern Ocean, *Discovery Reports*, 15, 124.
- Delworth, T., and M. Mann (2000), Observed and simulated multidecadal variability in the Northern Hemisphere, *Clim Dyn*, 16(9), 661–676.
- Deser, C., and M. Blackmon (1993), Surface climate variations over the North Atlantic Ocean during winter: 1900-1989, *J Clim*, 6(9), 1743–1753.
- Deser, C., and M. Blackmon (1995), On the relationship between tropical and North Pacific sea surface temperature variations, *J Clim*, 8(6), 1677–1680.
- Dong, B., and R. Sutton (2001), The dominant mechanisms of variability in Atlantic ocean heat transport in a coupled ocean-atmosphere GCM, *Geophys Res Lett*, 28(12), 2445–2448.
- Dong, B., and R. T. Sutton (2002a), Variability in North Atlantic heat content and heat transport in a coupled ocean-atmosphere GCM, *Clim Dyn*, 19(5-6), 485–497.
- Dong, B. W., and R. T. Sutton (2002b), Adjustment of the coupled ocean-atmosphere system to a sudden change in the thermohaline circulation, *Geophys Res Lett*, 29(15).

- Downes, S. M., A. Gnanadesikan, S. M. Griffies, and J. L. Sarmiento (2011), Water mass exchange in the Southern Ocean in coupled climate models, *J Phys Oceanogr*, *41*(9), 1756–1771.
- Edwards, J. M., and A. Slingo (1996), Studies with a flexible new radiation code .1. Choosing a configuration for a large-scale model, *Q J R Meteorol Soc*, *122*(531), 689–719.
- Enfield, D., and D. Mayer (1997), Tropical Atlantic sea surface temperature variability and its relation to El Nino Southern Oscillation, *J Geophys Res*, *102*(C1), 929–945.
- England, M., and F. Huang (2005), On the interannual variability of the Indonesian Throughflow and its linkage with ENSO, *J Clim*, *18*(9), 1435–1444.
- England, M., and E. Maier-Reimer (2001), Using chemical tracers to assess ocean models, *Rev Geophys*, *39*(1), 29–70.
- England, M. H. (1993), Representing the global-scale water masses in ocean general circulation models, *J Phys Oceanogr*, *23*(7), 1523–1552.
- Environment Canada (2011), Canadian Climate Normals or Averages 1971-2000, http://www.climate.weatheroffice.gc.ca/climate_normals/index_e.html, accessed 01/06/2011.
- Ganachaud, A., and C. Wunsch (2003), Large-scale ocean heat and freshwater transports during the World Ocean Circulation Experiment, *J Clim*, *16*(4), 696–705.
- Gent, P. R., and J. C. McWilliams (1990), Isopycnal mixing in ocean circulation models, *J Phys Oceanogr*, *20*(1), 150–155.
- Georgi, D. T. (1979), Modal properties of Antarctic Intermediate Water in the southeast Pacific and the South Atlantic, *J Phys Oceanogr*, *9*(3), 456–468.
- Godfrey, J. S. (1989), A sverdrup model of the depth-integrated flow for the world ocean allowing for island circulations, *Geophys Astrophys Fluid Dyn*, *45*, 89–112.
- Gordon, C., C. Cooper, C. A. Senior, H. Banks, J. M. Gregory, T. C. Johns, J. F. B. Mitchell, and R. A. Wood (2000), The simulation of SST, sea ice extents and ocean heat transports in a version of the Hadley Centre coupled model without flux adjustments, *Clim Dyn*, *16*(2-3), 147–168.
- Goulden, C. H. (1952), *Methods of Statistical Analysis*, Wiley, New York.
- Graham, J. A., D. P. Stevens, K. J. Heywood, and Z. Wang (2011), North Atlantic climate responses to perturbations in Antarctic Intermediate Water, *Clim Dyn*, *37*, 297–311.
- Gregory, D., R. Kershaw, and P. M. Inness (1997), Parametrization of momentum transport by convection .2. Tests in single-column and general circulation models, *Q J R Meteorol Soc*, *123*(541), 1153–1183.
- Gregory, J., K. Dixon, R. Stouffer, A. Weaver, E. Driesschaert, M. Eby, T. Fichefet, H. Hasumi, A. Hu, J. Jungclaus, I. Kamenkovich, A. Levermann, M. Montoya, S. Murakami, S. Nawrath, A. Oka, A. Sokolov, and R. Thorpe (2005), A model intercomparison of changes in the Atlantic thermohaline circulation in response to increasing atmospheric CO₂ concentration, *Geophys Res Lett*, *32*(12).

- Hall, A., and M. Visbeck (2002), Synchronous variability in the southern hemisphere atmosphere, sea ice, and ocean resulting from the annular mode, *J Clim*, 15(21), 3043–3057.
- Hátún, H., A. Sandø, H. Drange, B. Hansen, and H. Valdimarsson (2005), Influence of the Atlantic subpolar gyre on the thermohaline circulation, *Science*, 309(5742), 1841–1844.
- Hewitt, C. D., A. J. Broccoli, J. F. B. Mitchell, and R. J. Stouffer (2001), A coupled model study of the Last Glacial Maximum: Was part of the North Atlantic relatively warm?, *Geophys Res Lett*, 28, 1571–1574.
- Hibler, W. D. (1979), Dynamic thermodynamic sea ice model, *J Phys Oceanogr*, 9(4), 815–846.
- Holzer, M., F. Primeau, W. J. Smethie, and S. Khatiwala (2010), Where and how long ago was water in the western North Atlantic ventilated? Maximum entropy inversions of bottle data from WOCE line A20, *J Geophys Res*, 115.
- Hughes, T., and A. Weaver (1996), Sea surface temperature - Evaporation feedback and the ocean's thermohaline circulation, *J Phys Oceanogr*, 26(4), 644–654.
- IPCC (2001), *Climate Change 2001: The Scientific Basis. Contribution of Working Group I to the Third Assessment Report of the Intergovernmental Panel on Climate Change*, Cambridge University Press, Cambridge, United Kingdom and New York, NY, USA.
- IPCC (2007), *Climate Change 2007: The Physical Science Basis. Contribution of Working Group I to the Fourth Assessment Report of the Intergovernmental Panel on Climate Change*, Cambridge University Press, Cambridge, United Kingdom and New York, NY, USA.
- Iudicone, D., K. B. Rodgers, R. Schopp, and G. Madec (2007), An exchange window for the injection of Antarctic Intermediate Water into the South Pacific, *J Phys Oceanogr*, 37(1), 31–49.
- Johns, T. C., R. E. Carnell, J. F. Crossley, J. M. Gregory, J. F. B. Mitchell, C. A. Senior, S. F. B. Tett, and R. A. Wood (1997), The second Hadley Centre coupled ocean-atmosphere GCM: Model description, spinup and validation, *Clim Dyn*, 13(2), 103–134.
- Kraus, E. B., and J. S. Turner (1967), A one-dimensional model of seasonal thermocline .2. General theory and its consequences, *Tellus*, 19(1), 98–&.
- Kushnir, Y., W. Robinson, I. Blade, N. Hall, S. Peng, and R. Sutton (2002), Atmospheric GCM response to extratropical SST anomalies: Synthesis and evaluation, *J Clim*, 15(16), 2233–2256.
- Levitus, S., J. Antonov, and T. Boyer (2005), Warming of the world ocean, 1955-2003, *Geophys Res Lett*, 32(2).
- Levitus, S., J. I. Antonov, T. P. Boyer, R. A. Locarnini, H. E. Garcia, and A. V. Mishonov (2009), Global ocean heat content 1955-2008 in light of recently revealed instrumentation problems, *Geophys Res Lett*, 36.
- Mantua, N., S. Hare, Y. Zhang, J. Wallace, and R. Francis (1997), A Pacific interdecadal climate oscillation with impacts on salmon production, *Bull Amer Meteor Soc*, 78(6), 1069–1079.

- Marshall, D. (1997), Subduction of water masses in an eddying ocean, *J Mar Res*, 55(2), 201–222.
- Marshall, G. J., and W. M. Connolley (2006), Effect of changing Southern Hemisphere winter sea surface temperatures on Southern Annular Mode strength, *Geophys Res Lett*, 33(17).
- McAvaney, B., C. Covey, S. Joussaume, V. Kattsov, A. Kitoh, W. Ogana, A. Pitman, A. Weaver, R. Wood, and Z.-C. Zhao (2001), Model Evaluation, in: *Climate Change 2001: The Scientific Basis. Contribution of Working Group I to the Third Assessment Report of the Intergovernmental Panel on Climate Change* (Houghton, J., Y. Ding, D. Griggs, M. Noguer, P. van der Linden, X. Dai, K. Maskell, and C. Johnson, eds.), Cambridge University Press, Cambridge, United Kingdom and New York, NY, USA.
- McCarthy, G., E. McDonagh, and B. King (2011), Decadal variability of thermocline and intermediate waters at 24 degrees S in the South Atlantic, *J Phys Oceanogr*, 41(1), 157–165.
- McCartney, M. S. (1977), Subantarctic Mode Water, *Deep-Sea Res, A Voyage of Discovery, supplement to*, 103–119.
- McCartney, M. S. (1982), The subtropical recirculation of Mode Waters, *J Mar Res*, 40(Suppl. S), 427–464.
- McDougall, T. J. (1987), Thermobaricity, cabbeling, and water-mass conversion, *J Geophys Res*, 92, 5448–5464.
- Meehl, G., T. Stocker, W. Collins, P. Friedlingstein, A. Gaye, J. Gregory, A. Kitoh, R. Knutti, J. Murphy, A. Noda, S. Raper, I. Watterson, A. Weaver, and Z.-C. Zhao (2007), Global Climate Projections, in: *Climate Change 2007: The Physical Science Basis. Contribution of Working Group I to the Fourth Assessment Report of the Intergovernmental Panel on Climate Change* (Solomon, S., D. Qin, M. Manning, Z. Chen, M. Marquis, K. Averyt, M. Tignor, and H. Miller, eds.), Cambridge University Press, Cambridge, United Kingdom and New York, NY, USA.
- Megann, A. P., A. New, A. Blaker, and B. Sinha (2010), The sensitivity of a coupled climate model to its ocean component, *J Clim*, 23.
- Meyers, G. (1996), Variation of Indonesian throughflow and the El Nino Southern Oscillation, *J Geophys Res*, 101(C5), 12,255–12,263.
- Molinelli, E. (1981), The Antarctic influence on Antarctic Intermediate Water, *J Mar Res*, 39(2), 267–293.
- Naveira Garabato, A. C., L. Jullion, D. P. Stevens, K. J. Heywood, and B. A. King (2009), Variability of Subantarctic Mode Water and Antarctic Intermediate Water in the Drake Passage during the late-twentieth and early-twenty-first centuries, *J Clim*, 22(13), 3661–3688.
- Newman, M., G. Compo, and M. Alexander (2003), ENSO-forced variability of the Pacific Decadal Oscillation, *J Clim*, 16(23), 3853–3857.
- Oke, P., and M. England (2004), Oceanic response to changes in the latitude of the Southern Hemisphere subpolar westerly winds, *J Clim*, 17(5), 1040–1054.

- Oudot, C., J. TERNON, C. ANDRIE, E. BRAGA, and P. MORIN (1999), On the crossing of the equator by intermediate water masses in the western Atlantic Ocean: Identification and pathways of Antarctic Intermediate Water and Upper Circumpolar Water, *J Geophys Res*, 104(C9), 20,911–20,926.
- Pacanowski, R. C., and S. G. H. PHILANDER (1981), Parametrization of vertical mixing in numerical-models of tropical oceans, *J Phys Oceanogr*, 11(11), 1443–1451.
- Pardaens, A. K., H. T. BANKS, J. M. GREGORY, and P. R. ROWNTREE (2003), Freshwater transports in HadCM3, *Clim Dyn*, 21(2), 177–195.
- Piola, A. R., and D. T. GEORGI (1982), Circumpolar properties of Antarctic Intermediate Water and Subantarctic Mode Water, *Deep-Sea Res*, 29(6), 687–711.
- Piola, A. R., and A. L. GORDON (1989), Intermediate waters in the southwest South Atlantic, *Deep-Sea Res*, 36(1), 1–16.
- Pope, V. D., M. L. GALLANI, P. R. ROWNTREE, and R. A. STRATTON (2000), The impact of new physical parametrizations in the Hadley Centre climate model: HadAM3, *Clim Dyn*, 16(2-3), 123–146.
- Randall, D., R. WOOD, S. BONY, R. COLMAN, T. FICHEFET, J. FYFE, V. KATTSOV, A. PITMAN, J. SHUKLA, J. SRINIVASAN, R. STOUFFER, A. SUMI, and K. TAYLOR (2007), Climate Models and Their Evaluation, in: *Climate Change 2007: The Physical Science Basis. Contribution of Working Group I to the Fourth Assessment Report of the Intergovernmental Panel on Climate Change* (Solomon, S., D. Qin, M. Manning, Z. Chen, M. Marquis, K. Averyt, M. Tignor, and H. Miller, eds.), Cambridge University Press, Cambridge, United Kingdom and New York, NY, USA.
- RAPID-WATCH (2011), RAPID-WATCH: Monitoring the Atlantic Meridional Overturning Circulation, <http://www.noc.soton.ac.uk/rapid/rw/>, accessed 01/06/2011.
- Redi, M. H. (1982), Oceanic Isopycnal mixing by coordinate rotation, *J Phys Oceanogr*, 12(10), 1154–1158.
- Richardson, G. (2006), *Climate response to fresh water forcing in the Southern Ocean*, Ph.D. thesis, University of East Anglia.
- Richardson, G., M. R. WADLEY, K. J. HEYWOOD, D. P. STEVENS, and H. T. BANKS (2005), Short-term climate response to a freshwater pulse in the Southern Ocean, *Geophys Res Lett*, 32(3).
- Rintoul, S. (1991), South Atlantic interbasin exchange, *J Geophys Res*, 96, 2675–2692.
- Rintoul, S. R., and M. H. ENGLAND (2002), Ekman transport dominates local air-sea fluxes in driving variability of Subantarctic Mode Water, *J Phys Oceanogr*, 32(5), 1308–1321.
- Rintoul, S. R., C. W. HUGHES, and D. OLBERS (2001), The Antarctic Circumpolar Current System, in: *Ocean Circulation and Climate* (Siedler, G., J. Church, and J. Gould, eds.), pp. 271–302, Academic Press.
- Roberts, M. J., and R. A. WOOD (1997), Topographic sensitivity studies with a BryanCox-type ocean model, *J Phys Oceanogr*, 27, 823–836.

- Russell, J. L., R. J. Stouffer, and K. W. Dixon (2006), Intercomparison of the Southern Ocean circulations in IPCC coupled model control simulations, *J Clim*, *19*(18), 4560–4575.
- Saenko, O. A., A. J. Weaver, and J. M. Gregory (2003), On the link between the two modes of the ocean thermohaline circulation and the formation of global-scale water masses, *J Clim*, *16*(17), 2797–2801.
- Saji, N., B. Goswami, P. Vinayachandran, and T. Yamagata (1999), A dipole mode in the tropical Indian Ocean, *Nature*, *401*(6751), 360–363.
- Santoso, A., and M. H. England (2004), Antarctic Intermediate Water circulation and variability in a coupled climate model, *J Phys Oceanogr*, *34*(10), 2160–2179.
- Schmidtko, S., and G. C. Johnson (2011), Multi-decadal warming and shoaling of Antarctic Intermediate Water, *J Clim*, doi: 10.1175/JCLI-D-11-00021.1.
- Seager, R., Y. Kushnir, M. Visbeck, N. Naik, J. Miller, G. Krahnmann, and H. Cullen (2000), Causes of Atlantic Ocean climate variability between 1958 and 1998, *J Clim*, *13*(16), 2845–2862.
- Semtner, A. J. (1976), Model for thermodynamic growth of sea ice in numerical investigations of climate, *J Phys Oceanogr*, *6*(3), 379–389.
- Sen Gupta, A., and M. H. England (2006), Coupled ocean-atmosphere-ice response to variations in the Southern Annular Mode, *J Clim*, *19*(18), 4457–4486.
- Sen Gupta, A., and M. H. England (2007a), Coupled ocean-atmosphere feedback in the Southern Annular Mode, *J Clim*, *20*(14), 3677–3692.
- Sen Gupta, A., and M. H. England (2007b), Evaluation of interior circulation in a high-resolution global ocean model. Part II: Southern Hemisphere intermediate, mode, and thermocline waters, *J Phys Oceanogr*, *37*(11), 2612–2636.
- Sen Gupta, A., A. Santoso, A. S. Taschetto, C. C. Ummerhofer, J. Trevena, and M. H. England (2009), Projected changes to the Southern Hemisphere ocean and sea ice in the IPCC AR4 climate models, *J Clim*, *22*(11), 3047–3078.
- Shaffrey, L. C., I. Stevens, W. A. Norton, M. J. Roberts, P. L. Vidale, J. D. Harle, A. Jrrar, D. P. Stevens, M. J. Woodage, M. E. Demory, J. Donners, D. B. Clark, A. Clayton, J. W. Cole, S. S. Wilson, W. M. Connolley, T. M. Davies, A. M. Iwi, T. C. Johns, J. C. King, A. L. New, J. M. Slingo, A. Slingo, L. Steenman-Clark, and G. M. Martin (2009), U.K. HiGEM: The new U.K. High-Resolution Global Environment Model model description and basic evaluation, *J Clim*, *22*, 1861–1896.
- Sijp, W. P., and M. H. England (2008), The effect of a northward shift in the southern hemisphere westerlies on the global ocean, *Prog Oceanogr*, *79*(1), 1–19.
- Sloyan, B. M., and I. V. Kamenkovich (2007), Simulation of Subantarctic Mode and Antarctic Intermediate Waters in climate models, *J Clim*, *20*(20), 5061–5080.
- Sloyan, B. M., L. D. Talley, T. K. Chereskin, R. Fine, and J. Holte (2010), Antarctic Intermediate Water and Subantarctic Mode Water formation in the southeast Pacific: the role of turbulent mixing, *J Phys Oceanogr*, *40*(7), 1558–1574.
- Sørensen, J. V. T., J. Ribbe, and G. Shaffer (2001), Antarctic intermediate water mass formation in ocean general circulation models, *J Phys Oceanogr*, *31*(11), 3295–3311.

- Spencer, H., R. Sutton, J. Slingo, M. Roberts, and E. Black (2005), Indian Ocean climate and dipole variability in Hadley Centre coupled GCMs, *J Clim*, *18*(13), 2286–2307.
- Stark, S., C. Harris, and G. Richardson (2005), Southern Ocean variability and climate change in HadCM3, *CLIVAR Exchanges*, *10*(4), 39–41.
- Stark, S., R. A. Wood, and H. T. Banks (2006), Reevaluating the causes of observed changes in Indian Ocean water masses, *J Clim*, *19*(16), 4075–4086.
- Suga, T., and L. D. Talley (1995), Antarctic Intermediate Water circulation in the tropical and subtropical South Atlantic, *J Geophys Res*, *100*(C7), 13,441–13,453.
- Sutton, R. T., and D. L. R. Hodson (2005), Atlantic Ocean forcing of North American and European summer climate, *Science*, *309*(5731), 115–118.
- Sverdrup, H. (1940), Hydrology, Section 2. Discussion., Report B.A.N.Z. Ant. Res. Exped., 192931, Ser. A, *Oceanography*, *3*, 88126.
- Talley, L., and J. Yun (2001), The role of cabbeling and double diffusion in setting the density of the North Pacific Intermediate Water salinity minimum, *J Phys Oceanogr*, *31*(6), 1538–1549.
- Talley, L. D. (1996), Antarctic Intermediate Water in the South Atlantic, in: *South Atlantic - Present and Past Circulation* (Wefer, G., W. H. Berger, G. Siedler, and D. J. Webb, eds.), pp. 219–238, Springer-Verlag.
- Talley, L. D. (2003), Shallow, intermediate, and deep overturning components of the global heat budget, *J Phys Oceanogr*, *33*(3), 530–560.
- Tanaka, Y., and H. Hasumi (2008), Injection of Antarctic Intermediate Water into the Atlantic subtropical gyre in an eddy resolving ocean model, *Geophys Res Lett*, *35*(11).
- Thompson, D. W. J., and J. M. Wallace (2000), Annular modes in the extratropical circulation. Part I: Month-to-month variability, *J Clim*, *13*(5), 1000–1016.
- THOR (2011), Thermohaline Overturning at Risk?, <http://www.eu-thor.eu/>, accessed 01/06/2011.
- Thorpe, R. B., J. M. Gregory, T. C. Johns, R. A. Wood, and J. F. B. Mitchell (2001), Mechanisms determining the Atlantic thermohaline circulation response to greenhouse gas forcing in a non-flux-adjusted coupled climate model, *J Clim*, *14*(14), 3102–3116.
- Tomczak, M. (2007), Variability of Antarctic Intermediate Water properties in the South Pacific ocean, *Ocean Sci*, *3*(3), 363–377.
- Tourre, Y., and W. White (1995), ENSO signals in global upper-ocean temperature, *J Phys Oceanogr*, *25*(6, Part 1), 1317–1332.
- Trenberth, K., and J. Caron (2001), Estimates of meridional atmosphere and ocean heat transports, *J Clim*, *14*(16), 3433–3443.
- Tsuchiya, M. (1989), Circulation of the Antarctic Intermediate Water in the North Atlantic Ocean, *J Mar Res*, *47*(4), 747–755.
- UK Met Office (2011), East Anglia 1971–2000 averages, http://www.metoffice.gov.uk/climate/uk/averages/19712000/areal/east_anglia.html, accessed 01/06/2011.

- Vellinga, M., and R. A. Wood (2002), Global climatic impacts of a collapse of the Atlantic thermohaline circulation, *Clim Change*, 54(3), 251–267.
- Vellinga, M., and P. L. Wu (2004), Low-latitude freshwater influence on centennial variability of the Atlantic thermohaline circulation, *J Clim*, 17(23), 4498–4511.
- Visbeck, M., J. Marshall, T. Haine, and M. Spall (1997), Specification of eddy transfer coefficients in coarse-resolution ocean circulation models, *J Phys Oceanogr*, 27(3), 381–402.
- Weaver, A. J., M. Eby, E. C. Wiebe, C. M. Bitz, P. B. Duffy, T. L. Ewen, A. F. Fanning, M. M. Holland, A. MacFadyen, H. D. Matthews, K. J. Meissner, O. Saenko, A. Schmitner, H. X. Wang, and M. Yoshimori (2001), The UVic Earth System Climate Model: Model description, climatology, and applications to past, present and future climates, *Atmosphere-Ocean*, 39(4), 361–428.
- Weaver, A. J., O. A. Saenko, P. U. Clark, and J. X. Mitrovica (2003), Meltwater pulse 1A from Antarctica as a trigger of the Bølling-Allerød warm interval, *Science*, 299(5613), 1709–1713.
- Wijffels, S. E., N. Bray, S. Hautala, G. Meyers, and W. M. L. Morawitz (1996), The WOCE Indonesian Throughflow repeat hydrography sections: I10 and IR6, *Int. WOCE Newsl.*, pp. 25–28.
- Wong, A. P. S., N. L. Bindoff, and J. A. Church (1999), Large-scale freshening of intermediate waters in the Pacific and Indian oceans, *Nature*, 400(6743), 440–443.
- Wong, A. P. S., N. L. Bindoff, and J. A. Church (2001), Freshwater and heat changes in the North and South Pacific oceans between the 1960s and 1985–94, *J Clim*, 14(7), 1613–1633.
- Wüst, G. (1935), Schichtung und Zirkulation des Atlantischen Ozeans: Die Stratosphäre, in: *Wissenschaftliche Ergebnisse der Deutschen Atlantischen Expedition auf dem Forschungs- und Vermessungsschiff Meteor 1925/1927*, vol. 6, pp. 109–288, English translation, The stratosphere of the Atlantic Ocean, W. J. Emory, Ed., 1978, Amerind, New Delhi.
- Zhou, T., and R. Yu (2004), Sea-surface temperature induced variability of the Southern Annular Mode in an atmospheric general circulation model, *Geophys Res Lett*, 31(24).

List of Acronyms

AABW Antarctic Bottom Water.

AAIW Antarctic Intermediate Water.

AASW Antarctic Surface Water.

ACC Antarctic Circumpolar Current.

AOU Apparent Oxygen Utilisation.

AR4 Fourth Assessment Report (of the IPCC).

CFC chlorofluorocarbon.

CTD conductivity, temperature, depth.

DMI Dipole Mode Index.

DPT Drake Passage transport.

ENSO El Niño Southern Oscillation.

GIN Greenland, Iceland and Norwegian.

IOD Indian Ocean Dipole.

IPCC Intergovernmental Panel on Climate Change.

ITF Indonesian Through-Flow.

LGM last glacial maximum.

MIW Mediterranean Intermediate Water.

MOC meridional overturning circulation.

MSLP mean sea level pressure.

NAC North Atlantic Current.

NADW North Atlantic Deep Water.

NAO North Atlantic Oscillation.

OHT ocean heat transport.

PDO Pacific Decadal Oscillation.

PFZ Polar Frontal Zone.

SAF Subantarctic Front.

SAM Southern Annular Mode.

SAMW Subantarctic Mode Water.

SH Southern Hemisphere.

SO Southern Ocean.

SOI Southern Oscillation Index.

SOOS Southern Ocean Observing System.

SPG subpolar gyre.

SSS sea surface salinity.

SST sea surface temperature.

STG subtropical gyre.

TAR Third Assessment Report (of the IPCC).

THC thermohaline circulation.